Properties of Ion-Inertial Scale Plasmoids Observed by the Juno Spacecraft in the Jovian Magnetotail

Yash Sarkango[1], James A. Slavin[1], Xianzhe Jia[1], Gina A. DiBraccio[2], George B. Clark[3], Weijie Sun[4], Barry H. Mauk[5], William S. Kurth[6], and George B. Hospodarsky[6]

[1]University of Michigan-Ann Arbor
[2]NASA GSFC
[3]Johns Hopkins University Applied Physics Laboratory
[4]University of Michigan - Ann Arbor
[5]Johns Hopkins University
[6]University of Iowa

November 24, 2022

Abstract

We expand on previous observations of magnetic reconnection in Jupiter's magnetosphere by constructing a survey of ion-inertial scale plasmoids in the Jovian magnetotail. We developed an automated detection algorithm to identify reversals in the component and performed the minimum variance analysis for each identified plasmoid to characterize its helical structure. The magnetic field observations were complemented by data collected by the Juno Waves instrument, which is used to estimate the total electron density, and the JEDI energetic particle detectors. We identified 87 plasmoids with 'peak-to-peak' durations between 10 s and 300 s. 31 plasmoids possessed a core field and were classified as flux-ropes. The other 56 plasmoids had minimum field strength at their centers and were termed O-lines. Out of the 87 plasmoids, 58 had in situ signatures shorter than 60 s, despite the algorithm's upper limit to be 300 s, suggesting that smaller plasmoids with shorter durations were more likely to be detected by Juno. We estimate the diameter of these plasmoids assuming a circular cross-section and a travel speed equal to the Alfven speed in the surrounding lobes. Using the electron density inferred by Waves, we contend that these plasmoid diameters were within an order of the local ion-inertial length. Our results demonstrate that magnetic reconnection in the Jovian magnetotail occurs at ion scales like in other space environments. We show that ion-scale plasmoids would need to be released every 0.1 s or less to match the canonical 1 ton/s rate of plasma production due to Io.

Properties of Ion-Inertial Scale Plasmoids Observed by the Juno Spacecraft in the Jovian Magnetotail

Enter authors here:

Yash Sarkango[1], James A. Slavin[1], Xianzhe Jia[1], Gina A. DiBraccio[2], George B. Clark[3], Weijie Sun[1], Barry H. Mauk[3], William S. Kurth[4], and George B. Hospodarsky[4]

[1]University of Michigan - Ann Arbor, USA.

[2]NASA Goddard Space Flight Center, USA.

[3]John Hopkins University – Applied Physics Laboratory, USA

[4]University of Iowa, USA

Corresponding author: Yash Sarkango (sarkango@umich.edu)

Key Points:

- We identify and analyze 87 ion-inertial scale plasmoids (56 O-lines, 31 flux-ropes) in the Jovian magnetotail using an automated algorithm.
- North-South field reversals with peak-to-peak durations less than 60 s are more common than those with durations between 60 and 300 s.
- Ion-inertial scale plasmoids alone cannot account for the >500 kg/s loss-rate deficit unless they are being produced every ~0.1 s or less.

Abstract

We expand on previous observations of magnetic reconnection in Jupiter's magnetosphere by constructing a survey of ion-inertial scale plasmoids in the Jovian magnetotail. We developed an automated detection algorithm to identify reversals in the B_θ component and performed the minimum variance analysis for each identified plasmoid to characterize its helical structure. The magnetic field observations were complemented by data collected by the Juno Waves instrument, which is used to estimate the total electron density, and the JEDI energetic particle detectors. We identified 87 plasmoids with 'peak-to-peak' durations between 10 s and 300 s. 31 plasmoids possessed a core field and were classified as flux-ropes. The other 56 plasmoids had minimum field strength at their centers and were termed O-lines. Out of the 87 plasmoids, 58 had in situ signatures shorter than 60 s, despite the algorithm's upper limit to be 300 s, suggesting that smaller plasmoids with shorter durations were more likely to be detected by Juno. We estimate the diameter of these plasmoids assuming a circular cross-section and a travel speed equal to the Alfven speed in the surrounding lobes. Using the electron density inferred by Waves, we contend that these plasmoid diameters were within an order of the local ion-inertial length. Our results demonstrate that magnetic reconnection in the Jovian magnetotail occurs at ion scales like in other space environments. We show that ion-scale plasmoids would need to be released every 0.1 s or less to match the canonical 1 ton/s rate of plasma production due to Io.

1. Introduction

Magnetic reconnection can be the primary mechanism through which the plasma created in Jupiter's inner magnetosphere from Io and Europa is ultimately lost to the external solar wind (Vasyliunas, 1983; Krupp et al., 2004). Many in situ observations support this hypothesis through different particle and field signatures, which are briefly summarized in the following paragraphs.

Recurring bursts of energetic particles occur in the Jovian magnetotail with flow velocities deviating from the corotation direction (Krimigis et al., 1981; Krupp et al., 1998; Woch et al., 2002; Kronberg et al., 2005, 2007; Kronberg, Woch, Krupp, & Lagg, 2008; Kasahara et al., 2013). These flow bursts repeat on timescales between 1 to 4 days and can be directed either inward (sunward) or outward (anti-sunward). More inward flow bursts are seen at radial locations closer to Jupiter, whereas outward bursts are common farther away from the planet (Woch et al., 2002). They are associated with an increase in the energetic particle fluxes and a decrease in the ion energy spectral index γ, or hardening of the ion energy spectra (Krupp et al., 1998; Woch et al., 1998). The peak energy of the ions also increases, which suggests acceleration associated with these events (Woch et al., 1999).

Simultaneous magnetic field observations have shown that flow bursts occur during periods of reversals in the north-south component of the magnetic field (Nishida, 1983; Russell et al., 1998; Woch et al., 1999; Kronberg et al., 2005; Vogt et al., 2010, 2014, 2020). Under typical quiet conditions, the magnetic field in the Jovian magnetotail points predominantly southward at the magnetic equator. Abrupt north-south reversals indicate a change in the topology through magnetic reconnection. Persistent northward magnetic fields may indicate open magnetic flux that is 'disconnected' from Jupiter (Vogt et al., 2014). Multiple north-south reversals can be seen within a single reconfiguration event lasting over a period of several days (Kronberg et al., 2007). The sense of the reversal, i.e., from north to south or vice-versa, provides more information about the placement of the measuring spacecraft with respect to the reconnection X-line, which can be identified based on the meridional component for a given interval (Ge et al., 2010; Vogt et al., 2010). Some magnetic field reversals appear to have a helical or loop-like magnetic field structure that is characteristic of plasmoid events (Vogt et al., 2014). Also seen are magnetic signatures of 'dipolarizations', which are the result of plasma compression due to fast planetward flows in the so-called 'exhausts' emanating from the reconnection sites (Artemyev et al., 2013, 2020; Yao et al., 2020).

The simultaneous occurrences of magnetic field reversals and flow bursts repeating on similar timescales suggests a common origin. That such events recur over long timescales of 1-4 days, with no clear dependence on solar wind triggers, also suggests an internally driven phenomenon. The dominant field component in the lobes parallel to the current sheet (B_r) gradually increases between two consecutive active periods and decreases after the onset of the events, while the opposite is true for the component normal to the current sheet (B_θ) at the equator. This implies a gradual 'stretching' of the magnetodisc over the 1 to 4-day period (Ge et al., 2007; Kronberg et al., 2007). Based on the above points, it is believed that the magnetosphere experiences two states – a state of 'loading', characterized by an increase in magnetic stresses in the magnetotail, and a state of 'unloading', when magnetic stresses and plasma are released from the magnetosphere via magnetic reconnection and plasmoid release.

Based on these observations, which are also seen in Saturn's magnetosphere (Jackman et al., 2011; Garton et al., 2021), it is now generally believed that reconnection occurs in the Jovian magnetotail and produces plasmoids. But the question remains if plasmoids can account for the 1 ton/s mass addition rate produced in the inner magnetosphere (Bagenal & Delamere, 2011). Previous estimates vary on the size of and mass carried by Jovian plasmoids. Kronberg et al., (2008) assume plasmoid down-tail length pf 9 R_J, thickness of 2 R_J and azimuthal length of 200 R_J (1 R_J = 71492 km is the equatorial radius of Jupiter at 1 bar), and an oxygen ion density of 0.025 cm^{-3} and find that ~50 plasmoids should be released over the unloading period (~1 day) to balance a 250 kg/s production, with each plasmoid contributing ~800 tons. Bagenal, (2007) assumes a plasmoid diameter of 25 R_J, width of 2 R_J and density of 0.01 cm^{-3} and estimate the mass of each plasmoid to be ~500 tons, which effectively translates to a loss rate of ~150 kg/s if such plasmoids are released on an hourly basis. Vogt et al., (2014) consider larger plasmoid dimensions with the higher estimate of the down-tail length to be 20 R_J, a width of 6 R_J, a cross-tail length of 70 R_J, and density of 0.01 cm^{-3} and calculate an upper estimate of the net loss rate to be ~120 kg/s based on five such plasmoids released over one day. Similarly, Cowley et al., (2015) find that the rate of 1 ton/s can only be achieved after including the large post-plasmoid plasma sheet (PPPS), which may exist for the ~15 h recurrence time between consecutive reconnection events and would increase effective plasmoid down-tail lengths up to ~150 R_J. Hence, isolated, and infrequent plasmoids, which recur on a timescale of several hours or days, cannot match the contribution due to the Galilean satellites without the inclusion of the PPPS. It can also be noted from the widely varying numbers shown above that the dimensions for Jovian plasmoids are not well constrained because of the inherent limitations of single point measurements. Meanwhile, other theories have also been proposed to explain the observed deficit which allow for mass loss through other means e.g., through boundary interactions at the magnetopause (Delamere & Bagenal, 2013; Masters, 2017) or through diffusive processes occurring at smaller scales than what has been detected in the past (Kivelson & Southwood, 2005).

Observations of magnetotail reconnection noted above have analogs in the terrestrial magnetosphere with the primary difference being that the driving mechanism to stress the magnetotail in the terrestrial case is the external solar wind and interplanetary magnetic field

(Kronberg, Woch, Krupp, Lagg, et al., 2008). Our understanding of magnetic reconnection and plasmoids has improved with multi-spacecraft observations in the terrestrial magnetosphere, high cadence instrumentation and kinetic simulations. Plasmoids in the terrestrial magnetosphere and other regions of the space environment are often accompanied with a strong core field within the helical magnetic structure and are called magnetic flux-ropes (Slavin et al., 2003). The magnetic pressure of the core region balances the magnetic tension force exerted by the outer regions and in some cases, plasma pressure gradients are unnecessary to maintain this quasi-equilibrium. Flux-ropes in which pressure gradients are negligible and where the magnetic forces are self-balancing are referred to as 'force-free'. It has been argued that the force-free configuration contains minimum magnetic energy for helical structures (Taylor, 1974; Priest, 2011) toward which they tend to evolve with time. Hence, knowledge about a particular flux-rope event's magnetic structure could be used to determine its stage of evolution. Simultaneous energetic particle observations have shown that flux-ropes which are produced on the ion-inertial scale can interact with or trap electrons and ions, which get accelerated due to adiabatic processes such as due to the conservation of the adiabatic invariants, or through non-adiabatic processes such as electromagnetic turbulence (Grigorenko et al., 2015; Kronberg et al., 2019). Evidence exists for both Fermi and betatron acceleration, which manifest as increases in the electron fluxes in the parallel and perpendicular directions, respectively (Zhong et al., 2020; Vaivads et al., 2021). Similar results are found in particle-in-cell simulations (Drake et al., 2006).

Plasmoids observed in the Jovian magnetotail have predominantly contained minimum magnetic field strength in their interiors and are not force-free flux-ropes (Vogt et al., 2014). This could be a result of the very large plasma β in the Jovian magnetotail, which produces plasmoids containing dense plasma and large pressure gradients. The spatiotemporal scales over which these plasmoids, which are also referred to as O-lines, evolve and possibly convert to force-free flux-ropes are also not known. It is not clear which parameter determines the direction and strength of the core field for a plasmoid released in the magnetotail. For externally driven magnetospheres such as Earth's and Mercury's, studies have found both strong (Moldwin & Hughes, 1992; Slavin et al., 2003) or weak correlation (Smith, Slavin, Jackman, Poh, et al., 2017) between the IMF orientation and the direction of the core field. In Jupiter's magnetosphere, the solar wind influence and penetration of the IMF B_Y into the plasma sheet is minimal. However, the 'bend-back' of the magnetic field in the magnetodisc introduces a cross-tail magnetic field component in the mid-latitude regions (Khurana et al., 2004).

To understand the role of magnetic reconnection in facilitating mass loss, it is also important to consider alternative theories such as smaller-scale reconnection in the Jovian magnetotail. However, plasmoids observed in the Jovian magnetotail based on the Galileo measurements so far have been large, which could be due to the low temporal cadence of the available instrumentation onboard the Galileo spacecraft. Kronberg, Woch, Krupp, & Lagg, (2008) and Vogt et al., (2014) used data collected by Galileo to study the properties of tailward moving Jovian plasmoids and found their average diameters to between ~9 to 10 R_J and between 2.6 to 20 R_J, respectively. Vogt et al., (2014) inferred the plasmoid size based on the time difference between the two extrema in B_θ during the north-south reversal, whereas Kronberg, Woch, Krupp, & Lagg, (2008) also included the period during which the magnetic field gradually returned to the southward orientation, i.e., the post-plasmoid plasma sheet (PPPS). Kronberg, Woch, Krupp, & Lagg, (2008) observed plasmoid durations to vary between 0 and 50 minutes, with most events having durations between 10 and 20 minutes. They also calculated the plasma flow speeds during the plasmoid events to be between 200 and 1200 km/s. Most plasmoids were associated with flows of around 400 km/s. Similarly, in the Vogt et al., (2014) survey, the 2 to 20 R_J diameters correspond to an average in-situ duration of 6.8 minutes. The recent survey by (Vogt et al., 2020) used data collected by the Juno spacecraft to identify signatures of magnetic reconnection and found a similar result as for the Galileo data.

In a previous work, we reported on two Juno-based observations of flux-ropes in the Jovian magnetotail with diameters comparable to or less than the local ion-inertial length (Sarkango et al., 2021). This was made possible by the higher resolution magnetometer instrument aboard Juno, as well as the presence of heavy ions in the magnetosphere which increased plasma length scales. Our observations extended previous work on magnetic reconnection in the Jovian magnetosphere, as most plasmoids observed previously by Galileo or Juno were found to have large diameters, corresponding to in situ signatures lasting several minutes or longer. In contrast, the two events discussed in Sarkango et al., (2021) had durations of 22 s and 62 s respectively. Under the assumption that these plasmoids traveled at the Alfven speed corresponding to that in the lobes, we had calculated their diameters to be ~11,000 and ~30,000 km, respectively. Based on these observations, we hypothesized that magnetic reconnection in the Jovian magnetotail, like other regions in the space environment, proceeds via the tearing instability in the magnetotail current sheet. This had also been proposed by Kronberg et al., (2007), who demonstrated that the magnetotail loading process would take roughly 2 days or more to create conditions conducive for this instability to occur, which would lead to unloading.

In this work, we extend on previous works on plasmoids at Jupiter by conducting a survey of all possible Jovian plasmoids with in situ signatures shorter than 5 minutes and corresponding diameters less than ~2 R_J. This is achieved by using an automated detection algorithm to identify plasmoids using transient reversals in B_θ with ‘peak-to-peak’ signatures shorter than 5 minutes and longer than 10 seconds. By using an empirical density profile and the local Alfven speed in the surrounding lobes measured by Juno, we show that the events identified have diameters within an order of magnitude of the local oxygen ion-inertial length. We also classify plasmoids based on whether their core-region has magnetic fields that are stronger (flux-ropes) or weaker (O-lines) than the surrounding magnetic fields in the outer layers of the plasmoid. A force-free flux rope model is fitted to each flux-rope event, and it is found that out of the 31 plasmoids with strong core fields, 6 events fit the force-free model well, i.e., they are self-balanced due to internal magnetic stresses. However, 56 magnetic O-line-type plasmoids were identified and hence were more commonly observed than flux-ropes. We also use data from the JEDI instrument to show properties of the energetic electrons and ions during two example plasmoid events. The fluxes of electrons and ions are larger within these intervals and in the post-plasmoid plasma sheet. For one example, the electron pitch-angles were isotropic during the interval but field-aligned before and after, which could be due to betatron acceleration, as has been observed for electron distributions in the terrestrial magnetotail. Our results highlight that reconnection occurs in Jupiter’s magnetosphere over a wide range of scales and can accelerate plasma in the process. The frequent observations of plasmoids with small diameters, which are presumably easier to miss, by a single spacecraft in the magnetotail also raises questions about the occurrence of ion scale magnetic reconnection in other regions of the magnetosphere. Nevertheless, our estimates of the total mass carried by ion-inertial scale plasmoids suggest that they do not directly contribute in a substantial manner to the loss of mass from the magnetosphere.

2. Data and Methodology

2.1. Juno's Trajectory

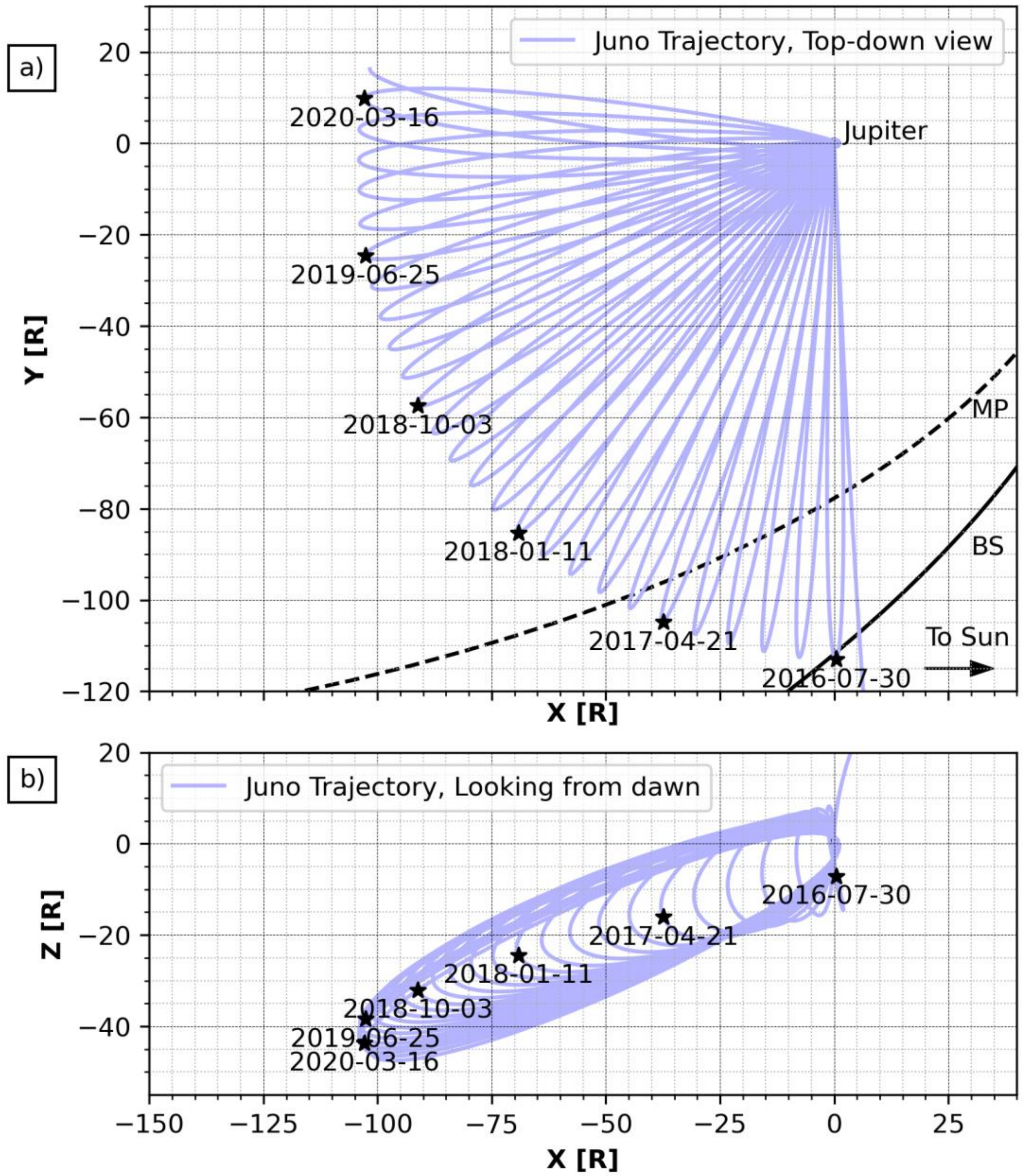

Figure 1. Juno's trajectory in the JSS coordinate system as seen in the equatorial and meridional projections. Dates and positions corresponding to every fifth apogee are highlighted. Also shown in panel (a) are the 75% percentile bow-shock (BS) and magnetopause (MP) model by Joy et al., (2002).

The Juno spacecraft was inserted into an elliptical orbit around Jupiter in June 2016 at around 06 LT (local time), or close to the dawn meridian. Each subsequent perijove pass was separated by a time of roughly 53 days. Over the years, Juno naturally precessed towards the nightside magnetotail, reaching 00 LT (midnight) in early 2020. Simultaneously, its apogee moved from near-equatorial to mid-latitudes in the southern hemisphere. Over the course of the highly elliptical trajectory (shown in Figure 1), Juno spent a considerable amount of time in the central plasma sheet, especially during the planet-bound portion of its orbit. During these periods, it frequently crossed the oscillating magnetotail current sheet, which can be seen in the periodic reversals of the radial component of the magnetic field (B_r) every 5 hours, or twice every Jovian rotation period. Juno was most likely to encounter the magnetodisc current sheet at different radial locations for different local times in the dawnside magnetotail. Initially (e.g., for years 2016-2018), when the orbit was less inclined, the current sheet crossings were observed over a broad range of radial distances, ranging from roughly 30 to 80 R_J. However, the increase in orbital inclination during the later years (e.g., 2020) meant that current sheet crossings near midnight (00 LT) could only be observed when the spacecraft was located at lower latitudes where the hinged oscillating current sheet was expected to occur, i.e., at radial distances nearer to the planet and in the middle magnetosphere between roughly 20 and 50 R_J. This also had direct implications for the detection of plasmoid signatures, as magnetic reconnection is also expected to occur close to the current sheet location, which was not sampled uniformly by Juno.

2.2. Data Description

In this work, we used 1-s resolution vector magnetic field intensity data collected in situ by Juno's onboard fluxgate magnetometers (Connerney et al., 2017). We used the magnetometer data to identify plasmoid signatures on the order of 10 s to 300 s, for which the 1 s cadence was reasonable as it provides at least 10 magnetic field vectors per event. We also used data from the Juno Waves instrument (Kurth et al., 2017), which measured the fluctuations in the electric field between frequencies of 50 Hz and 40 MHz, to identify the low-frequency cutoff for the continuum radiation and estimate the local electron density (Gurnett et al., 1981; Barnhart et al., 2009). We supported the fields observations using data from the JEDI energetic particle detectors (Mauk et al., 2013). Three JEDI instruments were located on the Juno spacecraft; two having a field-of-view in the spacecraft equatorial plane (JEDI-90 and JEDI-270) and one looking perpendicular to the spacecraft equatorial plane (JEDI-180). JEDI could measure electrons in the energy range between 18 keV to 740 keV. JEDI could also measure and distinguish between ion species based on the time-of-flight channels, specifically protons (~37 keV – 2 MeV), oxygen (~130 keV – 10 MeV) and sulfur (~130 keV – 11 MeV) ions. In favorable conditions, the rotation of Juno about its spin axis allowed for near-complete pitch-angle coverage with a typical collection time of 30 s. However, for most times when Juno was in the middle and outer magnetosphere, the JEDI instruments were operating at a lower data rate mode with reduced energy resolution to facilitate data transfer during these periods.

2.3. Magnetic signatures of plasmoids

We used the Juno data to search for plasmoids in the Jovian magnetotail by identifying reversals in the north-south component of the magnetic field, i.e., B_z or B_θ in Cartesian JSS or spherical JSS coordinate systems respectively. An illustration of the expected magnetic signature of a tailward moving plasmoid containing helical magnetic fields is illustrated in Figure 2 (a).

The sense of the B_z reversal, i.e., from north-to-south or vice-versa, can be used to infer the direction of travel of the plasmoid. Observations in the terrestrial magnetosphere have shown that plasmoids which travel tailward usually correspond to a B_z reversal from positive to negative values (Slavin et al., 2003). While the Earth's magnetic moment points predominantly southward, Jupiter's internal magnetic moment points northward. This implies that tailward moving plasmoids in the Jovian magnetotail would have the opposite sense of reversal as seen at Earth, i.e., B_z would change from negative to positive values (assuming that a single plasmoid is released). On the other hand, planetward moving plasmoids would result in B_z changing from positive to negative values.

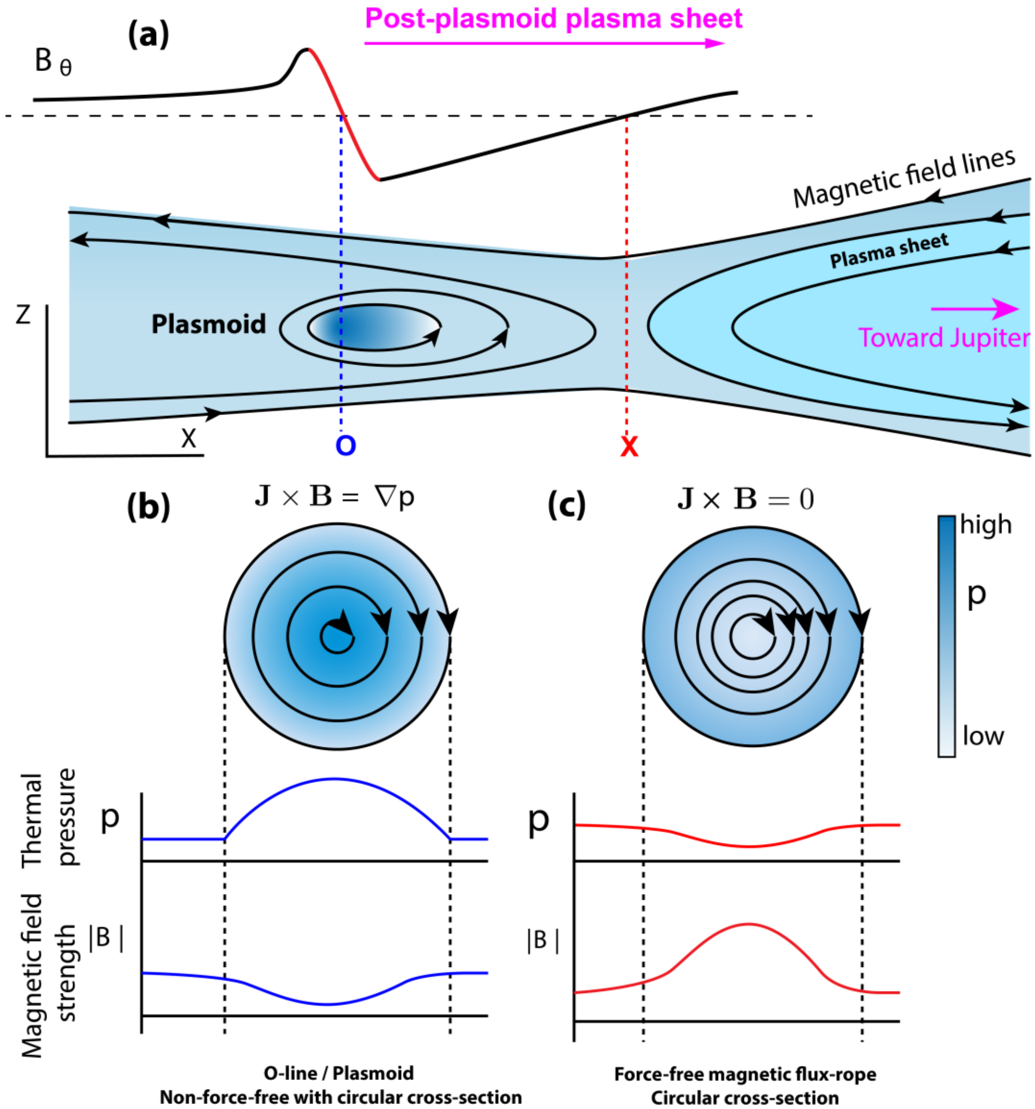

Figure 2. (a) Magnetic signature and representative geometry of a tailward moving plasmoid with a post-plasmoid plasma sheet. (b-c) Schematics showing the different magnetic field and thermal pressure profiles of magnetic O-lines (b) and force-free flux-ropes (c) with circular cross-sections.

To prevent ambiguity due to the oscillating Jovian current sheet and magnetodisc, analysis of magnetic field components in the Jovian system was conducted in the spherical JSS coordinate system where B_r, B_θ and B_ϕ represented the radial, co-latitudinal and azimuthal components of the magnetic field. In this system, the periodic motion of the current sheet is largely limited to the radial and azimuthal components (B_r and B_ϕ), which are anti-correlated due to the bend-back phenomena (Khurana et al., 2004). In a quiet time magnetotail and in the absence of reconnection, B_θ is predominantly positive (In our work, like the previous studies, positive B_θ corresponds to negative B_z at the equator). Hence, the magnetic signature of a tailward moving plasmoid would be a positive-to-negative reversal in B_θ, and opposite (negative-to-positive) for a planetward moving plasmoid (Figure 2). Additionally, plasmoids may or may not possess a core field inside the outer helical magnetic structures (flux-ropes), which can be seen predominantly in the azimuthal or radial components (B_ϕ or B_r) or as a localized increase in the magnetic field strength within the interval corresponding to the reversal of B_θ (Figure 2 (c)).

2.4. Minimum Variance Analysis

We used the magnetic field based minimum variance analysis (referred to as MVA or BMVA in the literature) to characterize the helical magnetic structure. A local cartesian coordinate system was determined, whose orthogonal directions represent the directions of maximum, intermediate and minimum variance of the magnetic field during the plasmoid interval. This was done by first constructing the variance matrix M according to the following equation (Sonnerup & Cahill, 1967),

$$M_{ij} = \langle B_i B_j \rangle - \langle B_i \rangle \langle B_j \rangle, \text{ for } i, j \in \{x, y, z\} \tag{1}$$

The eigenvectors of the variance matrix corresponding to the decreasing magnitude of the eigenvalues (λ_L, λ_M, λ_N) provided the directions of maximum ($\overrightarrow{x_L}$), intermediate ($\overrightarrow{x_M}$) and minimum variance ($\overrightarrow{x_N}$).

For plasmoid signatures in the magnetotail, the magnetic field varies most in the north-south (Z or θ) direction. The maximally varying component (B_L) also reverses sign. In the case of a flux-rope, the local increase in the core field direction can be seen in the component of intermediate variance (B_M). This leads to a near elliptical path when visualized as a hodogram of the B_L and B_M components, also referred to as a rotation (Slavin et al., 1989).

MVA fails to determine the orientation of the variance directions if two or more eigenvalues of the variance matrix are similar in magnitude. In other words, there are times when the variance coordinate system is *degenerate*. This is verified in the present work by requiring that the ratio of larger to smaller eigenvalues be greater than 3. Additionally, we also imposed the condition by Rosa Oliveira et al., (2020) using the metric P (shown below), where $P >$ 4.5 considered to be sufficient to validate the MVA eigensystem.

$$P = \frac{100}{\lambda_L^{1.5}} \times \left(\sqrt{\lambda_L} - \sqrt{\lambda_M}\right)\left(\sqrt{\lambda_L} - \sqrt{\lambda_N}\right)\left(\sqrt{\lambda_M} - \sqrt{\lambda_N}\right) \tag{2}$$

2.5. Force-free Flux-rope Modeling

Plasmoids with strong axial core fields are referred to as ‘flux-ropes’. A subset of flux-ropes within which pressure gradients are negligible and which are in force equilibrium due to the self-balancing magnetic forces are termed ‘force-free’ (Kivelson & Khurana, 1995). The expected pressure and magnetic field profile within O-line type plasmoids and magnetic flux ropes is shown in Figure 2. In the O-line type plasmoids, the magnetic pressure of the helical wraps is balanced by the thermal pressure gradient. One solution for axially symmetric force-free flux-ropes with circular cross-sections takes the following form (Lepping et al., 1990; Slavin et al., 2003),

$$B_A = B_0 J_0(\alpha r) \tag{3}$$

$$B_T = B_0 H J_1(\alpha r) \tag{4}$$

Where B_A and B_T are the axial and tangential components of the magnetic field, H is the handedness (either 1 or -1), J_0 and J_1 are the Bessel functions of the first kind, α is a constant parameter and r here refers to the ratio between the impact parameter, which is the distance from the center of the flux-rope at closest approach, and the radius of the flux-rope. In this work, $\alpha = 2.4048$ was chosen as it results in the tangential field component being zero when $r = 1$ (at the flux-rope edge).

For a given interval exhibiting a flux-rope-like signature, we used Eq. 3-4 to fit a constant-α flux-rope to the observations to determine whether the helical structures seen in the data were force-free. This was achieved by varying B_0, r, H and the spherical angles providing the axial orientation of the flux-rope, θ_A and ϕ_A, such that the Chi-squared error between the observations and the force-free model was minimized (Lepping et al., 1990).

$$\chi_r^2 = \frac{1}{N}\sum_{i=1}^{N}\left[\left(B_x - B_{x,m}\right)^2 + \left(B_y - B_{y,m}\right)^2 + \left(B_z - B_{z,m}\right)^2\right] \tag{5}$$

This was achieved in two steps using an open-source nonlinear least-squares fitting package (Newville et al., 2016). Firstly, the magnetic field components were normalized by the local magnetic field strength within the interval. Next, the flux-rope model was fitted to the observations for all parameters except for B_0. The initial values for θ_A and ϕ_A, i.e., the flux-rope orientation, were chosen based on the eigenvector for intermediate variance ($\overrightarrow{x_M}$) as provided by the minimum-variance analysis. Then the minimization was repeated, keeping all parameters fixed to their optimized values, but varying B_0 to scale the modeled flux-rope's core field.

2.6. Automated detection of plasmoids

We used an automated algorithm to detect possible plasmoid signatures in the magnetic field observations made by the Juno magnetometer. For identifying potential signatures, we used a method like that used by Smith, Slavin, Jackman, Fear, et al., (2017) for the Kronian magnetotail and by Vogt et al., (2014) for the Jovian magnetotail. Firstly, within an interval in the 1-s resolution magnetometer data, all times corresponding to a reversal in B_θ, either from positive-to-negative or vice-versa, were identified. Reversals which occurred beyond 05 LT on the dawnside and beyond 90 R_J in radial distance from the planet were discarded to prevent contamination due to proximity to the magnetopause, where the magnetic field is highly variable.

Next, for each reversal, the times corresponding to the extrema in B_θ for the event were identified. As there can be multiple local maxima and minima in the B_θ magnetic field observations, we adopted the method used by Smith, Slavin, Jackman, Fear, et al., (2017) and identified maxima-minima (or vice-versa) pairs within a period of +/- 10 min from the B_θ reversal. Pairs in which the peak-to-peak B_θ extrema were less than 2 nT or the standard deviation of the B_θ component during a 100 min interval centered on the reversal in question were considered inconclusive and discarded. Pairs in which the excursion into negative B_θ values was a factor of 6 smaller than that in the positive direction (and vice-versa) were also discarded. Additionally, only those extrema pairs were considered whose start and end times were separated by a duration of at least 10 s and at most 5 min, which form the lower and upper limit for the events identified in this study. The lower limit was chosen such that there are at least 10 vector measurements for subsequent analysis. As the purpose of this work was to study small-scale plasmoid events, we limited the algorithm to signatures lasting less than 5 min. The range in the present work overlaps with the lower bins of a previous survey by Vogt et al., (2014) of plasmoids identified by the Galileo magnetometer.

For each of the remaining pairs of extrema, which correspond to potential start and stop times for a plasmoid event, a linear function was fitted to the B_θ observations (Smith, Slavin, Jackman, Fear, et al., 2017). Those extrema pairs which showed low degree of correlation with the observations (quantified by the coefficient of determination $r^2 < 0.85$) were discarded.

Next, additional filters were applied based on the minimum-variance analysis, which was conducted on all remaining extrema pairs. Events in which the eigenvector corresponding to the direction of maximum variance did not have a predominantly Z_{JSS} component ($\widehat{x_L} \cdot \hat{z} < 0.8$) were discarded. Pairs for which the ratio of the maximum to intermediate and intermediate to minimum eigenvalues were less than 3, or for which the P value was less than 4.5, were also removed from consideration. Lastly, to only capture plasmoid events close to a magnetotail current sheet crossing and prevent identification of traveling compression regions (TCRs) in the magnetotail lobes (which was outside the scope of the present work), additional filters were applied to limit the detection to events in which the minimally varying component of the magnetic field (B_N) as well as the radial component in the JSS spherical coordinate system (B_r), were less than 2 nT.

Of the remaining extrema pairs, the pair which fits best the B_θ observations using a linear function was identified (i.e., highest r^2) and chosen to be the start and end time for that event. In this procedure to detect B_θ reversals no distinction was made between positive-to-negative or negative-to-positive sense, as both tailward and planetward moving plasmoids (respectively) are likely to occur in the magnetotail. The conservative approach used by this algorithm ensured good candidates for plasmoids in the Jovian magnetotail. The procedure was repeated for each B_θ reversals detected by Juno, though only 87 reversals passed all criteria.

3. Results

3.1. Case Studies: Magnetic field and energetic particle signatures of plasmoids

In this section we discuss the magnetic field and energetic particle signatures of two examples of ion-inertial scale plasmoids identified by our automated algorithm.

3.1.1. Example 1: Flux-rope - DOY 76, 2017

In Figure 3 (a)-(d) we show the magnetic field data in the spherical JSS coordinate system for a plasmoid event occurring on DOY 75 in 2017 roughly between 09:55:25 and 09:56:26 UTC. Juno was in the dawnside magnetotail near ~05 LT at ~86.5 R_J from Jupiter. This interval was close to a current sheet crossing, as can be seen in the smooth reversals in the radial (B_r) and azimuthal (B_ϕ) components from positive to negative values, or vice-versa. The southward-to-northward B_θ reversal is accompanied by an interval of negative B_θ. The sense of the reversal suggests that the plasmoid was moving tailward with respect to Juno.

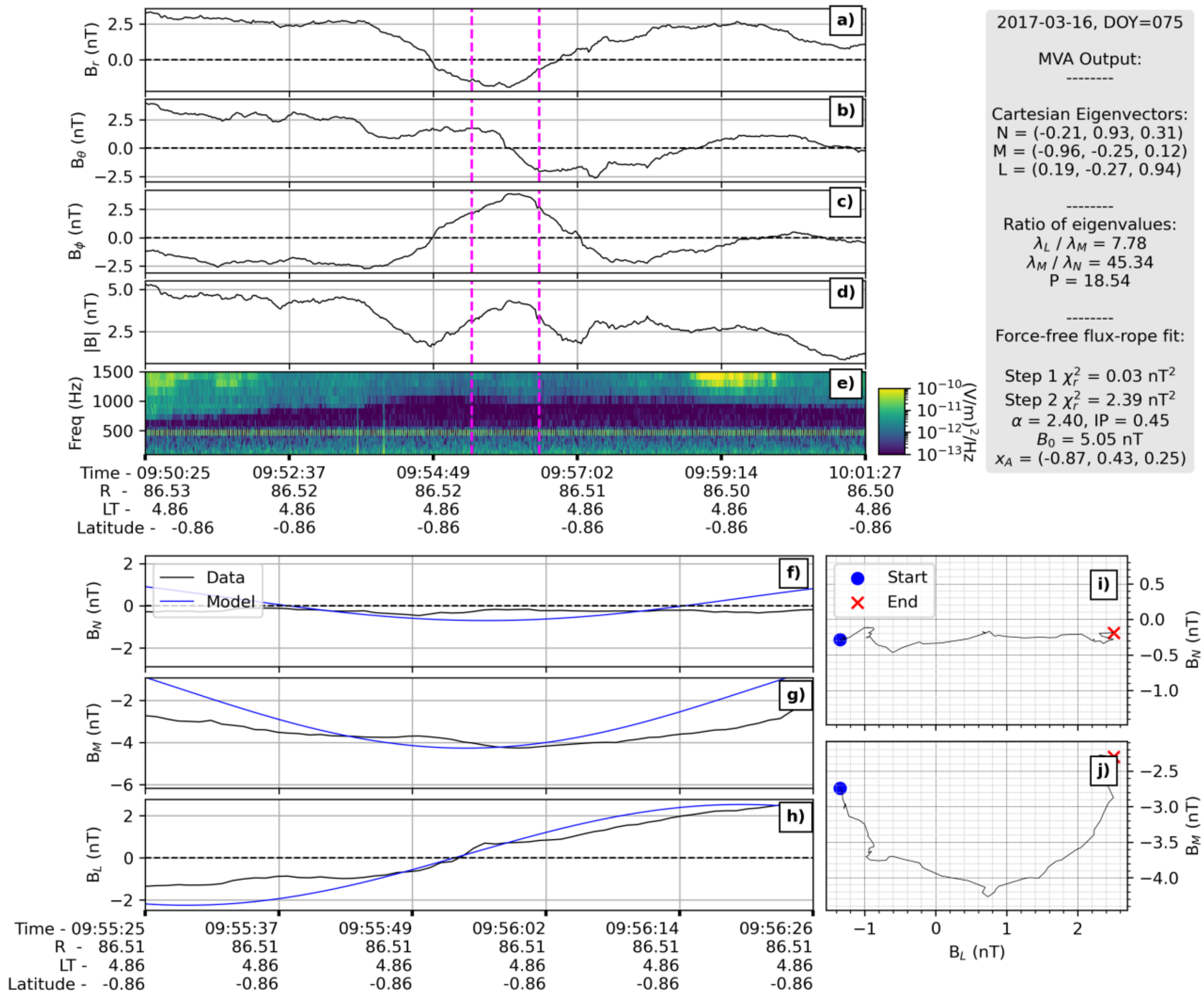

Figure 3. Magnetic field observations of a magnetic flux-rope event on DOY 75, 2017 by the Juno spacecraft in the dawnside magnetotail. Panels (a)-(d) show the magnetic field intensity in the spherical JSS coordinate system. The Waves electric field spectra is shown in Panel (e). Panels (f)-(g) show the components of the magnetic field in the minimum-variance coordinate system corresponding to the minimum, intermediate and maximum eigenvector. The magnetic signature of the best-fit modeled force-free flux-rope is shown in blue. Panels (h)-(i) show the hodograms between the field components in the MVA coordinates. Details of the minimum variance analysis and the force-free flux-rope modeling are shown in the grey box.

Results of the MVA and force-free modeling for this interval are shown in Figure 3 (f)-(j), where the magnetic field components are plotted in the variance coordinate system. The minimally varying component (B_N) was predominantly in the X_{JSS} direction with values less than 0.3 nT, compared to the field strength between 2 and 4 nT. A reversal could be seen in the maximally varying component (B_L) which was accompanied by a moderate increase in the intermediate component (B_M) near the center of the interval, which can also be visualized as a rotation in the $B_L - B_M$ hodogram (Figure 3 (j)). This transient increase in the core field was also seen in the magnetic field magnitude and we classified this event as a magnetic flux rope. The ratios of the eigenvalues of the variance matrix were 7.78 and 45.34, which were large enough to suggest that the MVA analysis unambiguously determined the variance coordinate system. Also shown in Figure 3 (f)-(j) is the modeled force-free flux rope (in blue) which results in the least χ_r^2. The reduced Chi-squared error between the data and the modeled flux-rope was large (~2.39 nT^2) compared to the mean field strength (~ 4 nT), which indicated that the observed flux-rope was not force-free. Nevertheless, the increase in the magnetic field strength and the intermediate component show that this event is a magnetic flux-rope with a strong axial core field.

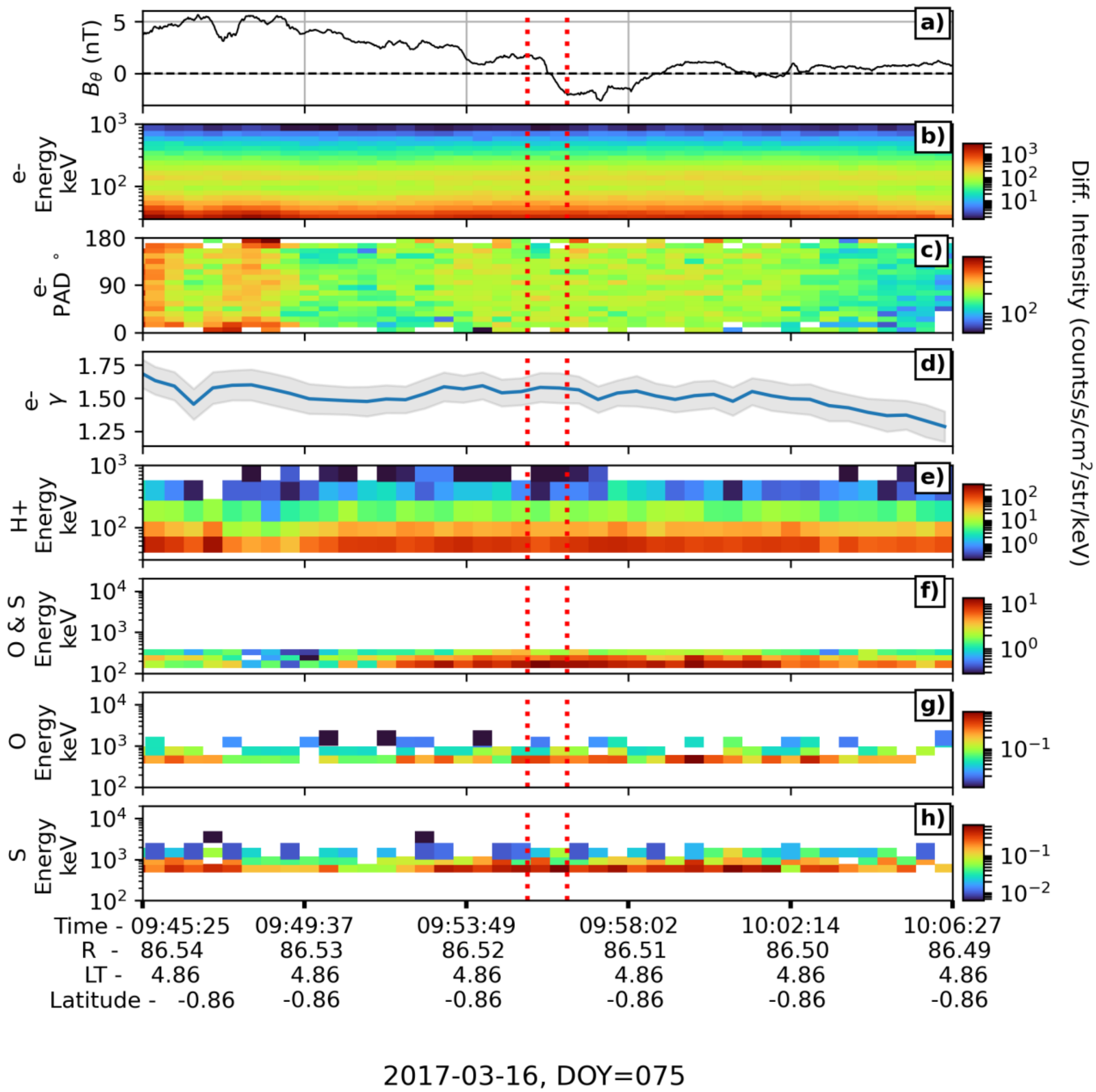

Figure 4. Energetic particle observations made by the JEDI instruments on board the Juno spacecraft for the same event as shown in Figure 4. Panel a) shows the variation of B_θ during the event for context. Each consecutive panel shows (b-c) the dynamic energy and pitch-angle spectra for the electrons, (d) the omnidirectional energy spectral index γ for the electrons, the

energy spectra for (e) protons, (f) indistinguishable sulfur and oxygen ions O/S, (g) oxygen ions, and (h) sulfur ions. All spectra have units of differential intensity i.e., counts/s/str/cm^2/keV.

Figure 3 (e) shows the dynamic spectra for the high-frequency fluctuations in the electric field as measured by the Juno Waves instrument. The continuum radiation was observed throughout the interval with a low-frequency cut-off at roughly 1000 Hz. Assuming this to be the electron plasma frequency, we estimated the local electron density during this interval to be ~0.012 cm^{-3}. Assuming quasi-neutrality and a singly charged ion mass of 16 amu, this density corresponds to an ion inertial length of 8178.15 km.

In Figure 4 we show the differential intensity measurements by the JEDI energetic particle detector for the same event as shown in Figure 3 for the electrons, protons, oxygen, and sulfur ions, averaged in bins of 30 s each. We show the energy and pitch-angle spectra for the electrons (b)-(c) since higher resolution electron data was available. Also shown for the electrons in (d) is the energy spectral index (γ) obtained by fitting the relation $I = I_0(E/E_0)^{-\gamma}$ to the omnidirectional differential intensities (I). Only the energy dynamic spectra are shown for the ions (e)-(h), and their data was limited due to the lesser energy channels and pitch-angle coverage. JEDI was unable to distinguish between the heavy ions at relatively low energies and these are shown together in panel (f). The JEDI data shown in this figure was resampled to a cadence of 30 s using data from all operating JEDI detectors. There was a moderate increase in the electron flux near the plasmoid event. The electron spectral index decreased after the passage of the plasmoid. Ion fluxes also increased near the plasmoid. The increase in ion flux is most prominent for the sulfur and low energy S/O ions.

3.1.2. Example 2: O-line - DOY 75, 2017

Juno observed another plasmoid event between 23:57:08 and 23:58:12 UTC on DOY 75, 2017. The magnetic field and Waves spectra for this example are shown in Figure 5. The magnetic field reversed from a southward to northward configuration before and after this event (B_θ changed from positive to negative) and there was no increase seen in the radial or azimuthal component within the reversal. This plasmoid did not have a core field signature and had its minimum field strength at the center of the interval and was therefore classified as a magnetic O-line. The minimum variance analysis showed a similar result, with a minimum in the intermediate variance component near the center of the interval. The core field direction, as inferred based on the direction of minimum variance for O-lines, was skewed in the XY plane with a large out-of-plane component. The ratios of the eigenvalues were very large ($\lambda_L/\lambda_M = 15.28$ and $\lambda_M/\lambda_N = 11.46$) indicating that the MVA coordinate system was well defined. As this event did not have a core field, no attempt was made to fit a force-free flux-rope. The Waves spectra, shown in panel (e) showed that the cutoff for the continuum radiation briefly increased during the plasmoid interval from ~500 Hz to 700 Hz. If the cutoff occurs at the electron plasma frequency, this transient increase indicated that the electron density also increased within the interval. This is consistent with the low magnetic field in the center for the O-line type plasmoid. The ~700 Hz cutoff frequency corresponds to an electron density close to 0.006 cm^{-3} and an ion inertial length of ~11683 km assuming quasi-neutrality and a singly charged oxygen ion.

Data from the JEDI detectors for this interval is shown in Figure 6. A moderate increase in the electron flux was seen during the plasmoid interval (b). On the other hand, proton, oxygen and sulfur fluxes increased by almost two orders of magnitude compared to times before the plasmoid event (e)-(h). The large ion fluxes were seen consistently even after the B_θ reversal and during the prolonged interval of negative B_θ, or the post-plasmoid plasma sheet. Increases in particle fluxes were also seen in data collected by the Galileo EPD (Kronberg et al., 2005) for the larger plasmoids discussed in previous surveys.

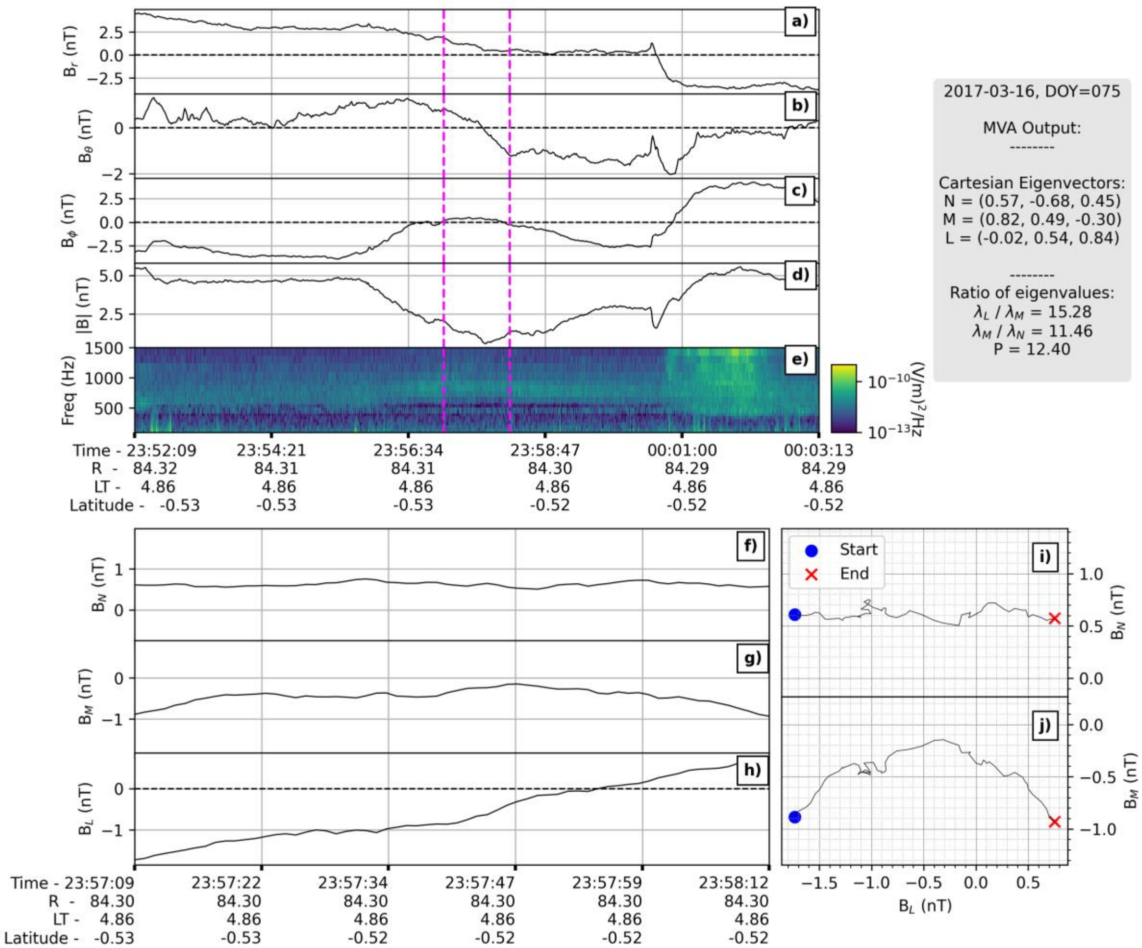

Figure 5. Magnetic field signatures (a)-(d) and electric field spectra (e) obtained by the Juno magnetometer and Waves instruments for a plasmoid event on DOY 75, 2017 in a similar format as Figure 3. No force-free flux rope was fitted for this interval as the field is weakest in the interior of the plasmoid and it is classified as a magnetic O-line.

There was near-complete pitch-angle coverage for the electrons, which were predominantly field-aligned before and after the plasmoid. Before the event, electrons were seen streaming mainly along the magnetic field. The distribution gradually became more isotropic near the plasmoid interval and gradually returned to being field aligned after the passage of the plasmoid, from 23:58 DOY 75 to ~02:00 DOY 76. It has been demonstrated that electron distributions near flux-ropes are influenced by the Fermi and betatron acceleration processes (Zhong et al., 2020; Vaivads et al., 2021) and it is plausible that similar processes are occurring in the present situation. The observed pitch-angle dispersion is seen primarily for electrons with pitch-angles less than 90°, which could also be because of the abundance of field-aligned electrons before and during this interval. Field-aligned and anti-field-aligned electrons are observed in the post-plasmoid plasma sheet (e.g., at DOY 76, 00:02). The electron spectral index γ, shown in

Figure 6 (d), increased until the plasmoid encounter and decreased gradually within the PPPS, i.e., the electron spectra 'hardened' in the reconnection exhaust.

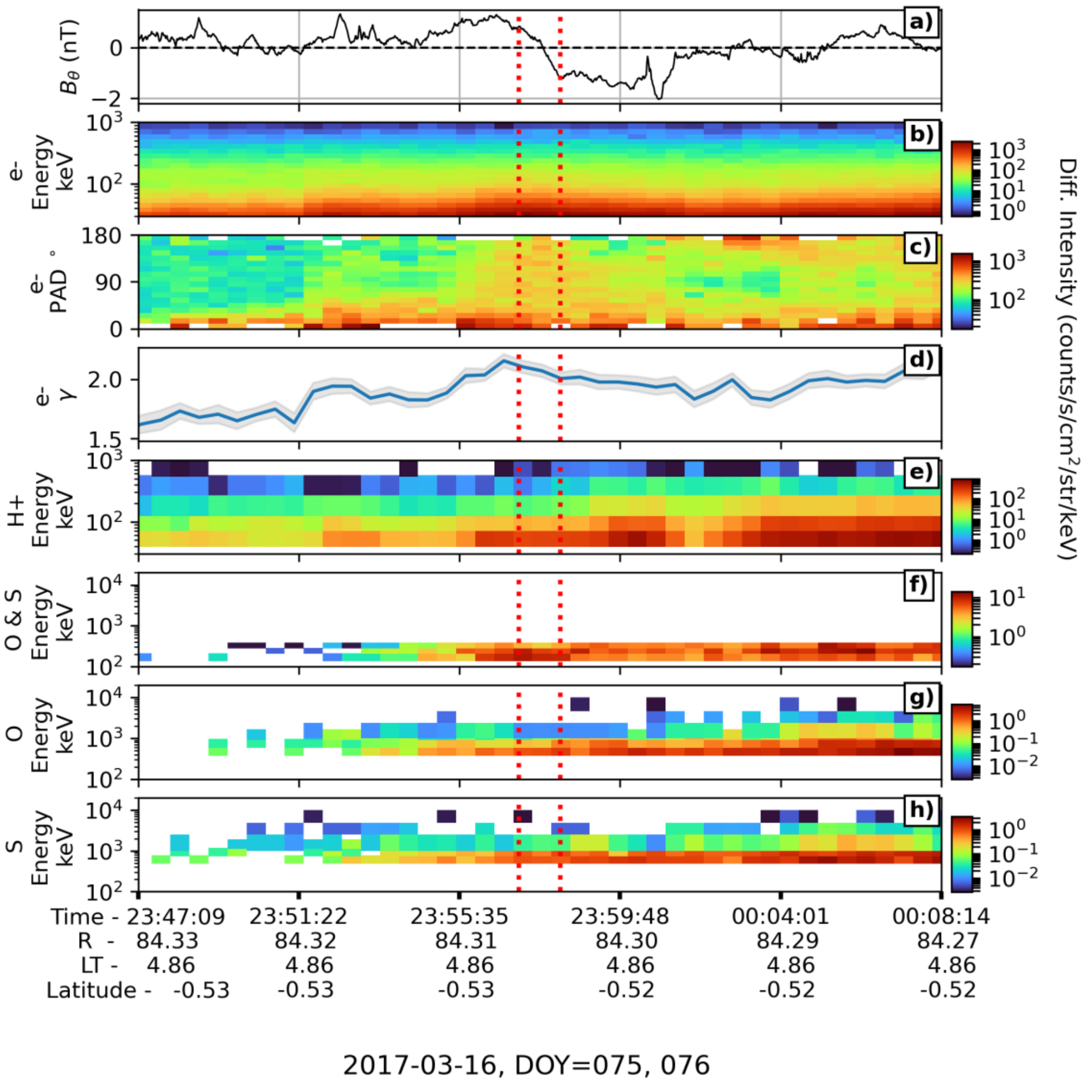

Figure 6. Energetic particle differential intensities measured by the JEDI instruments for the event shown in Figure 5 in a similar format as for Figure 4.

In Example 2, the magnetic field was predominantly southward before the event (positive B_θ) and was in a northward configuration (negative B_θ) for a brief period (>3 minutes) after. The gradual return to positive B_θ is consistent with the presence of a large post-plasmoid plasma sheet (PPPS). This is further supported by JEDI observations of higher ion fluxes lasting for the entire PPPS duration. This interpretation follows the schematic shown in Figure 2 (a) for a tailward moving plasmoid with a PPPS.

JEDI data for the electrons and ions was available at high cadence for the two examples discussed above. However, this was not the case for most events in our survey. For this reason, subsequent analysis of the plasmoids uses data gathered primarily by the Juno magnetometer and Waves instruments.

3.2. Survey results: Location and sense of magnetic field reversals

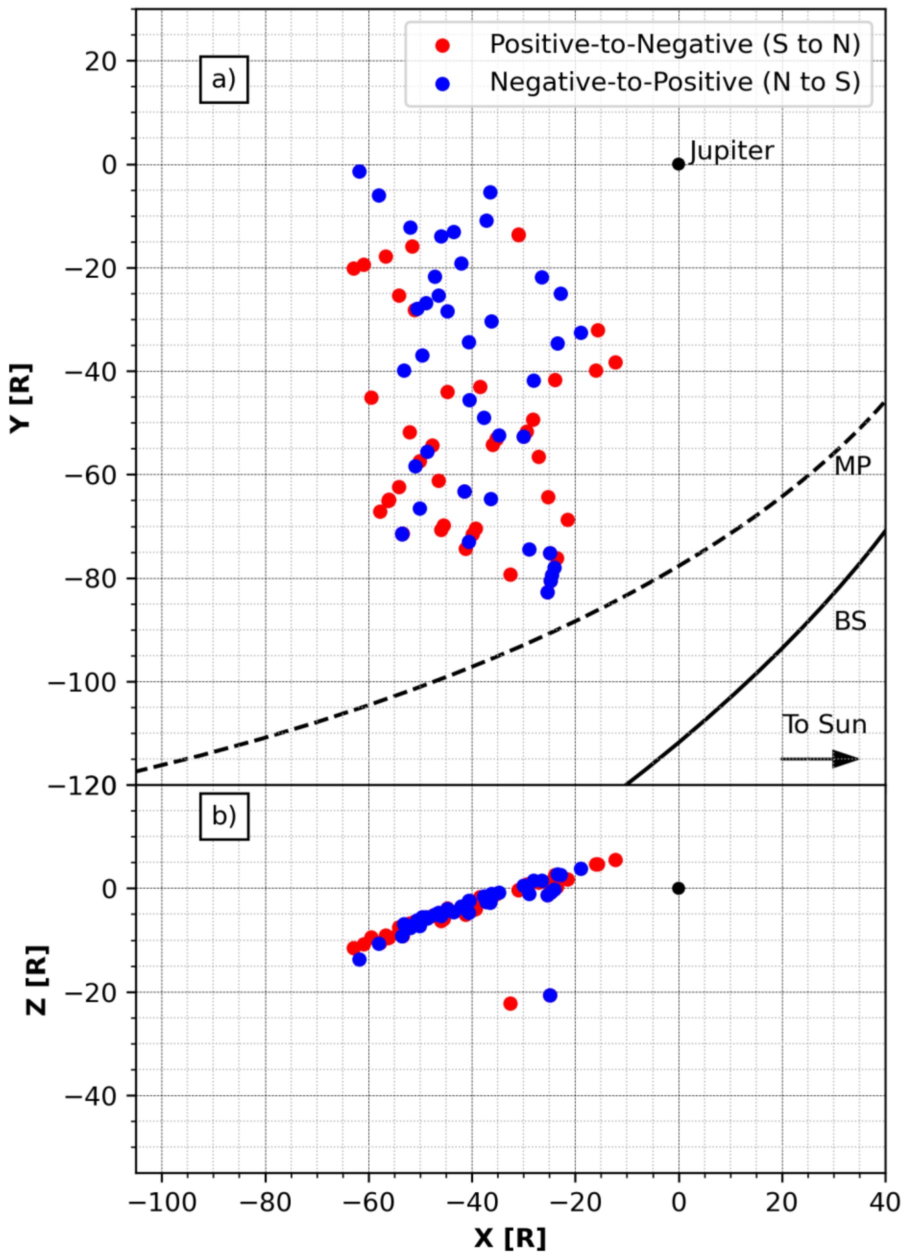

Figure 7. Locations of the plasmoid events in the JSS coordinate system identified by our automated algorithm, colored according to the sense of reversal in B_θ.

The automated algorithm searched for plasmoid signatures between DOY 49, 2017 and DOY 150, 2020. Although Juno was inserted into orbit in June 2016, earlier times were effectively not considered due to the LT < 5 filter used in the algorithm to prevent misidentification due to the magnetic field fluctuations near the magnetopause. In this period, corresponding to the stringent criteria described in Section 2.6, the algorithm detected 87 plasmoids with peak-to-peak durations less than 5 minutes. The list of the detected plasmoids is given in the Supporting Information. Out of the 87 events, 47 corresponded to a positive-to-negative reversal in B_θ and were thus likely tailward-moving plasmoids, while the remaining 40 events corresponded to a negative-to-positive reversal in B_θ and were planetward-moving plasmoids. The terms 'tailward' and 'planetward' are used interchangeably in this work with south-to-north and north-to-south reversals of the magnetic field, respectively, though this is strictly applicable only in the case of a single plasmoid.

The locations of the 87 events identified by the algorithm are shown in Figure 7. The vast majority (N=86) of events were identified in the planet-bound portion of Juno's orbit, which lies within the volume of the expected oscillating magnetotail current sheet. All events were located roughly between 23 and 05 LT due to Juno's orbit being in the midnight to dawn quadrant of the magnetotail between years 2016 and 2020.

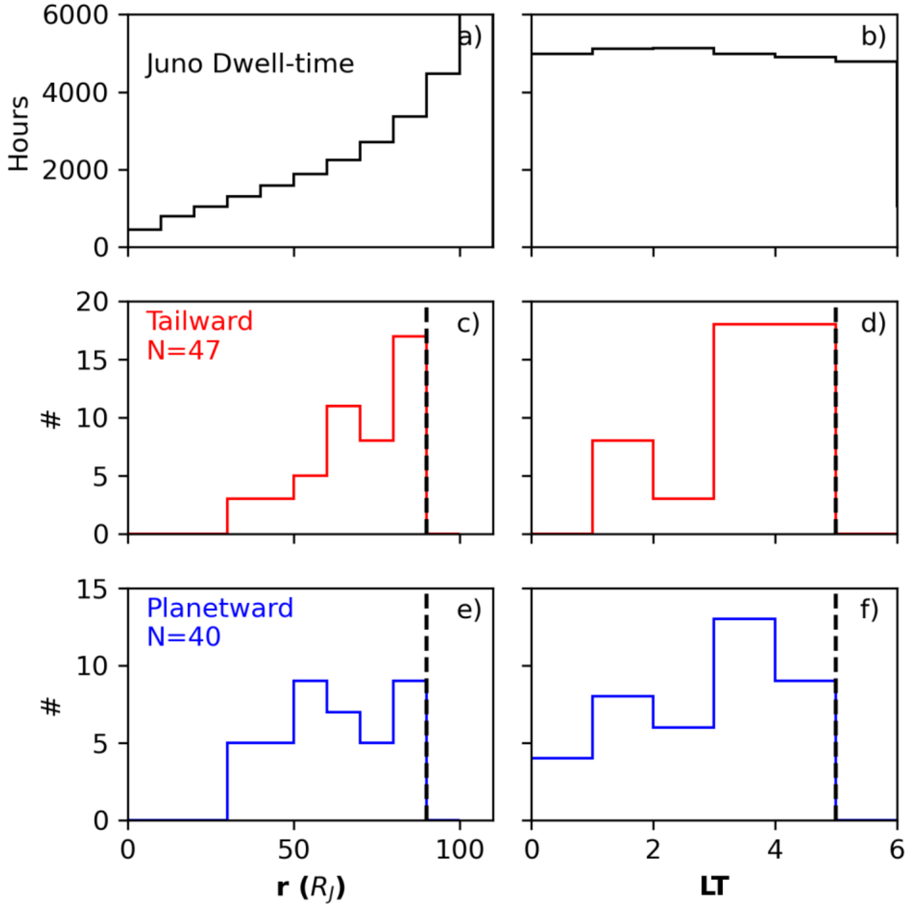

Figure 8. Histograms showing Juno's dwell time in hours in different radial and local time bins (a-b), as well as the number of tailward moving (c-d) and planetward-moving (e-f) plasmoids identified by the algorithm in the different bins. The dashed line marks the limits of the detection algorithm. Here, 'tailward' and 'planetward' refers to the motion expected for a single plasmoid based on the sense of the B_θ reversal.

In Figure 8 we show using histograms the time spent by Juno in different radial and local time regions (a)-(b). Due to Juno's elliptical orbit, it spent more time in the outer magnetosphere as it slowed down near its apogee. On the other hand, each local time between 00 and 06 was sampled almost equally. In panels (c)-(d) we show the occurrence of the planetward-moving plasmoids different radial and local bins. The 47 tailward moving plasmoids were identified between 30 and 90 R_J (the latter being specified by the automated algorithm). In general, tailward events were observed more frequently at larger radial distances, with the most events (N=18) being observed between 80 and 90 R_J. In terms of local time, >38 tailward events were seen between 03 and 05 LT, or close to the dawnside flank. The distribution for planetward moving plasmoids (N=40) was not skewed towards larger radial distances like for the tailward events, though out of a total of 40, 30 events were seen at distances beyond 50 R_J. Although they were observed at all local times, the maximum number of planetward events (N=13) were seen between 03 and 04 LT. 4 planetward plasmoids were also seen between 00 and 02 LT, or close to midnight.

In interpreting Figure 8, we note again that Juno's trajectory and increasing inclination with time implied that current sheet crossings, and thus, small-scale plasmoids which occur close to the current sheet, were more likely to be seen for the earlier years (2017-2019 or between 03-05 LT) at larger radial distances, and for the later years (2019-2020 or between 00-03 LT) at smaller radial distances closer to the planet, respectively (see Figure 1).

3.3. Duration and size of plasmoids

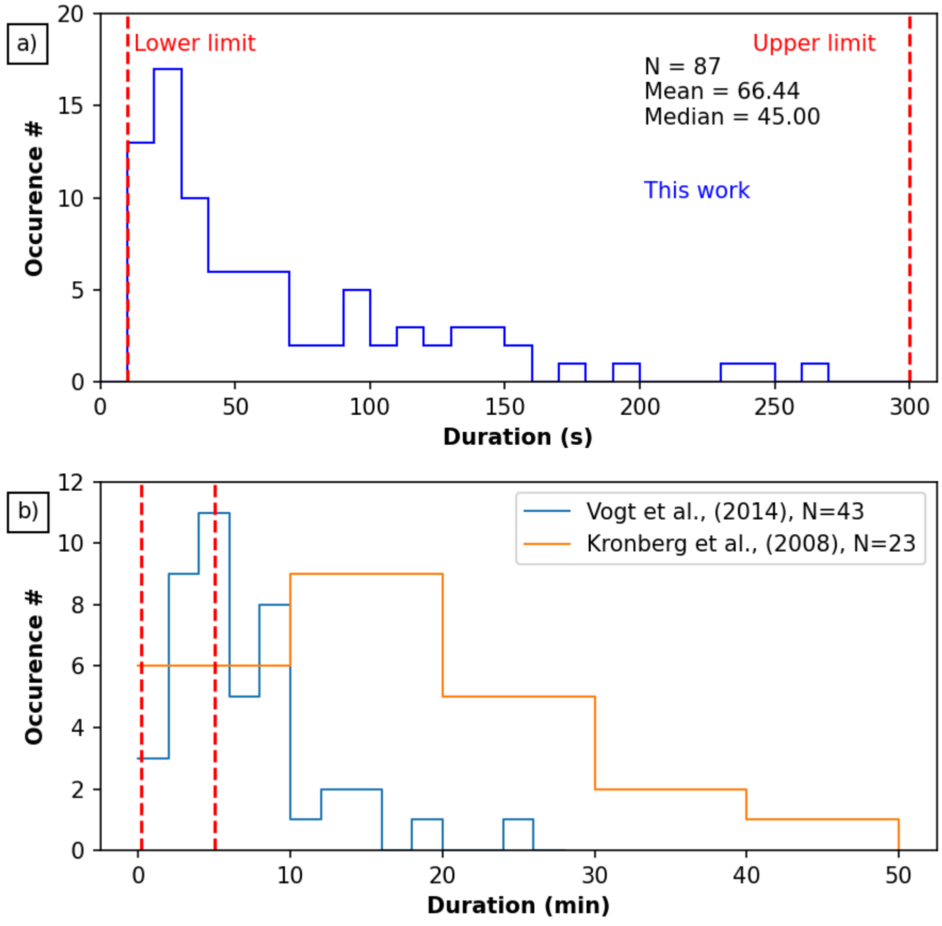

Figure 9. Histogram showing the "peak-to-peak" durations of the identified plasmoids in the present study (a) based on the Juno data and by Vogt et al., (2014) and Kronberg et al. (2008)

using data from the Galileo magnetometer (b). The lower and upper limits specified in our identification algorithm are highlighted using red dashed lines.

In Figure 9 (a) we show a histogram of the peak-to-peak durations of the 87 plasmoids identified by the algorithm. The minimum and maximum allowed event size were specified to be 10 s and 300 s respectively, as in this work we focus only on small-scale plasmoids with potential diameters comparable to the ion-inertial length. A majority (N=50) of the identified plasmoid events had durations less than 60 s. In general, plasmoids with shorter-duration in situ signatures (and hence smaller diameters), were observed more frequently than plasmoids with longer-duration in situ signatures. The mean and median durations for the small-scale plasmoids were found to be 66.44 s and 45 s, respectively. Small-scale events were most likely to be seen having signatures lasting between 10 and 30 s, with 30 out of the 87 events in these two bins. For comparison, the histogram of plasmoid durations by the Vogt et al., (2014) and Kronberg, Woch, Krupp, & Lagg, (2008) surveys are shown in Figure 9 (b), with dashed lines showing the event selection thresholds used by our algorithm. Vogt et al., (2014) found that plasmoids were most likely to have signatures lasting for 5 minutes, with a decreasing trend toward the 0-2 min and 2-4 min bins. (Kronberg, Woch, Krupp, & Lagg, 2008) use a different definition for the plasmoid duration, however, they found a similar result with the distribution being skewed towards smaller durations which were less than 20 min.

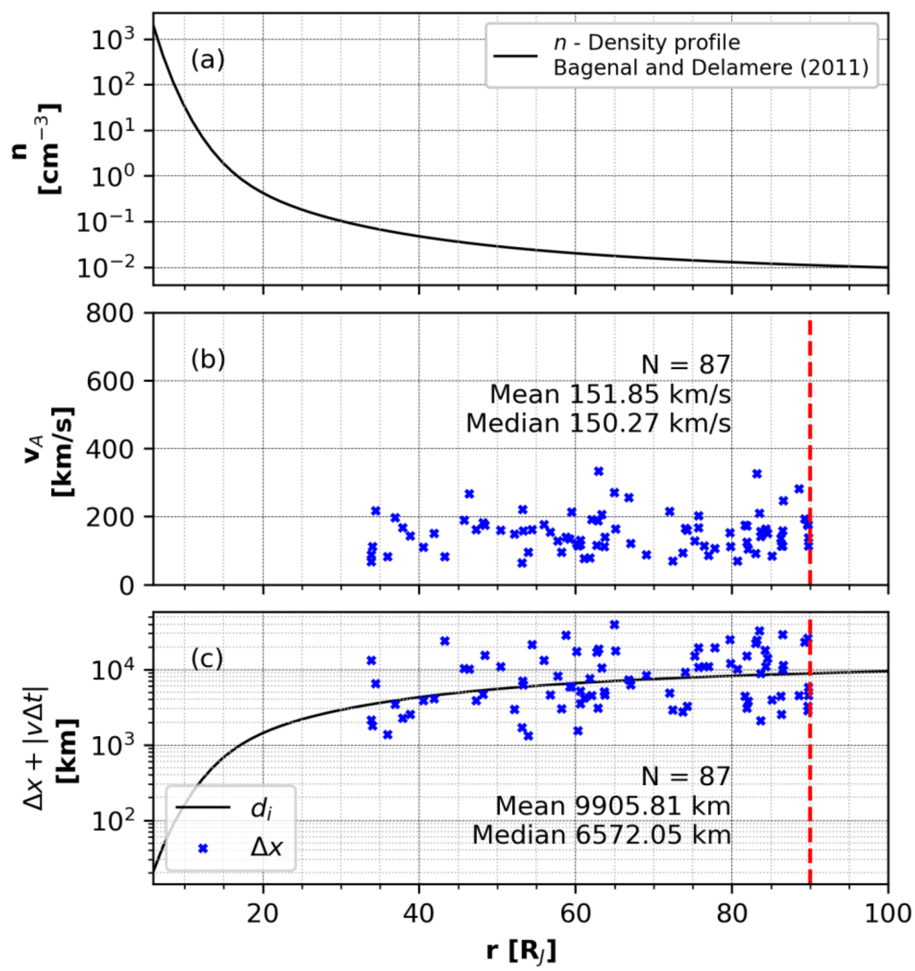

Figure 10. a) The Bagenal and Delamere (2011) density profile as a function of radial distance. b) The average magnetotail lobe Alfven speed +/- 5 min from the corresponding B_θ reversal for each plasmoid event. c) Scatter plot showing the diameters of the identified events, calculated by assuming that the plasmoids travel at the lobe Alfven speed shown in panel b. The solid line shows the expected ion-inertial length calculated using the Bagenal and Delamere (2011) density profile and using an ion mass of 16 amu. The dashed line marks the limit of the detection algorithm.

We estimated the diameters of the identified plasmoids by assuming that they were travelling at the Alfven speed in the magnetotail lobes, which we estimated based on the measured in situ magnetic field strength and an empirical density profile (Bagenal & Delamere, 2011). Figure 10 shows the typical Alfven speeds for each event (b) along with the empirical density profile used (a)-(b). The Alfven speed was calculated by averaging the magnetic field strength during an interval +/- 5 min from the reversal in B_θ. The mean and median Alfven speeds calculated in this manner was 151.85 km/s and 150.27 km/s, respectively. In Figure 10 (c), we show the calculated diameters of the identified plasmoids by multiplying the Alfven speed (b) with the peak-to-peak duration (Δt) for each event. The spacecraft travel distance (Δx) during the Δt time was also accounted for, although it is negligible compared to the plasmoid motion. Also shown in Figure 10 (c) is the ion-inertial length as a function of radial distance, calculated based on the same density profile. An ion mass of 16 amu was assumed for the calculations due to the dominance of heavy ions ($O^+/S^+/S^{++}$) in the Jovian magnetosphere. Figure 10 (c) illustrates that the diameters of all events with in-situ signatures shorter than 5 minutes are within an order of magnitude of the local ion inertial length, with some events having diameters even shorter than this length scale.

However, we note that defining the plasmoid duration between the two extrema in B_θ may lead to underestimation of the size of the plasmoid as the reversal alone does not account for the post-reversal post-plasmoid plasma sheet (PPPS) (Vogt et al., 2014; Cowley et al., 2015).

3.4. Relative occurrence of flux-ropes versus O-lines

For some plasmoids identified by the algorithm, we observed that an increase in the magnetic field strength near the center of the events i.e., near the reversal in B_θ, caused an increased in the component of the magnetic field in the direction of intermediate variance (B_M). However, these increases in B_M did not always correspond to an increase the overall magnetic field strength due to the near-zero values of the component of maximum variance (B_L) near the center of the event as it reversed sign during the plasmoid interval. Hence, in our work, we classified those events as flux-ropes in which the median of the intermediate-variance component (B_M) was larger than that measured at the beginning and end of the event interval. In other cases, where there was no localized increase in B_M, the reversal of the magnetic field usually resulted in a minimum field strength at the center of the event interval; such events were classified as magnetic O-lines. Out of 87 plasmoids events identified by the algorithm, 31 were classified as magnetic flux-ropes and 56 were classified as magnetic O-lines.

Figure 11 shows the distributions of flux-ropes and O-lines identified by the algorithm in radial distance and local time. Out of the 31 flux-ropes, 28 were found at radial distances beyond 50 R_J. Similarly, out of 56 O-lines, 43 were observed beyond 50 R_J, which could be due to the longer time spent by Juno in distances beyond 50 R_J. The greatest number of O-lines were observed between 80 and 90 R_J (N=18), whereas flux-ropes were found likely to occur between 50 and 90

R_J. More flux-ropes and O-lines were observed near the dawn-side magnetotail (03-05 LT) than near midnight (00-02 LT). This could be due to Juno's orbit, as between 00 and 02 LT it only crossed the current sheet at radial distances inward of 50 R_J, which could be planetward of the reconnection X-line in these local times.

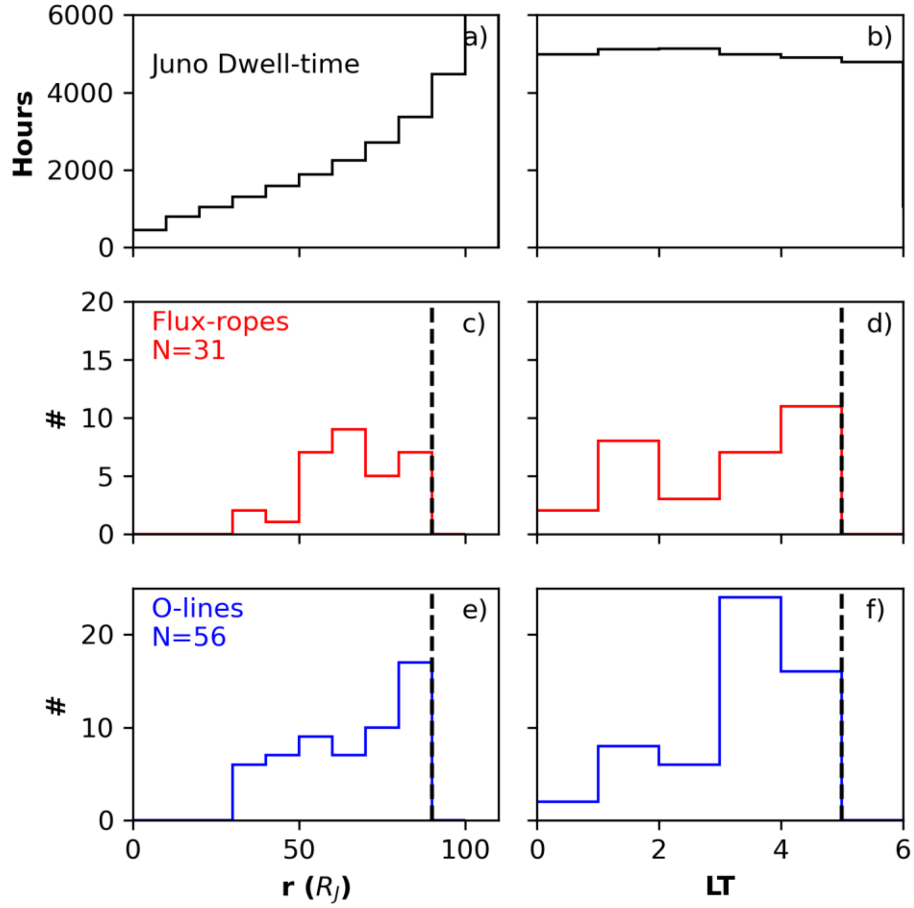

Figure 11. Histograms of the locations of the identified flux-rope and O-line events in radial distance and local time. Time spent by the Juno spacecraft in each bin is shown in panels a) and b). The dashed lines mark the limits of the detection algorithm.

The direction of the core field for a magnetic flux-rope is closely associated with the MVA eigenvector corresponding to the direction of intermediate variance ($\overrightarrow{x_M}$), which is illustrated in Figure 12 for all 31 flux-rope events. Also shown in Figure 12 are representative magnetic field lines from the Sarkango et al., (2019) MHD model which show the bend-back of the magnetic field lines due to the sub-corotation of the magnetospheric plasma. The flux-rope events were observed at nearly all local times sampled by Juno, with a wide range of core field orientations. Also shown in Figure 12 (b) are the eigenvectors corresponding to the direction of maximum variance ($\overrightarrow{x_L}$), which should be predominantly in the north-south direction as it was the basis on which these events were identified.

For an O-line, the direction of minimum variance of the field is used to infer the core-field direction as the intermediate variance is expected to be close to the radial direction. Figure 13 shows the MVA eigenvectors corresponding to the direction of minimum variance ($\overrightarrow{x_N}$) (top) and maximum variance ($\overrightarrow{x_L}$) for all 56 O-line events in a similar format as Figure 12. As for the flux-ropes, O-lines were observed at nearly all local times between 00 and 05 and had a wide range of core field orientations compared to the local bend-back direction. For both flux-ropes and O-lines, the direction of maximum variance was close to the Z direction in the JSS coordinate system.

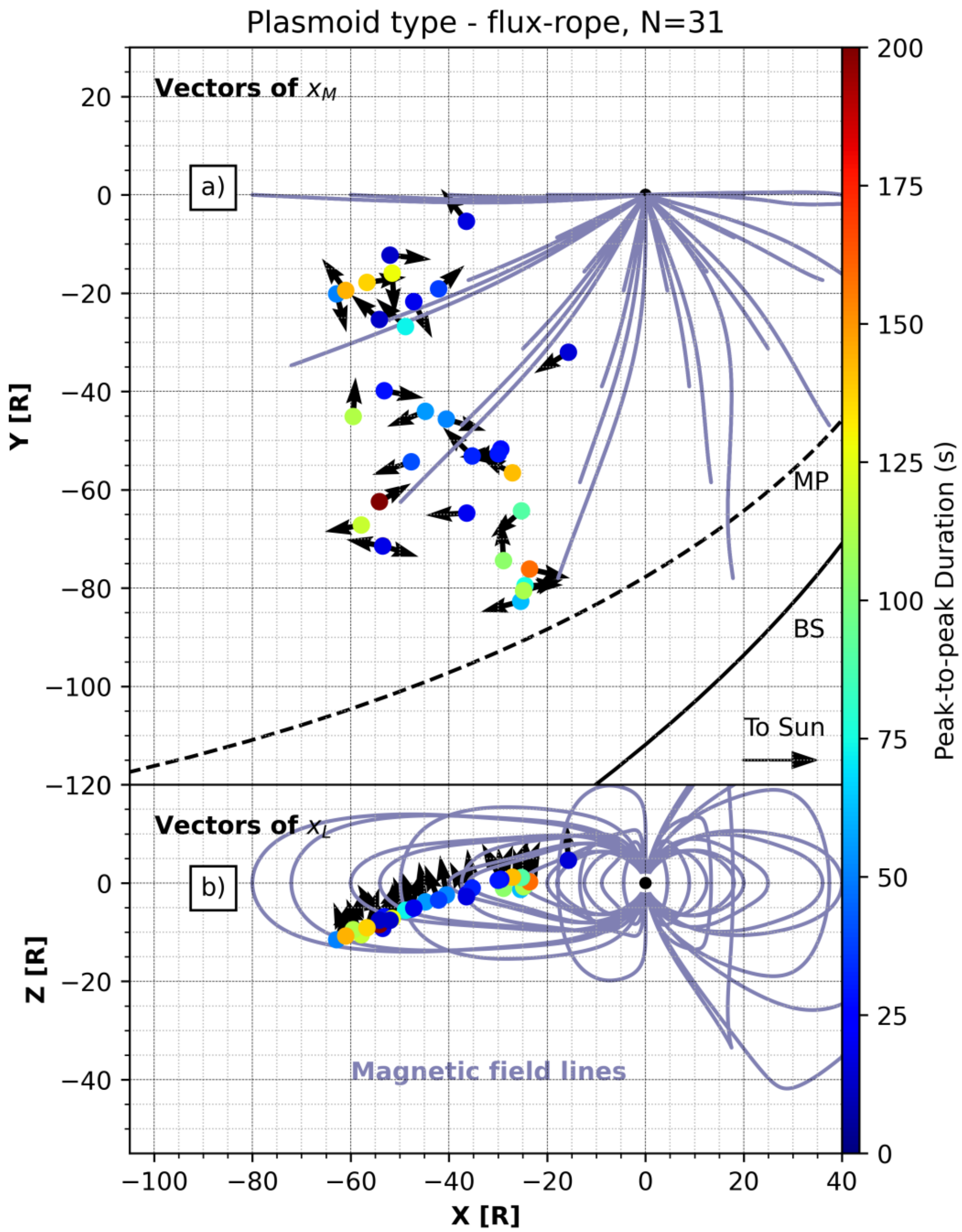

Figure 12. Eigenvectors of the intermediate and maximum variance shown in the equatorial and meridional projections for the 31 flux-rope events identified by the algorithm. Each event is colored according to its peak-to-peak duration. Also shown in blue are magnetic field lines from an MHD model.

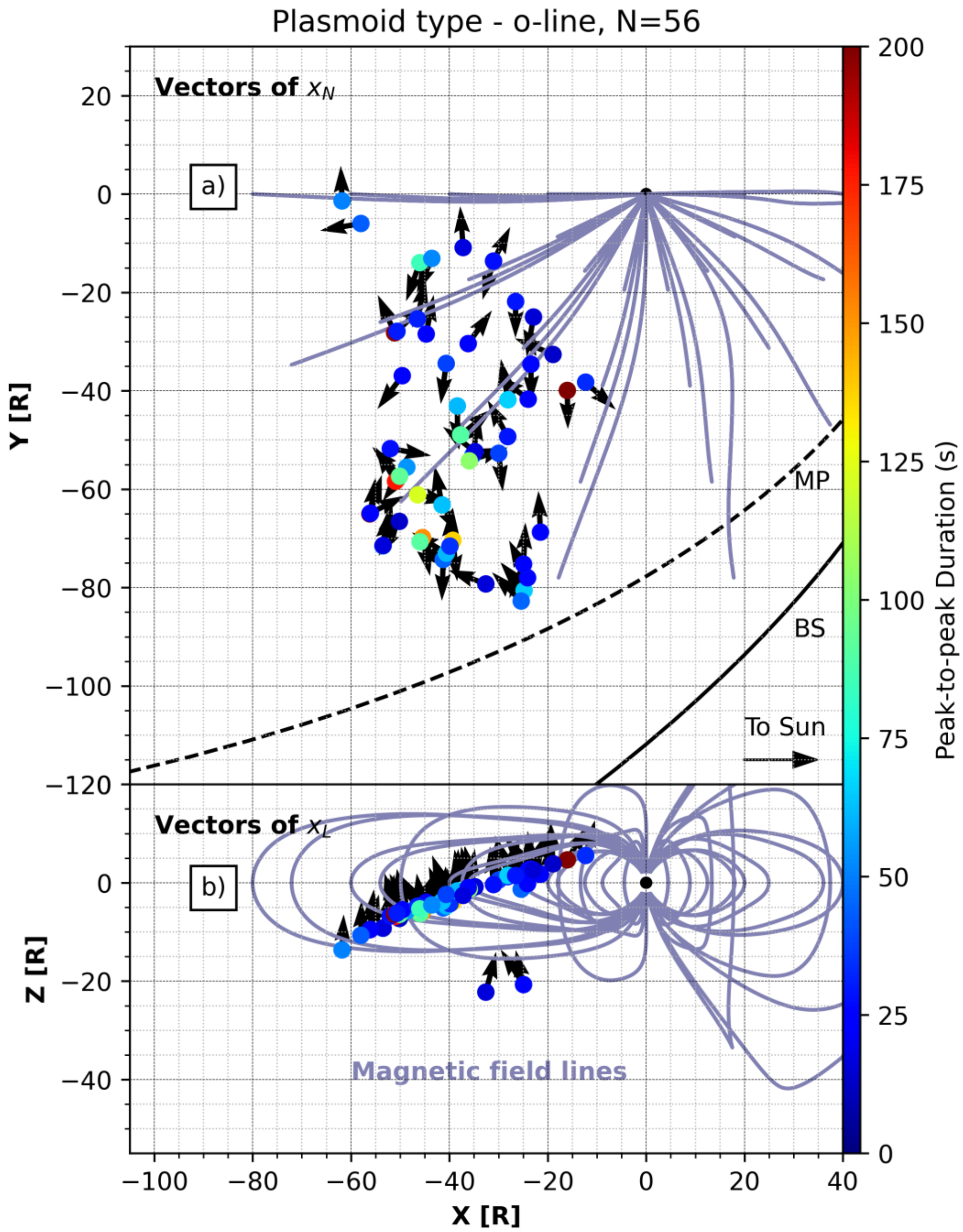

Figure 13. Eigenvectors of the minimum and maximum variance shown in the equatorial and meridional projections for the 56 O-line events identified by the algorithm. Each event is colored according to its peak-to-peak duration. Also shown in blue are magnetic field lines from an MHD model.

We compared the core-field directions of the flux-ropes and the O-lines with the local bend-back plane, which is presumably also the plane in which reconnection is occurring. The plane of the bend-back for each plasmoid events was determined by calculating the average of $\alpha = \tan^{-1}(B_\phi/B_r)$ for a 10-minute period starting 20 minutes prior to the observed B_θ reversal, during which time the spacecraft was typically sampling the off-equatorial / mid-latitudes, as seen in the anti-correlated azimuthal (B_ϕ) and radial (B_r) components of the magnetic field. In Figure 14, we show the angle between the core-field direction and the vector intersecting the local bend-back plane and the JSS equatorial plane ($\overrightarrow{x_\alpha}$). The direction of intermediate variance was chosen as the core-field direction for the magnetic flux-rope events whereas the minimum variance direction was chosen for the O-lines. Near 90° values of $\Delta\phi$ imply that the axial direction of the plasmoid was perpendicular to the bend-back plane, which is predominantly the case for O-lines, which show preferences for larger acute angles. Such a result is very consistent with the configuration of O-lines formed in the midnight-to-dawn quadrant in the global simulation of Saturn's magnetosphere by Jia et al., (2012). Although more flux-ropes were seen with $\Delta\phi > 45°$ (N=19) than vice-versa (N=13), the histograms show that angles between 20-30° were as likely to occur as those between 70-80°.

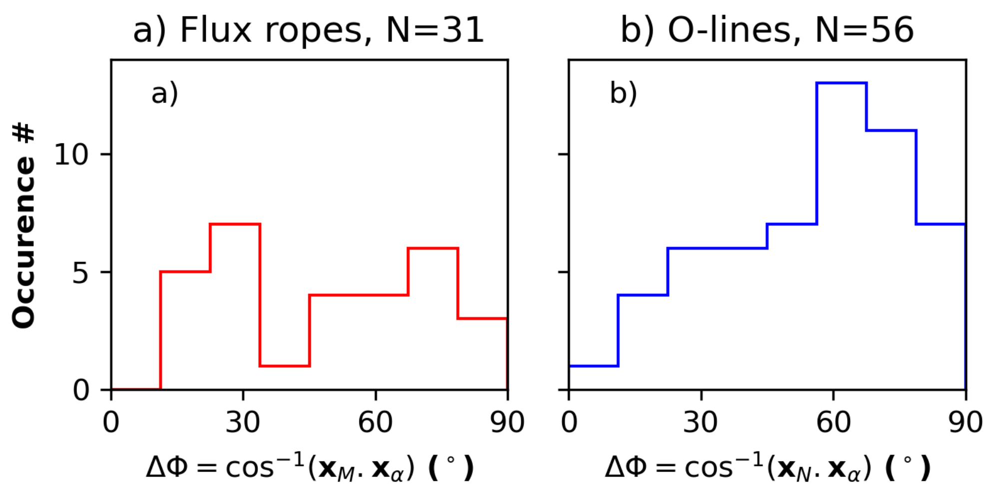

Figure 14. Histograms showing the acute angle between the core-field direction and the local bend-back plane for a) flux-ropes and b) O-lines identified by the algorithm.

A constant-α force-free flux-rope model was fitted to each flux-rope event (N=31) based on the methodology described in Section 2.5. Out of the 31 which were originally classified as flux-ropes, 6 produced reduced-chi-squared errors less than 0.3 nT^2 for an average field strength between 2 and 6 nT, which suggests that they were close to being force-free.

4. Discussion

4.1. Ion-inertial scale plasmoids in the Jovian magnetotail

The magnetic flux rope event shown in Figure 3 lasted approximately 61 s between the two extrema in B_θ, which roughly corresponds to a plasmoid diameter of 17141 km, assuming it travelled at the Alfven speed of ~281 km/s corresponding to that in the surrounding magnetotail lobes (B=4 nT, n_{lobe}=0.006 cm^{-3}, based on Waves data). This diameter was roughly 2 times the local ion inertial length, which we calculated to be ~8178 km (assuming quasi-neutrality and ion mass of 16 amu). The second example, shown in Figure 5, had a 'peak-to-peak' duration of 63 s. The magnetic field strength in the surrounding lobes was approximately 5 nT, which corresponds to an Alfven speed of ~498 km/s (for n_{lobe}=0.003 cm^{-3}) and a plasmoid diameter of ~31374 km.

The ion inertial length during this interval was also ~11683 km, making the plasmoid approximately 2.68 times larger than this length scale.

Figure 9 and Figure 10 illustrate the scale of the plasmoids detected by the algorithm using similar calculations. A majority (N=50 out of 87) of plasmoids were seen to last less than 60 s, measured between the peaks in B_θ. In contrast, previous surveys (Figure 9 (b)) have discussed larger plasmoids with durations longer than 2 min. In Figure 10, we calculated the diameters of the plasmoids based on the 'peak-to-peak' duration and the Alfven speed in the lobes and demonstrate that the diameters of all events were within one order of magnitude of the local oxygen ion-inertial length. Our survey demonstrates that reconnection occurs in the Jovian magnetotail at kinetic scales and produces ion-inertial scale plasmoids, like in other regions in the space environments such as the terrestrial magnetotail. Numerical simulations of ion-scale plasmoids have shown that they evolve by interacting with other plasmoids , i.e., via coalescence, which could ultimately produce the large plasmoids analyzed by previous surveys.

Our calculations of plasmoid diameters are subject to the assumption that the 'peak-to-peak' signature represents the entire plasmoid crossing. However, limiting the plasmoid duration between the two extrema in B_θ may underestimate the plasmoid size by a factor of 4 or more (Vogt et al., 2014). Note that we have used a mass of 16 amu or the mass of O^+ for the average mass of singly charged ions. Due to the abundance of singly charged sulfur ions, the ion inertial length in the Jovian magnetotail may be even larger than the numbers described above, which further supports our conclusions that our identified small-scale plasmoids have spatial sizes comparable to the local ion inertial length.

Our observations show that reconnection in Jupiter's magnetotail may be proceeding via current-sheet instabilities, as found in other magnetospheres The tearing instability is most likely to occur in a thin current sheet. In the magnetotail, this depends on the ratio of the radial field in the lobes ($B_{\mathrm{r,lobe}}$) and the meriodional field at the equator ($B_{\theta,\mathrm{equator}}$) (Kronberg et al., 2007), which changes over the course of the large-scale loading of the magnetosphere. Hence, on a global scale, there are no different onset conditions for the small-scale reconnection events. However, as smaller plasmoids with diameters roughly between ~10,000 to 50,000 km are easier to miss being detected by a single spacecraft in the magnetotail, the observations presented here raise new questions about the frequency at which reconnection occurs and whether it could also be occurring in other regions of the magnetosphere, such as the dusk side magnetotail.

4.2. Abundance of O-lines versus flux-ropes

On comparing the Waves electric field spectra for Example 1 (Figure 3 (e)), we observe that the cutoff for the continuum radiation briefly decreased from 1.1kHz to 0.9 kHz within the plasmoid event. This minor transient decrease was different from the larger increase in the cutoff frequency (from 500 Hz to 1 kHz) over the broader interval containing the plasmoid event, and the latter could a result of Juno entering the dense plasmasheet. The transient decrease in the cutoff frequency indicates a decrease in the plasma density within the plasmoid. The magnetic field strength increased within the event due to the core field, which led us to classify it as a magnetic flux-rope. Hence, the density decrease observed by Waves is consistent with the result that Example 1 was a flux-rope where the magnetic tension of the outer wraps is balanced by the larger magnetic pressure in the interior. However, this flux-rope was not entirely force-free, as discussed in Section 3.1.1.

The cutoff briefly increased to higher frequencies for Example 2 (Figure 5 (e)) from 500 Hz to 700 Hz, indicating that the plasma frequency and electron density also increased. Simultaneously, the magnetic field strength decreased within the interval. This supports our interpretation that the second plasmoid (Figure 5 and Figure 6) was an O-line, and the magnetic pressure of the outer helical structure was balanced by the larger thermal pressure contained within the plasmoid core. The relatively high cutoff frequency of ~1 kHz and corresponding higher density were also seen after the reversal in the post-plasmoid plasma sheet.

Like the Vogt et al., (2014) survey for Jupiter and the Jackman et al., (2011) survey for Saturn, we find that a majority of B_θ reversals associated with a plasmoid event do not have strong core fields. Out of the total 87 plasmoid candidates only 31 can be classified as magnetic flux-ropes, and out of these only 6 were found to fit the force-free model well with χ_r^2 less than 0.3 nT^2. This could be because the plasmoids are generated within a high β plasma, where plasma pressure gradients are very large. Dense plasma inside plasmoids could increase the thermal pressure which would oppose the magnetic tension of the outer helical wraps (Kivelson & Khurana, 1995). In contrast, the abundance of flux-ropes seen in the terrestrial-like magnetospheres could also be because of the stronger cross-magnetotail magnetic field introduced by the IMF (Slavin et al., 2003), which has a weaker, if not negligible, influence in the Jovian magnetosphere as the magnetopause reconnection is relatively weak. In the terrestrial case, the northern and southern magnetotail lobes are sheared due to the solar wind interaction (Cowley, 1981), which can contribute to a core-field for a plasmoid structure. (Here 'sheared' refers to the displacement of the two lobes with respect to each other, rather than to the anti-parallel magnetic field across the current sheet). Meanwhile, at Jupiter, the northern and southern lobes are not sheared, though the entire reconnection plane is likely skewed due to the bend-back effect (Russell et al., 1998). This could also result in more O-lines being generated than flux-ropes at Jupiter and Saturn.

Results of the minimum variance analysis on all flux-rope and O-line events showed that their core fields can be highly skewed in the XY plane (Figure 12 and Figure 13). In an ideal scenario, the core field of a newly produced plasmoid would be perpendicular to the plane of reconnection. In the Jovian magnetotail, this is determined by the 'bend-back' of the magnetic field lines due to sub-corotation of the plasma. So, it is interesting to compare the core field directions with the orientation of the local bend-back plane. In Figure 14 we showed the angle between these two vectors. The majority (~70%) of O-line events identified by our algorithm have core fields which are oriented larger than 45° from the bend-back plane. A similar but less prominent result is found for the flux-ropes, ~60% of which subtend angles larger than 45° with respect to the bend-back plane.

In Figure 11 we showed the occurrence of flux-ropes and O-lines detected by our algorithm at different radial distances and local times. Both flux-ropes and O-lines were seen more frequently at larger radial distances due to Juno's orbital bias. However, very few flux-ropes were seen at distances inward of 50 R_J, while O-lines were equally likely to occur at all bins between 30 and 70 R_J, though they are most likely between 70 and 90 R_J. Assuming that flux-ropes are plasmoids at a later stage during their evolution than O-lines, it is plausible that their signatures would be seen more frequently for regions in the deep magnetotail. Conversely, O-lines, which contain dense plasma and are possibly products of fresh reconnection, are more likely to occur closer to the planet.

4.3. Contribution of small-scale plasmoids to mass loss from the magnetosphere

We can produce cursory estimates of the mass carried by a small-scale plasmoid by assuming that it occupies a cylindrical volume with diameter equal to the average calculated in our survey, ~10,000 km and possesses a uniform density of 0.05 cm^{-3}. Consider three additional parameters: f, a factor to scale the plasmoid diameter to obtain the cross-tail dimension, $\dot{M}$, the net mass loss rate due to plasmoids, and δt, the time duration between two consecutive plasmoid events. With $f = 10$ (plasmoid cross tail length equal to 10 times its diameter), one plasmoid with cross-sectional diameter of 10000 km would need to be released every $\delta t = 0.1$ s to provide a total mass loss rate $\dot{M} = mnV/\delta t$ (where V is the plasmoid volume) equal to 100 kg/s. Note that the actual plasmoid-related mass loss deficit is >500 kg/s, which is even larger. Plasmoids which were released at such high frequencies would have been detected more often by Juno, which spent more than 150 hours at distances less than 10,000 km to the current sheet.

In the above calculation, the assumed plasmoid diameter is 0.13 R_J. In contrast, Cowley et al., (2015) assumed dimensions of ~150 R_J in the tailward direction, ~70 R_J in the cross-tail direction and ~7 R_J for the direction normal to the current sheet plane. They argue that the large tailward dimensions of the plasmoid are due to the post-plasmoid plasma sheet, which is present in the reconnection exhaust.

An alternative approach is to evaluate the effective outflow area needed to lose 1 ton/s of mass continuously, e.g., via steady reconnection instead of sporadic plasmoid release. If we assume the density at ~80 R_J downstream is ~ 0.01 cm^{-3} and the outflow speed is ~400 km/s, a total area of ~1828 R_J^2 would be needed to lose 1 ton of mass per second. This translates to a square region ~42.7 R_J in length on each side. The area and square length reduce to 366 R_J^2 and 19.1 R_J if the density is increased by a factor of 5. Since observations have shown that reconnection in the Jovian magnetotail does not appear to occur in a steady manner, and a period of several days passes between consecutive large-scale 'unloading' events, the combined dimensions (in at least two directions) of all plasmoids in an 'unloading' interval must be larger than the length scales needed for continuous outflow of plasma, if they must account for all 1 ton/s of production.

Hence, the conclusion from this discussion is that small-scale magnetic reconnection does not contribute in a substantial manner to mass loss from the Jovian magnetosphere, and only large plasmoids with a prolonged PPPS may potentially account for the loss of 1 ton/s of mass from the magnetosphere. Other loss mechanisms apart from magnetic reconnection are out of scope of the present work and are not discussed here.

4.4. Orbit-by-orbit variability and comparison with other studies

The number of plasmoid events identified by our algorithm varied between perijove passes or Juno orbits. It has been shown by Vogt et al., (2020) and Yao et al., (2019) that some orbits were more "active" than others, in the form of frequent in situ sightings of magnetic reconnection or of more dynamic aurora. We found a similar result, and in Figure 15 we compare the occurrence of the plasmoids presented in this survey with the reconnection events identified by Vogt et al., (2020) for different Juno perijoves. Both surveys show excellent agreement with each other. Orbits 5, 8, 9, 10, and 11 were especially active. On the other hand, fewer events were seen for orbit 7, and for orbit numbers beyond 12. The latter could perhaps be explained by Juno's increasing inclination and lack of sampling of larger radial distances (Section 2.1). The orbital bias is less prominent for adjacent perijoves like 6 and 7 which nevertheless show different levels of activity. This variation on time scales longer than fluctuations in the upstream solar wind conditions could be explained by a different internal magnetospheric state, e.g., due to changes in Io's volcanic activity. The two example plasmoid events discussed in Section 3.1 were observed by Juno on DOY 75 and 76, 2017 during orbit 5 within a longer period of unloading of the magnetosphere, which was discussed by Yao et al., (2019). They also noted that the UV aurora was dimmer during orbit 7 than orbit 5. The long-term variability of the Jovian magnetosphere may be linked to other visible changes such as in the strength of the magnetodisc current sheet and location of the Jovian aurora, which could occur due to changes in mass loading from Io rather than external solar wind conditions (Vogt et al., 2017).

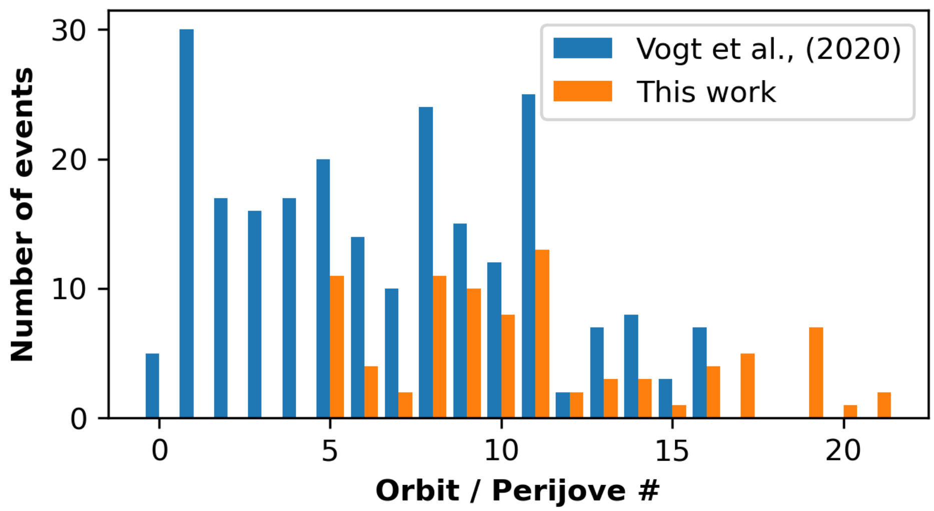

Figure 15. Histograms showing the occurrence of reconnection events in the Vogt et al., (2020) survey and of plasmoid events in our present work for different Juno orbits or perijoves. Orbits 4 and below were excluded from the present work.

5. Conclusions

In this work, we used data from the Juno spacecraft to identify plasmoids in the Jovian magnetotail with in situ durations on the order of 5 minutes or less. These small-scale events have diameters comparable to the ion inertial length, which is an important length scale as it is related to the size of the ion diffusion region in magnetic reconnection. We used data from the Juno magnetometer to identify reversals in the north-south component of the magnetic field, which is expected to occur in a reconfiguration of the magnetotail during magnetic reconnection. An automated algorithm is applied to detect B_θ reversals and identify corresponding extrema which determine the start and end of the event. Various filters are applied during the detection procedure based on the minimum variance analysis and other magnetic properties such as the proximity to the current sheet and the magnitude of the perturbation associated with the event. Based on our algorithm, we detected 87 plasmoids with 'peak-to-peak' durations between 10 s and 5 min, out of which 31 were seen to have an increase in the field component normal to the reconnection plane and were classified as magnetic flux-ropes, while the 56 events with minimum field strengths at their centers were classified as magnetic O-lines.

We examined two such plasmoid events in more detail due to the availability of simultaneous, higher cadence energetic particle intensities measured by the JEDI instruments. The results of the minimum variance analysis show that the first event can be classified as a magnetic flux-rope whereas the second had minimum field strength at its center and was an O-line. Energetic particle fluxes were seen to maximize for the second plasmoid event for the electrons, protons, oxygen and sulfur ions. Moreover, the electron pitch angle spectra indicate isotropic distributions within the magnetic loop structure, which could be due to betatron acceleration either at the front of, or within the plasmoid. For the second event, the isotropic pitch-angle distribution gradually tends to become field-aligned in the proximity of the plasmoids.

We used the 'peak-to-peak' duration between the two extrema in B_θ to calculate the duration for each plasmoid event identified by the algorithm. Within the interval of 10 s and 5 min chosen for the algorithm, a majority of plasmoids (N=50 out of 87) were seen with durations lasting less than 60 s. It is interesting to compare the distribution of plasmoid durations with previous surveys (Kronberg, Woch, Krupp, & Lagg, 2008; Vogt et al., 2014). Although the two previous studies used different definitions to define a plasmoid and looked for signatures on different timescales, their histograms also showed a similar behavior. In both studies, the histograms were skewed toward smaller values, indicating that smaller plasmoids were more likely to be observed, depending on the length scales under consideration. Similar results have also been reported for flux-ropes observed in the solar wind (Hu et al., 2018), and for plasmoids seen in Saturn's magnetosphere (Garton et al., 2021), which have shown that plasmoid diameters exhibit a power-law-like scaling. The duration of the 87 plasmoids observed in our survey is also used to estimate the plasmoids' diameters using the lobe Alfven speed. We demonstrate that all events with durations less than 5 minutes can have diameters within an order of magnitude larger or smaller than the local ion-inertial length. These results demonstrate that magnetic reconnection occurs in the Jovian magnetotail at ion kinetic scales, like in other regions in the space environments. This is important as multiple ion-inertial scale plasmoids can coalesce to form larger plasmoids, such as those analyzed by previous studies, and can also trap and accelerate ions and electrons.

The abundance of O-lines (N=56) versus flux-ropes (N=31) identified by the algorithm is consistent with previous surveys of plasmoids in Jupiter's (Vogt et al., 2014) and Saturn's (Jackman et al., 2011) magnetotail. Using the minimum variance analysis, we show that O-lines detected by our algorithm were more likely to have an axial direction perpendicular to the reconnection plane, which in the case of the Jovian magnetotail is assumed to be the local plane of bent-back magnetic field. The core-fields for the flux-ropes do not show a clear relationship with the bend-back plane, which could be because flux-ropes structures are at a later stage of plasmoid evolution and are 'de-coupled' from the corotation dynamics that cause the bend-back. Alternatively, the small number of flux ropes formed at Jupiter may simply be due to the weakness of the IMF at 5.2 AU combined with vast dimensions of this huge magnetosphere. As a result, reconnection deep in Jupiter's magnetosphere may not be aware of the direction of the IMF and any shearing of the two tail lobes due to IMF stress may be extremely weak. Such a situation may well favor the development of O-lines as opposed to flux-ropes. In contrast, in terrestrial-like magnetospheres like those of Earth and Mercury, the IMF B_Y component is an important factor to produce the core field of the plasmoid.

Despite being smaller, 87 ion-inertial scale plasmoids were detected by Juno and captured by our algorithm. We demonstrate that a plasmoid with a cross-sectional diameter of 10,000 km ($= 0.13\ R_J$) and density of 0.5 cm^{-3} would need to be released at least once every 0.1 s to result in a 100 kg/s loss rate. We argue that this release frequency is unlikely since Juno would have detected more such events had it been the case. Based on cursory calculations, we argue also that the total dimensions of plasmoids in at least two dimensions must be larger than several tens of R_J to match the dimensions of an effective outflow area needed to lose 1 ton/s of mass. This may become possible if the post-plasmoid plasma sheet is included in the calculations, as argued by Cowley et al., (2015). Hence, we suggest that ion-inertial scale plasmoid release, by itself, is an insignificant loss mechanism, unless several hundred such events are produced simultaneously every 1 s or less, which is unlikely according to the current observations.

Lastly, we compare the events detected by our algorithm with the survey of reconnection signatures observed by Vogt et al., (2020). The relative occurrence of plasmoid and reconnection events show a very good agreement and both studies find different magnetospheric behavior for different yet consecutive Juno orbits. For example, in both studies, the number of reconnection signatures seen during Juno orbit #8 were less than half of the total number seen during orbit #9. The mechanisms which can lead to such variability over the long timescale associated with each orbit (~53 days), need to be examined further.

Acknowledgments, Samples, and Data

This work was supported by NASA through the NASA Earth and Space Science Fellowship Grant 80NSSC17K0604 and Early Career Fellow Startup Grant 80NSSC20K1286. The research at the University of Iowa is supported by NASA through contract 699041X with the Southwest Research Institute. The Juno magnetometer (MAG), Waves and JEDI data used in this study is publicly available from the Planetary Plasma Interactions node of the Planetary Data System at https://pds-ppi.igpp.ucla.edu/ .

References

Artemyev, A. V., Kasahara, S., Ukhorskiy, A. Y., & Fujimoto, M. (2013). Acceleration of ions in the Jupiter magnetotail: Particle resonant interaction with dipolarization fronts. *Planetary and Space Science*, *82–83*, 134–148. https://doi.org/10.1016/j.pss.2013.04.013

Artemyev, A. V., Clark, G., Mauk, B., Vogt, M. F., & Zhang, X. J. (2020). Juno Observations of Heavy Ion Energization During Transient Dipolarizations in Jupiter Magnetotail. *Journal of Geophysical Research: Space Physics*, *125*(5), 1–14. https://doi.org/10.1029/2020JA027933

Bagenal, F. (2007). The magnetosphere of Jupiter: Coupling the equator to the poles. *Journal of Atmospheric and Solar-Terrestrial Physics*, *69*(3), 387–402. https://doi.org/10.1016/j.jastp.2006.08.012

Bagenal, F., & Delamere, P. A. (2011). Flow of mass and energy in the magnetospheres of Jupiter and Saturn. *Journal of Geophysical Research: Space Physics*, *116*(5). https://doi.org/10.1029/2010JA016294

Barnhart, B. L., Kurth, W. S., Groene, J. B., Faden, J. B., Santolik, O., & Gurnett, D. A. (2009). Electron densities in Jupiter's outer magnetosphere determined from Voyager 1 and 2 plasma wave spectra. *Journal of Geophysical Research: Space Physics*, *114*(5), 5218. https://doi.org/10.1029/2009JA014069

Connerney, J. E. P., Benn, M., Bjarno, J. B., Denver, T., Espley, J., Jorgensen, J. L., et al. (2017). The Juno Magnetic Field Investigation. *Space Science Reviews*.

https://doi.org/10.1007/s11214-017-0334-z

Cowley, S. W. H. (1981). Magnetospheric asymmetries associated with the y-component of the IMF. *Planetary and Space Science*, *29*(1), 79–96. https://doi.org/10.1016/0032-0633(81)90141-0

Cowley, S. W. H., Nichols, J. D., & Jackman, C. M. (2015). Down-tail mass loss by plasmoids in Jupiter's and Saturn's magnetospheres. *Journal of Geophysical Research A: Space Physics*, *120*(8), 6347–6356. https://doi.org/10.1002/2015JA021500

Delamere, P. A., & Bagenal, F. (2013). Magnetotail structure of the giant magnetospheres: Implications of the viscous interaction with the solar wind. *Journal of Geophysical Research: Space Physics*, *118*(11), 7045–7053. https://doi.org/10.1002/2013JA019179

Drake, J. F., Swisdak, M., Che, H., & Shay, M. A. (2006). Electron acceleration from contracting magnetic islands during reconnection. *Nature*, *443*(7111), 553–556. https://doi.org/10.1038/nature05116

Garton, T. M., Jackman, C. M., & Smith, A. W. (2021). Kronian Magnetospheric Reconnection Statistics Across Cassini's Lifetime. *Journal of Geophysical Research: Space Physics*, *126*(8), e2021JA029361. https://doi.org/10.1029/2021JA029361

Ge, Y. S., Jian, L. K., & Russell, C. T. (2007). Growth phase of Jovian substorms. *Geophysical Research Letters*, *34*(23), 1–6. https://doi.org/10.1029/2007GL031987

Ge, Y. S., Russell, C. T., & Khurana, K. K. (2010). Reconnection sites in Jupiter's magnetotail and relation to Jovian auroras. *Planetary and Space Science*, *58*(11), 1455–1469. https://doi.org/10.1016/j.pss.2010.06.013

Grigorenko, E. E., Malykhin, A. Y., Kronberg, E. A., Malova, K. V., & Daly, P. W. (2015). Acceleration of ions to suprathermal energies by turbulence in the plasmoid-like magnetic structures. *Journal of Geophysical Research A: Space Physics*, *120*(8), 6541–6558. https://doi.org/10.1002/2015JA021314

Gurnett, D. A., Scarf, F. L., Kurth, W. S., Shaw, R. R., & Poynter, R. L. (1981). Determination of Jupiter's electron density profile from plasma wave observations. *Journal of Geophysical Research: Space Physics*, *86*(A10), 8199–8212. https://doi.org/10.1029/JA086IA10P08199

Hu, Q., Zheng, J., Chen, Y., le Roux, J., & Zhao, L. (2018). Automated Detection of Small-scale Magnetic Flux Ropes in the Solar Wind: First Results from the Wind Spacecraft Measurements . *The Astrophysical Journal Supplement Series*, *239*(1), 12. https://doi.org/10.3847/1538-4365/aae57d

Jackman, C. M., Slavin, J. A., & Cowley, S. W. H. (2011). Cassini observations of plasmoid structure and dynamics: Implications for the role of magnetic reconnection in magnetospheric circulation at Saturn. *Journal of Geophysical Research: Space Physics*. https://doi.org/10.1029/2011JA016682

Jia, X., Hansen, K. C., Gombosi, T. I., Kivelson, M. G., Tóth, G., Dezeeuw, D. L., & Ridley, A. J. (2012). Magnetospheric configuration and dynamics of Saturn's magnetosphere: A global MHD simulation. *Journal of Geophysical Research: Space Physics*, *117*(5). https://doi.org/10.1029/2012JA017575

Joy, S. P., Kivelson, M. G., Walker, R. J., Khurana, K. K., Russell, C. T., & Ogino, T. (2002).

Probabilistic models of the Jovian magnetopause and bow shock locations. *Journal of Geophysical Research: Space Physics*, *107*(A10). https://doi.org/10.1029/2001JA009146

Kasahara, S., Kronberg, E. A., Kimura, T., Tao, C., Badman, S. V., Masters, A., et al. (2013). Asymmetric distribution of reconnection jet fronts in the Jovian nightside magnetosphere. *Journal of Geophysical Research: Space Physics*, *118*(1), 375–384. https://doi.org/10.1029/2012JA018130

Khurana, K. K., Kivelson, M. G., Vasyliunas, V. M., Krupp, N., Woch, J., Lagg, A., et al. (2004). The Configuration of Jupiter's Magnetosphere (Chapter 24). *Jupiter: The Planet, Satellites and Magnetosphere*.

Kivelson, M. G., & Khurana, K. K. (1995). Models of flux ropes embedded in a harris neutral sheet: Force-free solutions in low and high beta plasmas. *Journal of Geophysical Research*, *100*(A12), 23637. https://doi.org/10.1029/95ja01548

Kivelson, M. G., & Southwood, D. J. (2005). Dynamical consequences of two modes of centrifugal instability in Jupiter's outer magnetosphere. *Journal of Geophysical Research: Space Physics*, *110*(A12). https://doi.org/10.1029/2005JA011176

Krimigis, S. M., Carbary, J. F., Keath, E. P., Bostrom, C. O., Axford, W. I., Gloeckler, G., et al. (1981). Characteristics of hot plasma in the Jovian magnetosphere: Results from the Voyager spacecraft. *Journal of Geophysical Research: Space Physics*, *86*(A10), 8227–8257. https://doi.org/10.1029/JA086IA10P08227

Kronberg, E. A., Woch, J., Krupp, N., Lagg, A., Khurana, K. K., & Glassmeier, K. H. (2005). Mass release at Jupiter: Substorm-like processes in the Jovian magnetotail. *Journal of Geophysical Research: Space Physics*, *110*(A3), 1–10. https://doi.org/10.1029/2004JA010777

Kronberg, E. A., Glassmeier, K. H., Woch, J., Krupp, N., Lagg, A., & Dougherty, M. K. (2007). A possible intrinsic mechanism for the quasi-periodic dynamics of the Jovian magnetosphere. *Journal of Geophysical Research: Space Physics*, *112*(5). https://doi.org/10.1029/2006JA011994

Kronberg, E. A., Woch, J., Krupp, N., Lagg, A., Daly, P. W., & Korth, A. (2008). Comparison of periodic substorms at Jupiter and Earth. *Journal of Geophysical Research: Space Physics*, *113*(4), 1–11. https://doi.org/10.1029/2007JA012880

Kronberg, E. A., Woch, J., Krupp, N., & Lagg, A. (2008). Mass release process in the Jovian magnetosphere: Statistics on particle burst parameters. *Journal of Geophysical Research: Space Physics*, *113*(10). https://doi.org/10.1029/2008JA013332

Kronberg, E. A., Grigorenko, E. E., Malykhin, A., Kozak, L., Petrenko, B., Vogt, M. F., et al. (2019). Acceleration of Ions in Jovian Plasmoids: Does Turbulence Play a Role? *Journal of Geophysical Research: Space Physics*, *124*(7), 5056–5069. https://doi.org/10.1029/2019JA026553

Krupp, N., Woch, J., Lagg, A., Wilken, B., Livi, S., & Williams, D. J. (1998). Energetic particle bursts in the predawn Jovian magnetotail. *Geophysical Research Letters*, *25*(8), 1249–1252. https://doi.org/10.1029/98GL00863

Krupp, N., Vasyliunas, V. M., Woch, J., Lagg, A., Khurana, K. K., Kivelson, M. G., et al.

(2004). Dynamics of the Jovian Magnetosphere. In *Jupiter. The planet, satellites and magnetosphere*.

Kurth, W. S., Hospodarsky, G. B., Kirchner, D. L., Mokrzycki, B. T., Averkamp, T. F., Robison, W. T., et al. (2017). The Juno Waves Investigation. *Space Science Reviews*. https://doi.org/10.1007/s11214-017-0396-y

Lepping, R. P., Jones, J. A., & Burlaga, L. F. (1990). Magnetic field structure of interplanetary magnetic clouds at 1 AU. *Journal of Geophysical Research*, *95*(A8), 11957. https://doi.org/10.1029/ja095ia08p11957

Masters, A. (2017). Model-Based Assessments of Magnetic Reconnection and Kelvin-Helmholtz Instability at Jupiter's Magnetopause. *Journal of Geophysical Research: Space Physics*, *122*(11), 11,154-11,174. https://doi.org/10.1002/2017JA024736

Mauk, B. H., Haggerty, D. K., Jaskulek, S. E., Schlemm, C. E., Brown, L. E., Cooper, S. A., et al. (2013). The Jupiter Energetic Particle Detector Instrument (JEDI) Investigation for the Juno Mission. *Space Science Reviews 2013 213:1*, *213*(1), 289–346. https://doi.org/10.1007/S11214-013-0025-3

Moldwin, M. B., & Hughes, W. J. (1992). On the formation and evolution of plasmoids: A survey of ISEE 3 geotail data. *Journal of Geophysical Research: Space Physics*, *97*(A12), 19259–19282. https://doi.org/10.1029/92JA01598

Nishida, A. (1983). Reconnection in the Jovian magnetosphere. *Geophysical Research Letters*, *10*(6), 451–454. https://doi.org/10.1029/GL010i006p00451

Priest, E. R. (2011). The equilibrium of magnetic flux ropes (tutorial lecture). *Physics of Magnetic Flux Ropes (Eds C.T. Russell, E.R. Priest and L.C. Lee)*, 1–22. https://doi.org/10.1029/gm058p0001

Rosa Oliveira, R. A., da Silva Oliveira, M. W., Ojeda-González, A., & De La Luz, V. (2020). New Metric for Minimum Variance Analysis Validation in the Study of Interplanetary Magnetic Clouds. *Solar Physics*, *295*(3), 45. https://doi.org/10.1007/s11207-020-01610-6

Russell, C. T., Khurana, K. K., Huddleston, D. E., & Kivelson, M. G. (1998). Localized reconnection in the near jovian magnetotail. *Science*, *280*(5366), 1061–1064. https://doi.org/10.1126/science.280.5366.1061

Sarkango, Y., Jia, X., & Toth, G. (2019). Global MHD simulations of the Response of Jupiter's Magnetosphere and Ionosphere to Changes in the Solar Wind and IMF. *Journal of Geophysical Research: Space Physics*, *124*(7), 5317–5341. https://doi.org/10.1029/2019JA026787

Sarkango, Y., Slavin, J. A., Jia, X., DiBraccio, G. A., Gershman, D. J., Connerney, J. E. P., et al. (2021). Juno Observations of Ion-Inertial Scale Flux Ropes in the Jovian Magnetotail. *Geophysical Research Letters*, *48*(2). https://doi.org/10.1029/2020GL089721

Slavin, J. A., Baker, D. N., Craven, J. D., Elphic, R. C., Fairfield, D. H., Frank, L. A., et al. (1989). CDAW 8 observations of plasmoid signatures in the geomagnetic tail: An assessment. *Journal of Geophysical Research*, *94*(A11), 15153. https://doi.org/10.1029/ja094ia11p15153

Slavin, J. A., Lepping, R. P., Gjerloev, J., Fairfield, D. H., Hesse, M., Owen, C. J., et al. (2003).

Geotail observations of magnetic flux ropes in the plasma sheet. *Journal of Geophysical Research: Space Physics*, *108*(A1). https://doi.org/10.1029/2002JA009557

Smith, A. W., Slavin, J. A., Jackman, C. M., Fear, R. C., Poh, G. K., DiBraccio, G. A., et al. (2017). Automated force-free flux rope identification. *Journal of Geophysical Research: Space Physics*, *122*(1), 780–791. https://doi.org/10.1002/2016JA022994

Smith, A. W., Slavin, J. A., Jackman, C. M., Poh, G. K., & Fear, R. C. (2017). Flux ropes in the Hermean magnetotail: Distribution, properties, and formation. *Journal of Geophysical Research: Space Physics*, *122*(8), 8136–8153. https://doi.org/10.1002/2017JA024295

Sonnerup, B. U. Ö., & Cahill, L. J. (1967). Magnetopause structure and attitude from Explorer 12 observations. *Journal of Geophysical Research*, *72*(1), 171. https://doi.org/10.1029/jz072i001p00171

Taylor, J. B. (1974). Relaxation of toroidal plasma and generation of reverse magnetic fields. *Physical Review Letters*, *33*(19), 1139–1141. https://doi.org/10.1103/PhysRevLett.33.1139

Vaivads, A., Khotyaintsev, Y. V., Retinò, A., Fu, H. S., Kronberg, E. A., & Daly, P. W. (2021). Cluster Observations of Energetic Electron Acceleration Within Earthward Reconnection Jet and Associated Magnetic Flux Rope. *Journal of Geophysical Research: Space Physics*, *126*(8), 1–13. https://doi.org/10.1029/2021ja029545

Vasyliunas, V. M. (1983). Plasma distribution and flow. In *Physics of the Jovian Magnetosphere* (pp. 395–453). https://doi.org/10.1017/cbo9780511564574.013

Vogt, M. F., Kivelson, M. G., Khurana, K. K., Joy, S. P., & Walker, R. J. (2010). Reconnection and flows in the Jovian magnetotail as inferred from magnetometer observations. *Journal of Geophysical Research: Space Physics*, *115*(6). https://doi.org/10.1029/2009JA015098

Vogt, M. F., Jackman, C. M., Slavin, J. A., Bunce, E. J., Cowley, S. W. H., Kivelson, M. G., & Khurana, K. K. (2014). Structure and statistical properties of plasmoids in Jupiter's magnetotail. *Journal of Geophysical Research A: Space Physics*, *119*(2), 821–843. https://doi.org/10.1002/2013JA019393

Vogt, M. F., Bunce, E. J., Nichols, J. D., Clarke, J. T., & Kurth, W. S. (2017). Long-Term Variability of Jupiter's Magnetodisk and Implications for the Aurora. *Journal of Geophysical Research: Space Physics*, *122*(12), 12,090-12,110. https://doi.org/10.1002/2017JA024066

Vogt, M. F., Connerney, J. E. P., DiBraccio, G. A., Wilson, R. J., Thomsen, M. F., Ebert, R. W., et al. (2020). Magnetotail Reconnection at Jupiter: A Survey of Juno Magnetic Field Observations. *Journal of Geophysical Research: Space Physics*, *125*(3). https://doi.org/10.1029/2019JA027486

Woch, J., Krupp, N., Lagg, A., Wilken, B., Livi, S., & Williams, D. J. (1998). Quasi-periodic modulations of the Jovian magnetotail. *Geophysical Research Letters*, *25*(8), 1253–1256. https://doi.org/10.1029/98GL00861

Woch, J., Krupp, N., Khurana, K. K., Kivelson, M. G., Roux, A., Perraut, S., et al. (1999). Plasma sheet dynamics in the Jovian magnetotail: Signatures for substorm-like processes ? *Geophysical Research Letters*, *26*(14), 2137–2140. https://doi.org/10.1029/1999GL900493

Woch, J., Krupp, N., & Lagg, A. (2002). Particle bursts in the Jovian magnetosphere: Evidence for a near-Jupiter neutral line. *Geophysical Research Letters*, *29*(7), 42-1-42–4. https://doi.org/10.1029/2001GL014080

Yao, Z. H., Grodent, D., Kurth, W. S., Clark, G., Mauk, B. H., Kimura, T., et al. (2019). On the Relation Between Jovian Aurorae and the Loading/Unloading of the Magnetic Flux: Simultaneous Measurements From Juno, Hubble Space Telescope, and Hisaki. *Geophysical Research Letters*, *46*(21), 11632–11641. https://doi.org/10.1029/2019GL084201

Yao, Z. H., Bonfond, B., Clark, G., Grodent, D., Dunn, W. R., Vogt, M. F., et al. (2020). Reconnection- and Dipolarization-Driven Auroral Dawn Storms and Injections. *Journal of Geophysical Research: Space Physics*, *125*(8). https://doi.org/10.1029/2019JA027663

Zhong, Z. H., Zhou, M., Tang, R. X., Deng, X. H., Turner, D. L., Cohen, I. J., et al. (2020). Direct Evidence for Electron Acceleration Within Ion-Scale Flux Rope. *Geophysical Research Letters*, *47*(1), e2019GL085141. https://doi.org/10.1029/2019GL085141

AGU PUBLICATIONS

Journal of Geophysical Research – Space Physics

Supporting Information for

Properties of Ion-Inertial Scale Plasmoids Observed by the Juno Spacecraft in the Jovian Magnetotail

Yash Sarkango[1], James A. Slavin[1], Xianzhe Jia[1], Gina A. DiBraccio[2], George B. Clark[3], Weijie Sun[1], Barry H. Mauk[3], William S. Kurth[4], and George B. Hospodarsky[4]

[1]University of Michigan - Ann Arbor, USA., [2]NASA Goddard Space Flight Center, USA., [3]John Hopkins University – Applied Physics Laboratory, USA, [4]University of Iowa, USA

Contents of this file

Table S1
Figures S1-S120

Introduction

- This file contains a list of 87 plasmoids which were identified in the Jovian magnetotail. (Table S1)
- Magnetic field and Waves spectra, along with the results of MVA analysis are shown for each event. (Figures S1 – S87)
- Energetic particle spectra is shown for selective events for which high cadence JEDI data was available. (Figures S88 – S120)

Event #	Start	End	Reversal Sense	Plasmoid Type	Duration (s)	$< \|B\| >$ (nT)	ΔB_θ (nT)
1	2017-075T23:57:09	2017-075T23:58:14	tailward	o-line	65	1.16	2.07
2	2017-075T09:55:25	2017-075T09:56:27	tailward	flux-rope	62	3.85	3.84
3	2017-075T09:35:23	2017-075T09:36:08	planetward	o-line	45	2.13	4.79
4	2017-076T06:44:50	2017-076T06:46:05	planetward	flux-rope	75	4.13	6.82
5	2017-076T15:56:33	2017-076T15:56:58	planetward	o-line	25	2.34	2.93
6	2017-076T00:09:54	2017-076T00:11:45	planetward	flux-rope	111	2.58	3.64
7	2017-077T02:57:16	2017-077T02:59:55	tailward	flux-rope	159	2.22	3.16
8	2017-078T18:31:53	2017-078T18:32:15	tailward	o-line	22	1.63	3.48
9	2017-083T13:01:29	2017-083T13:02:02	tailward	o-line	33	2.87	8.45
10	2017-096T03:20:06	2017-096T03:21:31	planetward	o-line	85	2.86	5.19
11	2017-096T03:16:48	2017-096T03:17:12	tailward	o-line	24	1.62	2.05
12	2017-129T23:24:18	2017-129T23:26:02	planetward	flux-rope	104	2.10	2.92
13	2017-132T05:23:39	2017-132T05:25:09	tailward	flux-rope	90	3.26	2.09
14	2017-136T02:37:05	2017-136T02:41:32	tailward	o-line	267	1.93	4.58
15	2017-150T18:31:35	2017-150T18:31:51	tailward	o-line	16	1.63	3.22
16	2017-186T04:22:10	2017-186T04:24:32	tailward	flux-rope	142	2.25	2.49
17	2017-189T17:56:00	2017-189T17:56:15	tailward	flux-rope	15	1.06	2.31
18	2017-234T07:44:32	2017-234T07:45:17	tailward	o-line	45	2.30	3.68
19	2017-234T16:41:50	2017-234T16:42:51	planetward	o-line	61	1.95	5.67
20	2017-235T10:11:28	2017-235T10:13:45	tailward	o-line	137	1.18	3.00
21	2017-235T02:26:06	2017-235T02:26:41	tailward	o-line	35	2.17	2.49
22	2017-236T20:21:14	2017-236T20:21:34	planetward	flux-rope	20	3.67	3.50
23	2017-239T12:46:13	2017-239T12:46:40	tailward	flux-rope	27	2.00	2.31
24	2017-239T08:31:58	2017-239T08:32:27	tailward	flux-rope	29	2.67	3.23
25	2017-239T22:54:38	2017-239T22:55:07	tailward	o-line	29	1.63	2.42
26	2017-239T08:31:05	2017-239T08:31:43	planetward	o-line	38	1.73	3.33
27	2017-241T03:48:43	2017-241T03:49:08	tailward	o-line	25	5.23	11.12
28	2017-242T08:56:02	2017-242T08:56:15	planetward	o-line	13	2.19	2.48
29	2017-287T13:20:33	2017-287T13:23:05	tailward	o-line	152	2.97	7.91

30	2017-287T07:07:40	2017-287T07:09:11	tailward	o-line	91	1.71	4.29
31	2017-289T09:00:42	2017-289T09:02:16	tailward	o-line	94	4.96	2.22
32	2017-289T09:11:43	2017-289T09:12:46	planetward	o-line	63	2.28	4.18
33	2017-291T16:09:44	2017-291T16:10:27	tailward	o-line	43	1.06	2.18
34	2017-291T15:48:32	2017-291T15:49:04	tailward	flux-rope	32	3.58	4.85
35	2017-291T19:27:19	2017-291T19:27:35	planetward	o-line	16	1.93	2.20
36	2017-291T10:22:01	2017-291T10:23:45	tailward	o-line	104	1.87	3.29
37	2017-293T16:36:31	2017-293T16:37:37	planetward	o-line	66	1.88	4.29
38	2017-294T18:13:43	2017-294T18:14:09	planetward	o-line	26	2.31	3.68
39	2017-338T20:58:39	2017-338T20:59:11	planetward	o-line	32	1.67	2.67
40	2017-338T21:49:25	2017-338T21:51:52	tailward	flux-rope	147	4.54	5.87
41	2017-338T21:33:00	2017-338T21:33:18	planetward	flux-rope	18	1.35	3.53
42	2017-338T20:55:15	2017-338T20:56:04	tailward	o-line	49	3.51	5.32
43	2017-338T21:43:31	2017-338T21:43:47	tailward	o-line	16	2.89	2.12
44	2017-340T13:13:23	2017-340T13:13:36	planetward	o-line	13	0.94	2.75
45	2017-342T03:00:19	2017-342T03:02:21	tailward	o-line	122	1.64	2.13
46	2017-345T00:02:43	2017-345T00:04:13	planetward	o-line	90	1.47	2.30
47	2018-026T20:15:53	2018-026T20:17:51	tailward	flux-rope	118	3.76	3.82
48	2018-027T15:12:45	2018-027T15:16:54	tailward	o-line	249	2.31	2.56
49	2018-027T16:26:19	2018-027T16:26:51	tailward	o-line	32	1.26	2.19
50	2018-027T16:16:08	2018-027T16:16:30	tailward	o-line	22	2.19	2.25
51	2018-028T12:26:21	2018-028T12:30:13	tailward	flux-rope	232	2.04	2.05
52	2018-029T18:17:07	2018-029T18:20:05	planetward	o-line	178	1.26	3.42
53	2018-030T13:38:18	2018-030T13:39:12	planetward	o-line	54	1.67	3.27
54	2018-030T21:26:31	2018-030T21:27:11	tailward	flux-rope	40	1.84	2.16
55	2018-030T01:27:08	2018-030T01:28:41	tailward	o-line	93	1.38	3.12
56	2018-032T22:47:36	2018-032T22:48:27	planetward	flux-rope	51	2.68	2.62
57	2018-033T11:30:05	2018-033T11:31:06	tailward	o-line	61	1.69	3.09
58	2018-036T10:36:44	2018-036T10:36:59	planetward	o-line	15	1.94	4.82
59	2018-083T11:21:16	2018-083T11:21:44	tailward	o-line	28	1.34	3.33
60	2018-085T11:18:14	2018-085T11:19:09	tailward	flux-rope	55	2.59	4.27
61	2018-139T18:52:52	2018-139T18:53:30	planetward	o-line	38	4.15	6.16

62	2018-140T14:27:52	2018-140T14:28:15	planetward	o-line	23	2.42	3.25
63	2018-142T01:27:49	2018-142T01:28:18	planetward	o-line	29	4.73	6.55
64	2018-188T23:12:51	2018-188T23:14:44	tailward	flux-rope	113	1.86	2.27
65	2018-190T14:48:13	2018-190T14:48:41	planetward	flux-rope	28	1.54	3.01
66	2018-191T10:23:12	2018-191T10:23:35	planetward	o-line	23	5.36	4.88
67	2018-245T15:02:56	2018-245T15:03:20	planetward	o-line	24	0.89	2.21
68	2018-297T14:55:14	2018-297T14:58:31	tailward	o-line	197	2.34	3.60
69	2018-297T17:05:54	2018-297T17:06:24	planetward	o-line	30	1.11	2.58
70	2018-298T01:02:35	2018-298T01:03:48	planetward	flux-rope	73	3.59	5.47
71	2018-298T10:48:22	2018-298T10:48:53	planetward	o-line	31	1.84	4.51
72	2018-350T04:57:17	2018-350T04:57:30	tailward	flux-rope	13	2.41	2.72
73	2018-351T10:04:44	2018-351T10:05:03	planetward	flux-rope	19	1.93	2.08
74	2018-352T04:27:41	2018-352T04:28:18	planetward	flux-rope	37	4.27	9.31
75	2018-353T14:00:16	2018-353T14:02:33	tailward	o-line	137	2.71	4.46
76	2018-353T13:59:12	2018-353T13:59:40	tailward	o-line	28	1.95	5.25
77	2019-089T20:35:44	2019-089T20:36:34	tailward	flux-rope	50	4.46	2.59
78	2019-090T05:24:56	2019-090T05:27:20	tailward	flux-rope	144	6.35	3.12
79	2019-091T21:33:28	2019-091T21:35:36	tailward	flux-rope	128	3.56	2.81
80	2019-091T00:47:51	2019-091T00:50:08	tailward	flux-rope	137	2.02	3.63
81	2019-092T17:30:38	2019-092T17:32:03	planetward	o-line	85	2.33	4.62
82	2019-093T20:50:14	2019-093T20:50:31	planetward	o-line	17	2.04	5.95
83	2019-093T01:38:18	2019-093T01:39:10	planetward	o-line	52	2.72	3.23
84	2019-144T19:03:24	2019-144T19:03:37	planetward	flux-rope	13	2.63	4.10
85	2019-199T17:28:05	2019-199T17:28:22	planetward	flux-rope	17	1.72	3.52
86	2019-249T19:23:52	2019-249T19:24:35	planetward	o-line	43	1.09	2.30
87	2019-301T22:13:15	2019-301T22:14:05	planetward	o-line	50	2.29	4.75

Table S1. List of plasmoids identified by the algorithm.

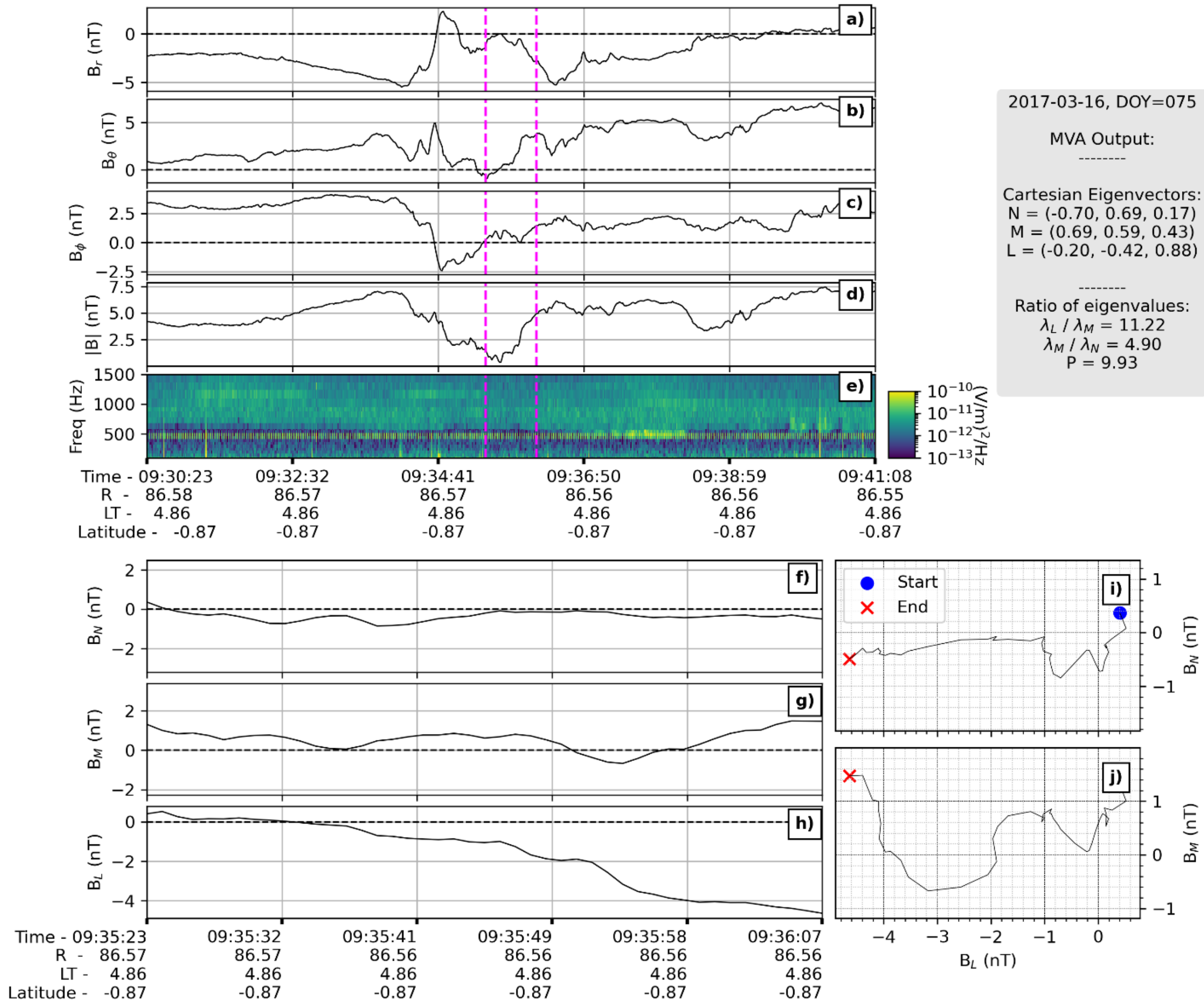

2017-03-16, DOY=075
MVA Output:

Cartesian Eigenvectors:
N = (-0.70, 0.69, 0.17)
M = (0.69, 0.59, 0.43)
L = (-0.20, -0.42, 0.88)

Ratio of eigenvalues:
λL / λM = 11.22
λM / λN = 4.90
P = 9.93
a)
b)
c)
d)
e)
f)
g)
h)
i)
j)
Br (nT)
Bθ (nT)
Bϕ (nT)
|B| (nT)
Freq (Hz)
(V/m)²/Hz
BN (nT)
BM (nT)
BL (nT)
Start
End
Time - 09:30:23 09:32:32 09:34:41 09:36:50 09:38:59 09:41:08
R - 86.58 86.57 86.57 86.56 86.56 86.55
LT - 4.86 4.86 4.86 4.86 4.86 4.86
Latitude - -0.87 -0.87 -0.87 -0.87 -0.87 -0.87
Time - 09:35:23 09:35:32 09:35:41 09:35:49 09:35:58 09:36:07
R - 86.57 86.57 86.56 86.56 86.56 86.56
LT - 4.86 4.86 4.86 4.86 4.86 4.86
Latitude - -0.87 -0.87 -0.87 -0.87 -0.87 -0.87

Figure S1

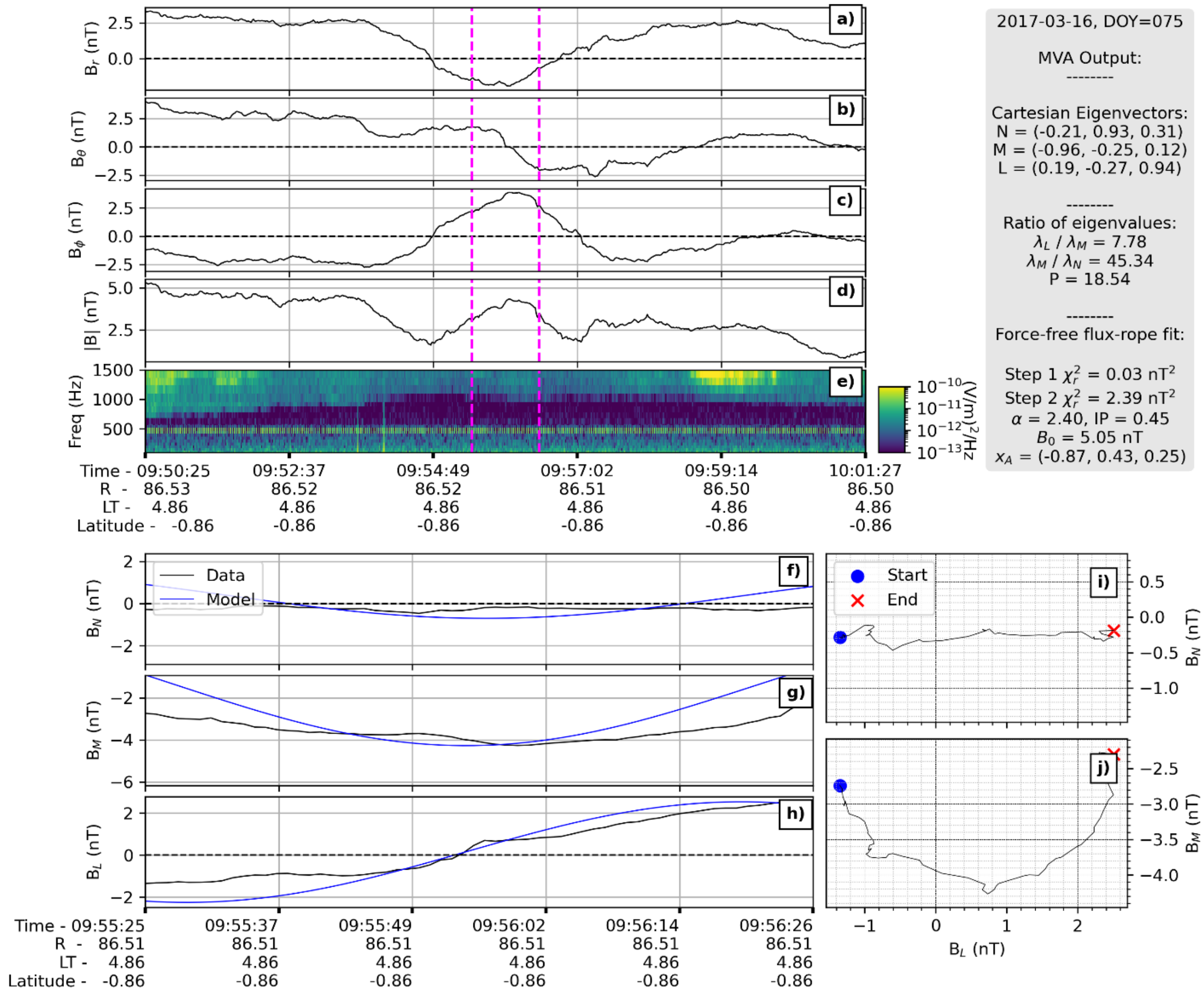
2017-03-16, DOY=075
MVA Output:
Cartesian Eigenvectors:
N = (-0.21, 0.93, 0.31)
M = (-0.96, -0.25, 0.12)
L = (0.19, -0.27, 0.94)
Ratio of eigenvalues:
λ_L / λ_M = 7.78
λ_M / λ_N = 45.34
P = 18.54
Force-free flux-rope fit:
Step 1 χ_r^2 = 0.03 nT^2
Step 2 χ_r^2 = 2.39 nT^2
α = 2.40, IP = 0.45
B_0 = 5.05 nT
x_A = (-0.87, 0.43, 0.25)
Data
Model
Start
End

Figure S2

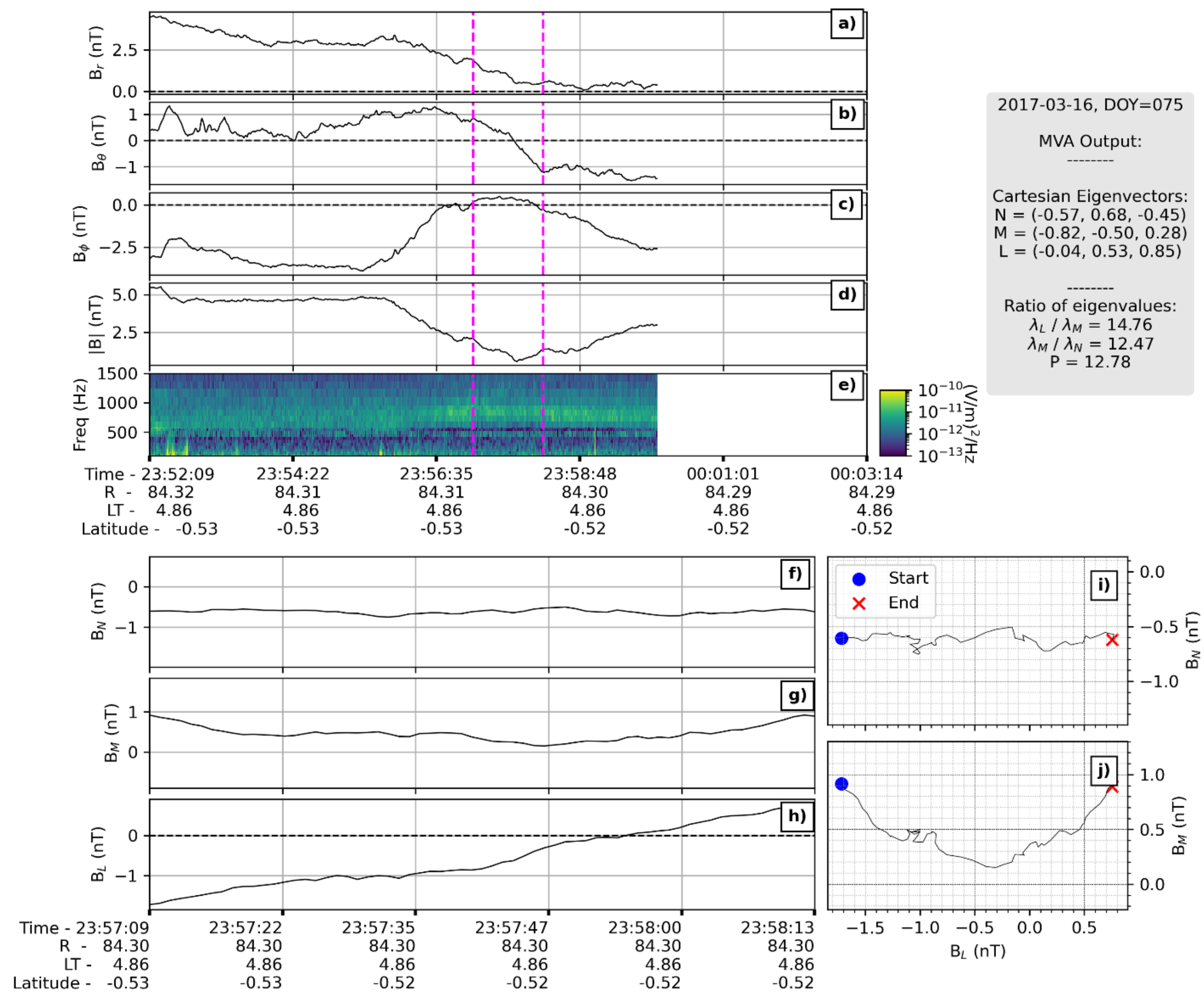
a)
b)
c)
d)
e)
f)
g)
h)
i)
j)
2017-03-16, DOY=075
MVA Output:

Cartesian Eigenvectors:
N = (-0.57, 0.68, -0.45)
M = (-0.82, -0.50, 0.28)
L = (-0.04, 0.53, 0.85)

Ratio of eigenvalues:
λL / λM = 14.76
λM / λN = 12.47
P = 12.78
Time - 23:52:09 23:54:22 23:56:35 23:58:48 00:01:01 00:03:14
R - 84.32 84.31 84.31 84.30 84.29 84.29
LT - 4.86 4.86 4.86 4.86 4.86 4.86
Latitude - -0.53 -0.53 -0.53 -0.52 -0.52 -0.52
Time - 23:57:09 23:57:22 23:57:35 23:57:47 23:58:00 23:58:13
R - 84.30 84.30 84.30 84.30 84.30 84.30
LT - 4.86 4.86 4.86 4.86 4.86 4.86
Latitude - -0.53 -0.53 -0.52 -0.52 -0.52 -0.52
Start
End
Freq (Hz)
(V/m)²/Hz

Figure S3

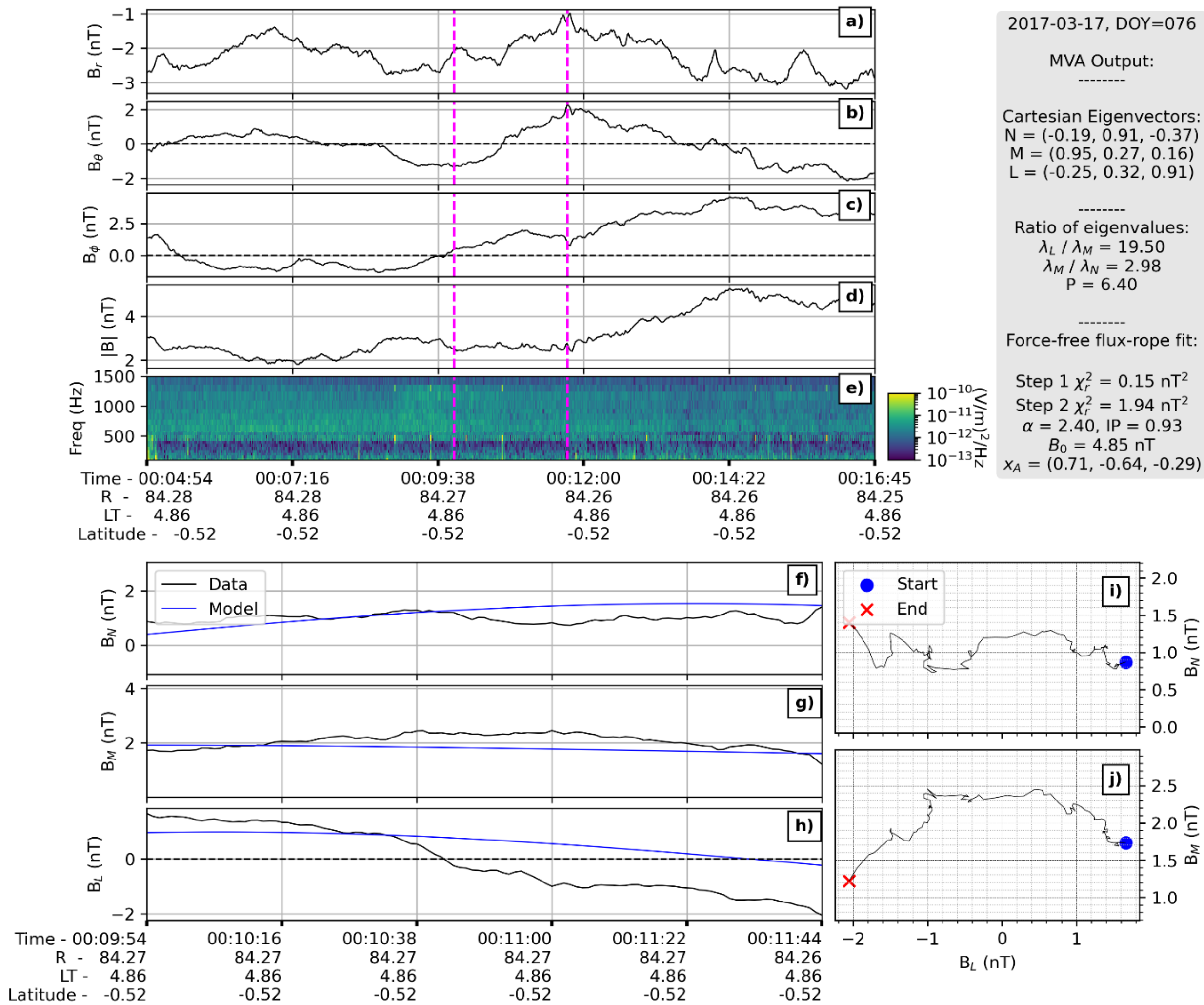
2017-03-17, DOY=076
MVA Output:

Cartesian Eigenvectors:
N = (-0.19, 0.91, -0.37)
M = (0.95, 0.27, 0.16)
L = (-0.25, 0.32, 0.91)

Ratio of eigenvalues:
λ_L / λ_M = 19.50
λ_M / λ_N = 2.98
P = 6.40

Force-free flux-rope fit:
Step 1 χ_r^2 = 0.15 nT^2
Step 2 χ_r^2 = 1.94 nT^2
α = 2.40, IP = 0.93
B_0 = 4.85 nT
x_A = (0.71, -0.64, -0.29)
Time - 00:04:54 00:07:16 00:09:38 00:12:00 00:14:22 00:16:45
R - 84.28 84.28 84.27 84.26 84.26 84.25
LT - 4.86 4.86 4.86 4.86 4.86 4.86
Latitude - -0.52 -0.52 -0.52 -0.52 -0.52 -0.52
Data
Model
Start
End
Time - 00:09:54 00:10:16 00:10:38 00:11:00 00:11:22 00:11:44
R - 84.27 84.27 84.27 84.27 84.27 84.26
LT - 4.86 4.86 4.86 4.86 4.86 4.86
Latitude - -0.52 -0.52 -0.52 -0.52 -0.52 -0.52

Figure S4

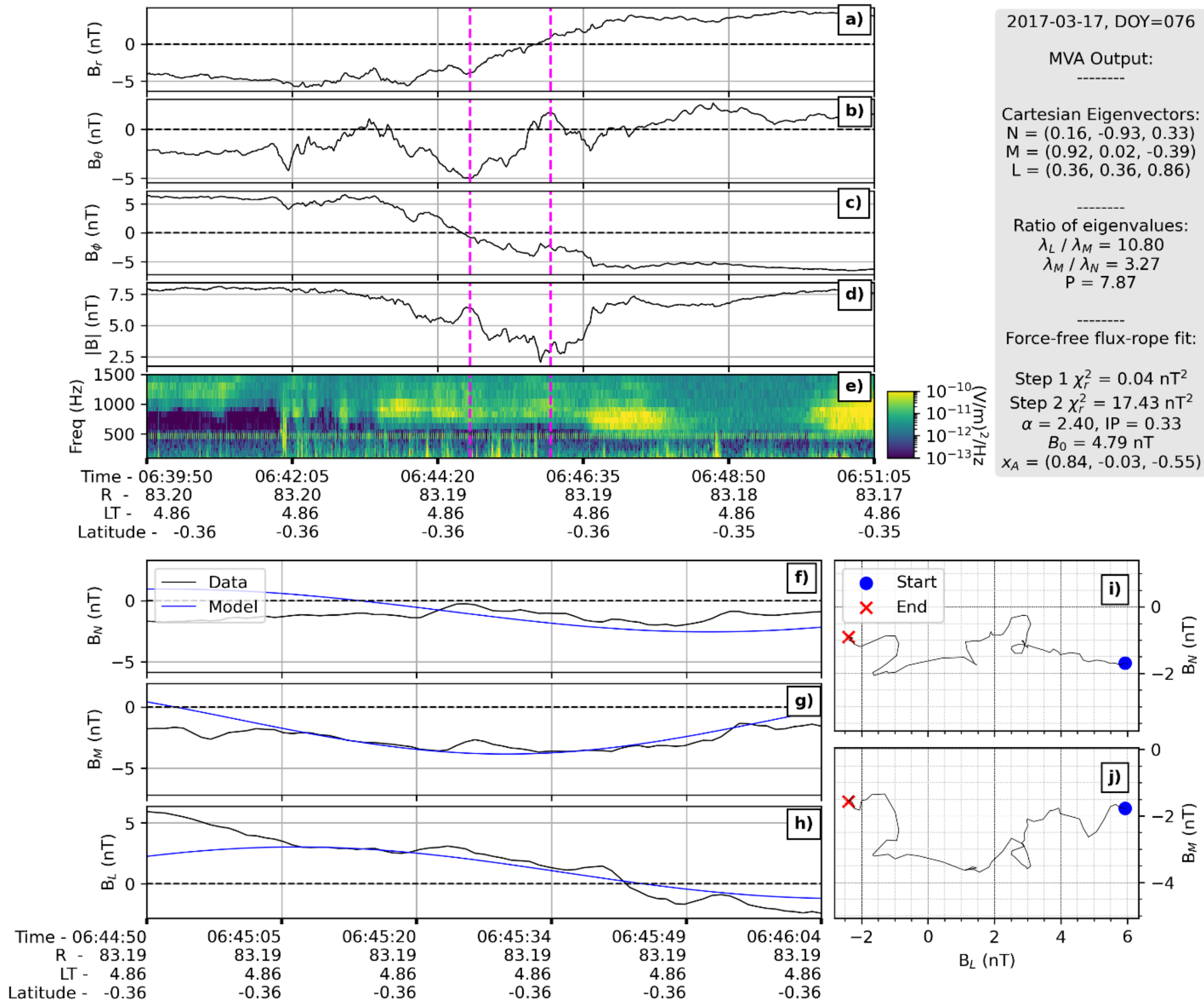
2017-03-17, DOY=076
MVA Output:
Cartesian Eigenvectors:
N = (0.16, -0.93, 0.33)
M = (0.92, 0.02, -0.39)
L = (0.36, 0.36, 0.86)
Ratio of eigenvalues:
λ_L / λ_M = 10.80
λ_M / λ_N = 3.27
P = 7.87
Force-free flux-rope fit:
Step 1 χ_r^2 = 0.04 nT^2
Step 2 χ_r^2 = 17.43 nT^2
α = 2.40, IP = 0.33
B_0 = 4.79 nT
x_A = (0.84, -0.03, -0.55)
Data
Model
Start
End

Figure S5

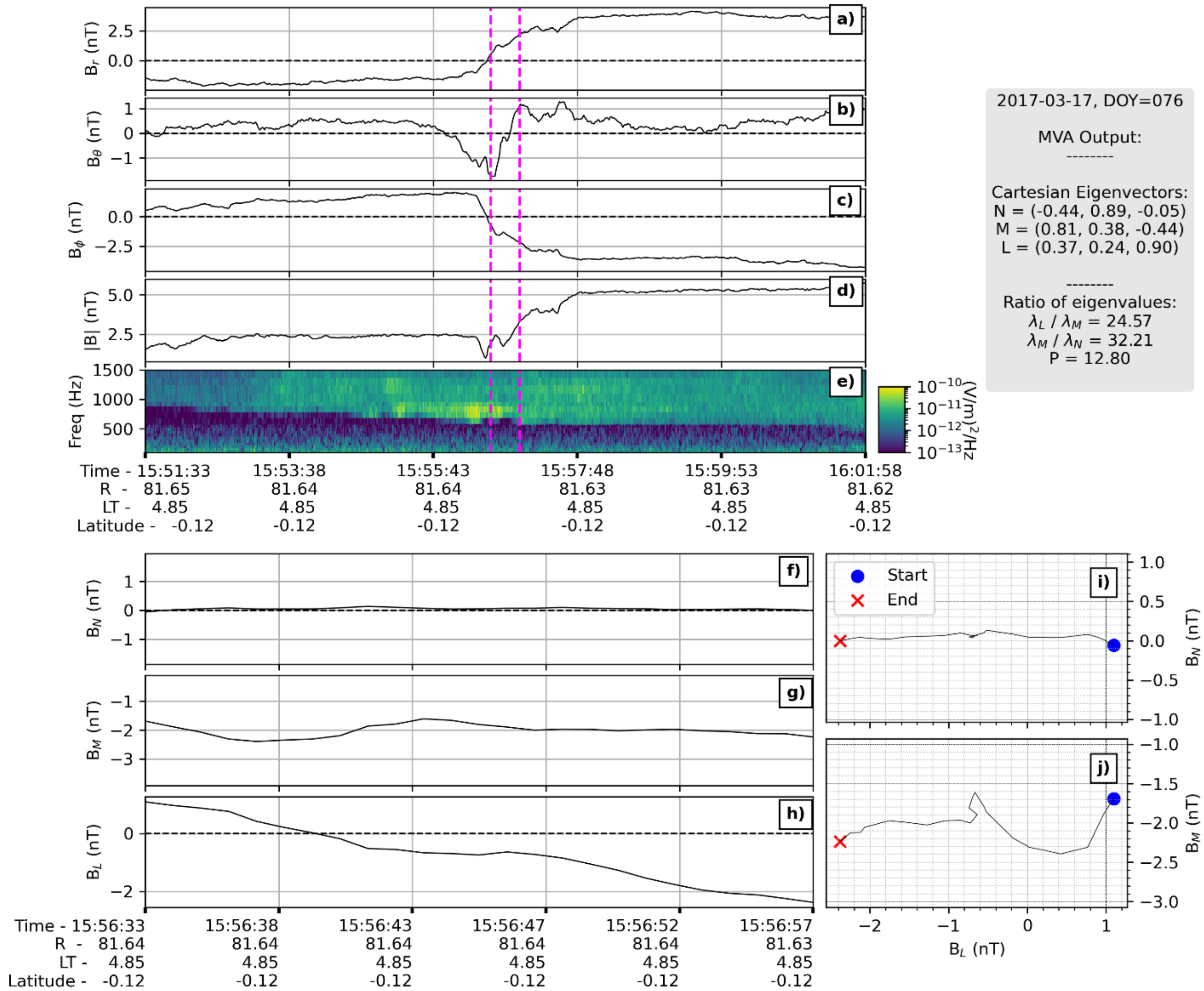
a)
b)
c)
d)
e)
f)
g)
h)
i)
j)
2017-03-17, DOY=076
MVA Output:
Cartesian Eigenvectors:
N = (-0.44, 0.89, -0.05)
M = (0.81, 0.38, -0.44)
L = (0.37, 0.24, 0.90)
Ratio of eigenvalues:
λL / λM = 24.57
λM / λN = 32.21
P = 12.80
Start
End
Time - 15:51:33 15:53:38 15:55:43 15:57:48 15:59:53 16:01:58
R - 81.65 81.64 81.64 81.63 81.63 81.62
LT - 4.85 4.85 4.85 4.85 4.85 4.85
Latitude - -0.12 -0.12 -0.12 -0.12 -0.12 -0.12
Time - 15:56:33 15:56:38 15:56:43 15:56:47 15:56:52 15:56:57
R - 81.64 81.64 81.64 81.64 81.64 81.63
LT - 4.85 4.85 4.85 4.85 4.85 4.85
Latitude - -0.12 -0.12 -0.12 -0.12 -0.12 -0.12
Freq (Hz)
(V/m)²/Hz
BL (nT)
BN (nT)
BM (nT)

Figure S6

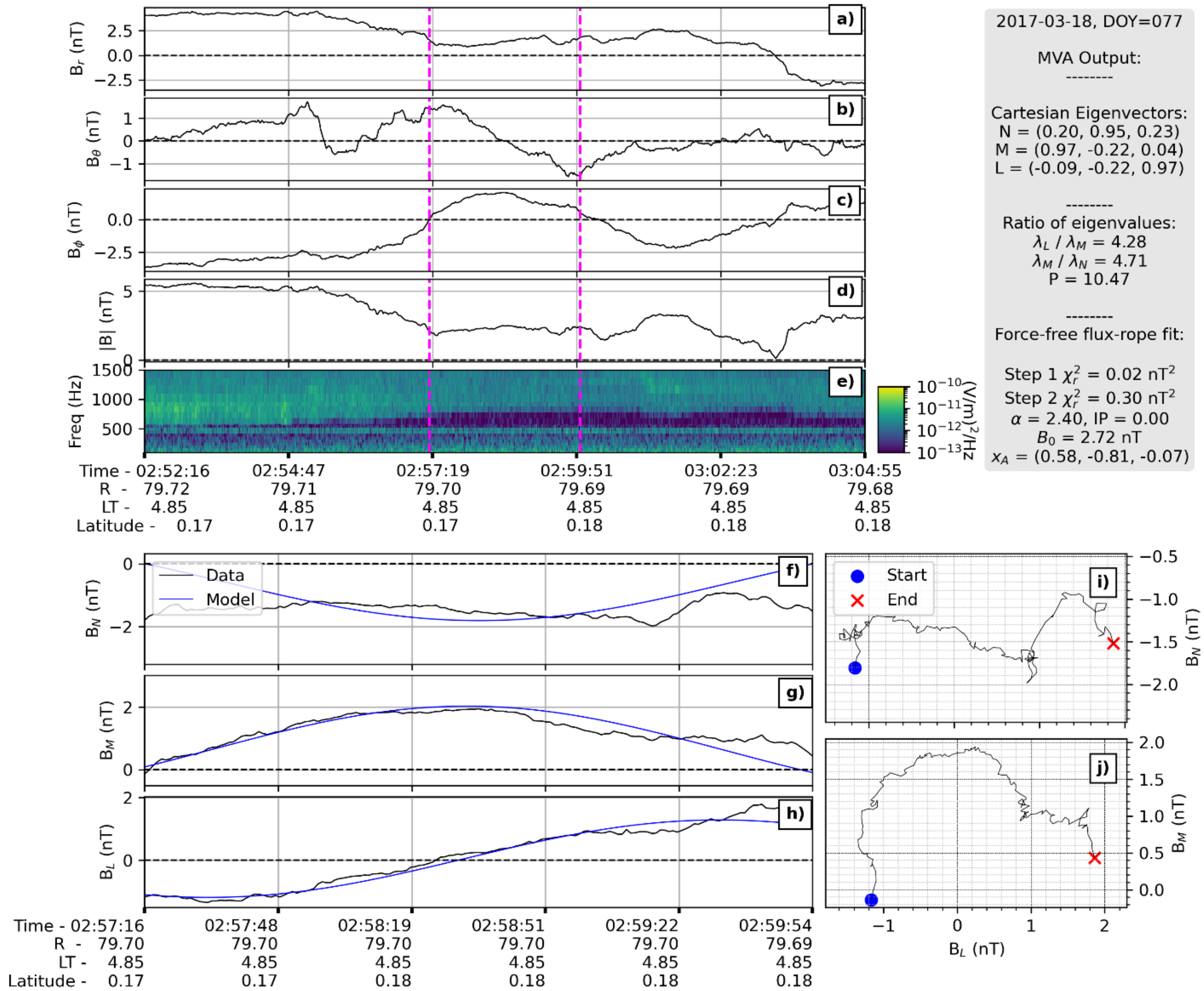
2017-03-18, DOY=077
MVA Output:
Cartesian Eigenvectors:
N = (0.20, 0.95, 0.23)
M = (0.97, -0.22, 0.04)
L = (-0.09, -0.22, 0.97)
Ratio of eigenvalues:
λ_L / λ_M = 4.28
λ_M / λ_N = 4.71
P = 10.47
Force-free flux-rope fit:
Step 1 χ_r^2 = 0.02 nT^2
Step 2 χ_r^2 = 0.30 nT^2
α = 2.40, IP = 0.00
B_0 = 2.72 nT
x_A = (0.58, -0.81, -0.07)
Data
Model
Start
End

Figure S7

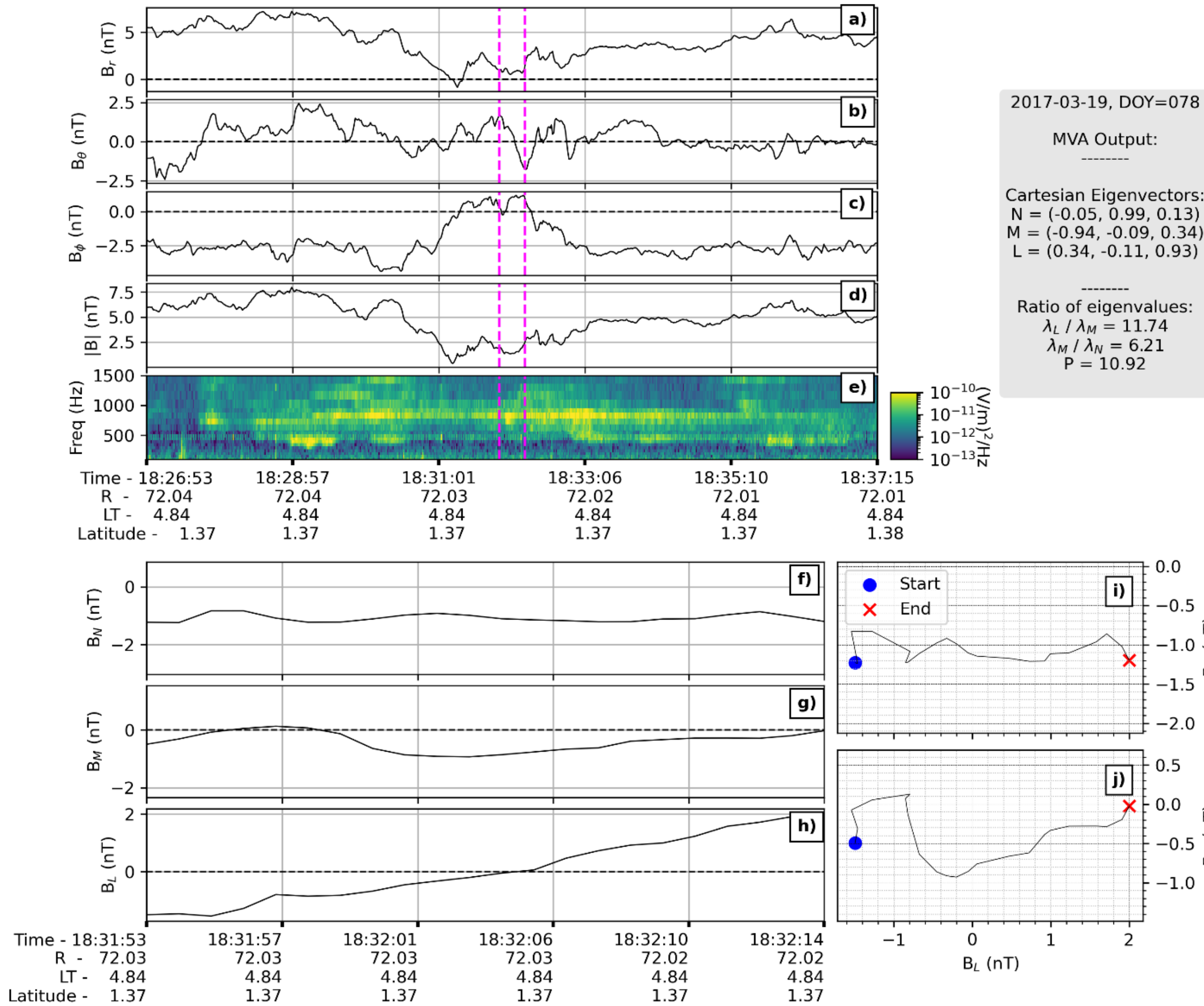

2017-03-19, DOY=078
MVA Output:

Cartesian Eigenvectors:
N = (-0.05, 0.99, 0.13)
M = (-0.94, -0.09, 0.34)
L = (0.34, -0.11, 0.93)

Ratio of eigenvalues:
λL / λM = 11.74
λM / λN = 6.21
P = 10.92
Time - 18:26:53 18:28:57 18:31:01 18:33:06 18:35:10 18:37:15
R - 72.04 72.04 72.03 72.02 72.01 72.01
LT - 4.84 4.84 4.84 4.84 4.84 4.84
Latitude - 1.37 1.37 1.37 1.37 1.37 1.38
Time - 18:31:53 18:31:57 18:32:01 18:32:06 18:32:10 18:32:14
R - 72.03 72.03 72.03 72.03 72.02 72.02
LT - 4.84 4.84 4.84 4.84 4.84 4.84
Latitude - 1.37 1.37 1.37 1.37 1.37 1.37
Start
End

Figure S8

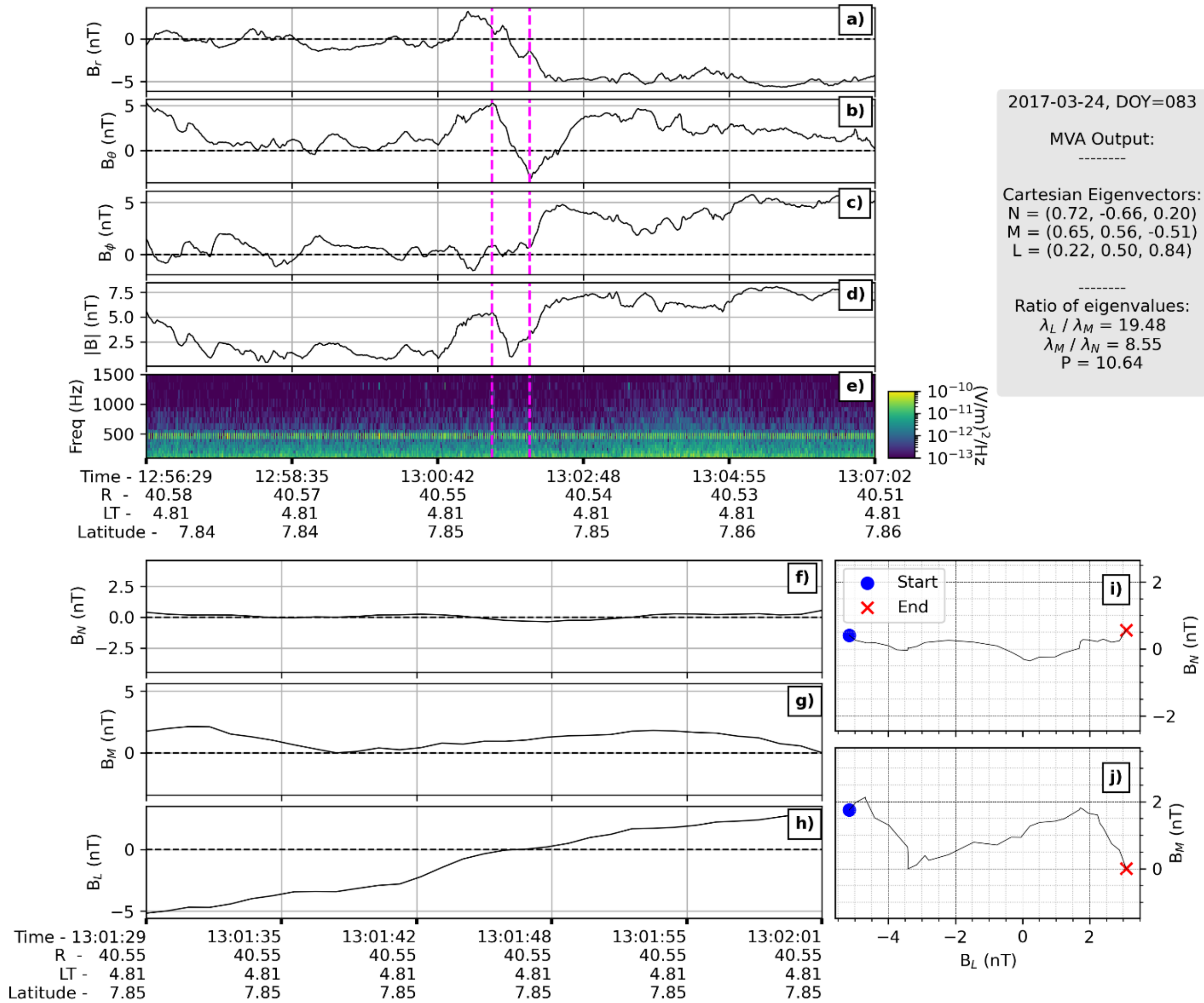
2017-03-24, DOY=083
MVA Output:
Cartesian Eigenvectors:
N = (0.72, -0.66, 0.20)
M = (0.65, 0.56, -0.51)
L = (0.22, 0.50, 0.84)
Ratio of eigenvalues:
λ_L / λ_M = 19.48
λ_M / λ_N = 8.55
P = 10.64
Start
End
Time - 12:56:29 12:58:35 13:00:42 13:02:48 13:04:55 13:07:02
R - 40.58 40.57 40.55 40.54 40.53 40.51
LT - 4.81 4.81 4.81 4.81 4.81 4.81
Latitude - 7.84 7.84 7.85 7.85 7.86 7.86
Time - 13:01:29 13:01:35 13:01:42 13:01:48 13:01:55 13:02:01
R - 40.55 40.55 40.55 40.55 40.55 40.55
LT - 4.81 4.81 4.81 4.81 4.81 4.81
Latitude - 7.85 7.85 7.85 7.85 7.85 7.85

Figure S9

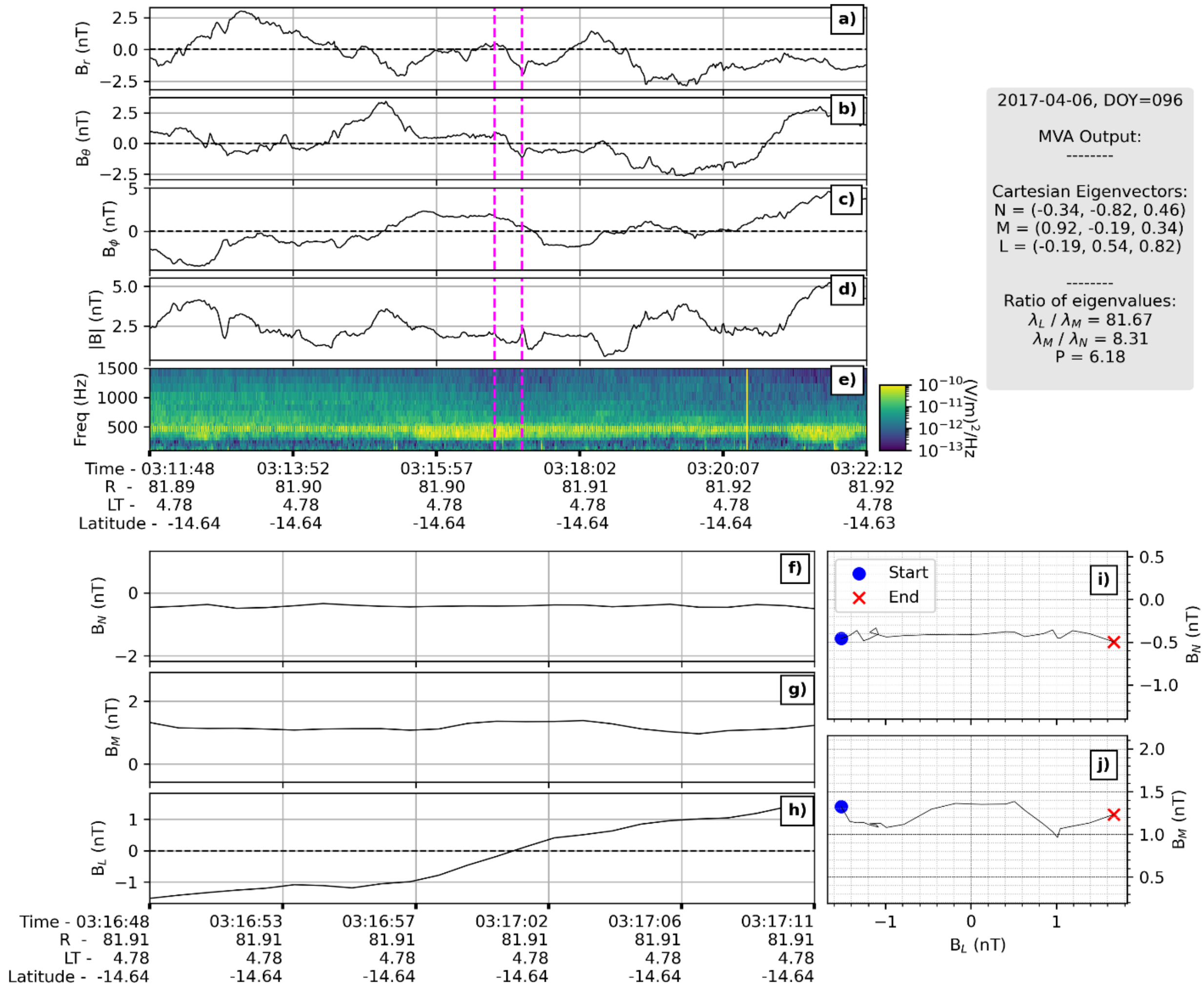
2017-04-06, DOY=096
MVA Output:

Cartesian Eigenvectors:
N = (-0.34, -0.82, 0.46)
M = (0.92, -0.19, 0.34)
L = (-0.19, 0.54, 0.82)

Ratio of eigenvalues:
λ_L / λ_M = 81.67
λ_M / λ_N = 8.31
P = 6.18
Time - 03:11:48 03:13:52 03:15:57 03:18:02 03:20:07 03:22:12
R - 81.89 81.90 81.90 81.91 81.92 81.92
LT - 4.78 4.78 4.78 4.78 4.78 4.78
Latitude - -14.64 -14.64 -14.64 -14.64 -14.64 -14.63
Time - 03:16:48 03:16:53 03:16:57 03:17:02 03:17:06 03:17:11
R - 81.91 81.91 81.91 81.91 81.91 81.91
LT - 4.78 4.78 4.78 4.78 4.78 4.78
Latitude - -14.64 -14.64 -14.64 -14.64 -14.64 -14.64
Start
End

Figure S10

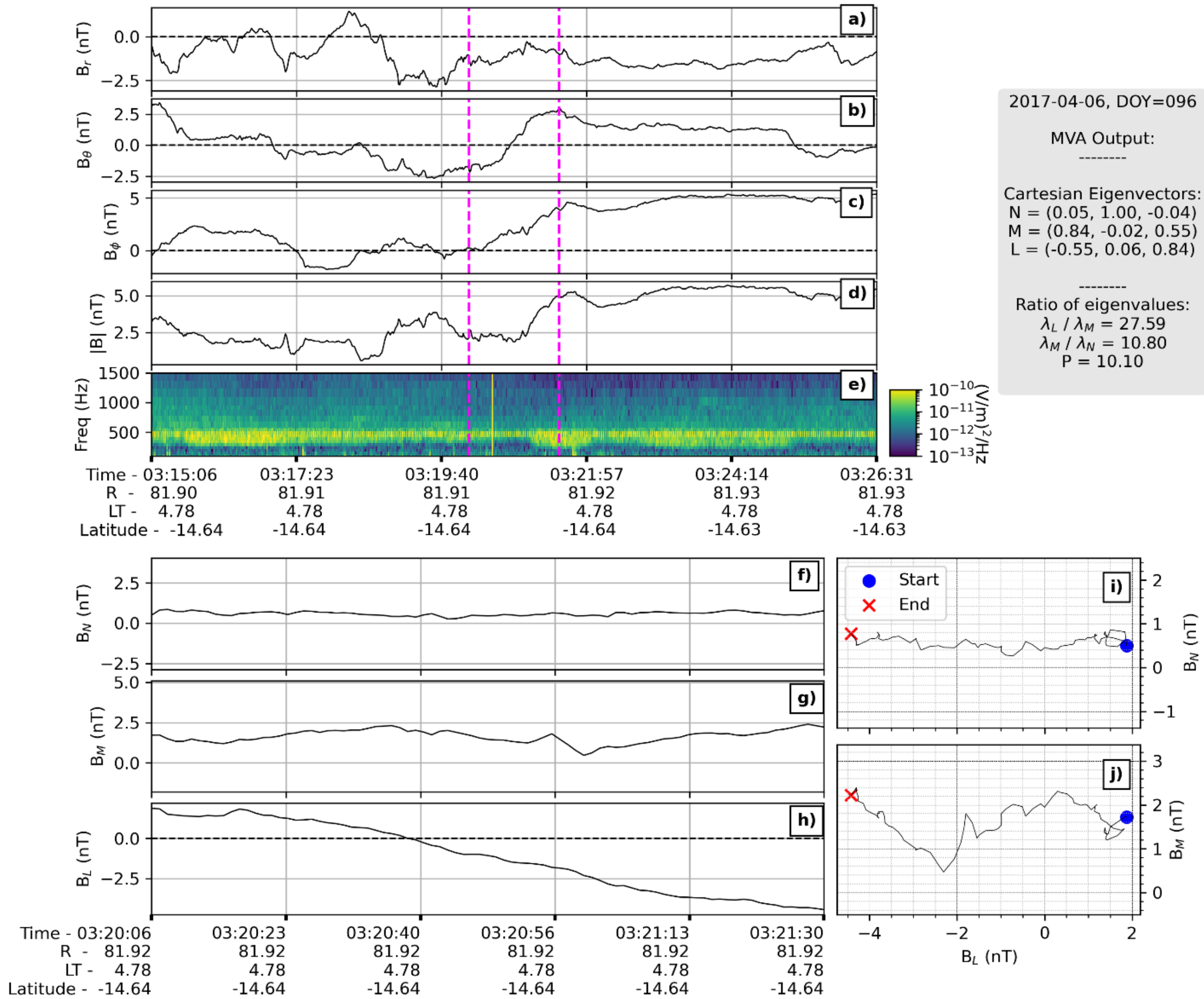

a)
b)
c)
d)
e)
f)
g)
h)
i)
j)
B_r (nT)
B_θ (nT)
B_ϕ (nT)
|B| (nT)
Freq (Hz)
(V/m)^2/Hz
B_N (nT)
B_M (nT)
B_L (nT)
Start
End
Time - 03:15:06 03:17:23 03:19:40 03:21:57 03:24:14 03:26:31
R - 81.90 81.91 81.91 81.92 81.93 81.93
LT - 4.78 4.78 4.78 4.78 4.78 4.78
Latitude - -14.64 -14.64 -14.64 -14.64 -14.63 -14.63
Time - 03:20:06 03:20:23 03:20:40 03:20:56 03:21:13 03:21:30
R - 81.92 81.92 81.92 81.92 81.92 81.92
LT - 4.78 4.78 4.78 4.78 4.78 4.78
Latitude - -14.64 -14.64 -14.64 -14.64 -14.64 -14.64
2017-04-06, DOY=096
MVA Output:

Cartesian Eigenvectors:
N = (0.05, 1.00, -0.04)
M = (0.84, -0.02, 0.55)
L = (-0.55, 0.06, 0.84)

Ratio of eigenvalues:
λ_L / λ_M = 27.59
λ_M / λ_N = 10.80
P = 10.10

Figure S11

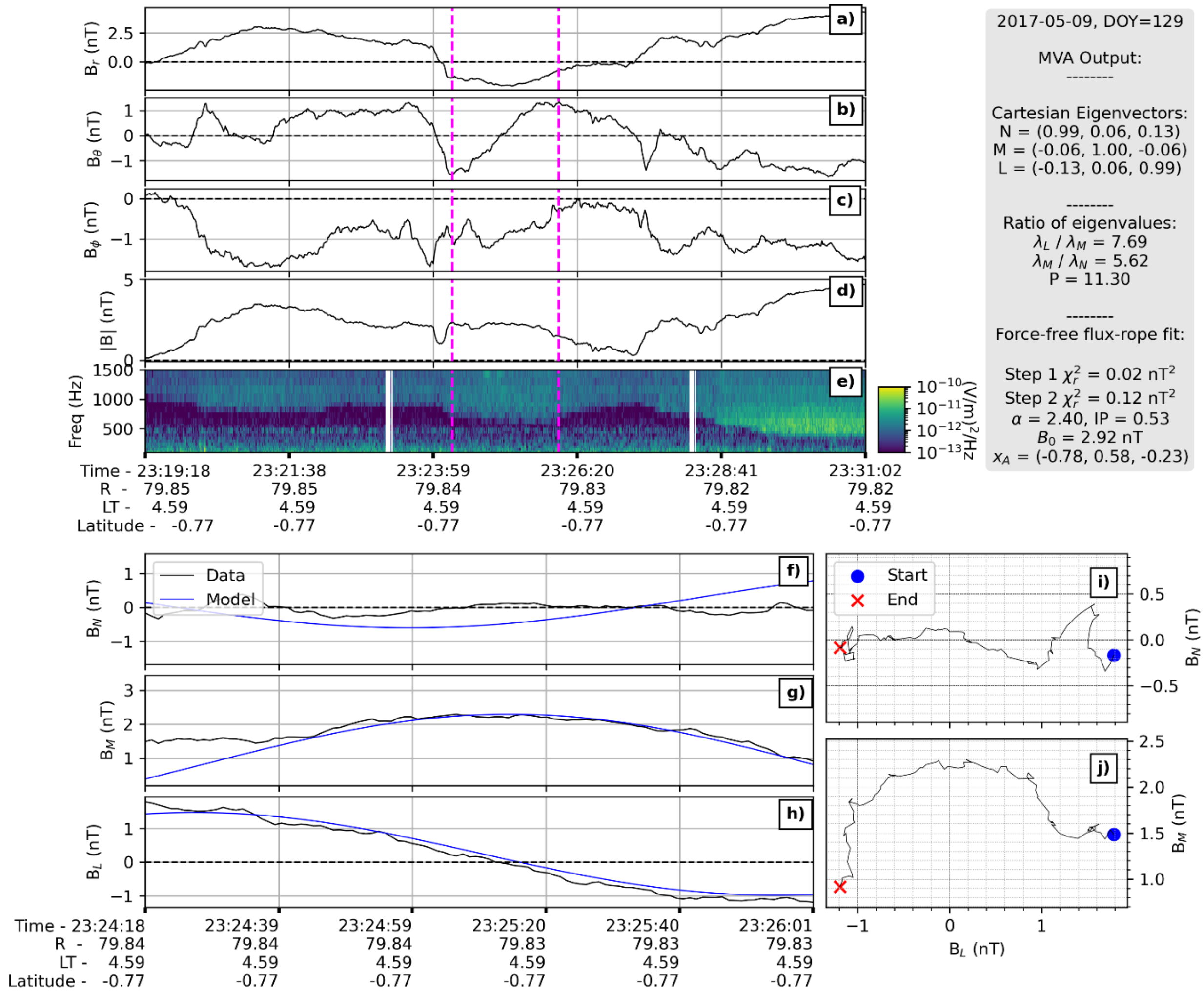
2017-05-09, DOY=129
MVA Output:
Cartesian Eigenvectors:
N = (0.99, 0.06, 0.13)
M = (-0.06, 1.00, -0.06)
L = (-0.13, 0.06, 0.99)
Ratio of eigenvalues:
λ_L / λ_M = 7.69
λ_M / λ_N = 5.62
P = 11.30
Force-free flux-rope fit:
Step 1 χ_r^2 = 0.02 nT^2
Step 2 χ_r^2 = 0.12 nT^2
α = 2.40, IP = 0.53
B_0 = 2.92 nT
x_A = (-0.78, 0.58, -0.23)
Data
Model
Start
End

Figure S12

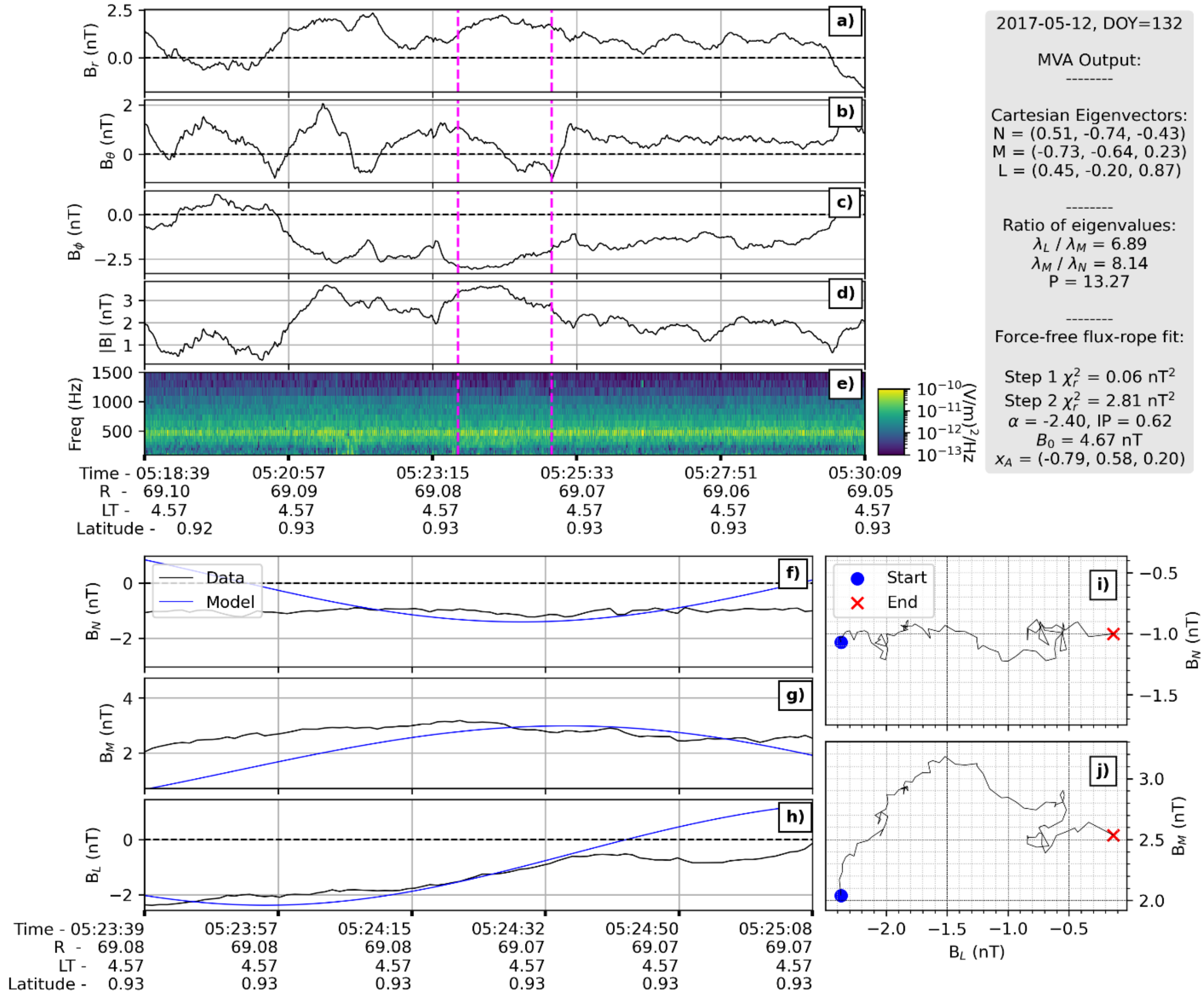
2017-05-12, DOY=132
MVA Output:
Cartesian Eigenvectors:
N = (0.51, -0.74, -0.43)
M = (-0.73, -0.64, 0.23)
L = (0.45, -0.20, 0.87)
Ratio of eigenvalues:
λ_L / λ_M = 6.89
λ_M / λ_N = 8.14
P = 13.27
Force-free flux-rope fit:
Step 1 χ_r^2 = 0.06 nT^2
Step 2 χ_r^2 = 2.81 nT^2
α = -2.40, IP = 0.62
B_0 = 4.67 nT
x_A = (-0.79, 0.58, 0.20)
Time - 05:18:39 05:20:57 05:23:15 05:25:33 05:27:51 05:30:09
R - 69.10 69.09 69.08 69.07 69.06 69.05
LT - 4.57 4.57 4.57 4.57 4.57 4.57
Latitude - 0.92 0.93 0.93 0.93 0.93 0.93
Data
Model
Start
End
Time - 05:23:39 05:23:57 05:24:15 05:24:32 05:24:50 05:25:08
R - 69.08 69.08 69.08 69.07 69.07 69.07
LT - 4.57 4.57 4.57 4.57 4.57 4.57
Latitude - 0.93 0.93 0.93 0.93 0.93 0.93
B_L (nT)

Figure S13

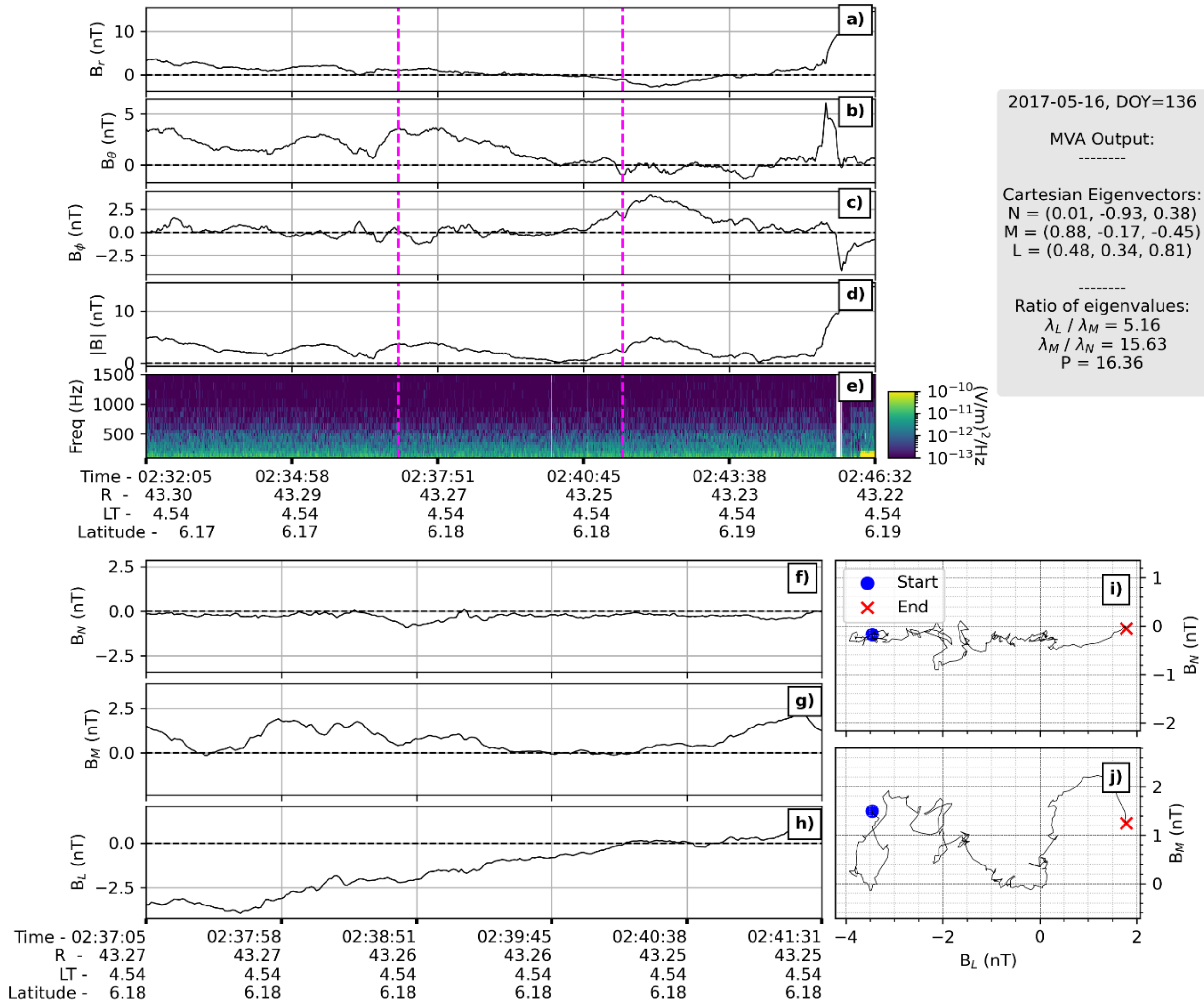
2017-05-16, DOY=136
MVA Output:
Cartesian Eigenvectors:
N = (0.01, -0.93, 0.38)
M = (0.88, -0.17, -0.45)
L = (0.48, 0.34, 0.81)
Ratio of eigenvalues:
λ_L / λ_M = 5.16
λ_M / λ_N = 15.63
P = 16.36
Start
End
Time - 02:32:05 02:34:58 02:37:51 02:40:45 02:43:38 02:46:32
Time - 02:37:05 02:37:58 02:38:51 02:39:45 02:40:38 02:41:31

Figure S14

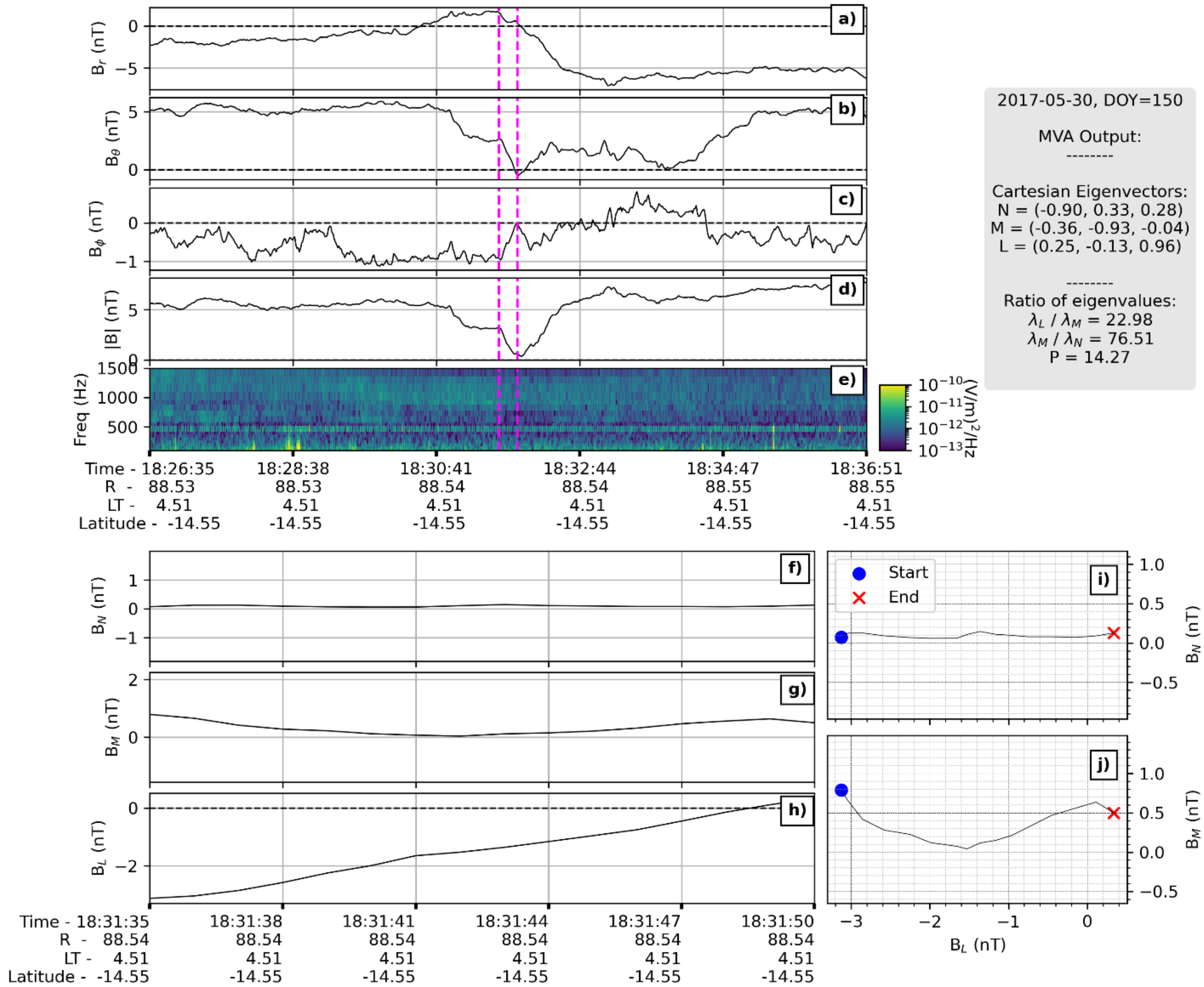
a)
b)
c)
d)
e)
f)
g)
h)
i)
j)
2017-05-30, DOY=150
MVA Output:
Cartesian Eigenvectors:
N = (-0.90, 0.33, 0.28)
M = (-0.36, -0.93, -0.04)
L = (0.25, -0.13, 0.96)
Ratio of eigenvalues:
λL / λM = 22.98
λM / λN = 76.51
P = 14.27
Start
End
Time - 18:26:35 18:28:38 18:30:41 18:32:44 18:34:47 18:36:51
R - 88.53 88.53 88.54 88.54 88.55 88.55
LT - 4.51 4.51 4.51 4.51 4.51 4.51
Latitude - -14.55 -14.55 -14.55 -14.55 -14.55 -14.55
Time - 18:31:35 18:31:38 18:31:41 18:31:44 18:31:47 18:31:50
R - 88.54 88.54 88.54 88.54 88.54 88.54
LT - 4.51 4.51 4.51 4.51 4.51 4.51
Latitude - -14.55 -14.55 -14.55 -14.55 -14.55 -14.55

Figure S15

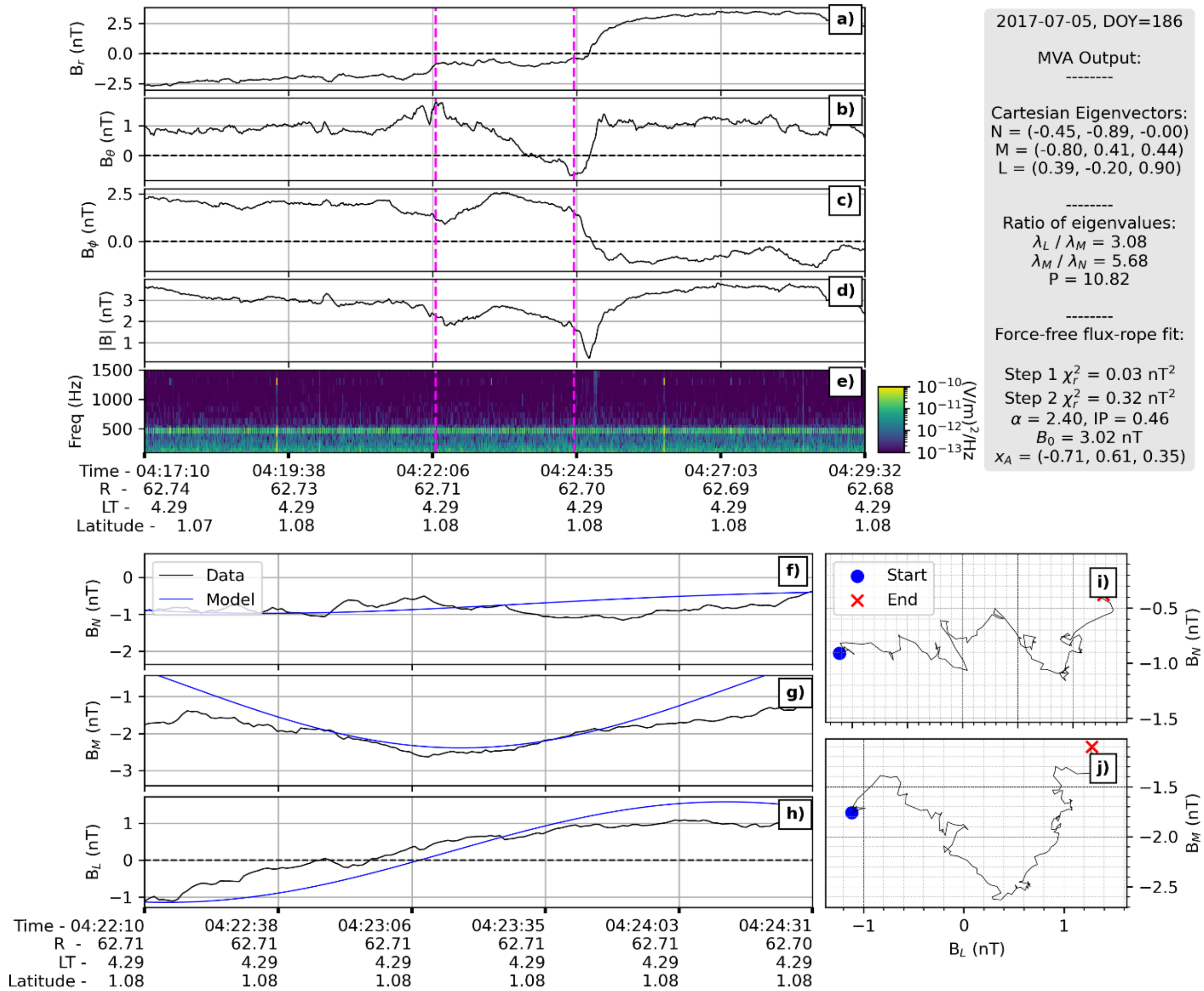
2017-07-05, DOY=186
MVA Output:
Cartesian Eigenvectors:
N = (-0.45, -0.89, -0.00)
M = (-0.80, 0.41, 0.44)
L = (0.39, -0.20, 0.90)
Ratio of eigenvalues:
λ_L / λ_M = 3.08
λ_M / λ_N = 5.68
P = 10.82
Force-free flux-rope fit:
Step 1 χ_r^2 = 0.03 nT^2
Step 2 χ_r^2 = 0.32 nT^2
α = 2.40, IP = 0.46
B_0 = 3.02 nT
x_A = (-0.71, 0.61, 0.35)
Time - 04:17:10 04:19:38 04:22:06 04:24:35 04:27:03 04:29:32
R - 62.74 62.73 62.71 62.70 62.69 62.68
LT - 4.29 4.29 4.29 4.29 4.29 4.29
Latitude - 1.07 1.08 1.08 1.08 1.08 1.08
Time - 04:22:10 04:22:38 04:23:06 04:23:35 04:24:03 04:24:31
R - 62.71 62.71 62.71 62.71 62.71 62.70
LT - 4.29 4.29 4.29 4.29 4.29 4.29
Latitude - 1.08 1.08 1.08 1.08 1.08 1.08
Data
Model
Start
End

Figure S16

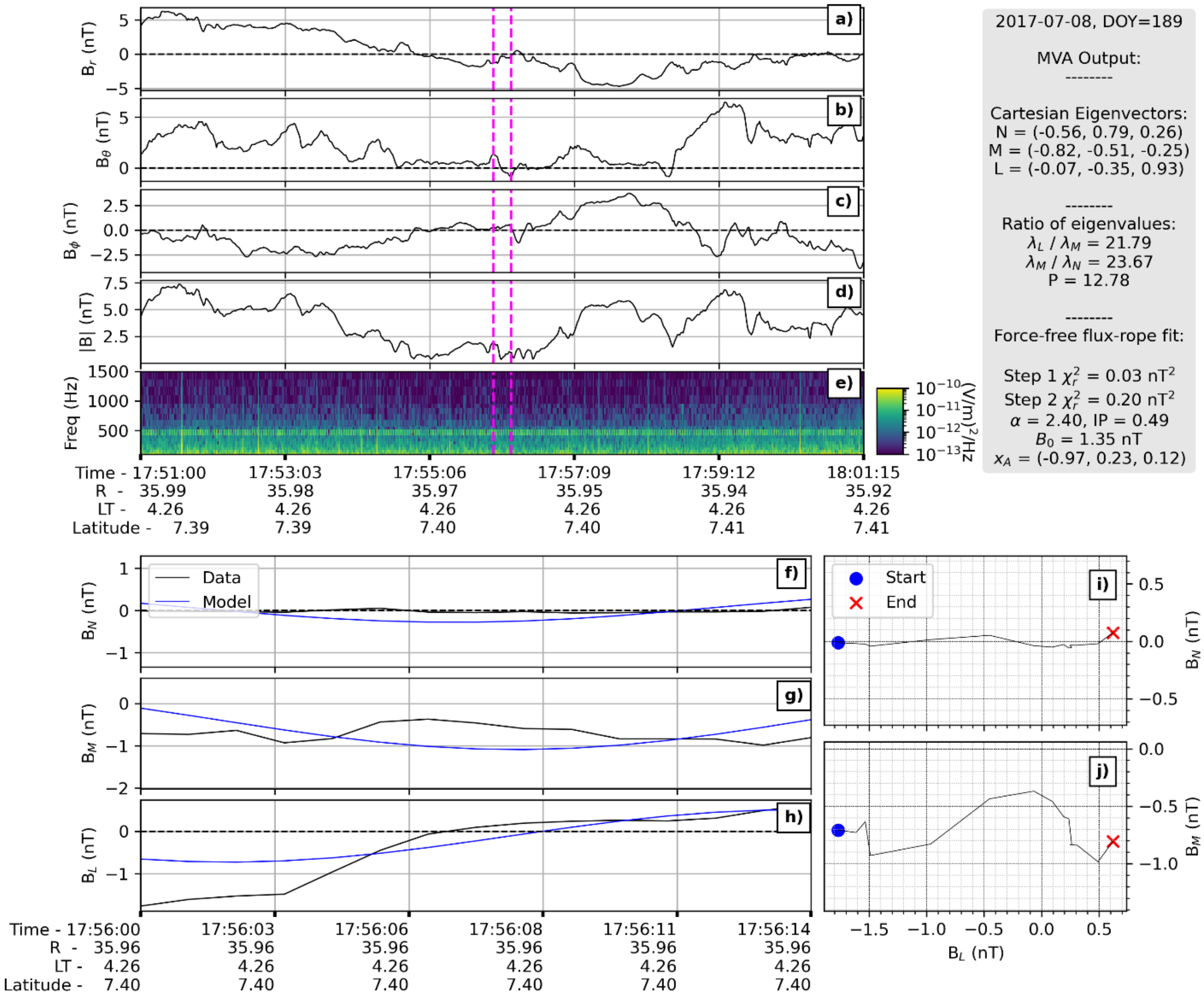

2017-07-08, DOY=189
MVA Output:
Cartesian Eigenvectors:
N = (-0.56, 0.79, 0.26)
M = (-0.82, -0.51, -0.25)
L = (-0.07, -0.35, 0.93)
Ratio of eigenvalues:
λ_L / λ_M = 21.79
λ_M / λ_N = 23.67
P = 12.78
Force-free flux-rope fit:
Step 1 χ_r^2 = 0.03 nT^2
Step 2 χ_r^2 = 0.20 nT^2
α = 2.40, IP = 0.49
B_0 = 1.35 nT
x_A = (-0.97, 0.23, 0.12)

Figure S17

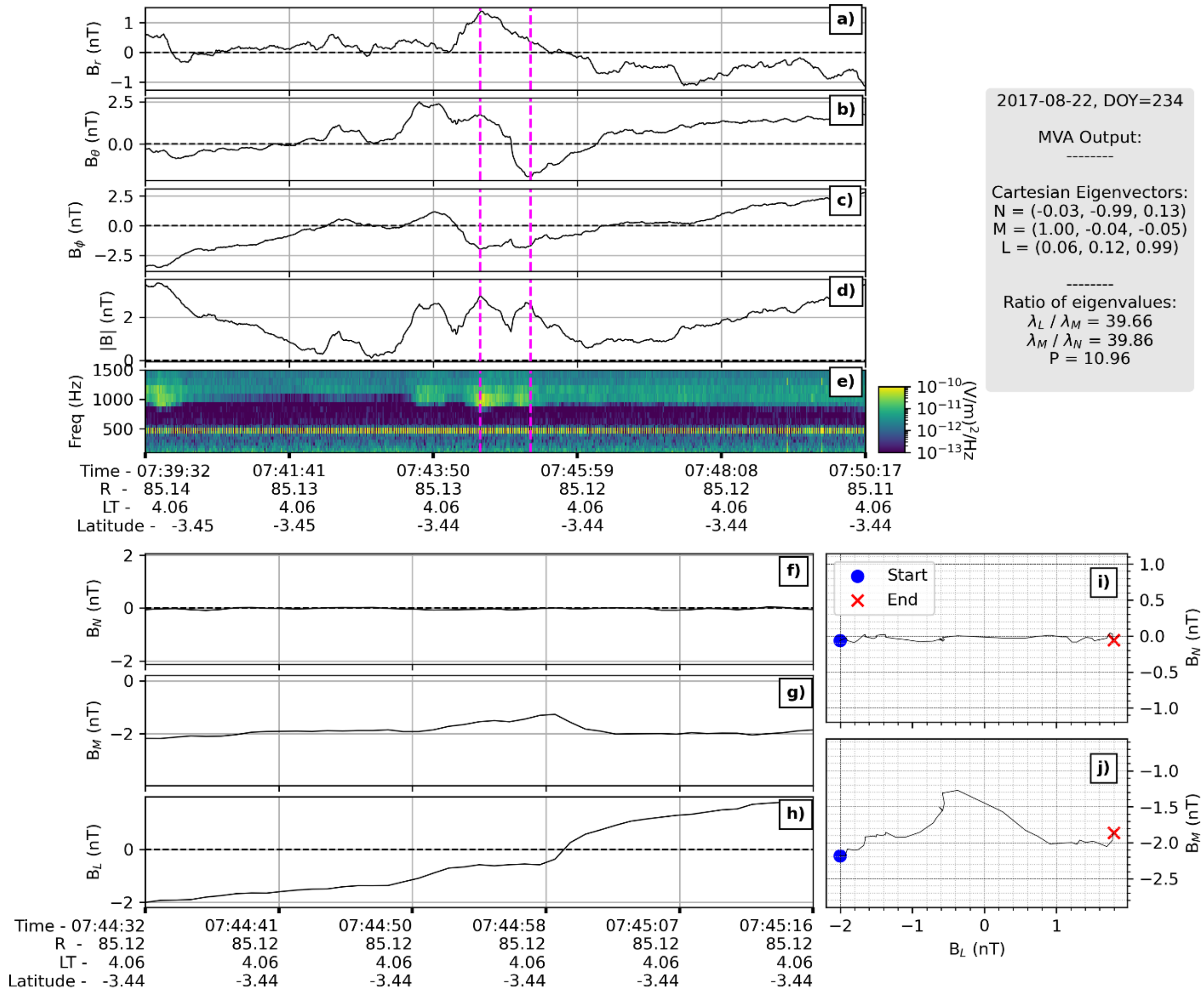
2017-08-22, DOY=234
MVA Output:

Cartesian Eigenvectors:
N = (-0.03, -0.99, 0.13)
M = (1.00, -0.04, -0.05)
L = (0.06, 0.12, 0.99)

Ratio of eigenvalues:
λL / λM = 39.66
λM / λN = 39.86
P = 10.96
a)
b)
c)
d)
e)
f)
g)
h)
i)
j)
Start
End
Time - 07:39:32
R - 85.14
LT - 4.06
Latitude - -3.45
Time - 07:44:32
R - 85.12
LT - 4.06
Latitude - -3.44

Figure S18

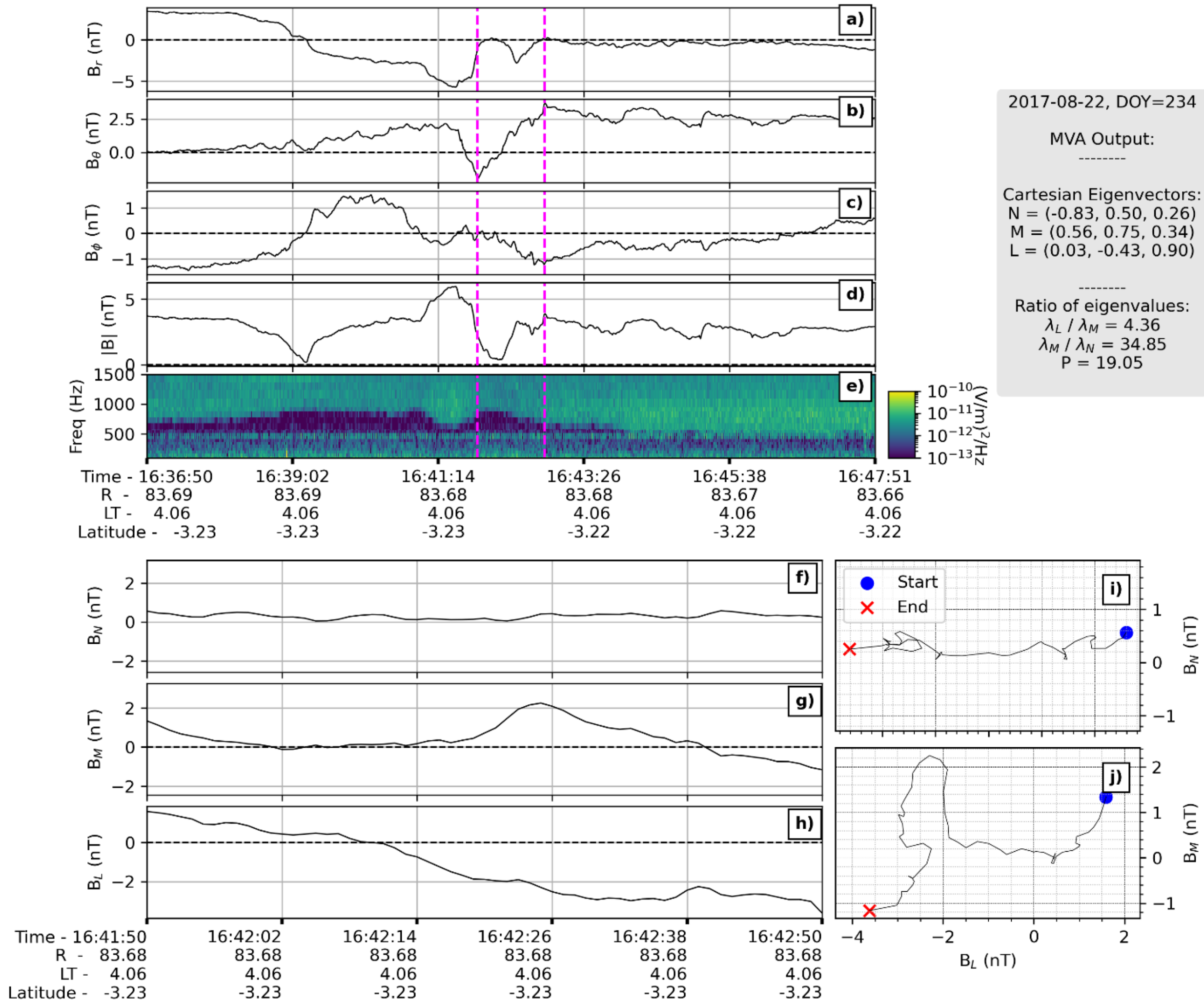

2017-08-22, DOY=234
MVA Output:
Cartesian Eigenvectors:
N = (-0.83, 0.50, 0.26)
M = (0.56, 0.75, 0.34)
L = (0.03, -0.43, 0.90)
Ratio of eigenvalues:
λL / λM = 4.36
λM / λN = 34.85
P = 19.05
a)
b)
c)
d)
e)
f)
g)
h)
i)
j)
Start
End
Time - 16:36:50
R - 83.69
LT - 4.06
Latitude - -3.23
Time - 16:41:50

Figure S19

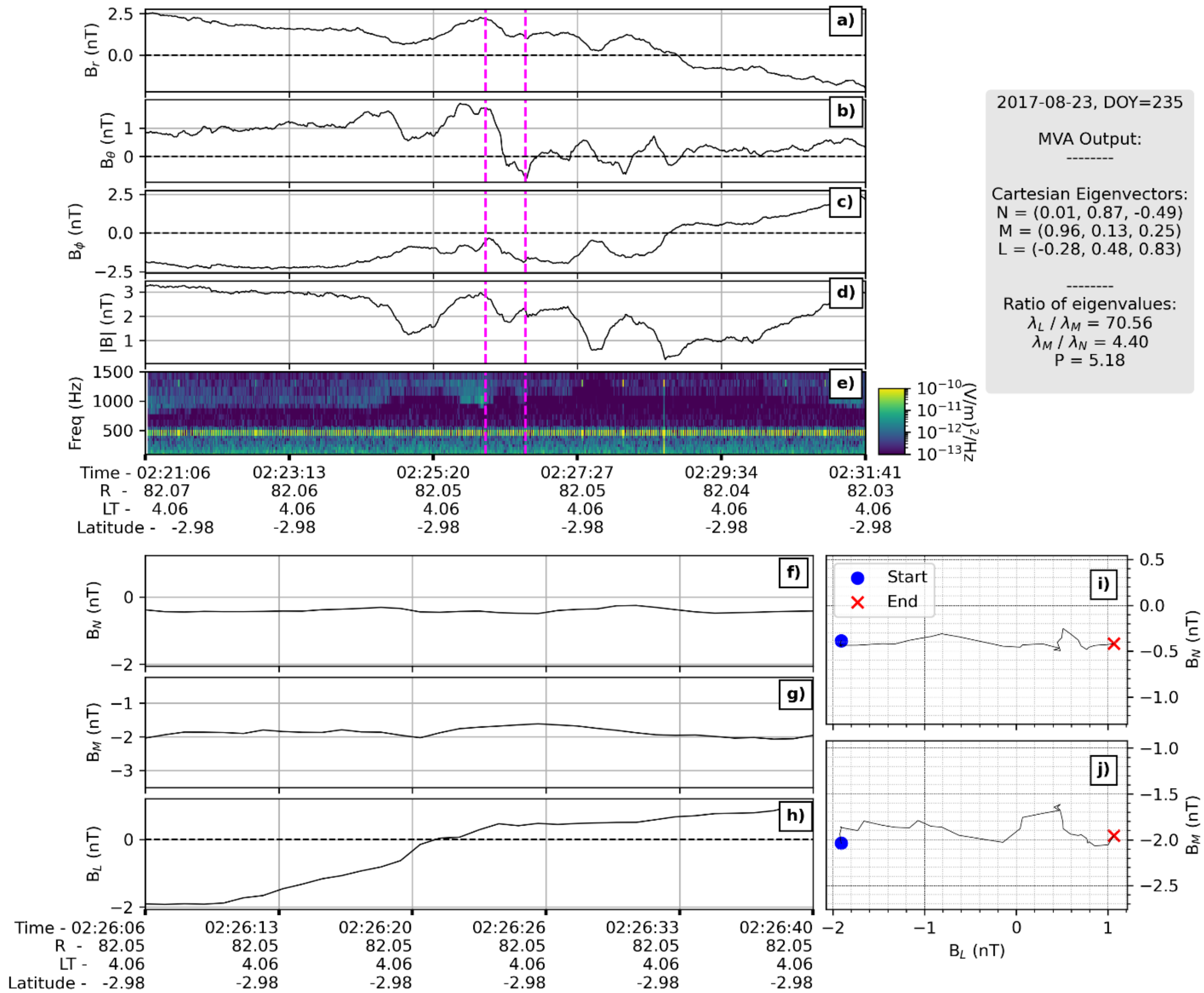

2017-08-23, DOY=235
MVA Output:

Cartesian Eigenvectors:
N = (0.01, 0.87, -0.49)
M = (0.96, 0.13, 0.25)
L = (-0.28, 0.48, 0.83)

Ratio of eigenvalues:
λ_L / λ_M = 70.56
λ_M / λ_N = 4.40
P = 5.18
Time - 02:21:06 02:23:13 02:25:20 02:27:27 02:29:34 02:31:41
R - 82.07 82.06 82.05 82.05 82.04 82.03
LT - 4.06 4.06 4.06 4.06 4.06 4.06
Latitude - -2.98 -2.98 -2.98 -2.98 -2.98 -2.98
Time - 02:26:06 02:26:13 02:26:20 02:26:26 02:26:33 02:26:40
R - 82.05 82.05 82.05 82.05 82.05 82.05
LT - 4.06 4.06 4.06 4.06 4.06 4.06
Latitude - -2.98 -2.98 -2.98 -2.98 -2.98 -2.98
Start
End
B_r (nT)
B_θ (nT)
B_ϕ (nT)
|B| (nT)
Freq (Hz)
$(V/m)^2$/Hz
B_N (nT)
B_M (nT)
B_L (nT)

Figure S20

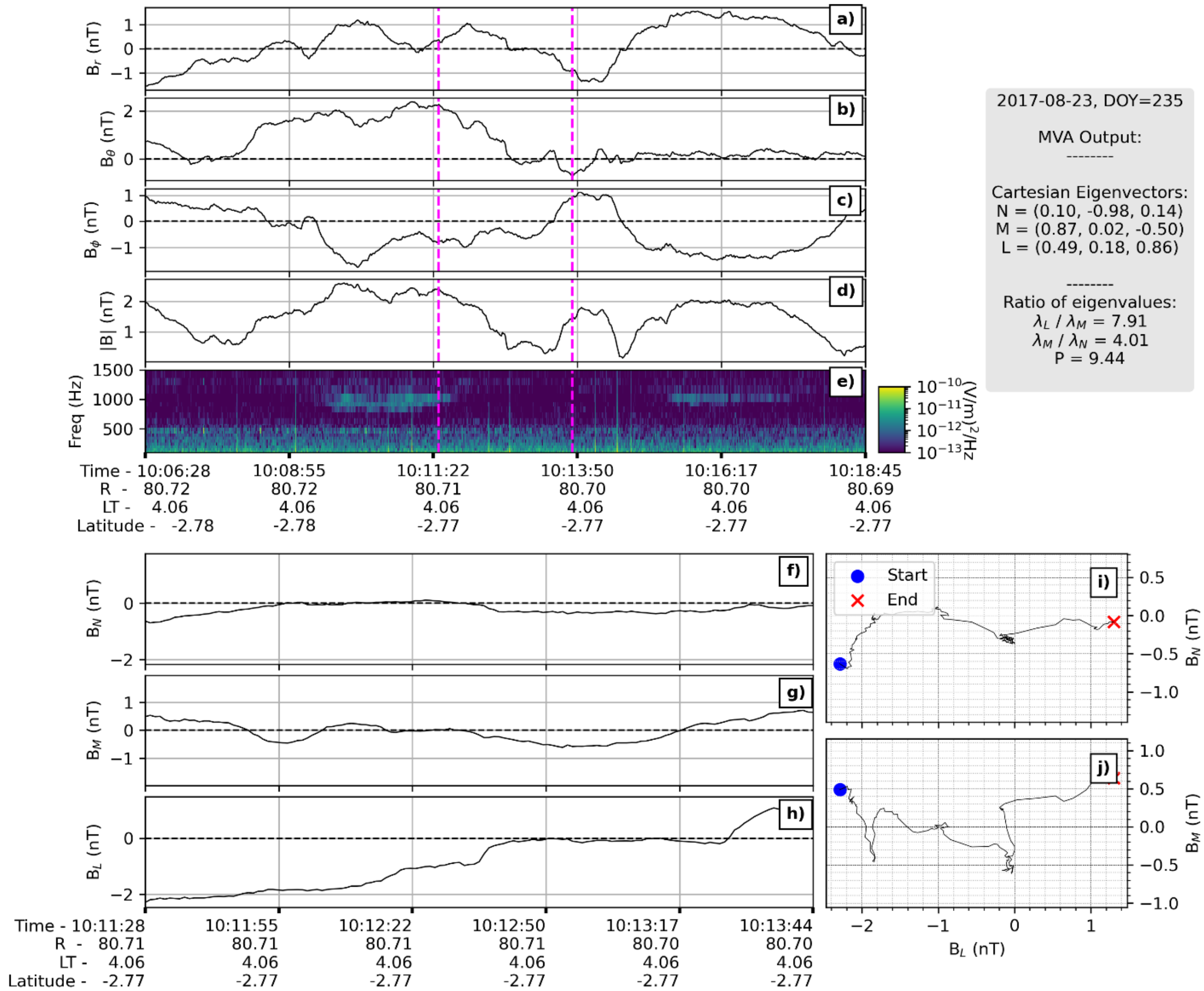
a)
b)
c)
d)
e)
B_r (nT)
B_θ (nT)
B_ϕ (nT)
|B| (nT)
Freq (Hz)
10^{-10}
10^{-11}
10^{-12}
10^{-13}
(V/m)^2/Hz
Time - 10:06:28 10:08:55 10:11:22 10:13:50 10:16:17 10:18:45
R - 80.72 80.72 80.71 80.70 80.70 80.69
LT - 4.06 4.06 4.06 4.06 4.06 4.06
Latitude - -2.78 -2.78 -2.77 -2.77 -2.77 -2.77
2017-08-23, DOY=235
MVA Output:

Cartesian Eigenvectors:
N = (0.10, -0.98, 0.14)
M = (0.87, 0.02, -0.50)
L = (0.49, 0.18, 0.86)

Ratio of eigenvalues:
λ_L / λ_M = 7.91
λ_M / λ_N = 4.01
P = 9.44
f)
g)
h)
i)
j)
B_N (nT)
B_M (nT)
B_L (nT)
Start
End
Time - 10:11:28 10:11:55 10:12:22 10:12:50 10:13:17 10:13:44
R - 80.71 80.71 80.71 80.71 80.70 80.70
LT - 4.06 4.06 4.06 4.06 4.06 4.06
Latitude - -2.77 -2.77 -2.77 -2.77 -2.77 -2.77

Figure S21

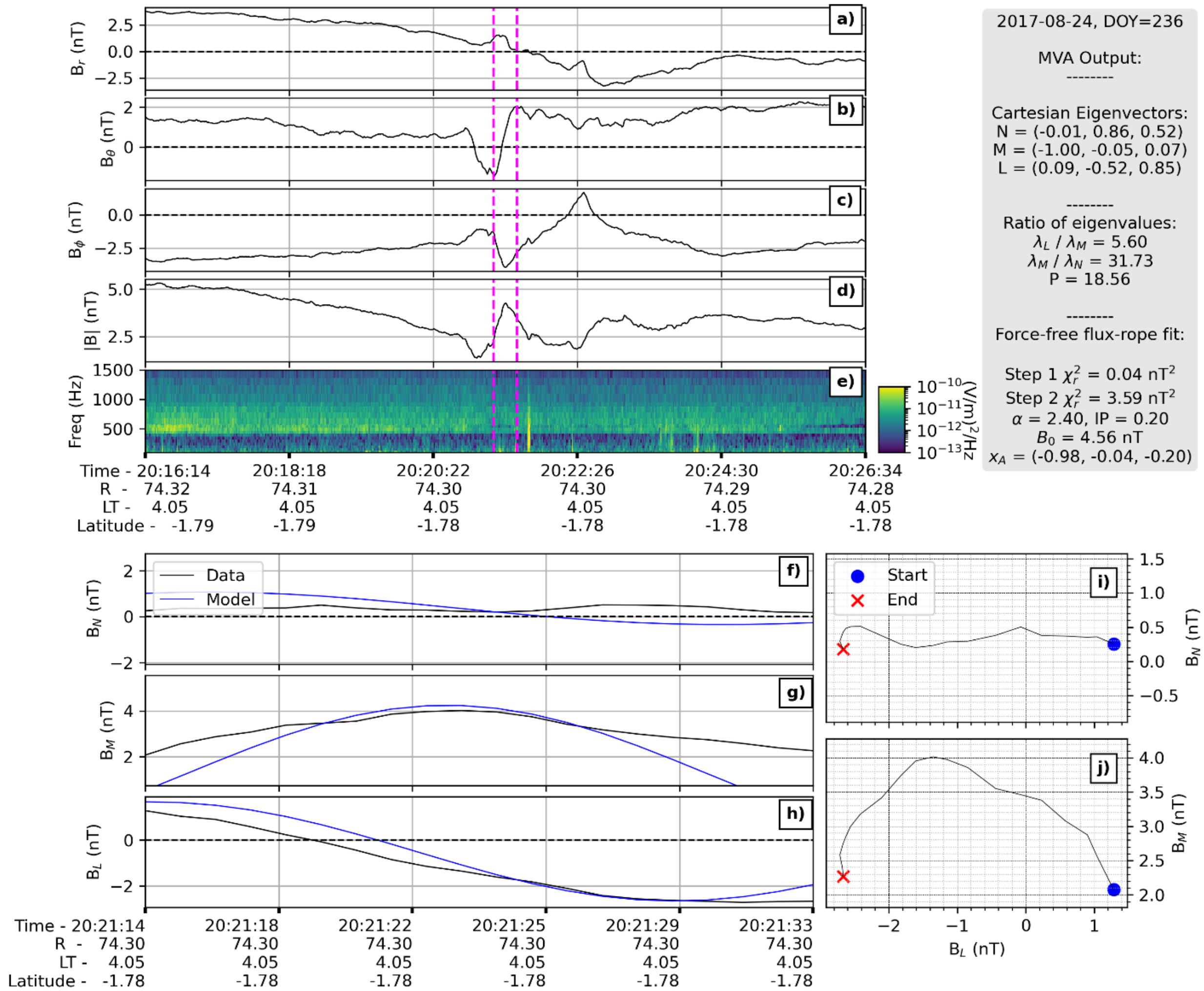
2017-08-24, DOY=236
MVA Output:
Cartesian Eigenvectors:
N = (-0.01, 0.86, 0.52)
M = (-1.00, -0.05, 0.07)
L = (0.09, -0.52, 0.85)
Ratio of eigenvalues:
λ_L / λ_M = 5.60
λ_M / λ_N = 31.73
P = 18.56
Force-free flux-rope fit:
Step 1 χ_r^2 = 0.04 nT^2
Step 2 χ_r^2 = 3.59 nT^2
α = 2.40, IP = 0.20
B_0 = 4.56 nT
x_A = (-0.98, -0.04, -0.20)
Data
Model
Start
End

Figure S22

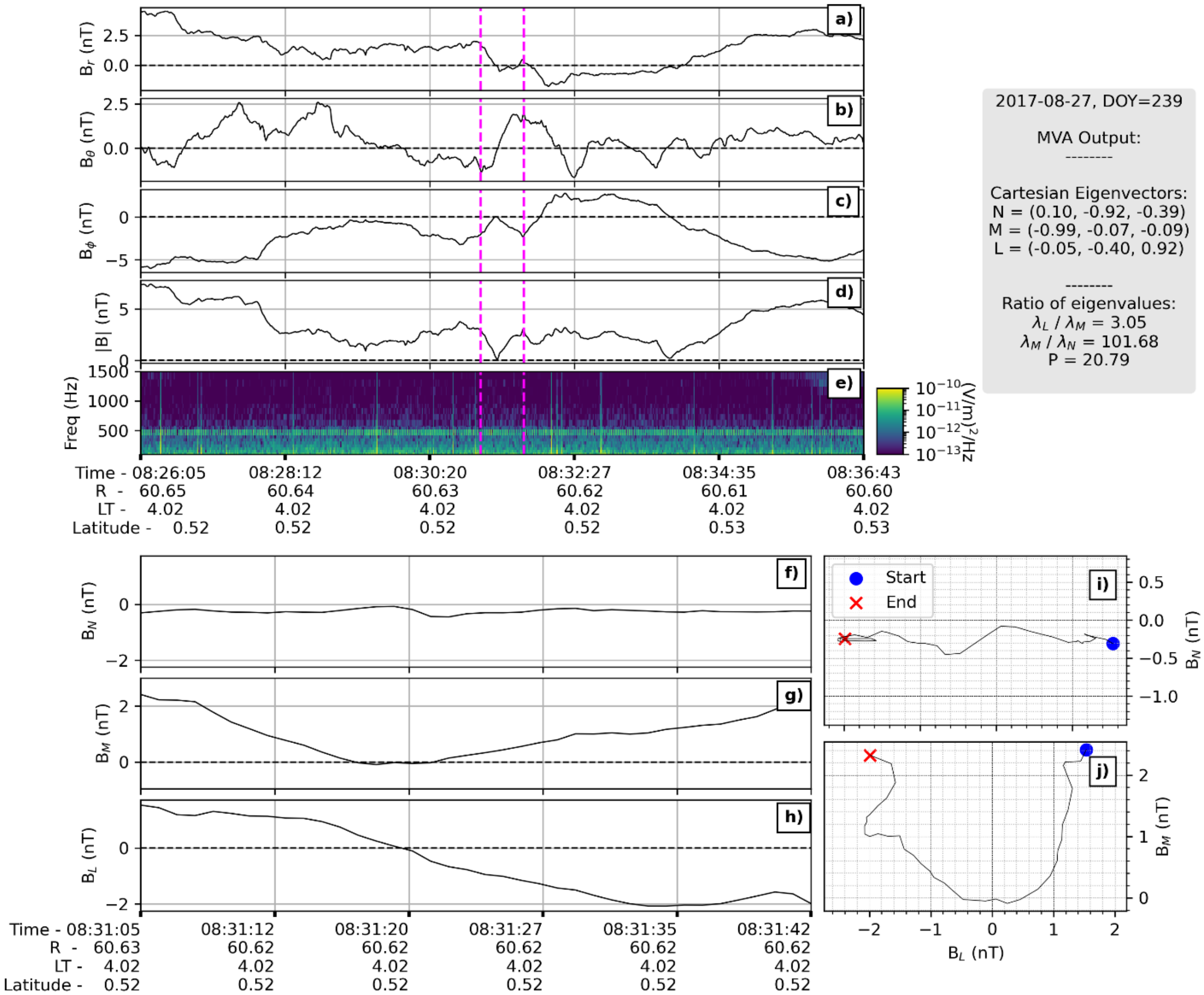

2017-08-27, DOY=239
MVA Output:

Cartesian Eigenvectors:
N = (0.10, -0.92, -0.39)
M = (-0.99, -0.07, -0.09)
L = (-0.05, -0.40, 0.92)

Ratio of eigenvalues:
λ_L / λ_M = 3.05
λ_M / λ_N = 101.68
P = 20.79
a)
b)
c)
d)
e)
f)
g)
h)
i)
j)
B_r (nT)
B_θ (nT)
B_ϕ (nT)
|B| (nT)
Freq (Hz)
$(V/m)^2/Hz$
B_N (nT)
B_M (nT)
B_L (nT)
Start
End
Time - 08:26:05 08:28:12 08:30:20 08:32:27 08:34:35 08:36:43
R - 60.65 60.64 60.63 60.62 60.61 60.60
LT - 4.02 4.02 4.02 4.02 4.02 4.02
Latitude - 0.52 0.52 0.52 0.52 0.53 0.53
Time - 08:31:05 08:31:12 08:31:20 08:31:27 08:31:35 08:31:42
R - 60.63 60.62 60.62 60.62 60.62 60.62
LT - 4.02 4.02 4.02 4.02 4.02 4.02
Latitude - 0.52 0.52 0.52 0.52 0.52 0.52

Figure S23

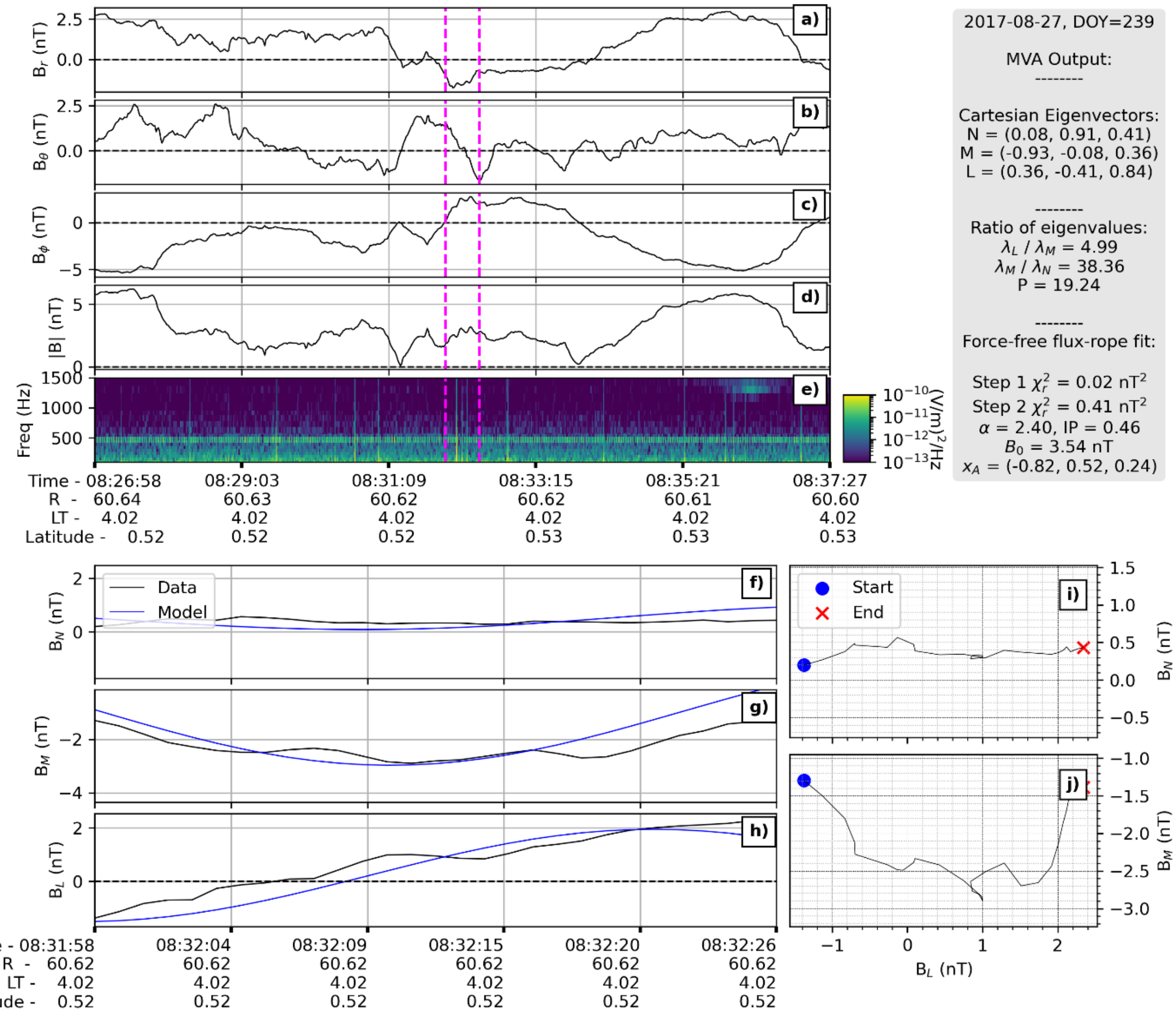
2017-08-27, DOY=239
MVA Output:
Cartesian Eigenvectors:
N = (0.08, 0.91, 0.41)
M = (-0.93, -0.08, 0.36)
L = (0.36, -0.41, 0.84)
Ratio of eigenvalues:
$\lambda_L / \lambda_M = 4.99$
$\lambda_M / \lambda_N = 38.36$
P = 19.24
Force-free flux-rope fit:
Step 1 $\chi_r^2 = 0.02$ nT^2
Step 2 $\chi_r^2 = 0.41$ nT^2
$\alpha = 2.40$, IP = 0.46
$B_0 = 3.54$ nT
$x_A = (-0.82, 0.52, 0.24)$
Time - 08:26:58 08:29:03 08:31:09 08:33:15 08:35:21 08:37:27
R - 60.64 60.63 60.62 60.62 60.61 60.60
LT - 4.02 4.02 4.02 4.02 4.02 4.02
Latitude - 0.52 0.52 0.52 0.53 0.53 0.53
Data
Model
Start
End
Time - 08:31:58 08:32:04 08:32:09 08:32:15 08:32:20 08:32:26
R - 60.62 60.62 60.62 60.62 60.62 60.62
LT - 4.02 4.02 4.02 4.02 4.02 4.02
Latitude - 0.52 0.52 0.52 0.52 0.52 0.52

Figure S24

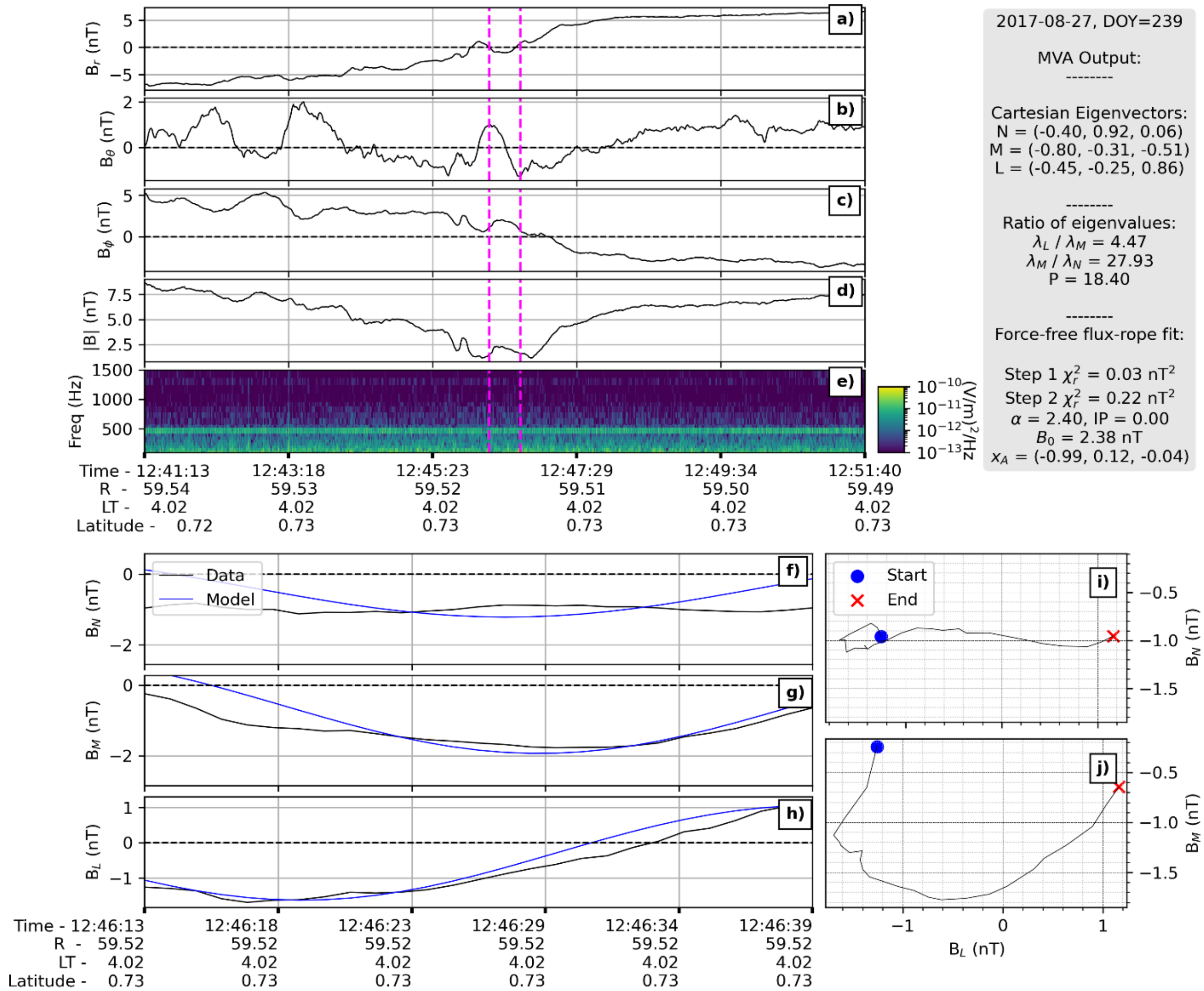
2017-08-27, DOY=239
MVA Output:
Cartesian Eigenvectors:
N = (-0.40, 0.92, 0.06)
M = (-0.80, -0.31, -0.51)
L = (-0.45, -0.25, 0.86)
Ratio of eigenvalues:
λ_L / λ_M = 4.47
λ_M / λ_N = 27.93
P = 18.40
Force-free flux-rope fit:
Step 1 χ_r^2 = 0.03 nT^2
Step 2 χ_r^2 = 0.22 nT^2
α = 2.40, IP = 0.00
B_0 = 2.38 nT
x_A = (-0.99, 0.12, -0.04)
Time - 12:41:13 12:43:18 12:45:23 12:47:29 12:49:34 12:51:40
R - 59.54 59.53 59.52 59.51 59.50 59.49
LT - 4.02 4.02 4.02 4.02 4.02 4.02
Latitude - 0.72 0.73 0.73 0.73 0.73 0.73
Time - 12:46:13 12:46:18 12:46:23 12:46:29 12:46:34 12:46:39
R - 59.52 59.52 59.52 59.52 59.52 59.52
LT - 4.02 4.02 4.02 4.02 4.02 4.02
Latitude - 0.73 0.73 0.73 0.73 0.73 0.73
Data
Model
Start
End
B_r (nT)
B_θ (nT)
B_ϕ (nT)
|B| (nT)
Freq (Hz)
(V/m)^2/Hz
B_N (nT)
B_M (nT)
B_L (nT)

Figure S25

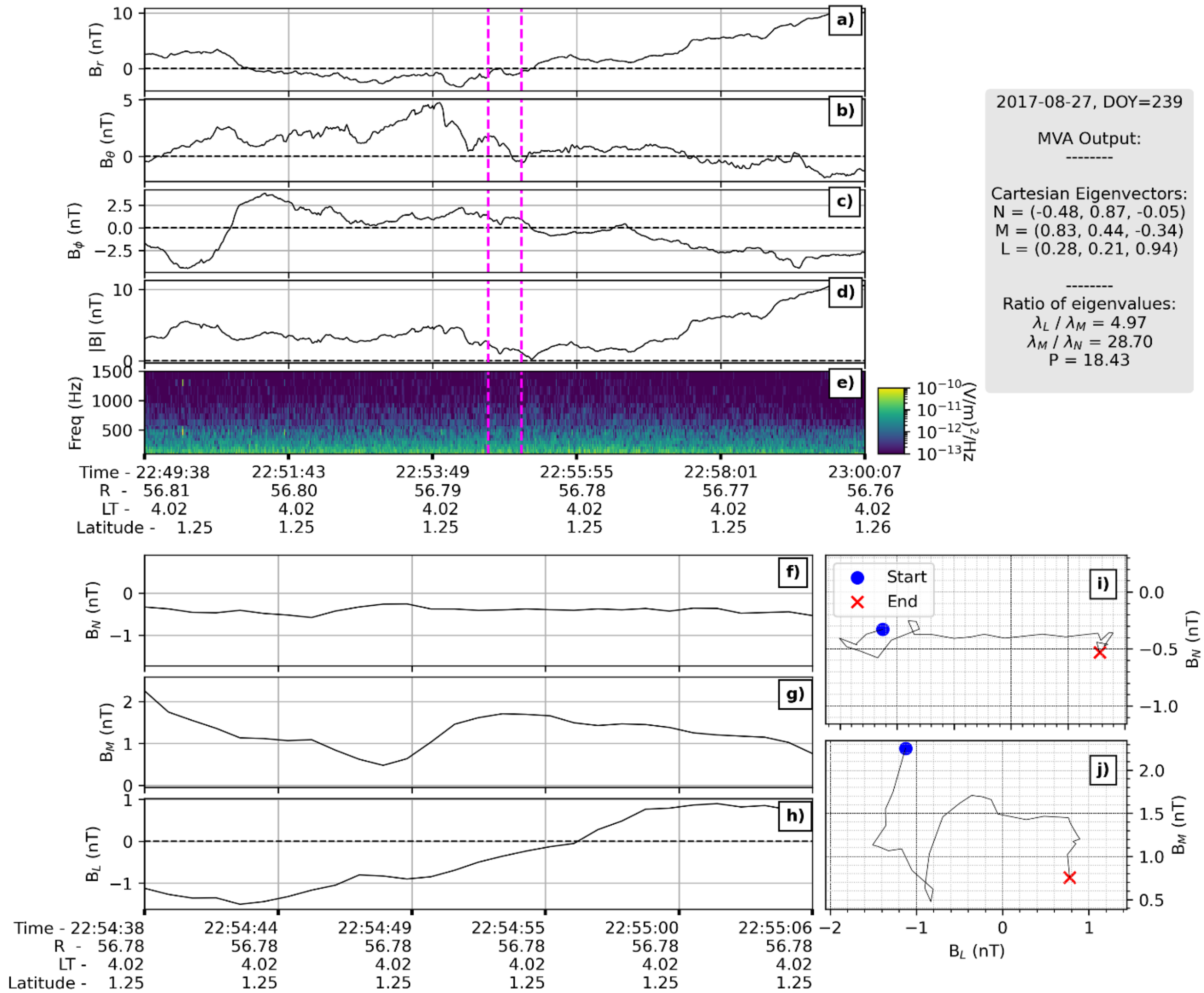
2017-08-27, DOY=239
MVA Output:

Cartesian Eigenvectors:
N = (-0.48, 0.87, -0.05)
M = (0.83, 0.44, -0.34)
L = (0.28, 0.21, 0.94)

Ratio of eigenvalues:
λ_L / λ_M = 4.97
λ_M / λ_N = 28.70
P = 18.43
Time - 22:49:38 22:51:43 22:53:49 22:55:55 22:58:01 23:00:07
R - 56.81 56.80 56.79 56.78 56.77 56.76
LT - 4.02 4.02 4.02 4.02 4.02 4.02
Latitude - 1.25 1.25 1.25 1.25 1.25 1.26
Time - 22:54:38 22:54:44 22:54:49 22:54:55 22:55:00 22:55:06
R - 56.78 56.78 56.78 56.78 56.78 56.78
LT - 4.02 4.02 4.02 4.02 4.02 4.02
Latitude - 1.25 1.25 1.25 1.25 1.25 1.25
Start
End

Figure S26

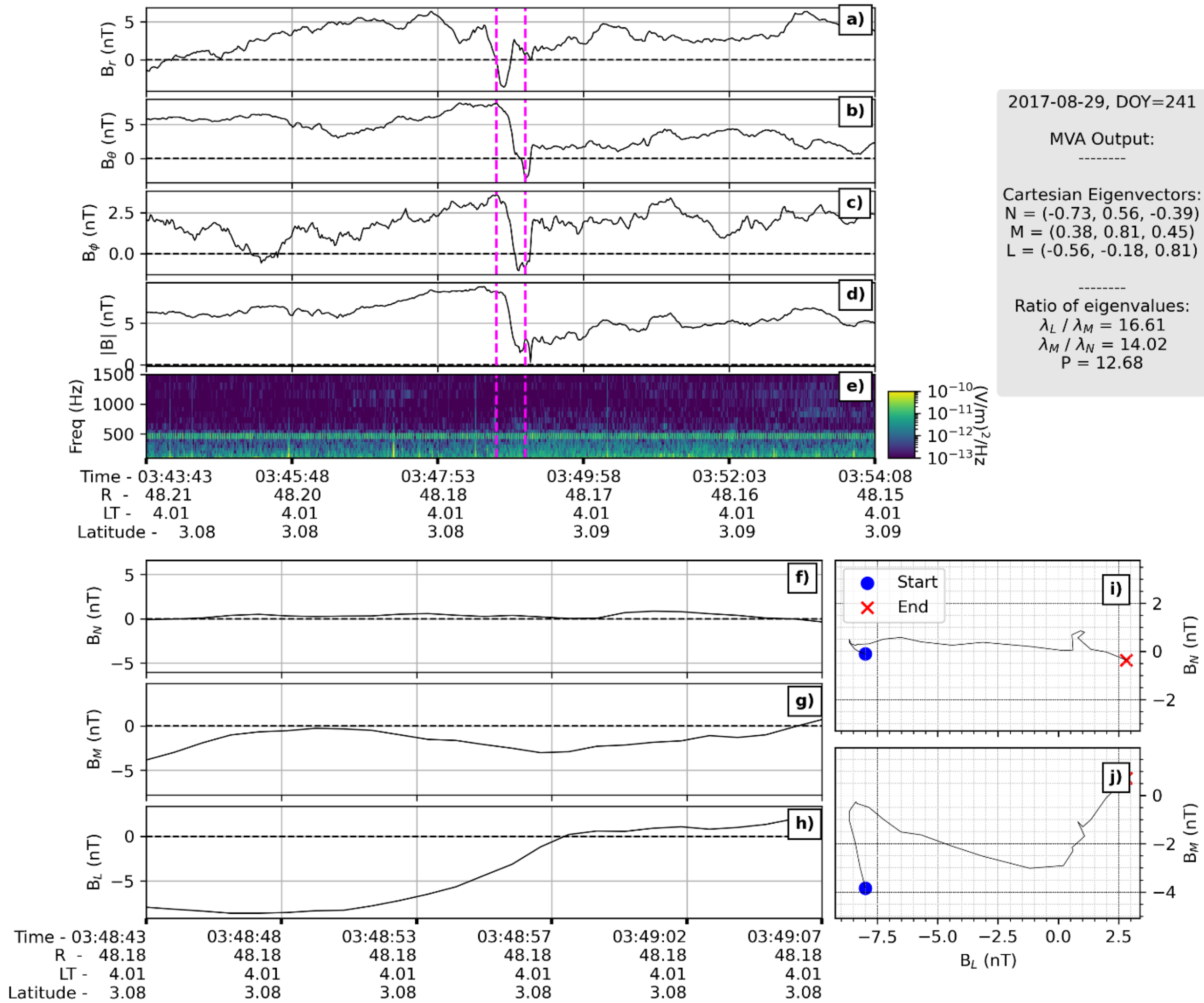

2017-08-29, DOY=241
MVA Output:
Cartesian Eigenvectors:
N = (-0.73, 0.56, -0.39)
M = (0.38, 0.81, 0.45)
L = (-0.56, -0.18, 0.81)
Ratio of eigenvalues:
λL / λM = 16.61
λM / λN = 14.02
P = 12.68
Time - 03:43:43 03:45:48 03:47:53 03:49:58 03:52:03 03:54:08
R - 48.21 48.20 48.18 48.17 48.16 48.15
LT - 4.01 4.01 4.01 4.01 4.01 4.01
Latitude - 3.08 3.08 3.08 3.09 3.09 3.09
Time - 03:48:43 03:48:48 03:48:53 03:48:57 03:49:02 03:49:07
R - 48.18 48.18 48.18 48.18 48.18 48.18
LT - 4.01 4.01 4.01 4.01 4.01 4.01
Latitude - 3.08 3.08 3.08 3.08 3.08 3.08
Start
End

Figure S27

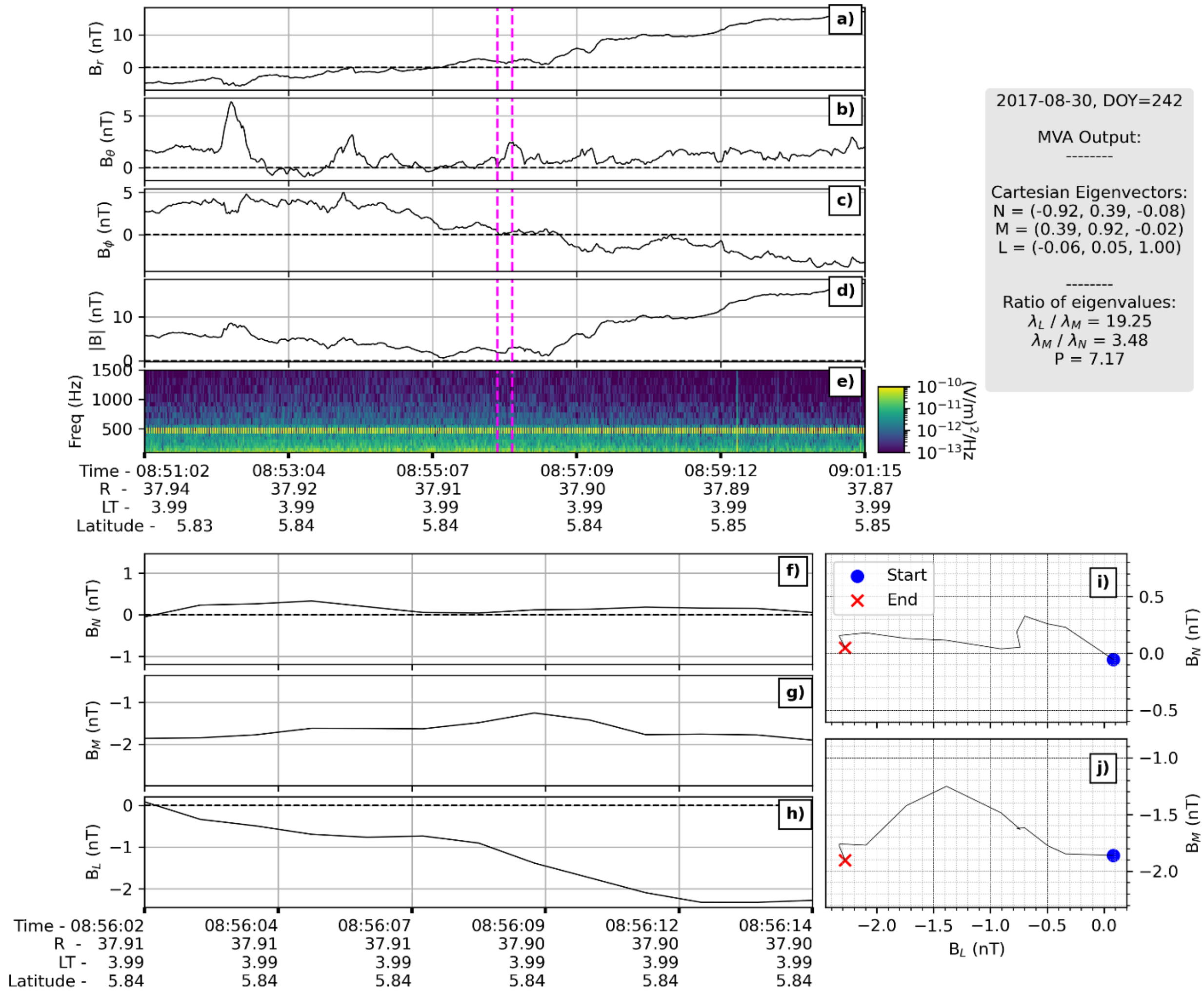
a)
b)
c)
d)
e)
f)
g)
h)
i)
j)
2017-08-30, DOY=242
MVA Output:
Cartesian Eigenvectors:
N = (-0.92, 0.39, -0.08)
M = (0.39, 0.92, -0.02)
L = (-0.06, 0.05, 1.00)
Ratio of eigenvalues:
λL / λM = 19.25
λM / λN = 3.48
P = 7.17
Start
End
Time - 08:51:02 08:53:04 08:55:07 08:57:09 08:59:12 09:01:15
R - 37.94 37.92 37.91 37.90 37.89 37.87
LT - 3.99 3.99 3.99 3.99 3.99 3.99
Latitude - 5.83 5.84 5.84 5.84 5.85 5.85
Time - 08:56:02 08:56:04 08:56:07 08:56:09 08:56:12 08:56:14
R - 37.91 37.91 37.91 37.90 37.90 37.90
LT - 3.99 3.99 3.99 3.99 3.99 3.99
Latitude - 5.84 5.84 5.84 5.84 5.84 5.84

Figure S28

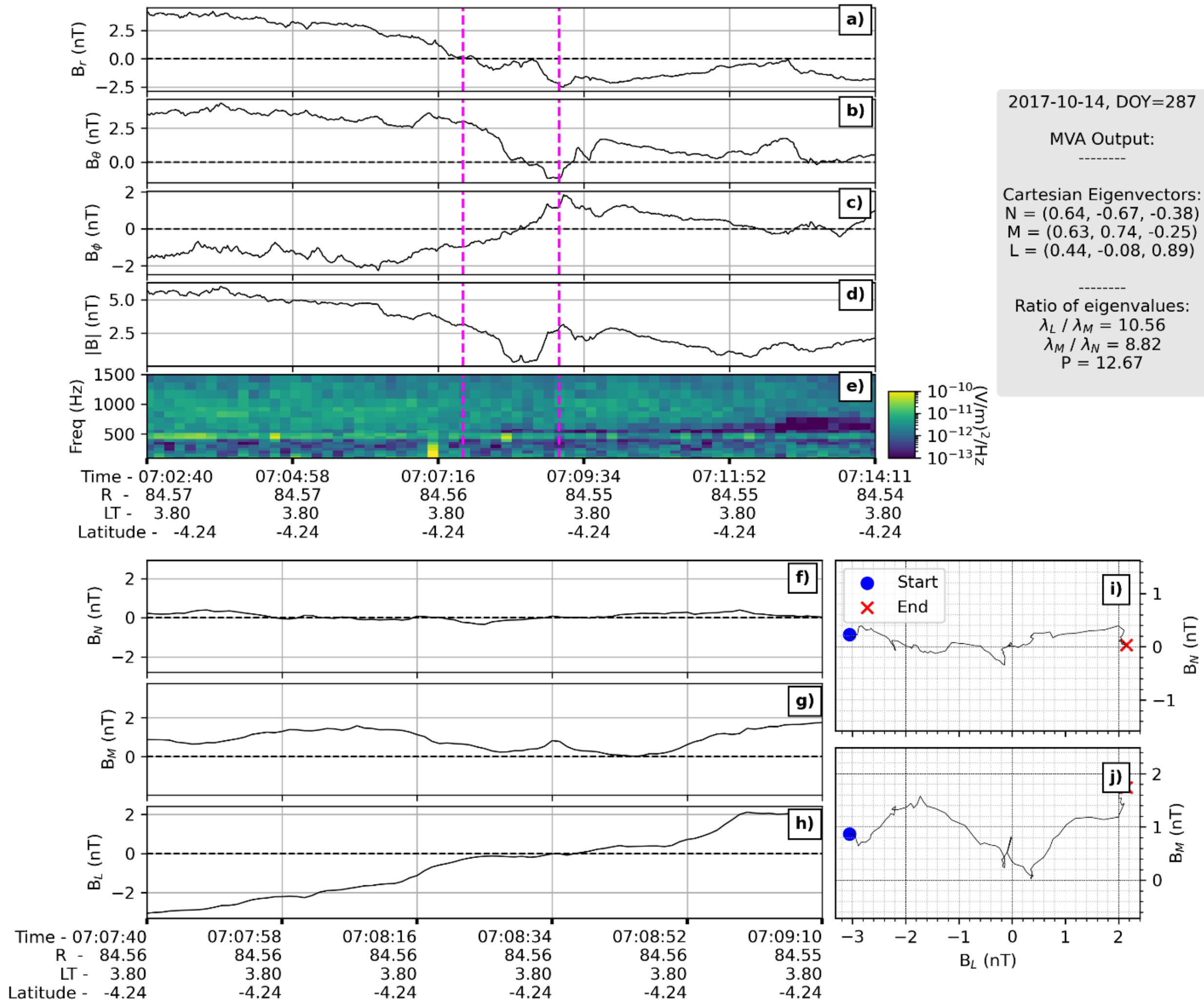

a)
b)
c)
d)
e)
f)
g)
h)
i)
j)
B$_r$ (nT)
B$_\theta$ (nT)
B$_\phi$ (nT)
|B| (nT)
Freq (Hz)
(V/m)^2/Hz
Time - 07:02:40 07:04:58 07:07:16 07:09:34 07:11:52 07:14:11
R - 84.57 84.57 84.56 84.55 84.55 84.54
LT - 3.80 3.80 3.80 3.80 3.80 3.80
Latitude - -4.24 -4.24 -4.24 -4.24 -4.24 -4.24
2017-10-14, DOY=287
MVA Output:
Cartesian Eigenvectors:
N = (0.64, -0.67, -0.38)
M = (0.63, 0.74, -0.25)
L = (0.44, -0.08, 0.89)
Ratio of eigenvalues:
λ_L / λ_M = 10.56
λ_M / λ_N = 8.82
P = 12.67
B$_N$ (nT)
B$_M$ (nT)
B$_L$ (nT)
Time - 07:07:40 07:07:58 07:08:16 07:08:34 07:08:52 07:09:10
R - 84.56 84.56 84.56 84.56 84.56 84.55
LT - 3.80 3.80 3.80 3.80 3.80 3.80
Latitude - -4.24 -4.24 -4.24 -4.24 -4.24 -4.24
Start
End

Figure S29

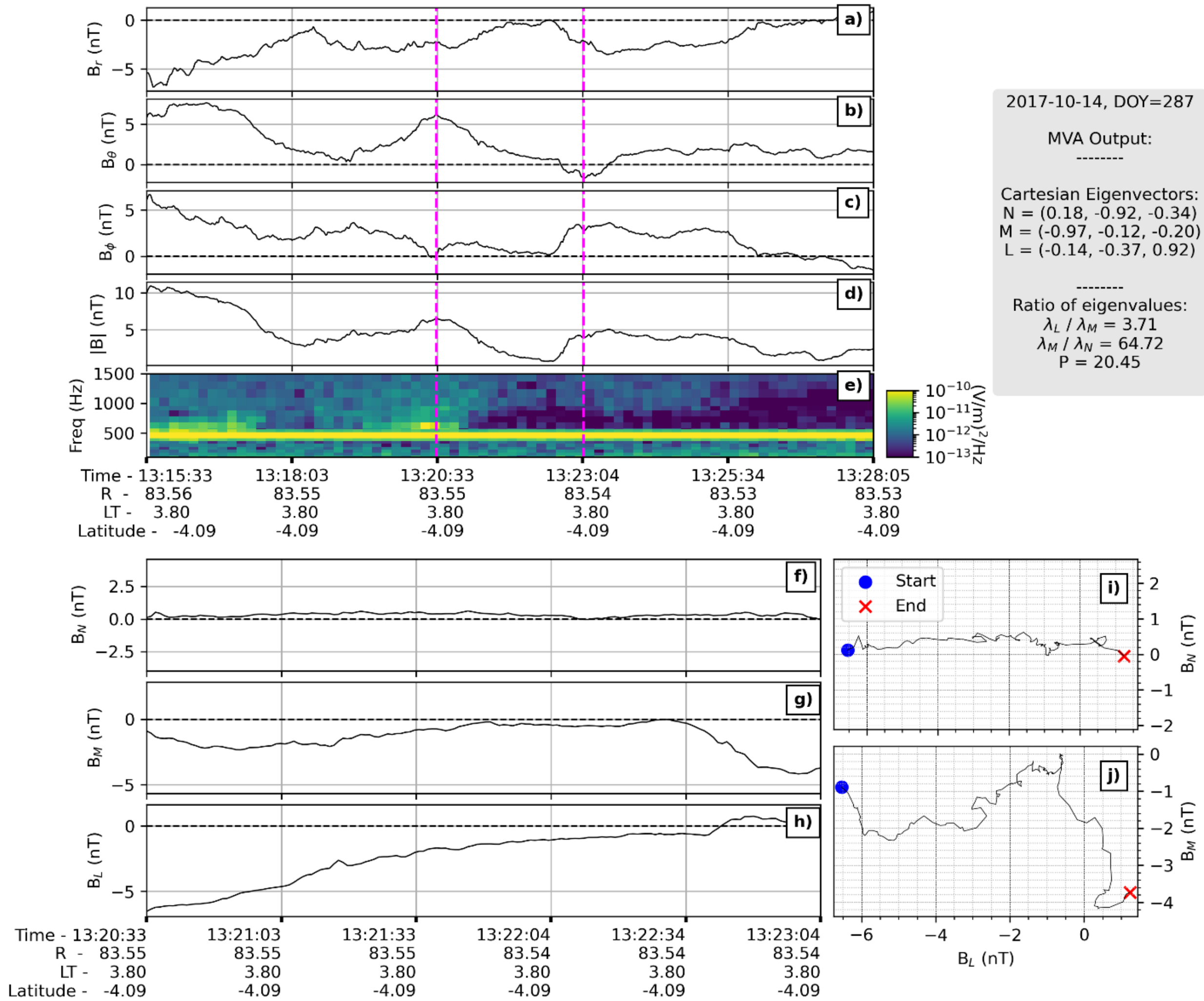
2017-10-14, DOY=287
MVA Output:

Cartesian Eigenvectors:
N = (0.18, -0.92, -0.34)
M = (-0.97, -0.12, -0.20)
L = (-0.14, -0.37, 0.92)

Ratio of eigenvalues:
λL / λM = 3.71
λM / λN = 64.72
P = 20.45
Start
End
Time - 13:15:33 13:18:03 13:20:33 13:23:04 13:25:34 13:28:05
R - 83.56 83.55 83.55 83.54 83.53 83.53
LT - 3.80 3.80 3.80 3.80 3.80 3.80
Latitude - -4.09 -4.09 -4.09 -4.09 -4.09 -4.09
Time - 13:20:33 13:21:03 13:21:33 13:22:04 13:22:34 13:23:04
R - 83.55 83.55 83.55 83.54 83.54 83.54
LT - 3.80 3.80 3.80 3.80 3.80 3.80
Latitude - -4.09 -4.09 -4.09 -4.09 -4.09 -4.09

Figure S30

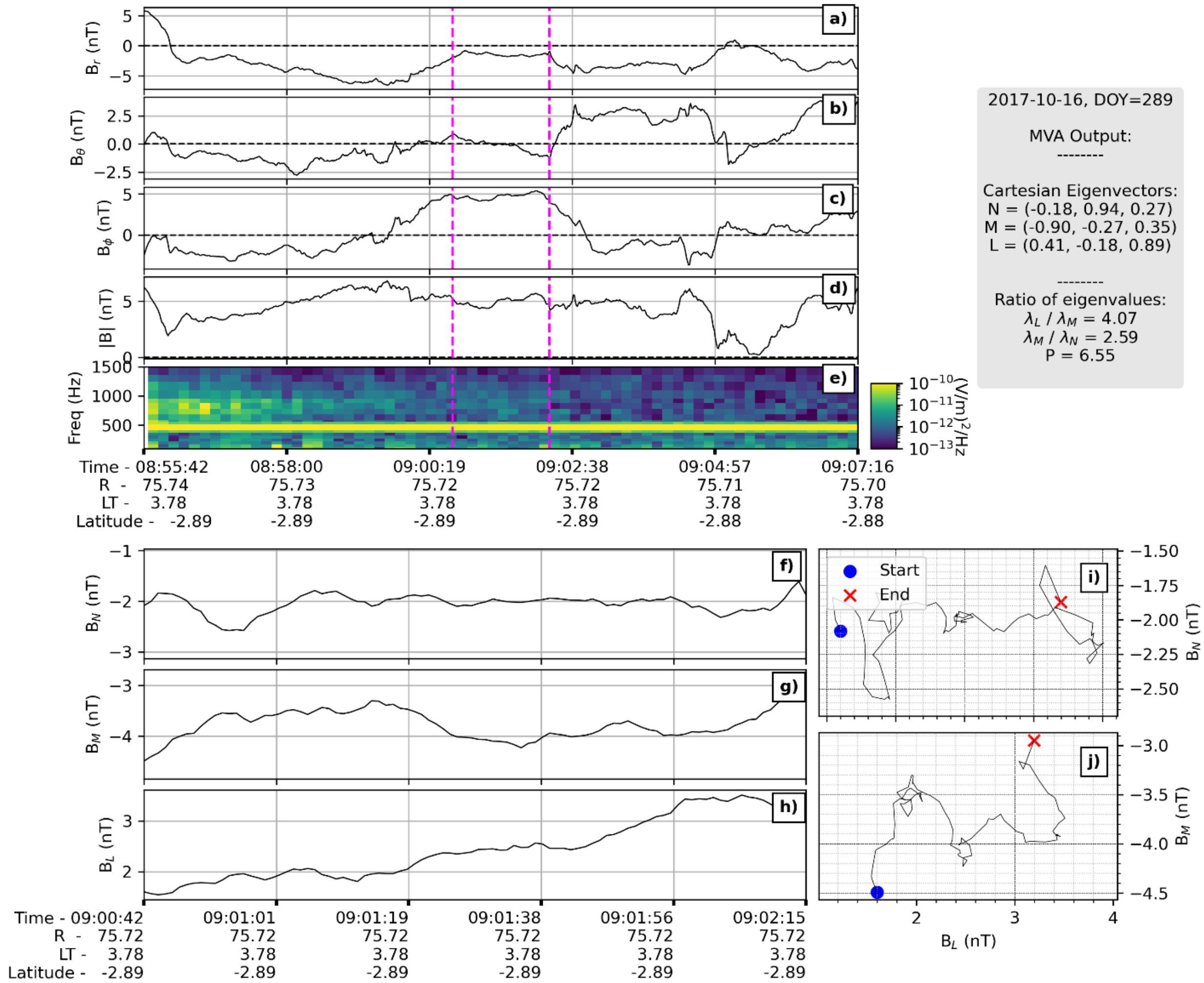

2017-10-16, DOY=289
MVA Output:

Cartesian Eigenvectors:
N = (-0.18, 0.94, 0.27)
M = (-0.90, -0.27, 0.35)
L = (0.41, -0.18, 0.89)

Ratio of eigenvalues:
λ_L / λ_M = 4.07
λ_M / λ_N = 2.59
P = 6.55
Time - 08:55:42 08:58:00 09:00:19 09:02:38 09:04:57 09:07:16
R - 75.74 75.73 75.72 75.72 75.71 75.70
LT - 3.78 3.78 3.78 3.78 3.78 3.78
Latitude - -2.89 -2.89 -2.89 -2.89 -2.88 -2.88
Time - 09:00:42 09:01:01 09:01:19 09:01:38 09:01:56 09:02:15
R - 75.72 75.72 75.72 75.72 75.72 75.72
LT - 3.78 3.78 3.78 3.78 3.78 3.78
Latitude - -2.89 -2.89 -2.89 -2.89 -2.89 -2.89
Start
End

Figure S31

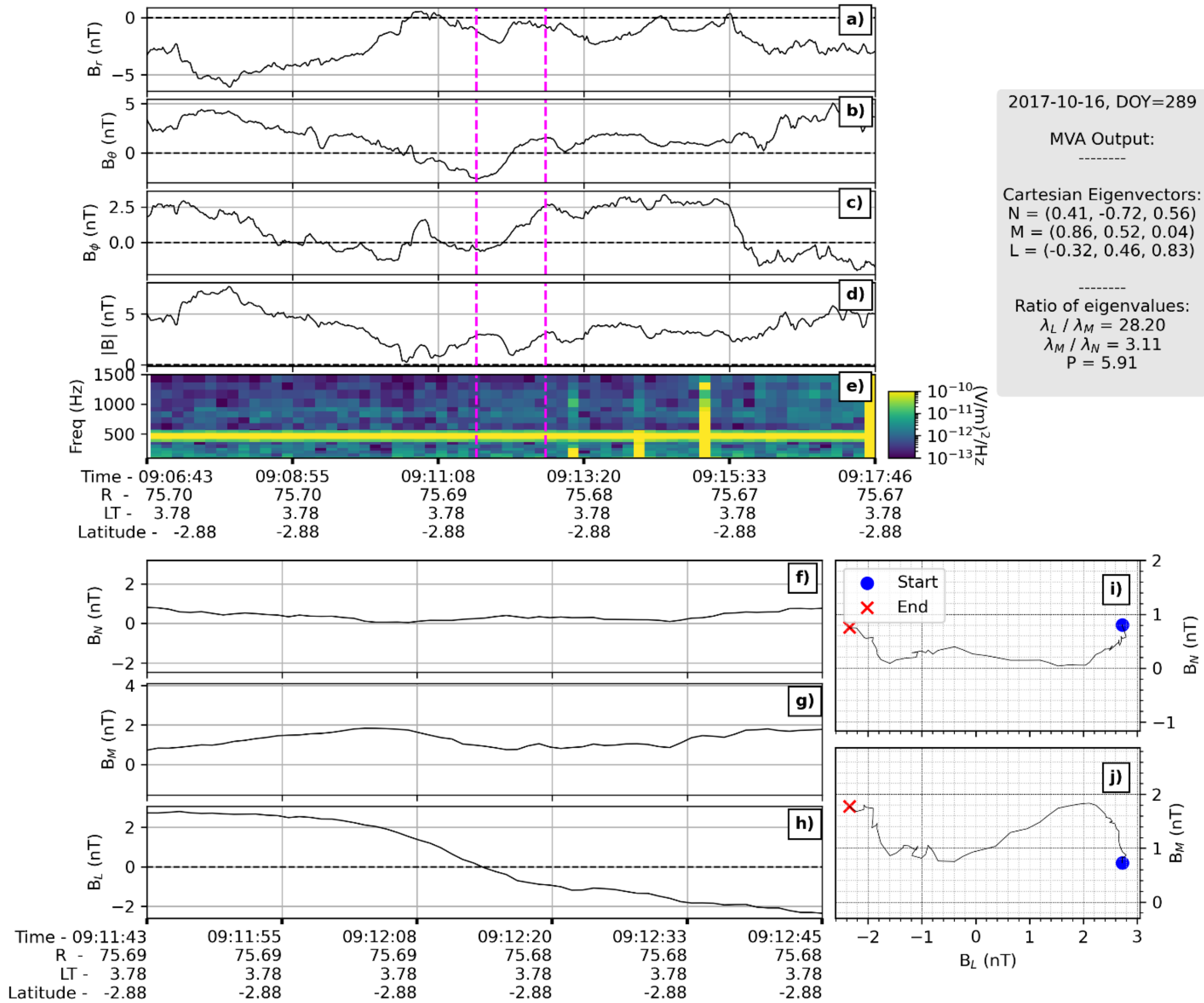
2017-10-16, DOY=289
MVA Output:
Cartesian Eigenvectors:
N = (0.41, -0.72, 0.56)
M = (0.86, 0.52, 0.04)
L = (-0.32, 0.46, 0.83)
Ratio of eigenvalues:
λL / λM = 28.20
λM / λN = 3.11
P = 5.91
Start
End
Time - 09:06:43
R - 75.70
LT - 3.78
Latitude - -2.88
Time - 09:11:43
Freq (Hz)
Br (nT)
Bθ (nT)
Bϕ (nT)
|B| (nT)
BN (nT)
BM (nT)
BL (nT)

Figure S32

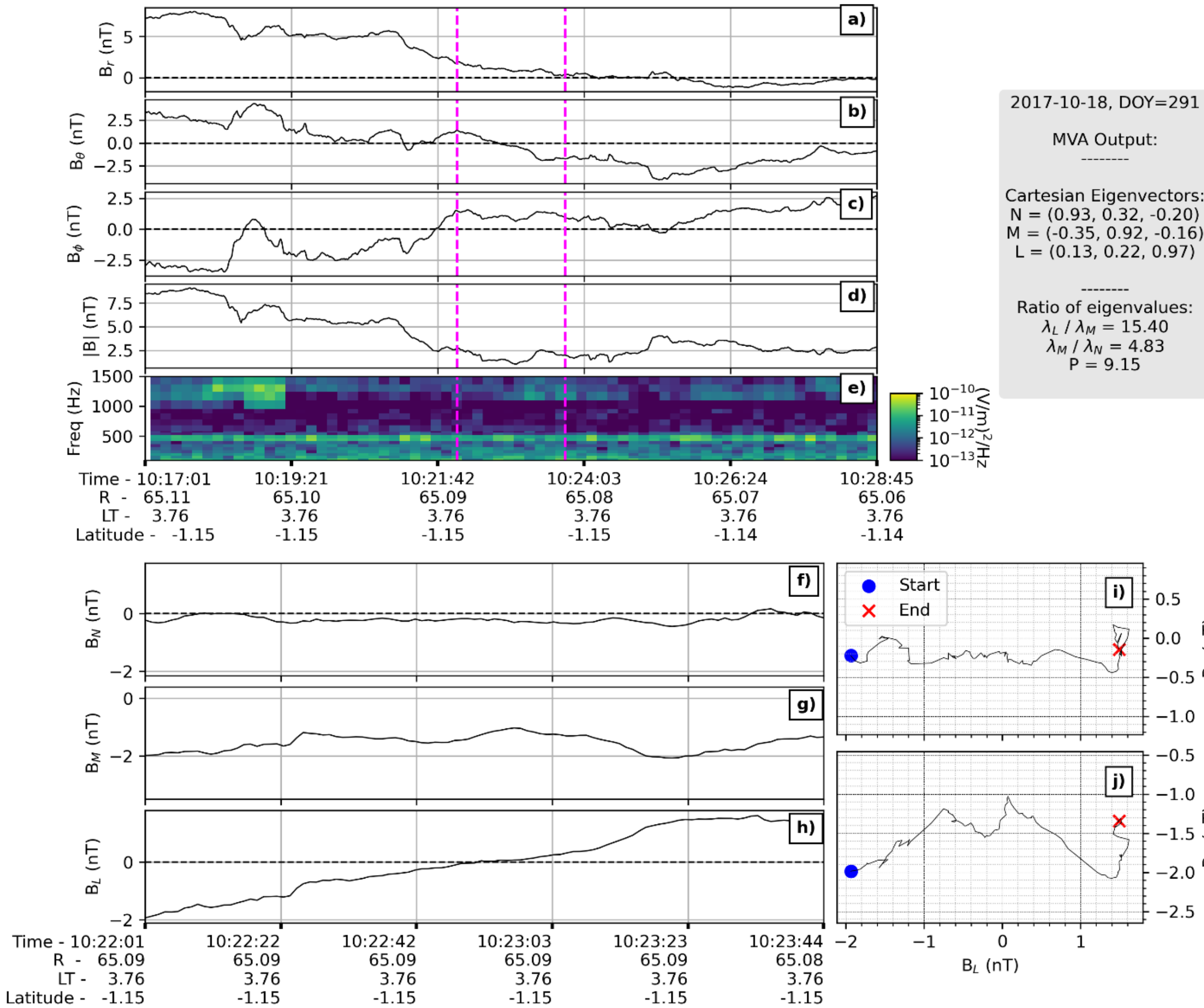

2017-10-18, DOY=291
MVA Output:

Cartesian Eigenvectors:
N = (0.93, 0.32, -0.20)
M = (-0.35, 0.92, -0.16)
L = (0.13, 0.22, 0.97)

Ratio of eigenvalues:
λL / λM = 15.40
λM / λN = 4.83
P = 9.15
Time - 10:17:01 10:19:21 10:21:42 10:24:03 10:26:24 10:28:45
R - 65.11 65.10 65.09 65.08 65.07 65.06
LT - 3.76 3.76 3.76 3.76 3.76 3.76
Latitude - -1.15 -1.15 -1.15 -1.15 -1.14 -1.14
Time - 10:22:01 10:22:22 10:22:42 10:23:03 10:23:23 10:23:44
R - 65.09 65.09 65.09 65.09 65.09 65.08
LT - 3.76 3.76 3.76 3.76 3.76 3.76
Latitude - -1.15 -1.15 -1.15 -1.15 -1.15 -1.15
Start
End

Figure S33

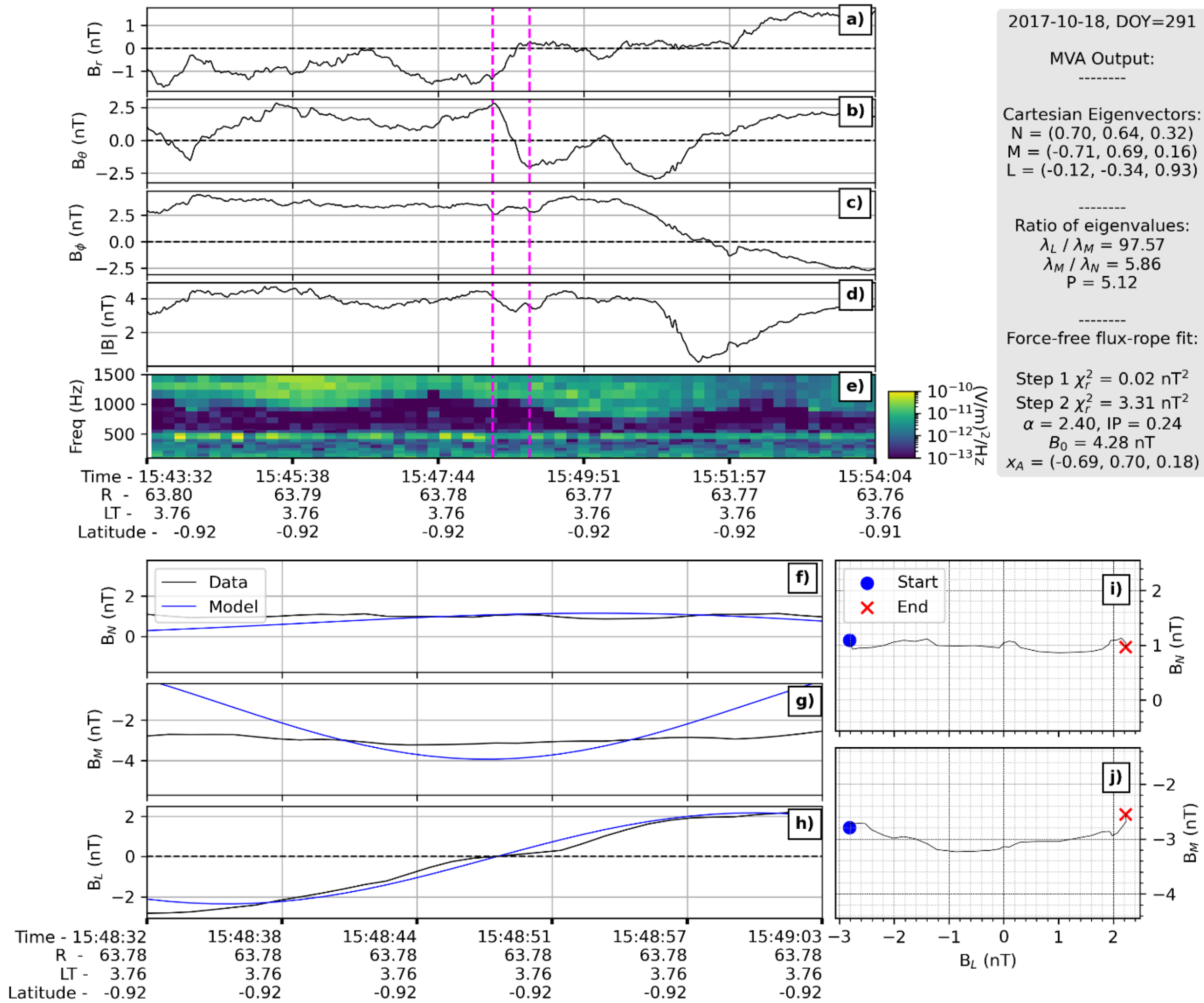
2017-10-18, DOY=291
MVA Output:

Cartesian Eigenvectors:
N = (0.70, 0.64, 0.32)
M = (-0.71, 0.69, 0.16)
L = (-0.12, -0.34, 0.93)

Ratio of eigenvalues:
λ_L / λ_M = 97.57
λ_M / λ_N = 5.86
P = 5.12

Force-free flux-rope fit:
Step 1 χ_r^2 = 0.02 nT^2
Step 2 χ_r^2 = 3.31 nT^2
α = 2.40, IP = 0.24
B_0 = 4.28 nT
x_A = (-0.69, 0.70, 0.18)
Time - 15:43:32 15:45:38 15:47:44 15:49:51 15:51:57 15:54:04
R - 63.80 63.79 63.78 63.77 63.77 63.76
LT - 3.76 3.76 3.76 3.76 3.76 3.76
Latitude - -0.92 -0.92 -0.92 -0.92 -0.92 -0.91
Data
Model
Start
End
Time - 15:48:32 15:48:38 15:48:44 15:48:51 15:48:57 15:49:03
R - 63.78 63.78 63.78 63.78 63.78 63.78
LT - 3.76 3.76 3.76 3.76 3.76 3.76
Latitude - -0.92 -0.92 -0.92 -0.92 -0.92 -0.92

Figure S34

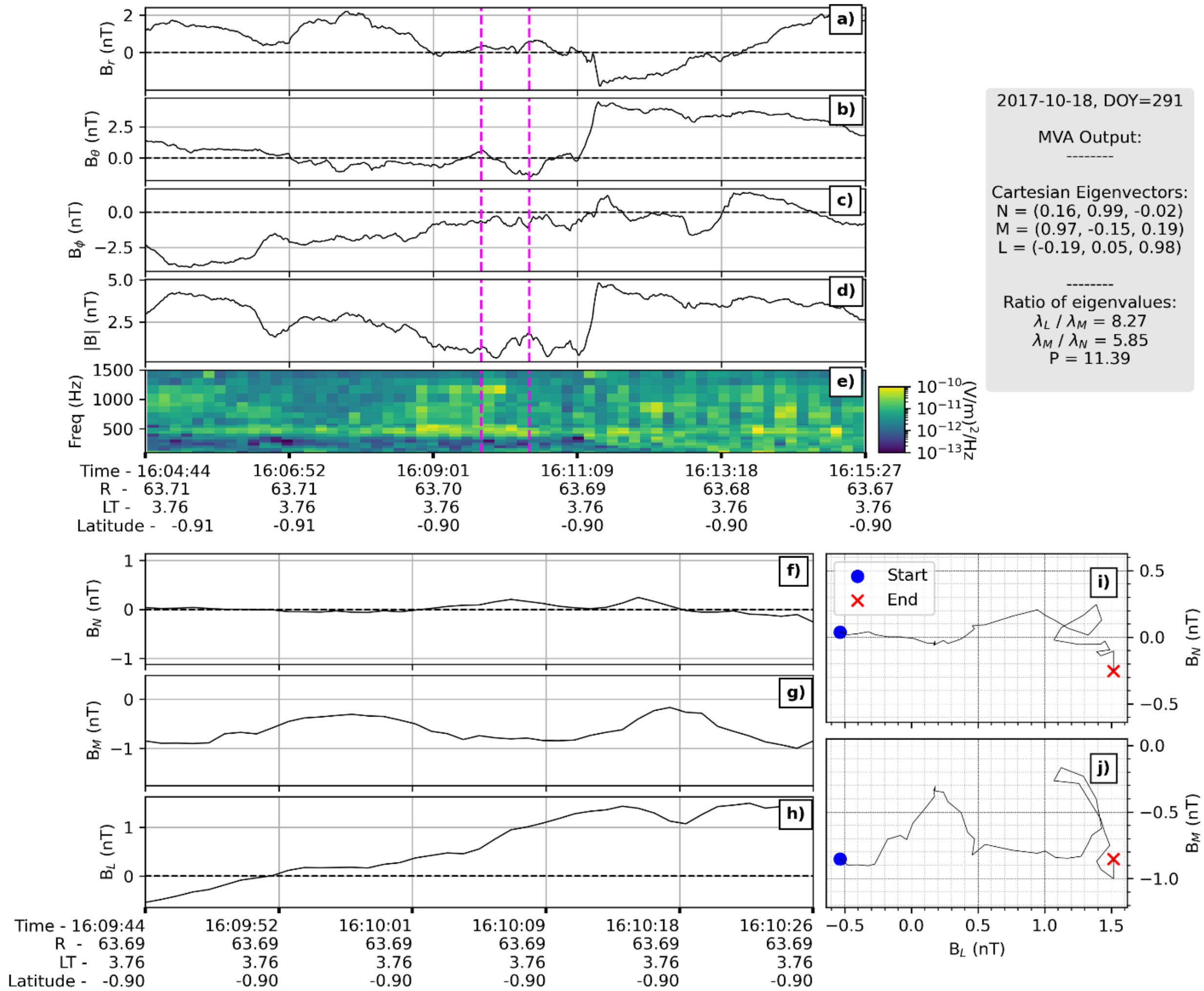

2017-10-18, DOY=291
MVA Output:

Cartesian Eigenvectors:
N = (0.16, 0.99, -0.02)
M = (0.97, -0.15, 0.19)
L = (-0.19, 0.05, 0.98)

Ratio of eigenvalues:
λL / λM = 8.27
λM / λN = 5.85
P = 11.39
Time - 16:04:44 16:06:52 16:09:01 16:11:09 16:13:18 16:15:27
R - 63.71 63.71 63.70 63.69 63.68 63.67
LT - 3.76 3.76 3.76 3.76 3.76 3.76
Latitude - -0.91 -0.91 -0.90 -0.90 -0.90 -0.90
Time - 16:09:44 16:09:52 16:10:01 16:10:09 16:10:18 16:10:26
R - 63.69 63.69 63.69 63.69 63.69 63.69
LT - 3.76 3.76 3.76 3.76 3.76 3.76
Latitude - -0.90 -0.90 -0.90 -0.90 -0.90 -0.90
Start
End
BL (nT)
BN (nT)
BM (nT)

Figure S35

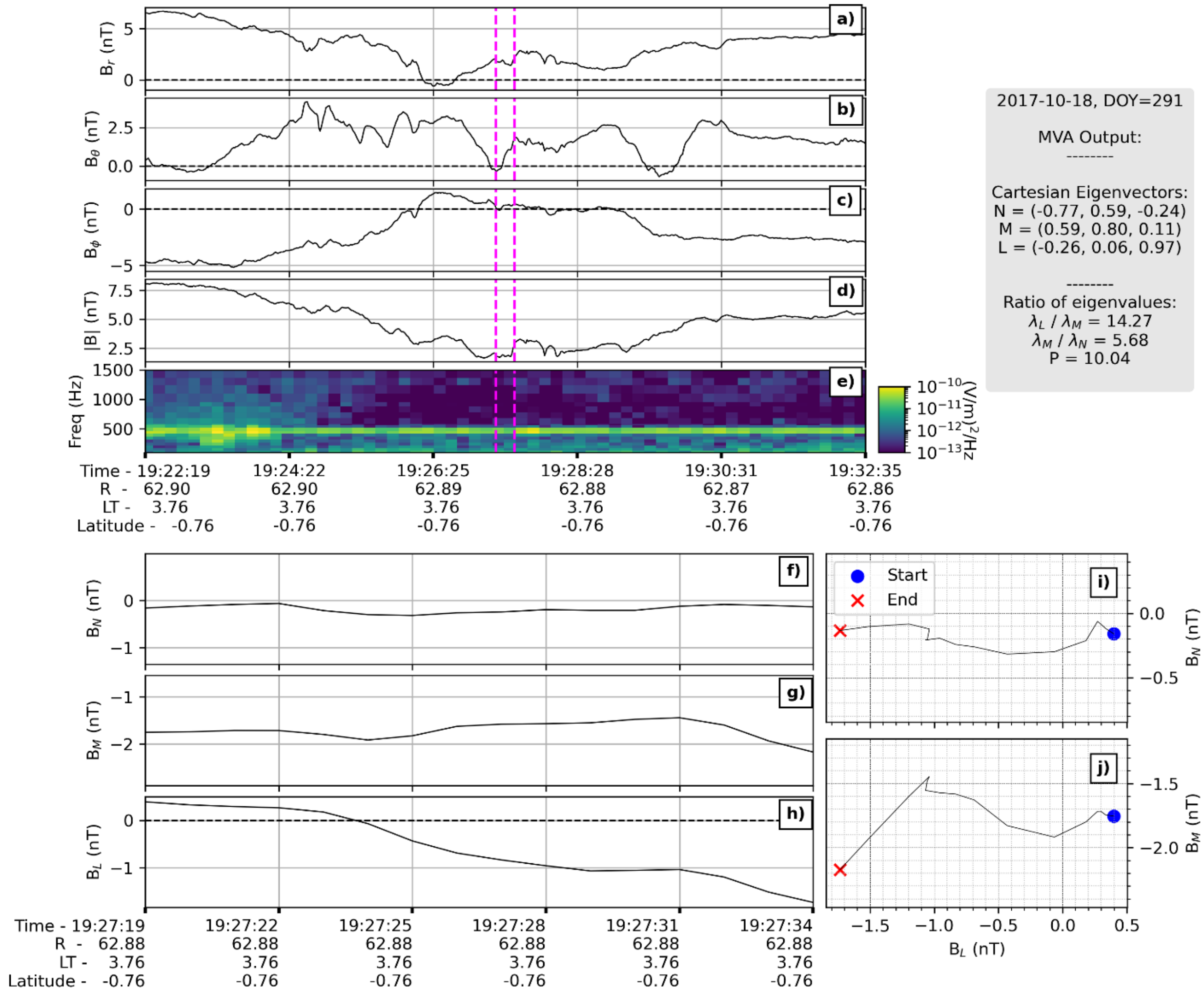
2017-10-18, DOY=291
MVA Output:
Cartesian Eigenvectors:
N = (-0.77, 0.59, -0.24)
M = (0.59, 0.80, 0.11)
L = (-0.26, 0.06, 0.97)
Ratio of eigenvalues:
λL / λM = 14.27
λM / λN = 5.68
P = 10.04
Start
End
Time - 19:22:19 19:24:22 19:26:25 19:28:28 19:30:31 19:32:35
R - 62.90 62.90 62.89 62.88 62.87 62.86
LT - 3.76 3.76 3.76 3.76 3.76 3.76
Latitude - -0.76 -0.76 -0.76 -0.76 -0.76 -0.76
Time - 19:27:19 19:27:22 19:27:25 19:27:28 19:27:31 19:27:34
R - 62.88 62.88 62.88 62.88 62.88 62.88
LT - 3.76 3.76 3.76 3.76 3.76 3.76
Latitude - -0.76 -0.76 -0.76 -0.76 -0.76 -0.76

Figure S36

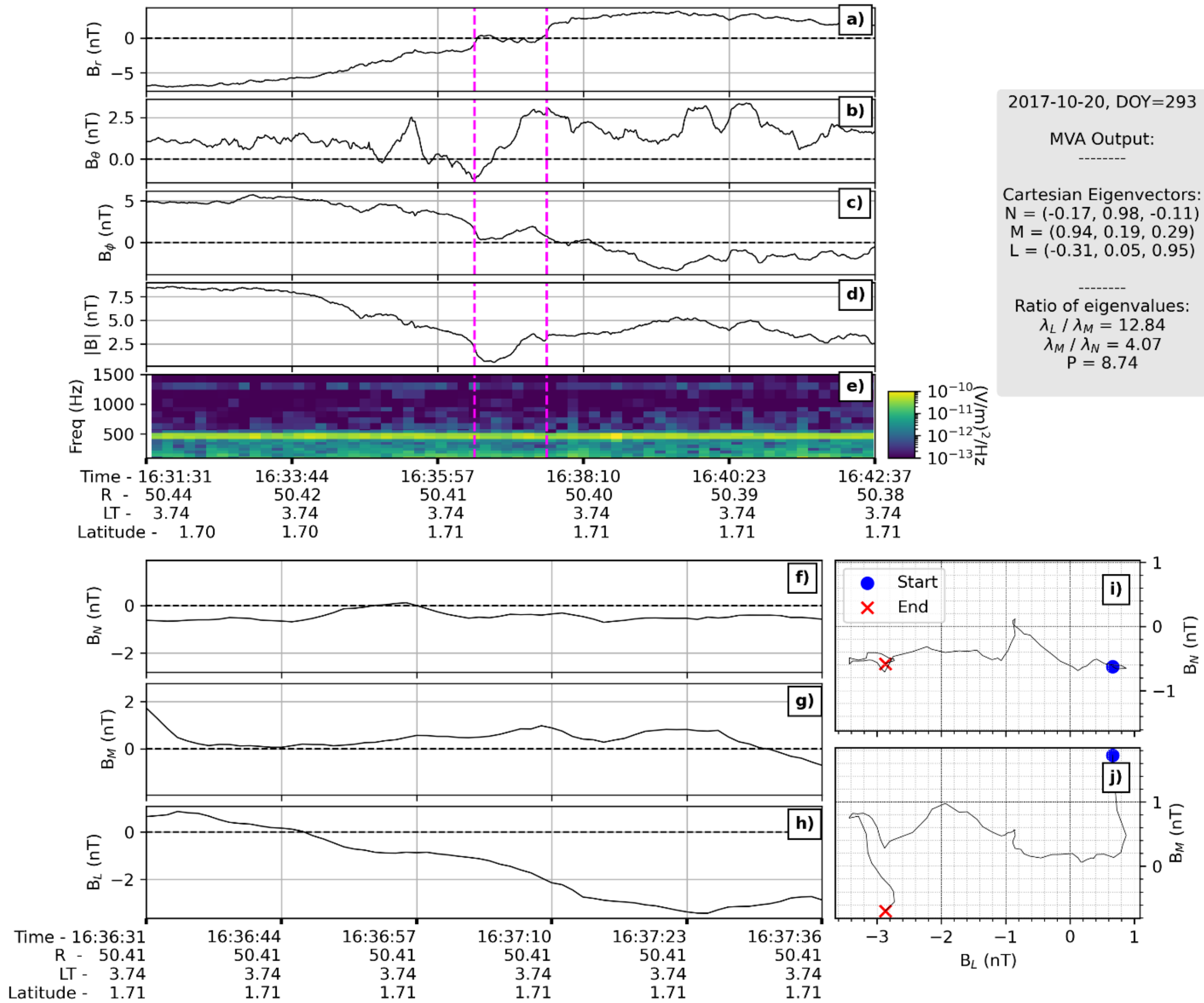
2017-10-20, DOY=293
MVA Output:

Cartesian Eigenvectors:
N = (-0.17, 0.98, -0.11)
M = (0.94, 0.19, 0.29)
L = (-0.31, 0.05, 0.95)

Ratio of eigenvalues:
λ_L / λ_M = 12.84
λ_M / λ_N = 4.07
P = 8.74
Start
End
Time - 16:31:31 16:33:44 16:35:57 16:38:10 16:40:23 16:42:37
R - 50.44 50.42 50.41 50.40 50.39 50.38
LT - 3.74 3.74 3.74 3.74 3.74 3.74
Latitude - 1.70 1.70 1.71 1.71 1.71 1.71
Time - 16:36:31 16:36:44 16:36:57 16:37:10 16:37:23 16:37:36
R - 50.41 50.41 50.41 50.41 50.41 50.41
LT - 3.74 3.74 3.74 3.74 3.74 3.74
Latitude - 1.71 1.71 1.71 1.71 1.71 1.71

Figure S37

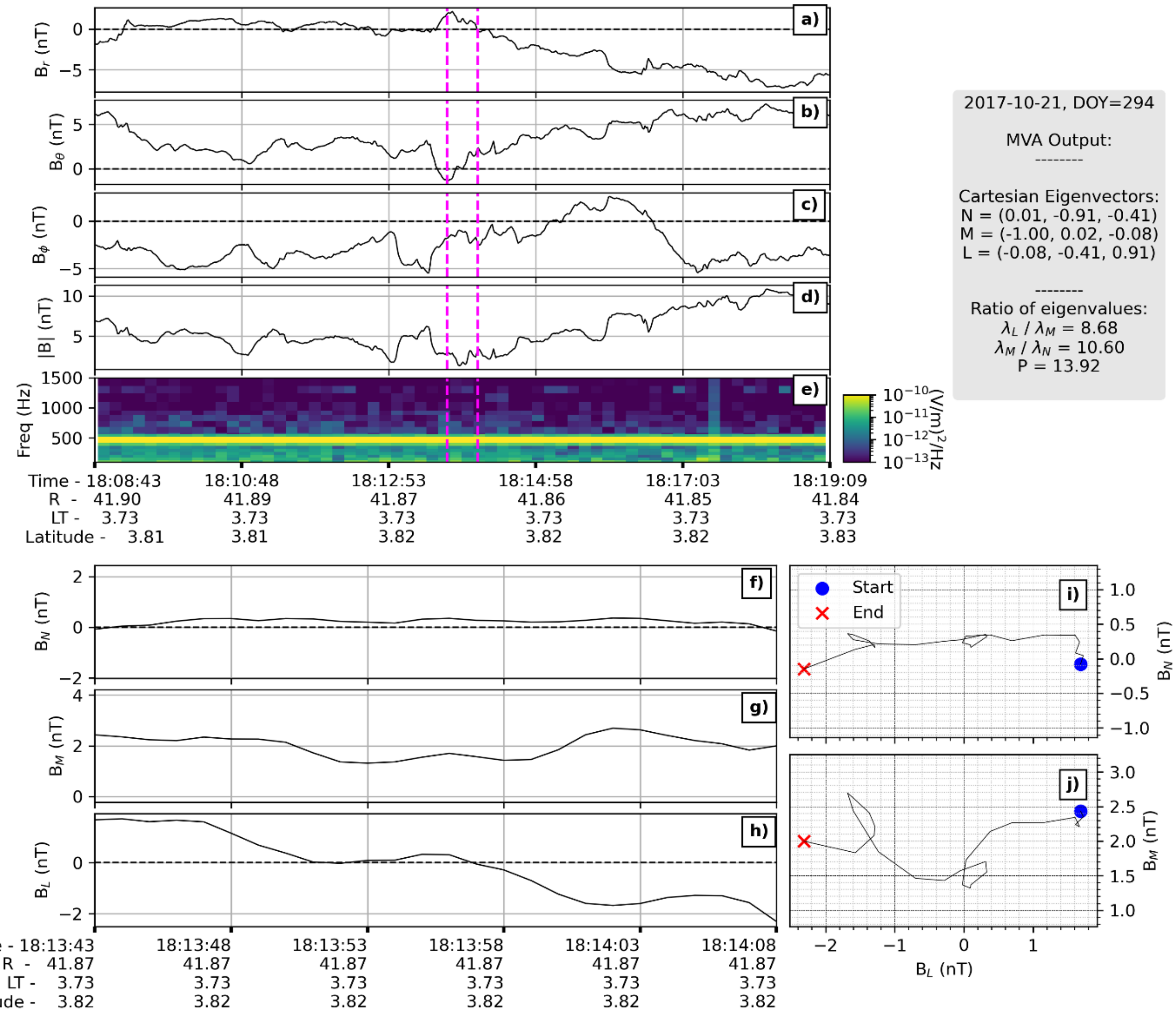

a)
b)
c)
d)
e)
f)
g)
h)
i)
j)
B$_r$ (nT)
B$_\theta$ (nT)
B$_\phi$ (nT)
|B| (nT)
Freq (Hz)
(V/m)^2/Hz
Time - 18:08:43 18:10:48 18:12:53 18:14:58 18:17:03 18:19:09
R - 41.90 41.89 41.87 41.86 41.85 41.84
LT - 3.73 3.73 3.73 3.73 3.73 3.73
Latitude - 3.81 3.81 3.82 3.82 3.82 3.83
2017-10-21, DOY=294
MVA Output:

Cartesian Eigenvectors:
N = (0.01, -0.91, -0.41)
M = (-1.00, 0.02, -0.08)
L = (-0.08, -0.41, 0.91)

Ratio of eigenvalues:
λ_L / λ_M = 8.68
λ_M / λ_N = 10.60
P = 13.92
B$_N$ (nT)
B$_M$ (nT)
B$_L$ (nT)
Start
End
Time - 18:13:43 18:13:48 18:13:53 18:13:58 18:14:03 18:14:08
R - 41.87 41.87 41.87 41.87 41.87 41.87
LT - 3.73 3.73 3.73 3.73 3.73 3.73
Latitude - 3.82 3.82 3.82 3.82 3.82 3.82

Figure S38

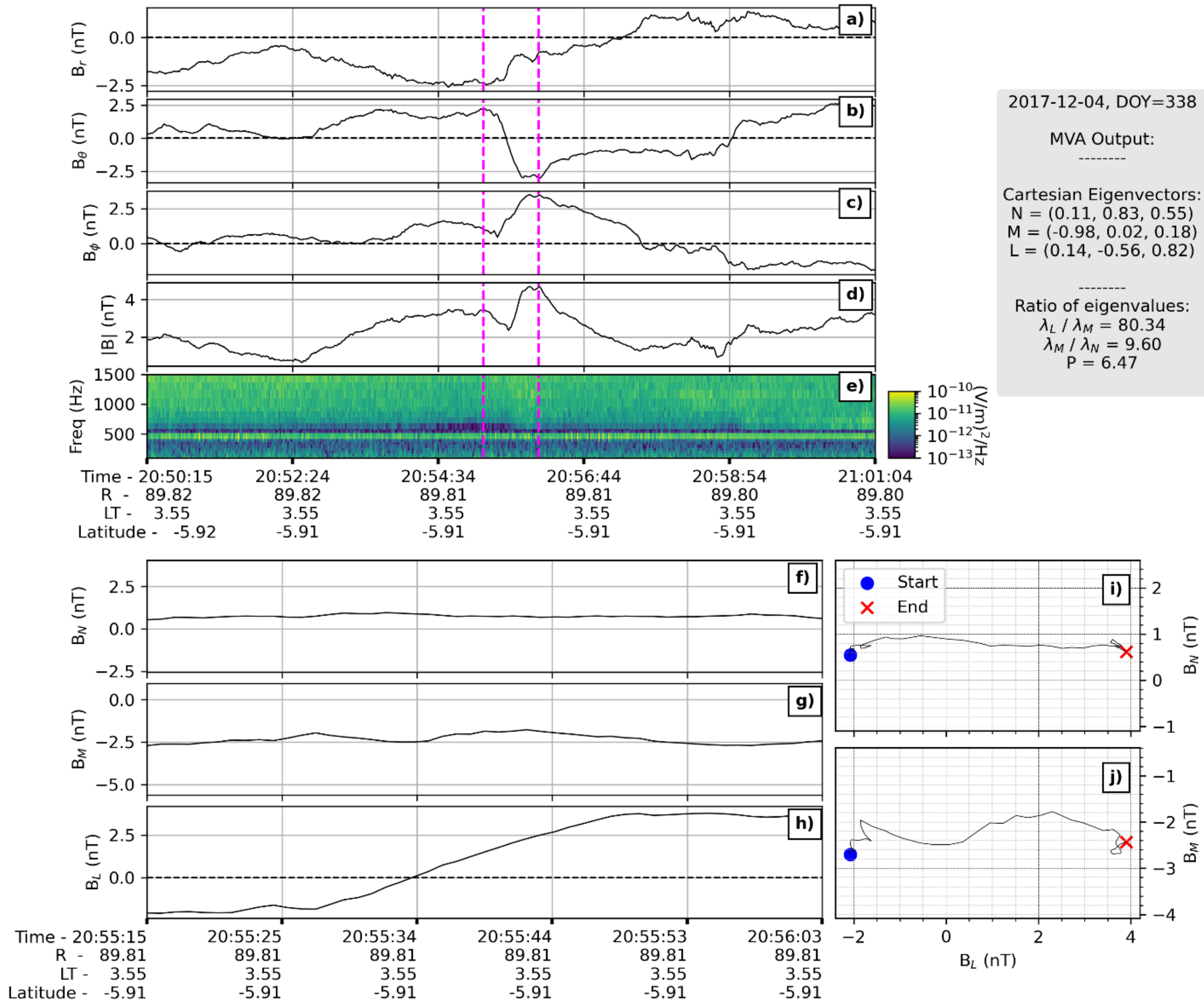

2017-12-04, DOY=338
MVA Output:

Cartesian Eigenvectors:
N = (0.11, 0.83, 0.55)
M = (-0.98, 0.02, 0.18)
L = (0.14, -0.56, 0.82)

Ratio of eigenvalues:
λ_L / λ_M = 80.34
λ_M / λ_N = 9.60
P = 6.47
B_r (nT)
B_θ (nT)
B_ϕ (nT)
|B| (nT)
Freq (Hz)
(V/m)^2/Hz
Time - 20:50:15 | 20:52:24 | 20:54:34 | 20:56:44 | 20:58:54 | 21:01:04
R - 89.82 | 89.82 | 89.81 | 89.81 | 89.80 | 89.80
LT - 3.55 | 3.55 | 3.55 | 3.55 | 3.55 | 3.55
Latitude - -5.92 | -5.91 | -5.91 | -5.91 | -5.91 | -5.91
B_N (nT)
B_M (nT)
B_L (nT)
Start
End
Time - 20:55:15 | 20:55:25 | 20:55:34 | 20:55:44 | 20:55:53 | 20:56:03
R - 89.81 | 89.81 | 89.81 | 89.81 | 89.81 | 89.81
LT - 3.55 | 3.55 | 3.55 | 3.55 | 3.55 | 3.55
Latitude - -5.91 | -5.91 | -5.91 | -5.91 | -5.91 | -5.91

Figure S39

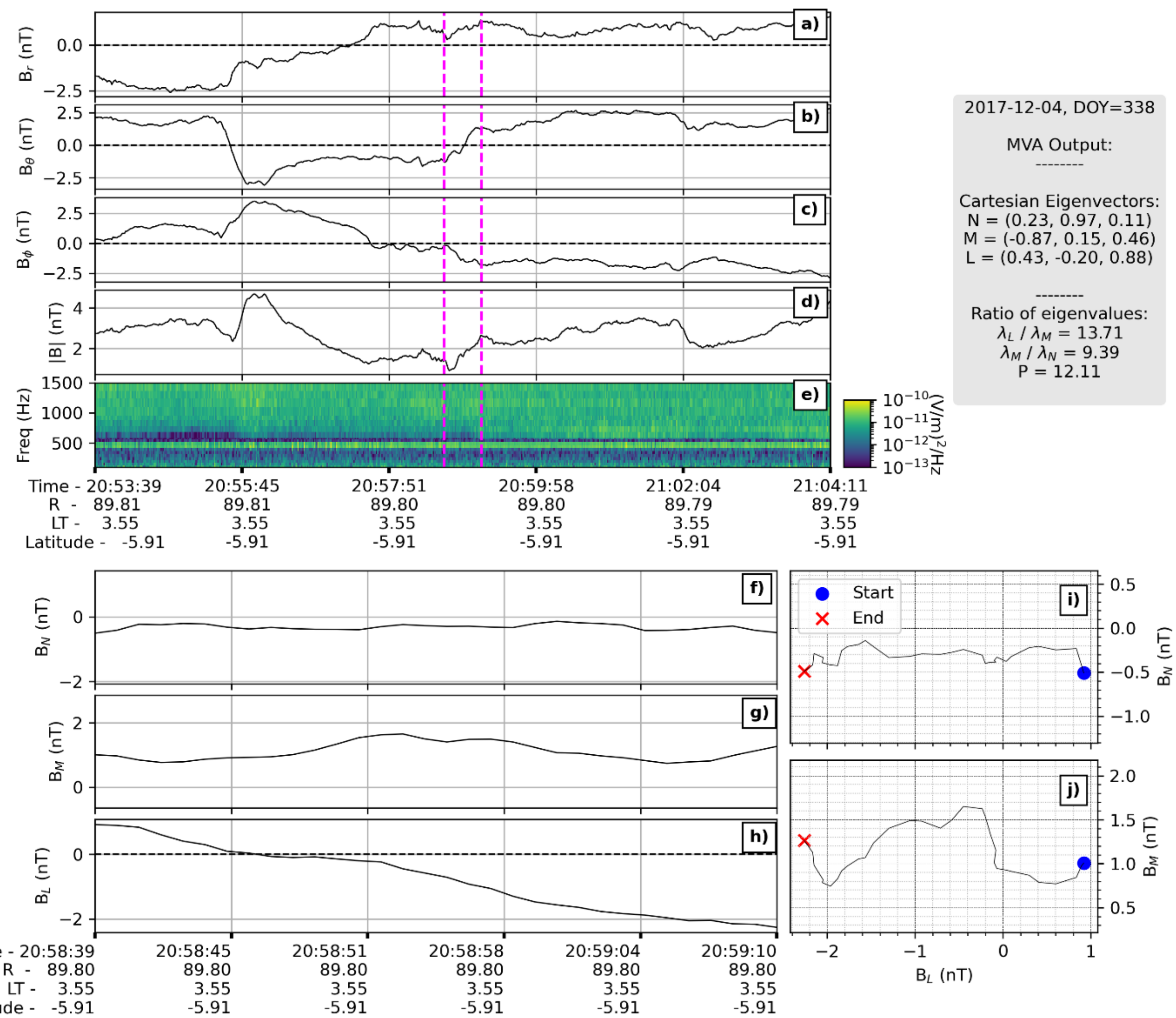

a)
b)
c)
d)
e)
f)
g)
h)
i)
j)
B$_r$ (nT)
B$_\theta$ (nT)
B$_\phi$ (nT)
|B| (nT)
Freq (Hz)
(V/m)^2/Hz
2017-12-04, DOY=338
MVA Output:

Cartesian Eigenvectors:
N = (0.23, 0.97, 0.11)
M = (-0.87, 0.15, 0.46)
L = (0.43, -0.20, 0.88)

Ratio of eigenvalues:
λ_L / λ_M = 13.71
λ_M / λ_N = 9.39
P = 12.11
Time - 20:53:39 20:55:45 20:57:51 20:59:58 21:02:04 21:04:11
R - 89.81 89.81 89.80 89.80 89.79 89.79
LT - 3.55 3.55 3.55 3.55 3.55 3.55
Latitude - -5.91 -5.91 -5.91 -5.91 -5.91 -5.91
B$_N$ (nT)
B$_M$ (nT)
B$_L$ (nT)
Start
End
Time - 20:58:39 20:58:45 20:58:51 20:58:58 20:59:04 20:59:10
R - 89.80 89.80 89.80 89.80 89.80 89.80
LT - 3.55 3.55 3.55 3.55 3.55 3.55
Latitude - -5.91 -5.91 -5.91 -5.91 -5.91 -5.91
B$_L$ (nT)

Figure S40

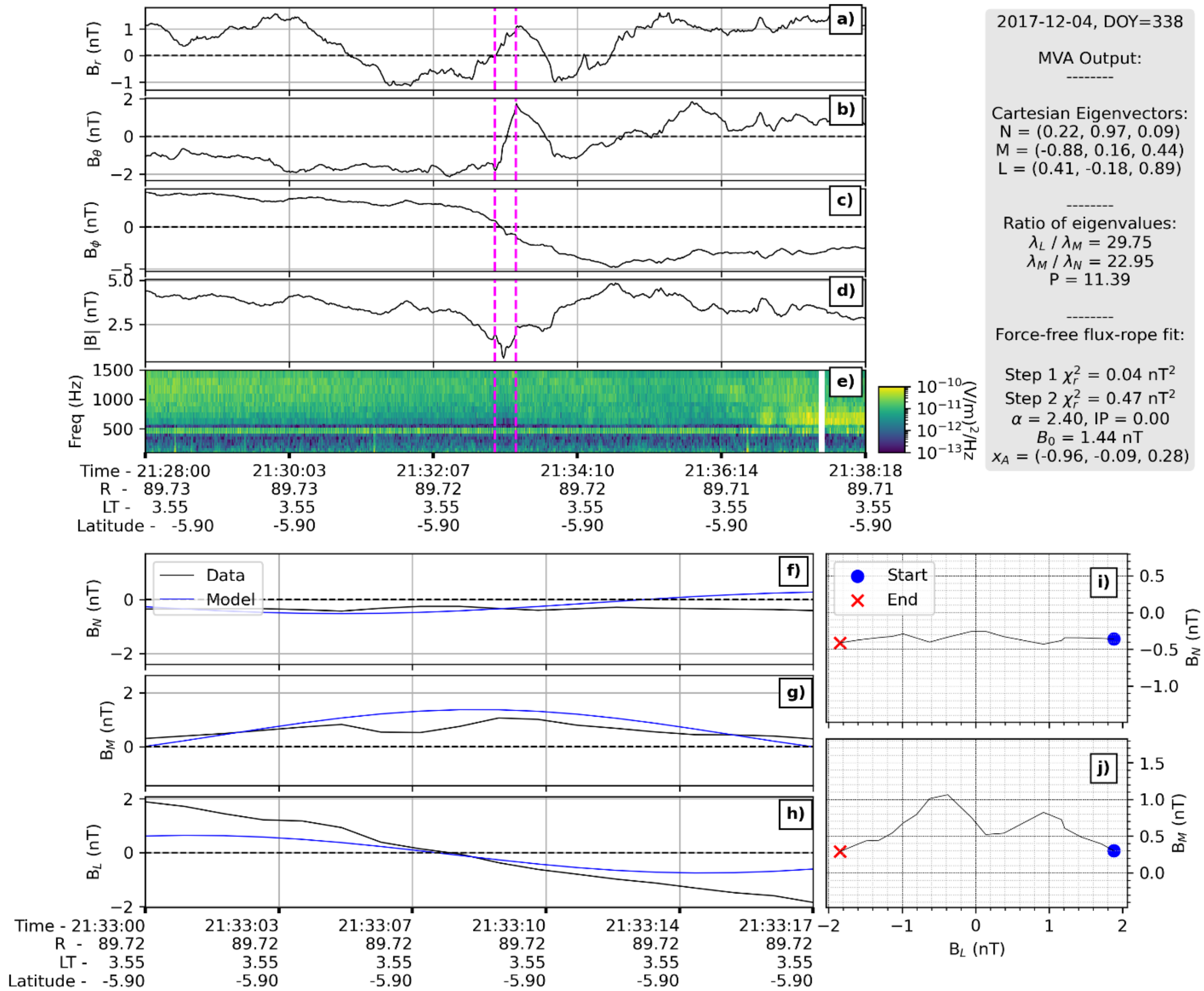
2017-12-04, DOY=338
MVA Output:
Cartesian Eigenvectors:
N = (0.22, 0.97, 0.09)
M = (-0.88, 0.16, 0.44)
L = (0.41, -0.18, 0.89)
Ratio of eigenvalues:
λ_L / λ_M = 29.75
λ_M / λ_N = 22.95
P = 11.39
Force-free flux-rope fit:
Step 1 χ_r^2 = 0.04 nT^2
Step 2 χ_r^2 = 0.47 nT^2
α = 2.40, IP = 0.00
B_0 = 1.44 nT
x_A = (-0.96, -0.09, 0.28)
Time - 21:28:00 21:30:03 21:32:07 21:34:10 21:36:14 21:38:18
R - 89.73 89.73 89.72 89.72 89.71 89.71
LT - 3.55
Latitude - -5.90
Time - 21:33:00 21:33:03 21:33:07 21:33:10 21:33:14 21:33:17
R - 89.72
Data
Model
Start
End

Figure S41

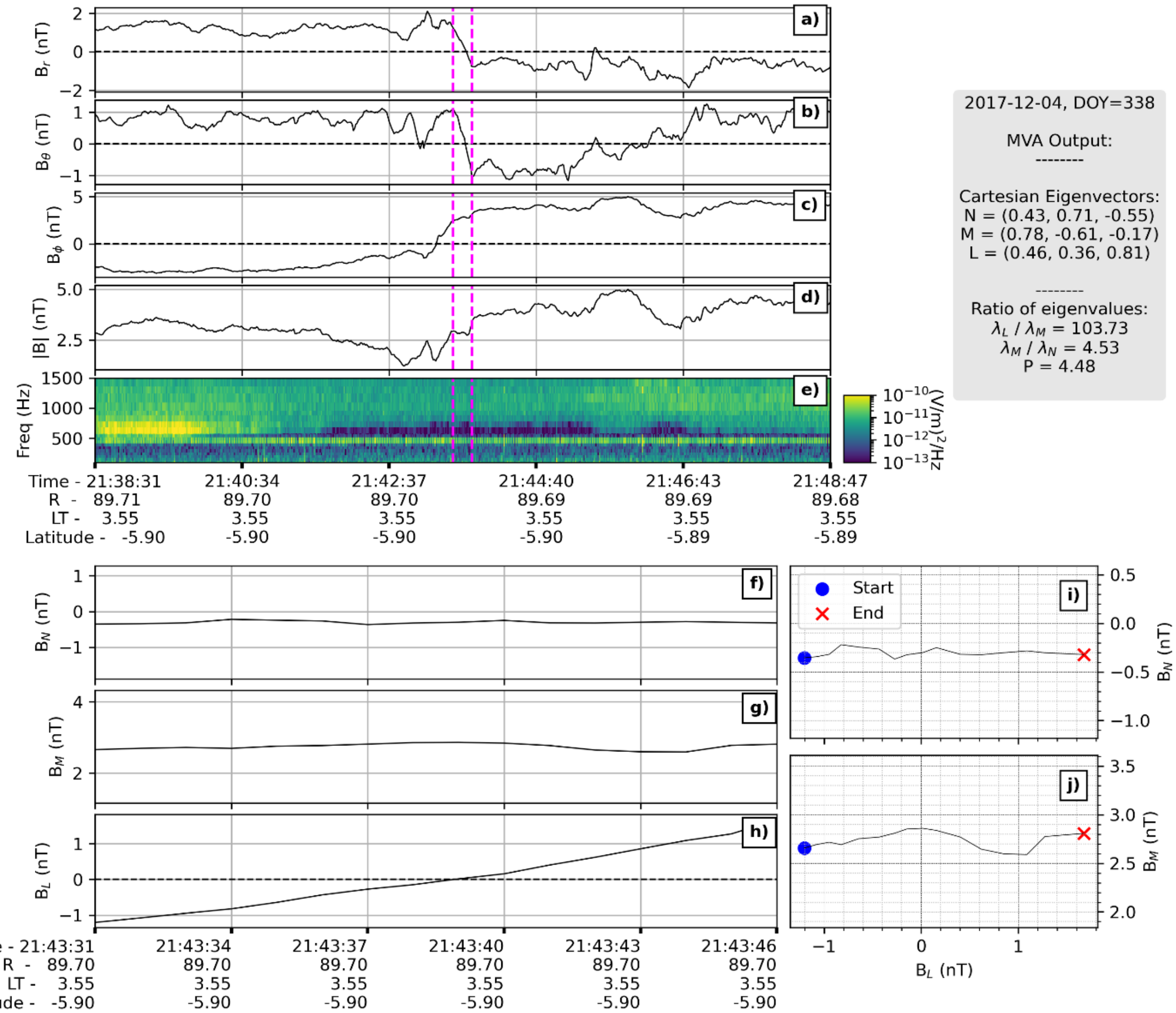
2017-12-04, DOY=338
MVA Output:

Cartesian Eigenvectors:
N = (0.43, 0.71, -0.55)
M = (0.78, -0.61, -0.17)
L = (0.46, 0.36, 0.81)

Ratio of eigenvalues:
λ_L / λ_M = 103.73
λ_M / λ_N = 4.53
P = 4.48
a)
b)
c)
d)
e)
f)
g)
h)
i)
j)
B_r (nT)
B_θ (nT)
B_ϕ (nT)
|B| (nT)
Freq (Hz)
(V/m)^2/Hz
Time - 21:38:31 21:40:34 21:42:37 21:44:40 21:46:43 21:48:47
R - 89.71 89.70 89.70 89.69 89.69 89.68
LT - 3.55 3.55 3.55 3.55 3.55 3.55
Latitude - -5.90 -5.90 -5.90 -5.90 -5.89 -5.89
B_N (nT)
B_M (nT)
B_L (nT)
Time - 21:43:31 21:43:34 21:43:37 21:43:40 21:43:43 21:43:46
R - 89.70 89.70 89.70 89.70 89.70 89.70
LT - 3.55 3.55 3.55 3.55 3.55 3.55
Latitude - -5.90 -5.90 -5.90 -5.90 -5.90 -5.90
Start
End
B_L (nT)

Figure S42

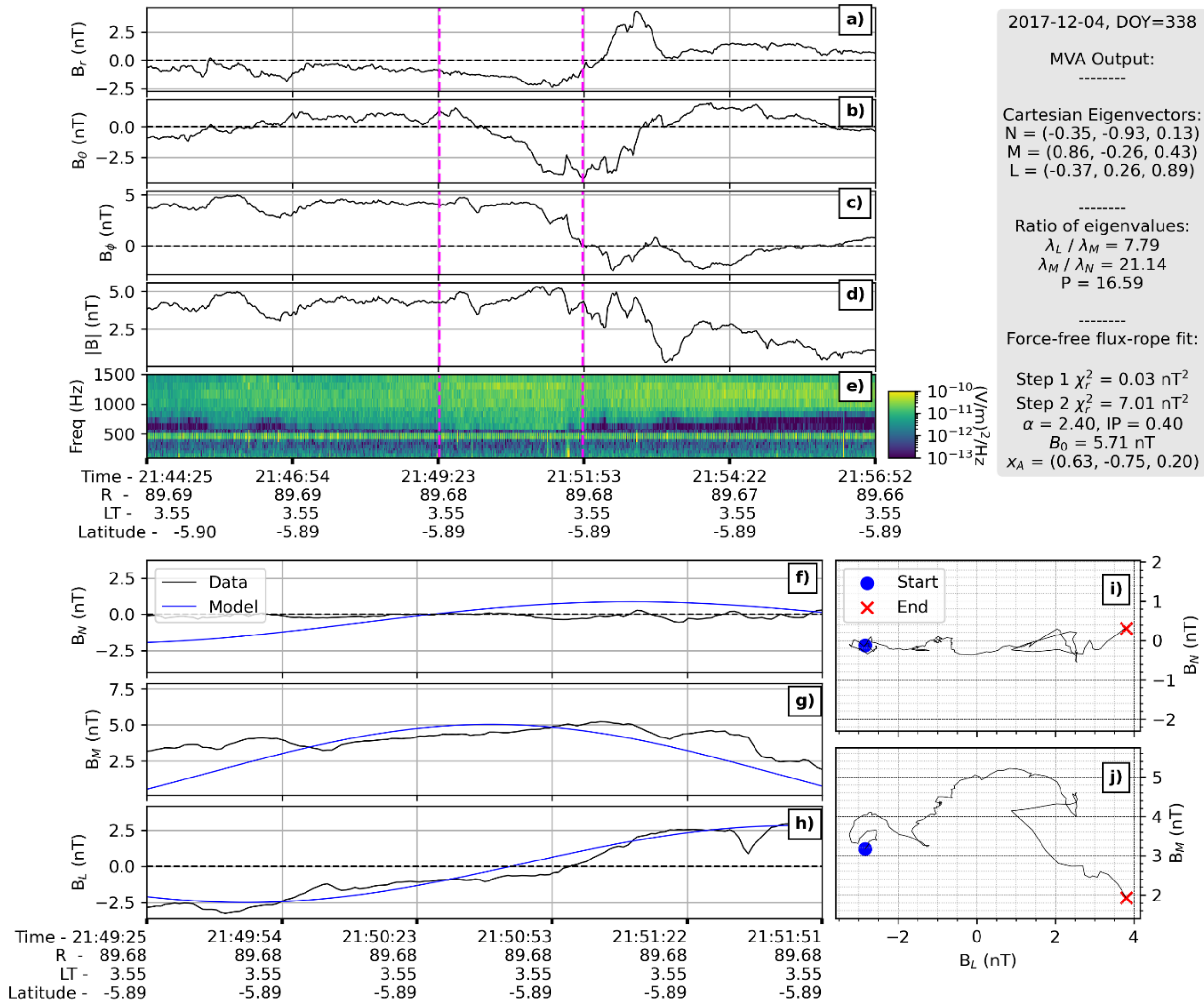
2017-12-04, DOY=338
MVA Output:
Cartesian Eigenvectors:
N = (-0.35, -0.93, 0.13)
M = (0.86, -0.26, 0.43)
L = (-0.37, 0.26, 0.89)
Ratio of eigenvalues:
λ_L / λ_M = 7.79
λ_M / λ_N = 21.14
P = 16.59
Force-free flux-rope fit:
Step 1 χ_r^2 = 0.03 nT^2
Step 2 χ_r^2 = 7.01 nT^2
α = 2.40, IP = 0.40
B_0 = 5.71 nT
x_A = (0.63, -0.75, 0.20)
Data
Model
Start
End

Figure S43

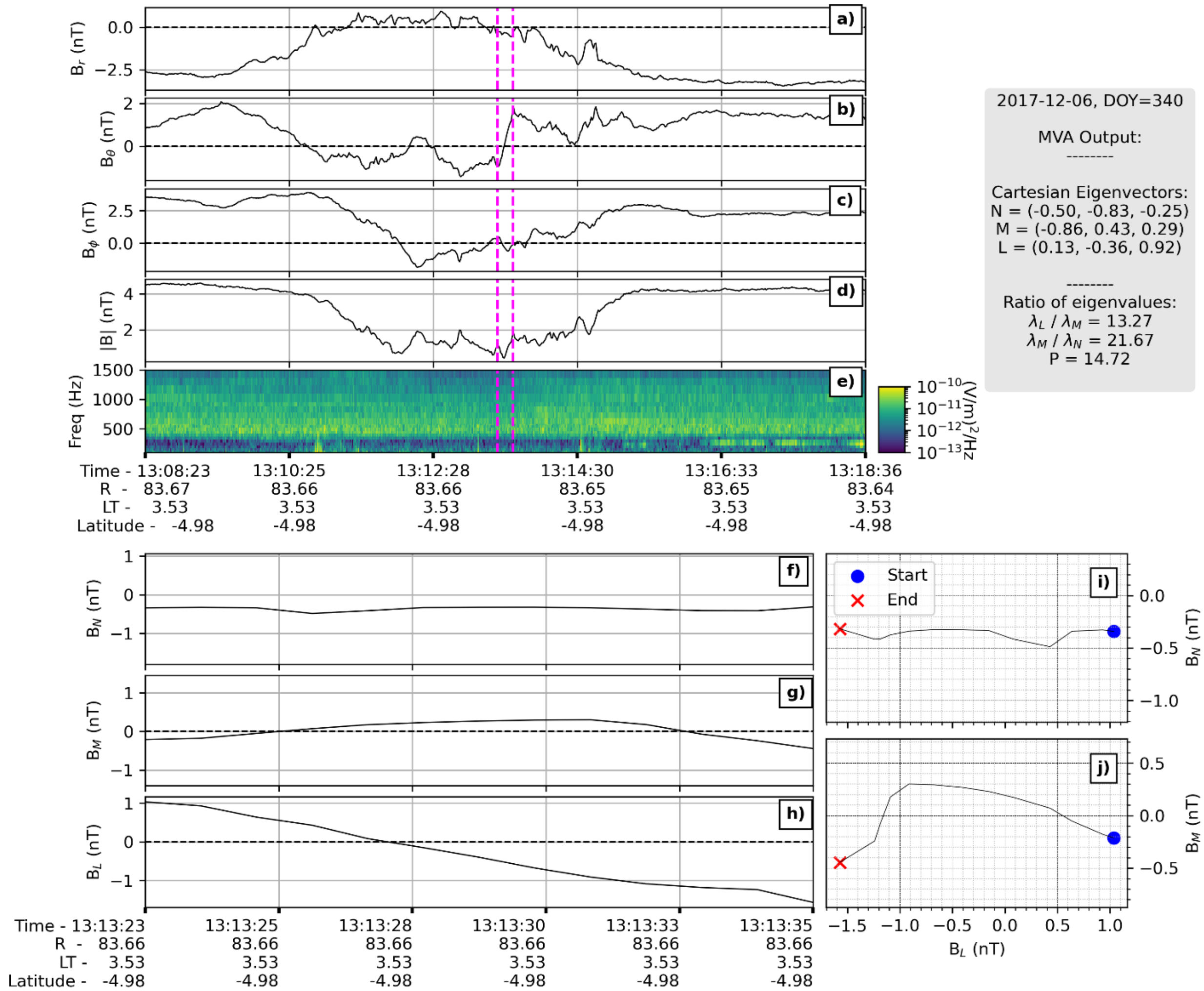

2017-12-06, DOY=340
MVA Output:
Cartesian Eigenvectors:
N = (-0.50, -0.83, -0.25)
M = (-0.86, 0.43, 0.29)
L = (0.13, -0.36, 0.92)
Ratio of eigenvalues:
λ_L / λ_M = 13.27
λ_M / λ_N = 21.67
P = 14.72
Time - 13:08:23 13:10:25 13:12:28 13:14:30 13:16:33 13:18:36
R - 83.67 83.66 83.66 83.65 83.65 83.64
LT - 3.53 3.53 3.53 3.53 3.53 3.53
Latitude - -4.98 -4.98 -4.98 -4.98 -4.98 -4.98
Time - 13:13:23 13:13:25 13:13:28 13:13:30 13:13:33 13:13:35
R - 83.66 83.66 83.66 83.66 83.66 83.66
LT - 3.53 3.53 3.53 3.53 3.53 3.53
Latitude - -4.98 -4.98 -4.98 -4.98 -4.98 -4.98
Start
End

Figure S44

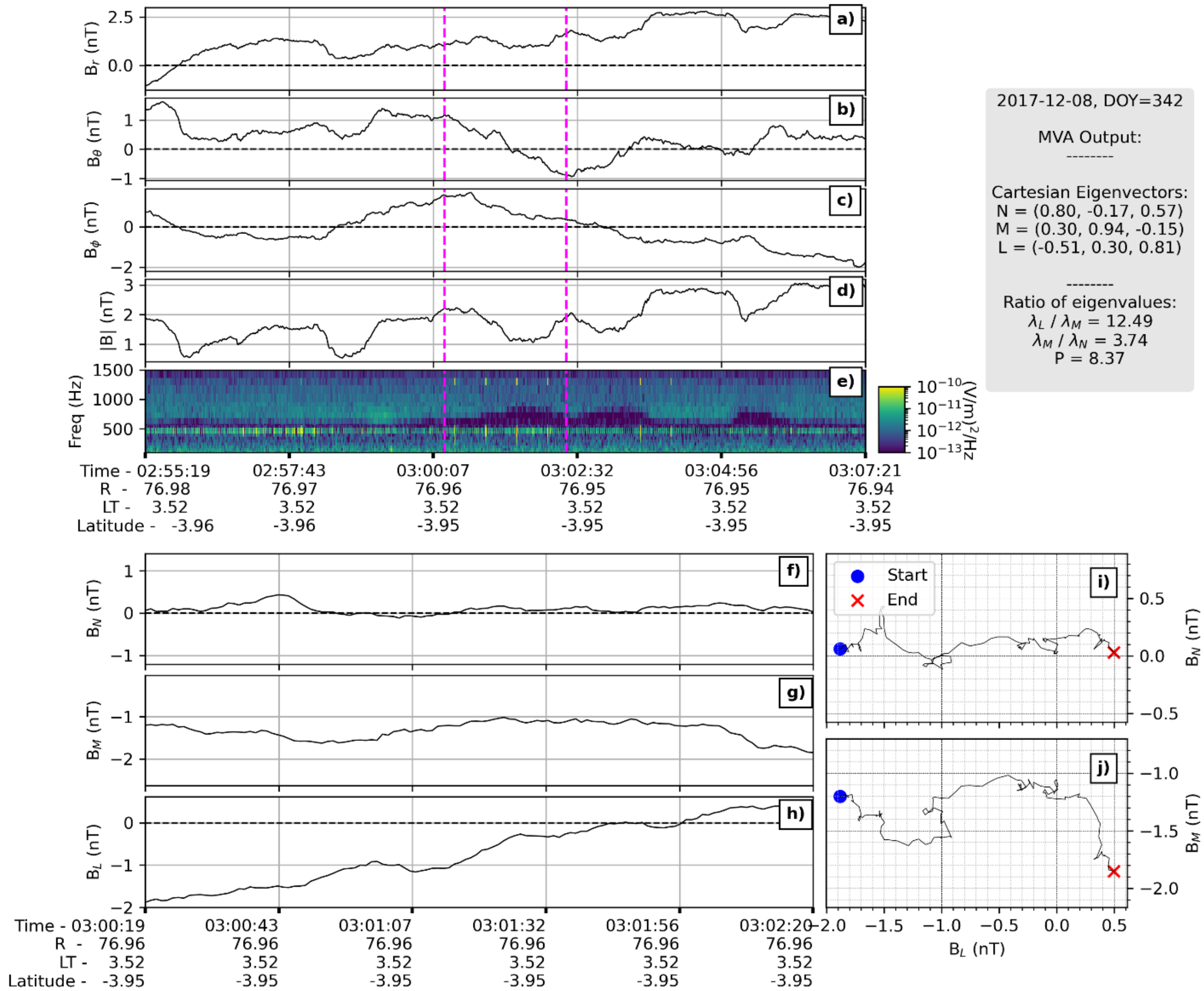
2017-12-08, DOY=342
MVA Output:
Cartesian Eigenvectors:
N = (0.80, -0.17, 0.57)
M = (0.30, 0.94, -0.15)
L = (-0.51, 0.30, 0.81)
Ratio of eigenvalues:
λ_L / λ_M = 12.49
λ_M / λ_N = 3.74
P = 8.37
Time - 02:55:19 02:57:43 03:00:07 03:02:32 03:04:56 03:07:21
R - 76.98 76.97 76.96 76.95 76.95 76.94
LT - 3.52 3.52 3.52 3.52 3.52 3.52
Latitude - -3.96 -3.96 -3.95 -3.95 -3.95 -3.95
Time - 03:00:19 03:00:43 03:01:07 03:01:32 03:01:56 03:02:20
R - 76.96 76.96 76.96 76.96 76.96 76.96
LT - 3.52 3.52 3.52 3.52 3.52 3.52
Latitude - -3.95 -3.95 -3.95 -3.95 -3.95 -3.95
Start
End
B_L (nT)
B_N (nT)
B_M (nT)

Figure S45

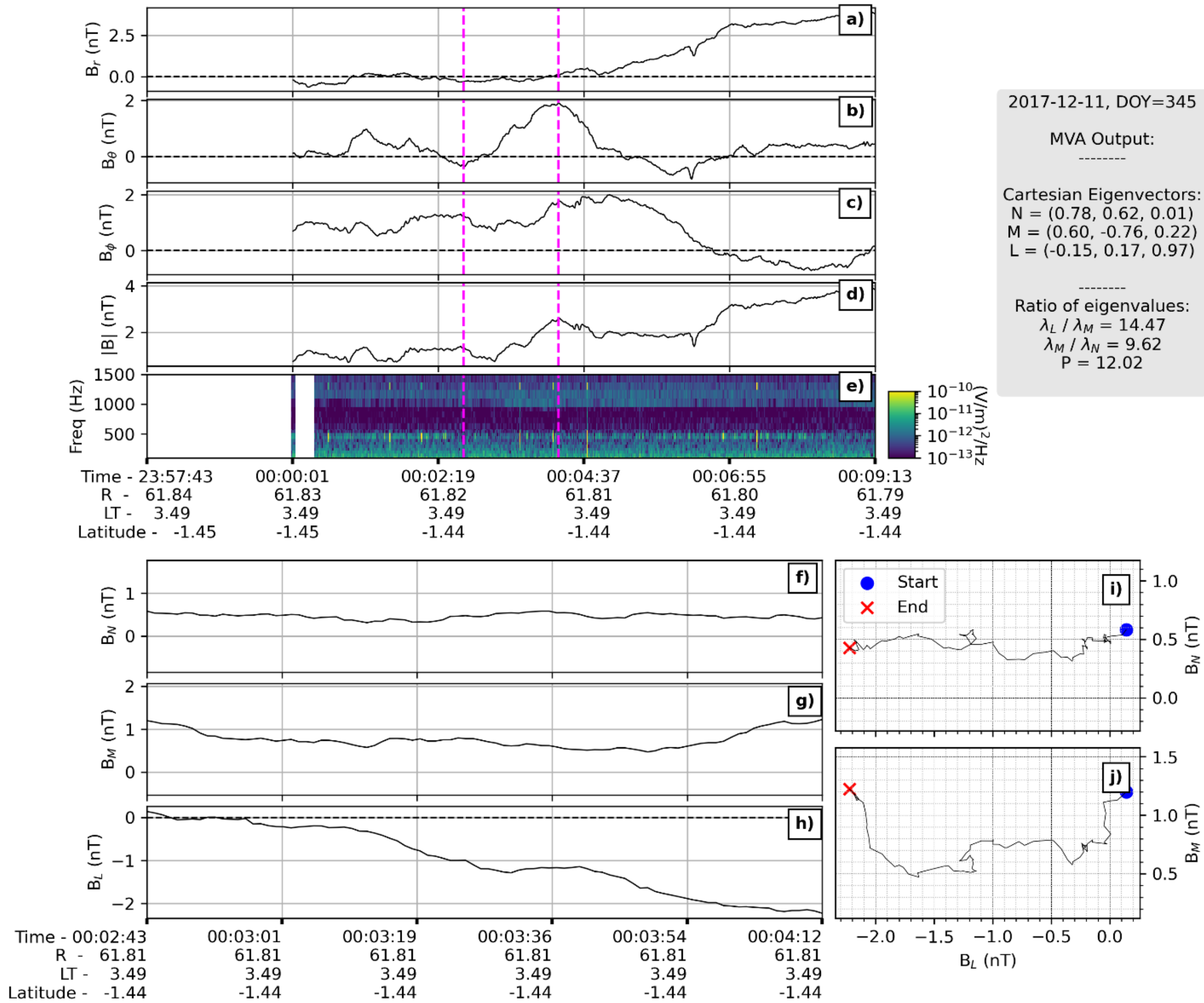

2017-12-11, DOY=345
MVA Output:
Cartesian Eigenvectors:
N = (0.78, 0.62, 0.01)
M = (0.60, -0.76, 0.22)
L = (-0.15, 0.17, 0.97)
Ratio of eigenvalues:
λ_L / λ_M = 14.47
λ_M / λ_N = 9.62
P = 12.02

Figure S46

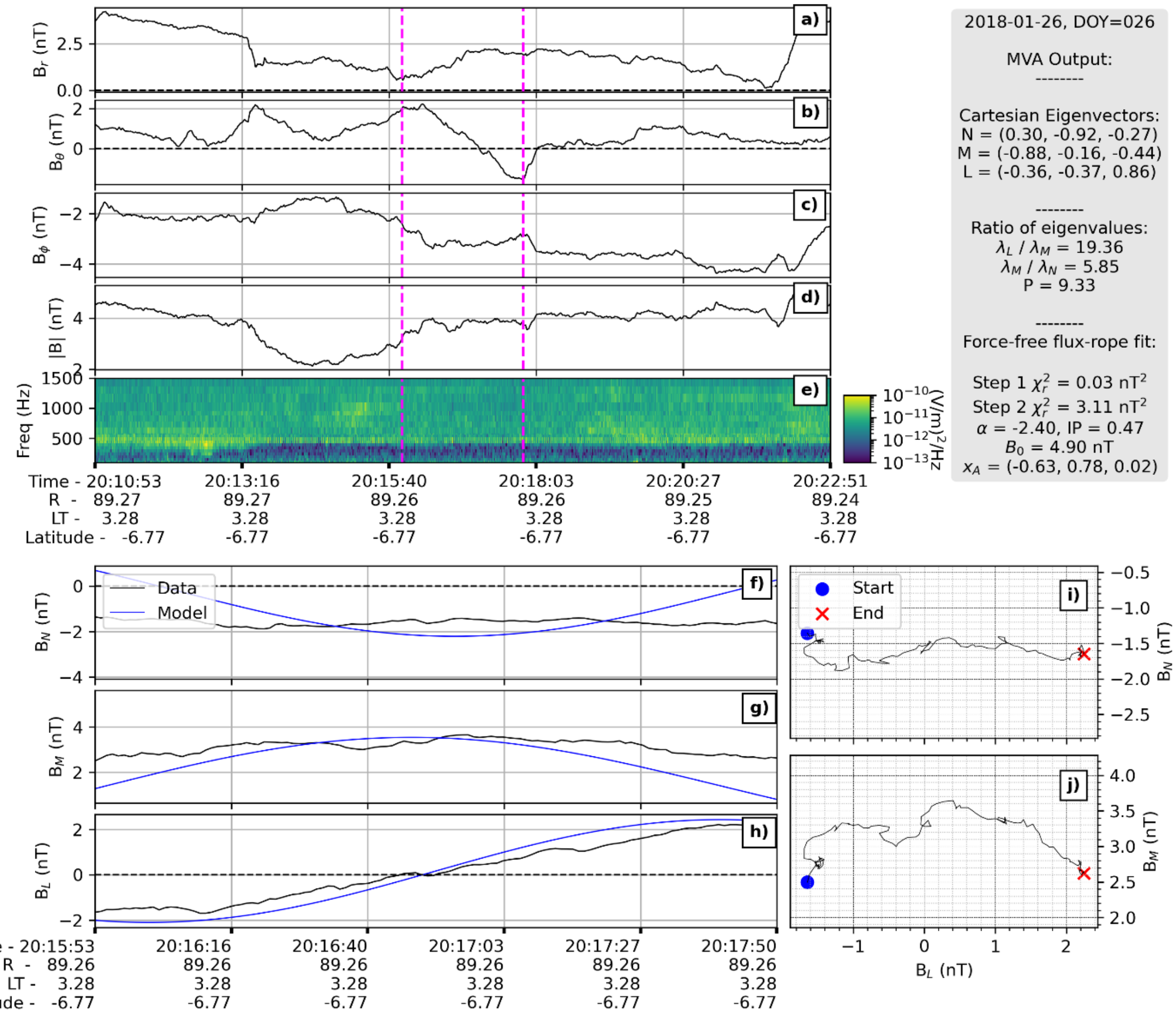

a)
b)
c)
d)
e)
f)
g)
h)
i)
j)
2018-01-26, DOY=026
MVA Output:
Cartesian Eigenvectors:
N = (0.30, -0.92, -0.27)
M = (-0.88, -0.16, -0.44)
L = (-0.36, -0.37, 0.86)
Ratio of eigenvalues:
λL / λM = 19.36
λM / λN = 5.85
P = 9.33
Force-free flux-rope fit:
Step 1 χr² = 0.03 nT²
Step 2 χr² = 3.11 nT²
α = -2.40, IP = 0.47
B0 = 4.90 nT
xA = (-0.63, 0.78, 0.02)
Time - 20:10:53 20:13:16 20:15:40 20:18:03 20:20:27 20:22:51
R - 89.27 89.27 89.26 89.26 89.25 89.24
LT - 3.28 3.28 3.28 3.28 3.28 3.28
Latitude - -6.77 -6.77 -6.77 -6.77 -6.77 -6.77
Data
Model
Start
End
Time - 20:15:53 20:16:16 20:16:40 20:17:03 20:17:27 20:17:50
R - 89.26 89.26 89.26 89.26 89.26 89.26
LT - 3.28 3.28 3.28 3.28 3.28 3.28
Latitude - -6.77 -6.77 -6.77 -6.77 -6.77 -6.77

Figure S47

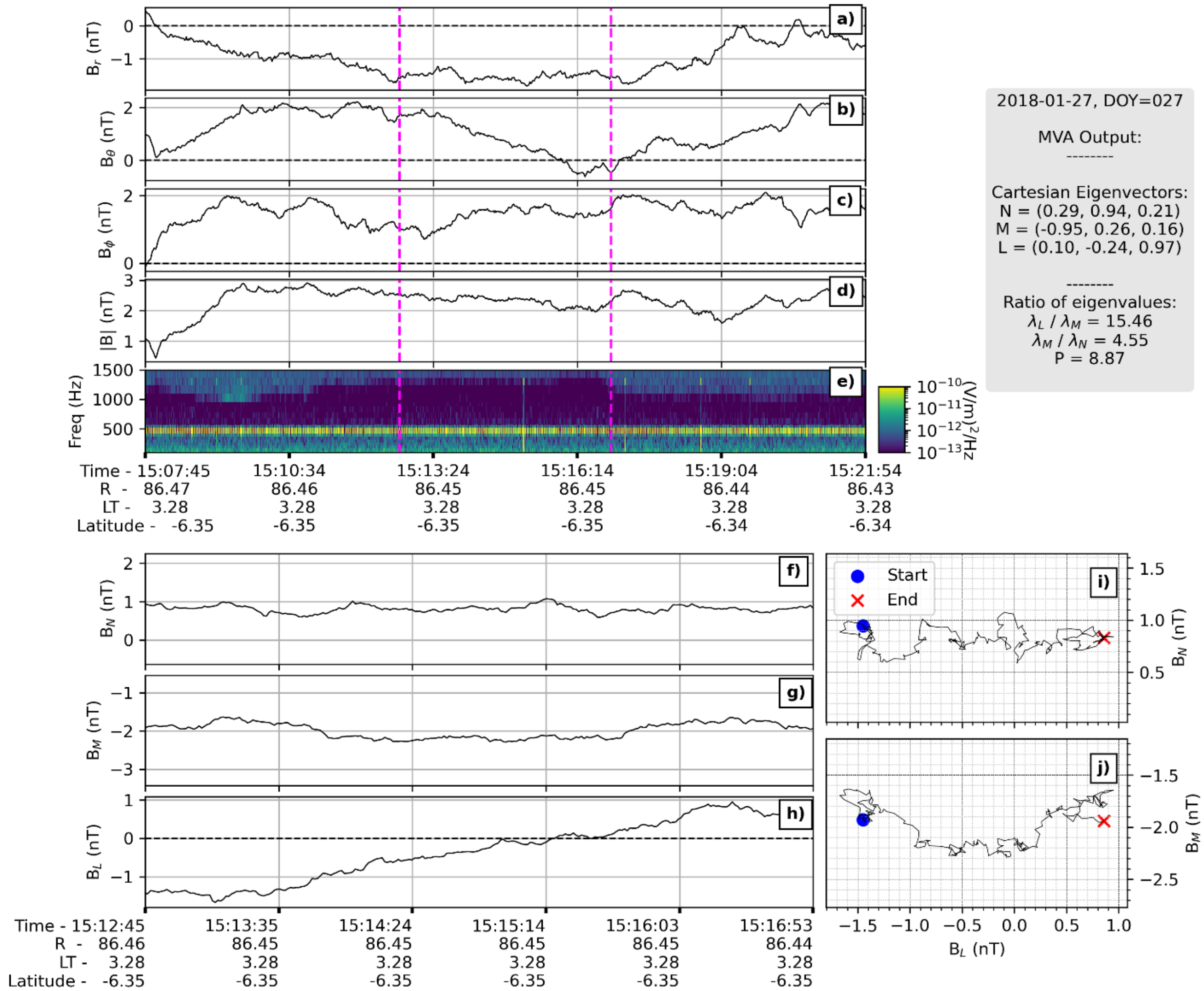

2018-01-27, DOY=027
MVA Output:

Cartesian Eigenvectors:
N = (0.29, 0.94, 0.21)
M = (-0.95, 0.26, 0.16)
L = (0.10, -0.24, 0.97)

Ratio of eigenvalues:
λL / λM = 15.46
λM / λN = 4.55
P = 8.87
Time - 15:07:45 15:10:34 15:13:24 15:16:14 15:19:04 15:21:54
R - 86.47 86.46 86.45 86.45 86.44 86.43
LT - 3.28 3.28 3.28 3.28 3.28 3.28
Latitude - -6.35 -6.35 -6.35 -6.35 -6.34 -6.34
Time - 15:12:45 15:13:35 15:14:24 15:15:14 15:16:03 15:16:53
R - 86.46 86.45 86.45 86.45 86.45 86.44
LT - 3.28 3.28 3.28 3.28 3.28 3.28
Latitude - -6.35 -6.35 -6.35 -6.35 -6.35 -6.35
Start
End

Figure S48

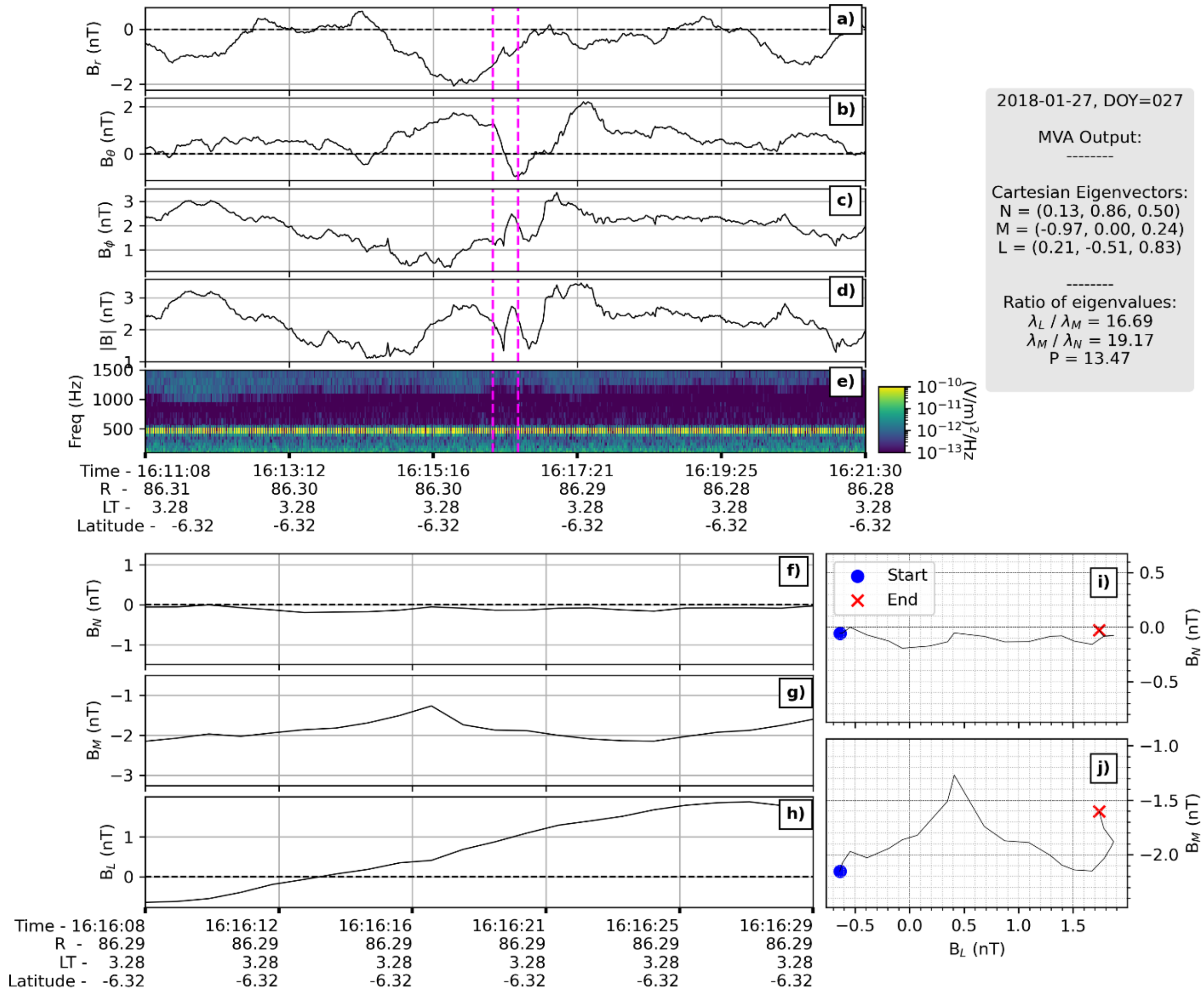
2018-01-27, DOY=027
MVA Output:

Cartesian Eigenvectors:
N = (0.13, 0.86, 0.50)
M = (-0.97, 0.00, 0.24)
L = (0.21, -0.51, 0.83)

Ratio of eigenvalues:
λ_L / λ_M = 16.69
λ_M / λ_N = 19.17
P = 13.47
Time - 16:11:08 16:13:12 16:15:16 16:17:21 16:19:25 16:21:30
R - 86.31 86.30 86.30 86.29 86.28 86.28
LT - 3.28 3.28 3.28 3.28 3.28 3.28
Latitude - -6.32 -6.32 -6.32 -6.32 -6.32 -6.32
Time - 16:16:08 16:16:12 16:16:16 16:16:21 16:16:25 16:16:29
R - 86.29 86.29 86.29 86.29 86.29 86.29
LT - 3.28 3.28 3.28 3.28 3.28 3.28
Latitude - -6.32 -6.32 -6.32 -6.32 -6.32 -6.32
Start
End
B_L (nT)

Figure S49

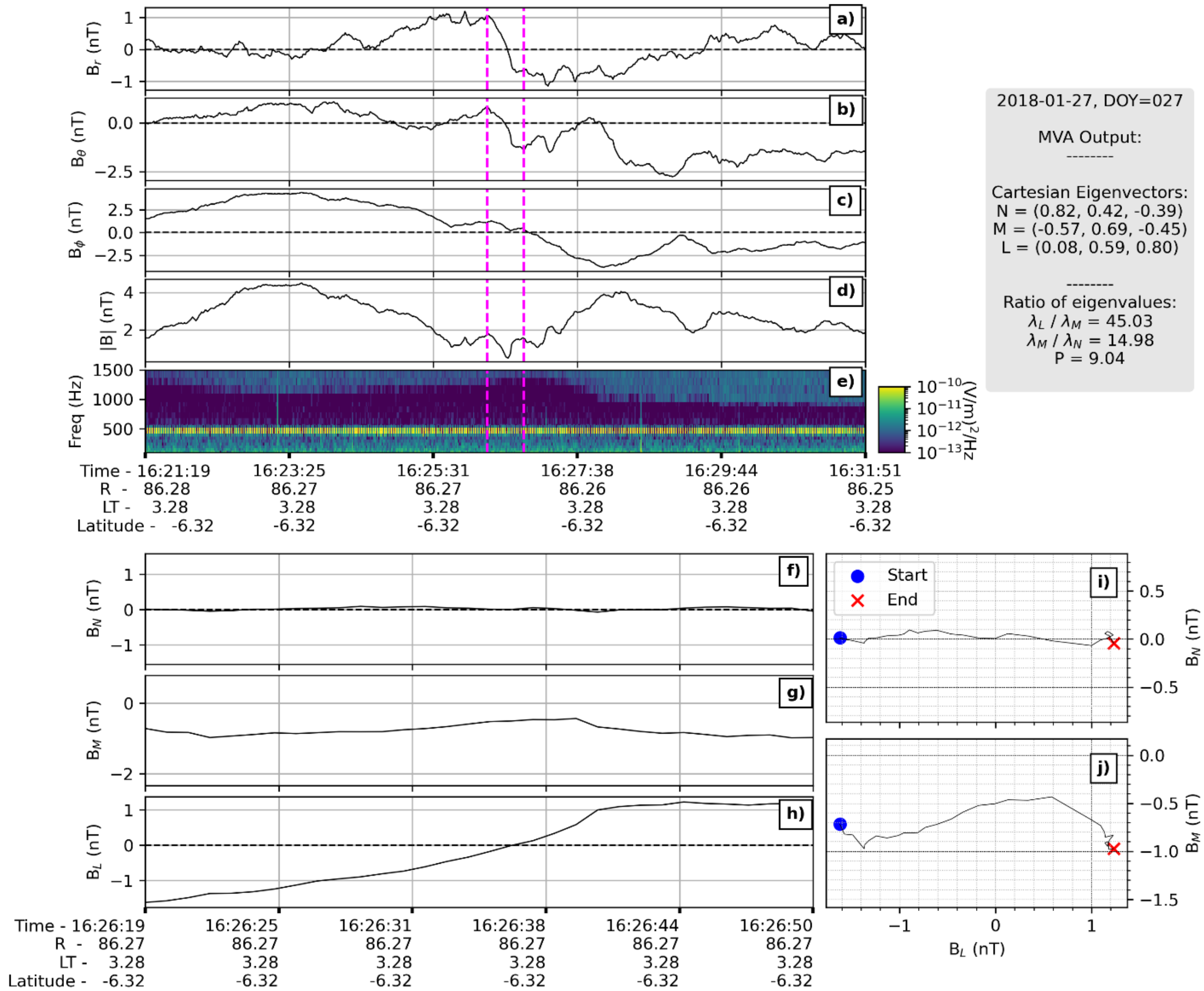
2018-01-27, DOY=027
MVA Output:
Cartesian Eigenvectors:
N = (0.82, 0.42, -0.39)
M = (-0.57, 0.69, -0.45)
L = (0.08, 0.59, 0.80)
Ratio of eigenvalues:
λL / λM = 45.03
λM / λN = 14.98
P = 9.04
Start
End
Time - 16:21:19 16:23:25 16:25:31 16:27:38 16:29:44 16:31:51
Time - 16:26:19 16:26:25 16:26:31 16:26:38 16:26:44 16:26:50
R - 86.28 86.27 86.27 86.26 86.26 86.25
LT - 3.28
Latitude - -6.32
Freq (Hz)
BL (nT)

Figure S50

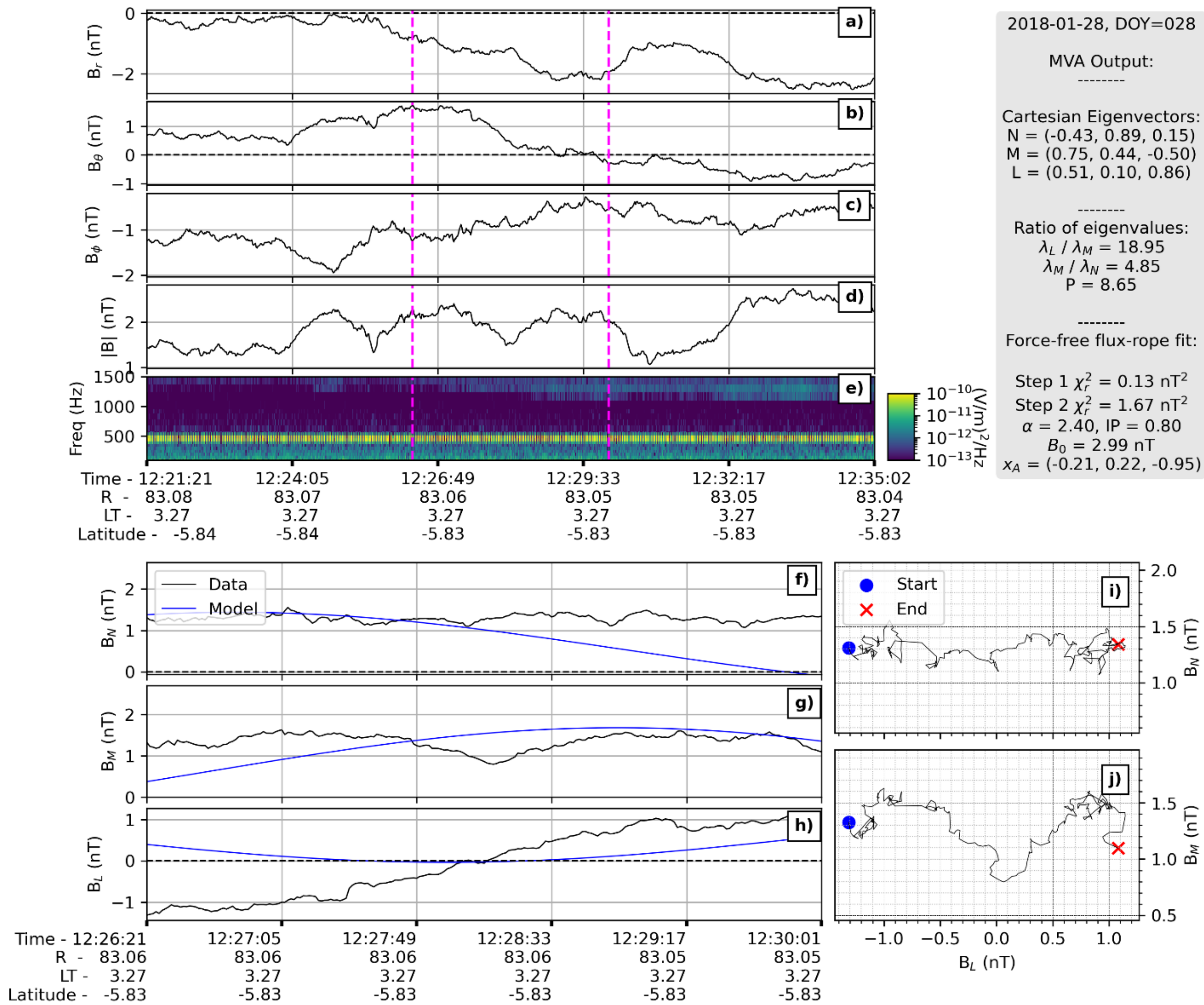

a)
b)
c)
d)
e)
f)
g)
h)
i)
j)
B_r (nT)
B_θ (nT)
B_ϕ (nT)
|B| (nT)
Freq (Hz)
(V/m)^2/Hz
Time - 12:21:21 12:24:05 12:26:49 12:29:33 12:32:17 12:35:02
R - 83.08 83.07 83.06 83.05 83.05 83.04
LT - 3.27 3.27 3.27 3.27 3.27 3.27
Latitude - -5.84 -5.84 -5.83 -5.83 -5.83 -5.83
2018-01-28, DOY=028
MVA Output:
Cartesian Eigenvectors:
N = (-0.43, 0.89, 0.15)
M = (0.75, 0.44, -0.50)
L = (0.51, 0.10, 0.86)
Ratio of eigenvalues:
λ_L / λ_M = 18.95
λ_M / λ_N = 4.85
P = 8.65
Force-free flux-rope fit:
Step 1 χ_r^2 = 0.13 nT^2
Step 2 χ_r^2 = 1.67 nT^2
α = 2.40, IP = 0.80
B_0 = 2.99 nT
x_A = (-0.21, 0.22, -0.95)
Data
Model
B_N (nT)
B_M (nT)
B_L (nT)
Start
End
Time - 12:26:21 12:27:05 12:27:49 12:28:33 12:29:17 12:30:01
R - 83.06 83.06 83.06 83.06 83.05 83.05
LT - 3.27 3.27 3.27 3.27 3.27 3.27
Latitude - -5.83 -5.83 -5.83 -5.83 -5.83 -5.83

Figure S51

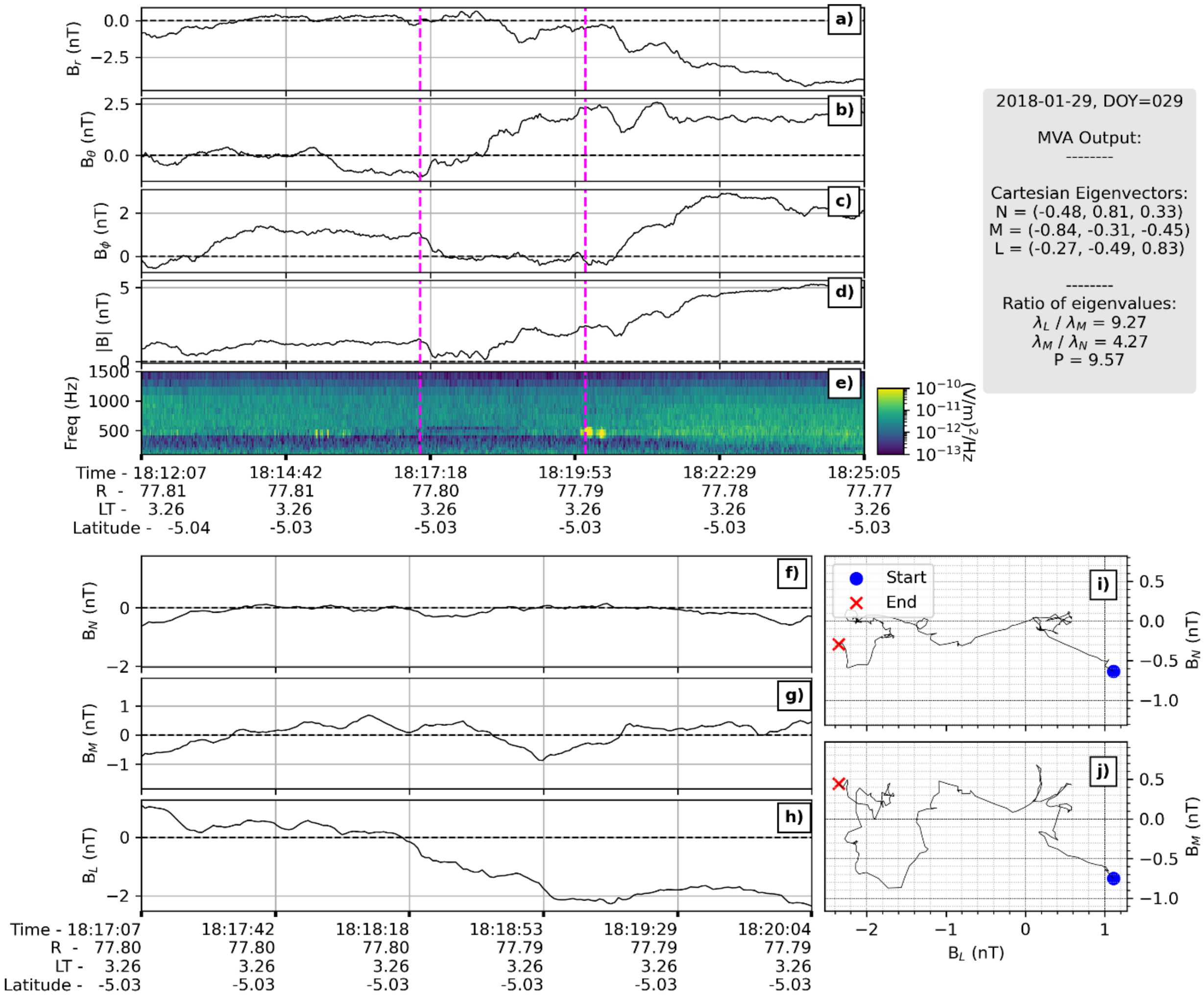

2018-01-29, DOY=029
MVA Output:

Cartesian Eigenvectors:
N = (-0.48, 0.81, 0.33)
M = (-0.84, -0.31, -0.45)
L = (-0.27, -0.49, 0.83)

Ratio of eigenvalues:
λ_L / λ_M = 9.27
λ_M / λ_N = 4.27
P = 9.57
Time - 18:12:07 18:14:42 18:17:18 18:19:53 18:22:29 18:25:05
R - 77.81 77.81 77.80 77.79 77.78 77.77
LT - 3.26 3.26 3.26 3.26 3.26 3.26
Latitude - -5.04 -5.03 -5.03 -5.03 -5.03 -5.03
Time - 18:17:07 18:17:42 18:18:18 18:18:53 18:19:29 18:20:04
R - 77.80 77.80 77.80 77.79 77.79 77.79
LT - 3.26 3.26 3.26 3.26 3.26 3.26
Latitude - -5.03 -5.03 -5.03 -5.03 -5.03 -5.03
Start
End

Figure S52

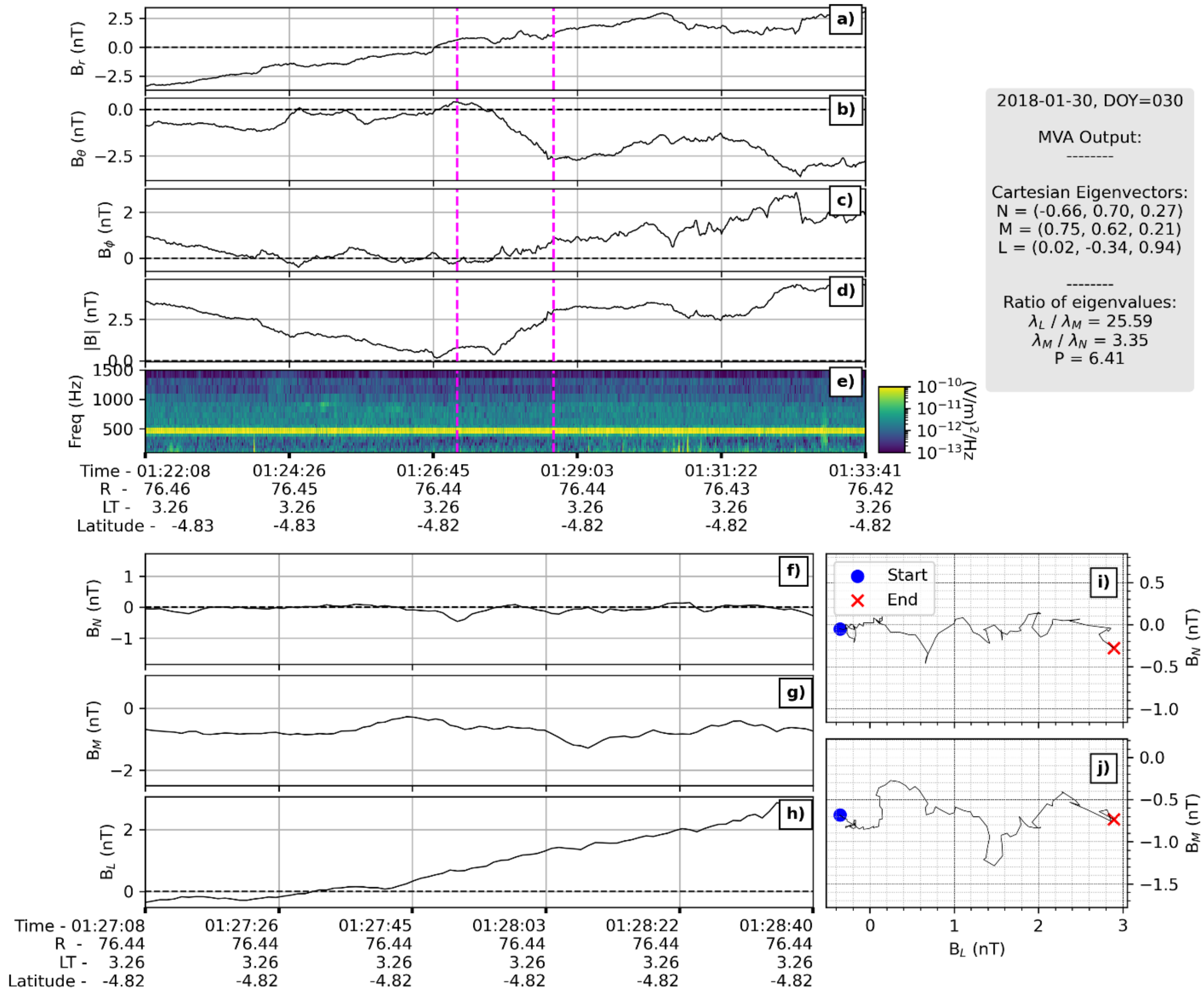
2018-01-30, DOY=030
MVA Output:
Cartesian Eigenvectors:
N = (-0.66, 0.70, 0.27)
M = (0.75, 0.62, 0.21)
L = (0.02, -0.34, 0.94)
Ratio of eigenvalues:
λ_L / λ_M = 25.59
λ_M / λ_N = 3.35
P = 6.41
Start
End
Time - 01:22:08
R - 76.46
LT - 3.26
Latitude - -4.83
Time - 01:27:08
R - 76.44
LT - 3.26
Latitude - -4.82

Figure S53

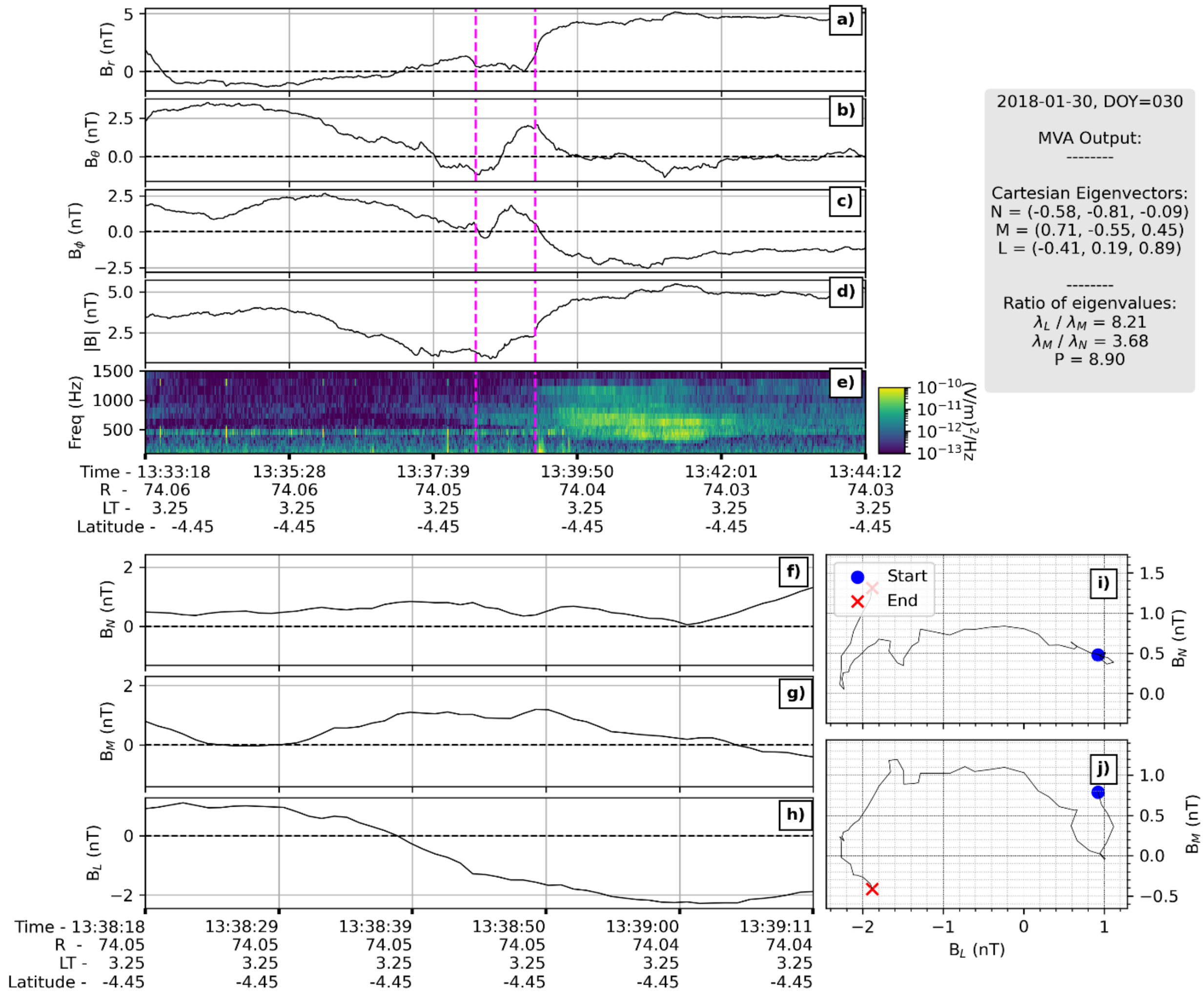
2018-01-30, DOY=030
MVA Output:

Cartesian Eigenvectors:
N = (-0.58, -0.81, -0.09)
M = (0.71, -0.55, 0.45)
L = (-0.41, 0.19, 0.89)

Ratio of eigenvalues:
λ_L / λ_M = 8.21
λ_M / λ_N = 3.68
P = 8.90
Time - 13:33:18 13:35:28 13:37:39 13:39:50 13:42:01 13:44:12
R - 74.06 74.06 74.05 74.04 74.03 74.03
LT - 3.25 3.25 3.25 3.25 3.25 3.25
Latitude - -4.45 -4.45 -4.45 -4.45 -4.45 -4.45
Time - 13:38:18 13:38:29 13:38:39 13:38:50 13:39:00 13:39:11
R - 74.05 74.05 74.05 74.05 74.04 74.04
LT - 3.25 3.25 3.25 3.25 3.25 3.25
Latitude - -4.45 -4.45 -4.45 -4.45 -4.45 -4.45
Start
End

Figure S54

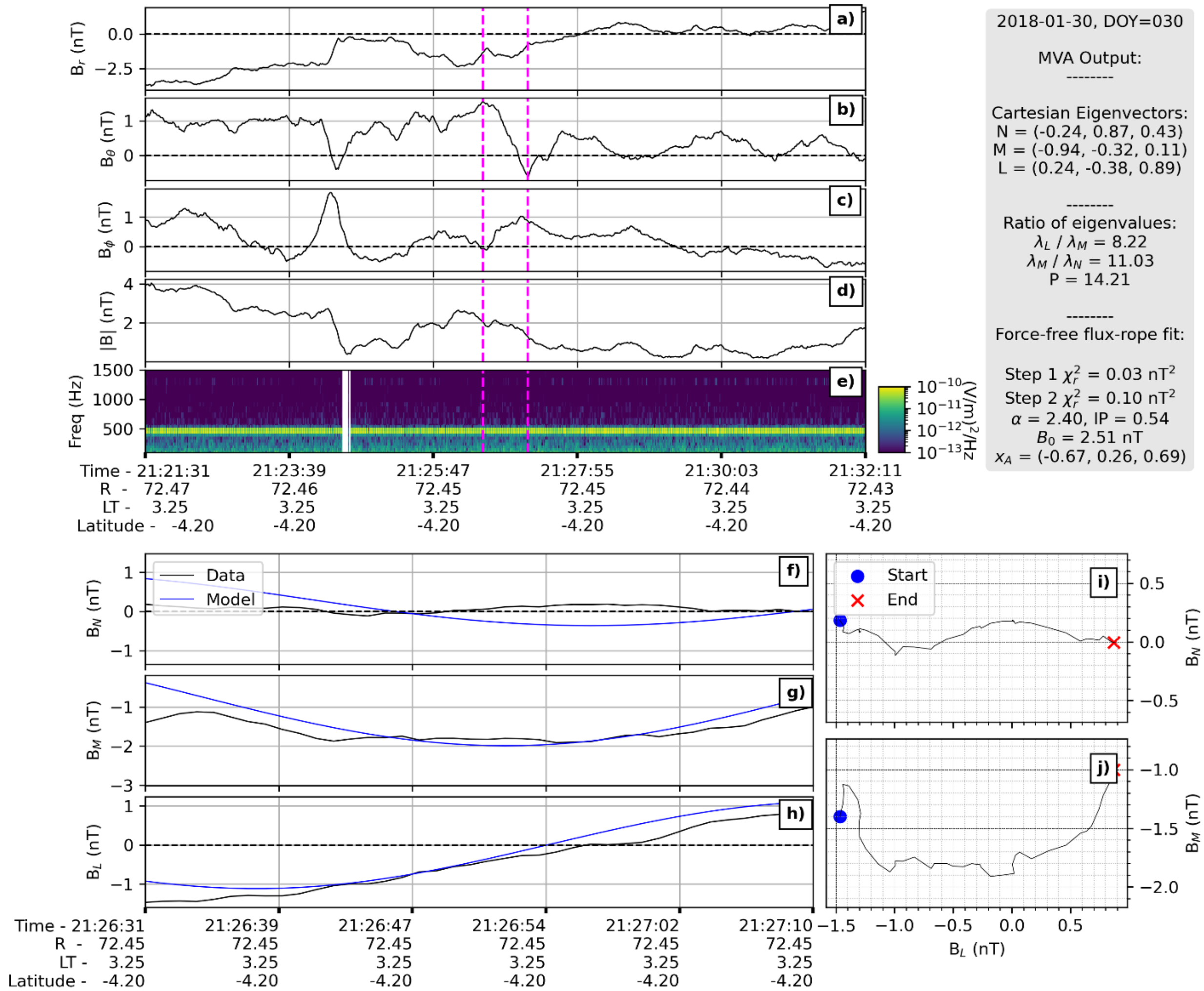

2018-01-30, DOY=030
MVA Output:
Cartesian Eigenvectors:
N = (-0.24, 0.87, 0.43)
M = (-0.94, -0.32, 0.11)
L = (0.24, -0.38, 0.89)
Ratio of eigenvalues:
λ_L / λ_M = 8.22
λ_M / λ_N = 11.03
P = 14.21
Force-free flux-rope fit:
Step 1 χ_r^2 = 0.03 nT^2
Step 2 χ_r^2 = 0.10 nT^2
α = 2.40, IP = 0.54
B_0 = 2.51 nT
x_A = (-0.67, 0.26, 0.69)
Time - 21:21:31 21:23:39 21:25:47 21:27:55 21:30:03 21:32:11
R - 72.47 72.46 72.45 72.45 72.44 72.43
LT - 3.25
Latitude - -4.20
Data
Model
Start
End
Time - 21:26:31 21:26:39 21:26:47 21:26:54 21:27:02 21:27:10
R - 72.45
B_L (nT)
B_N (nT)
B_M (nT)

Figure S55

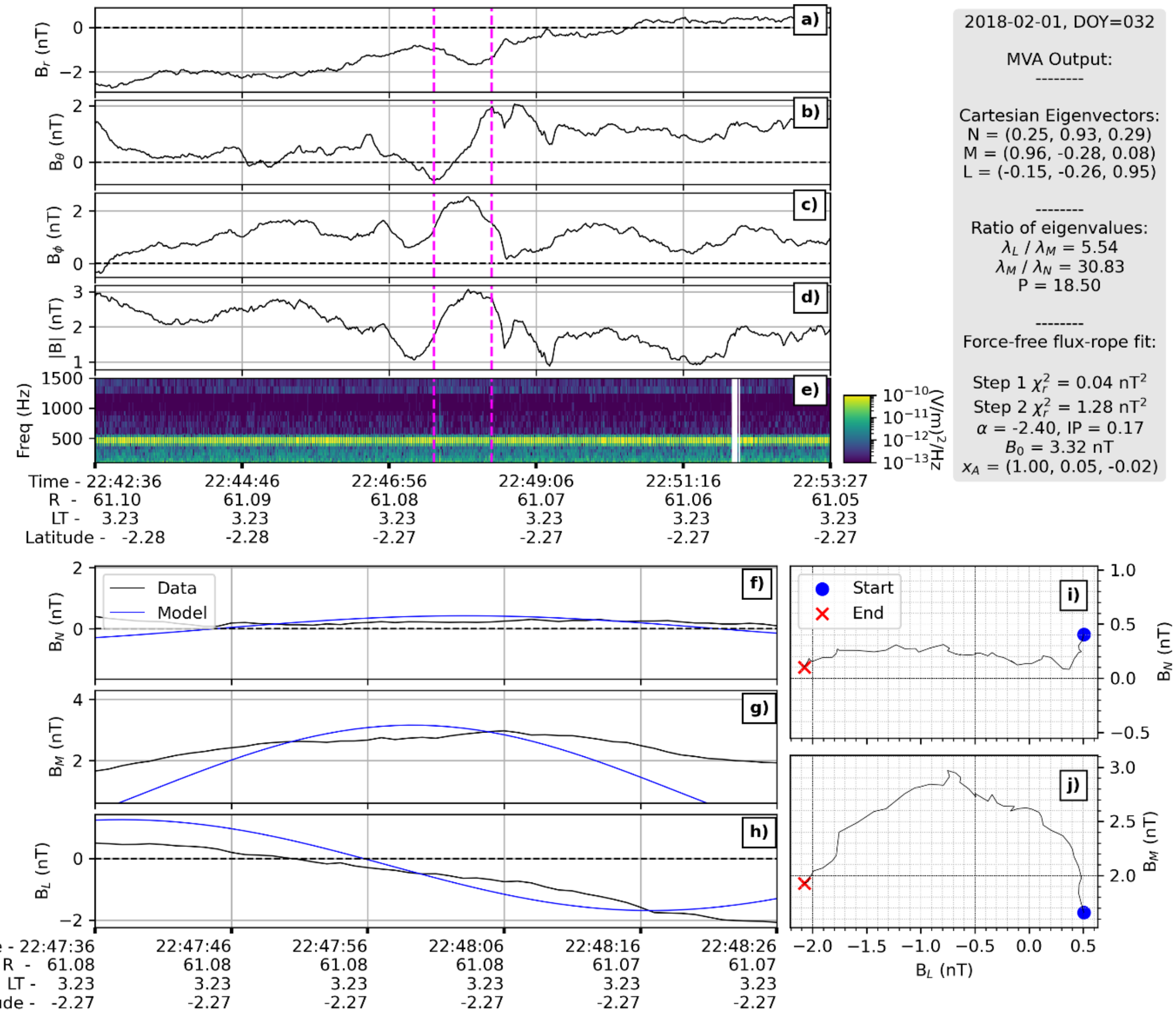

2018-02-01, DOY=032
MVA Output:
Cartesian Eigenvectors:
N = (0.25, 0.93, 0.29)
M = (0.96, -0.28, 0.08)
L = (-0.15, -0.26, 0.95)
Ratio of eigenvalues:
λ_L / λ_M = 5.54
λ_M / λ_N = 30.83
P = 18.50
Force-free flux-rope fit:
Step 1 χ_r^2 = 0.04 nT^2
Step 2 χ_r^2 = 1.28 nT^2
α = -2.40, IP = 0.17
B_0 = 3.32 nT
x_A = (1.00, 0.05, -0.02)
Time - 22:42:36 22:44:46 22:46:56 22:49:06 22:51:16 22:53:27
R - 61.10 61.09 61.08 61.07 61.06 61.05
LT - 3.23 3.23 3.23 3.23 3.23 3.23
Latitude - -2.28 -2.28 -2.27 -2.27 -2.27 -2.27
Data
Model
Start
End
Time - 22:47:36 22:47:46 22:47:56 22:48:06 22:48:16 22:48:26
R - 61.08 61.08 61.08 61.08 61.07 61.07
LT - 3.23 3.23 3.23 3.23 3.23 3.23
Latitude - -2.27 -2.27 -2.27 -2.27 -2.27 -2.27

Figure S56

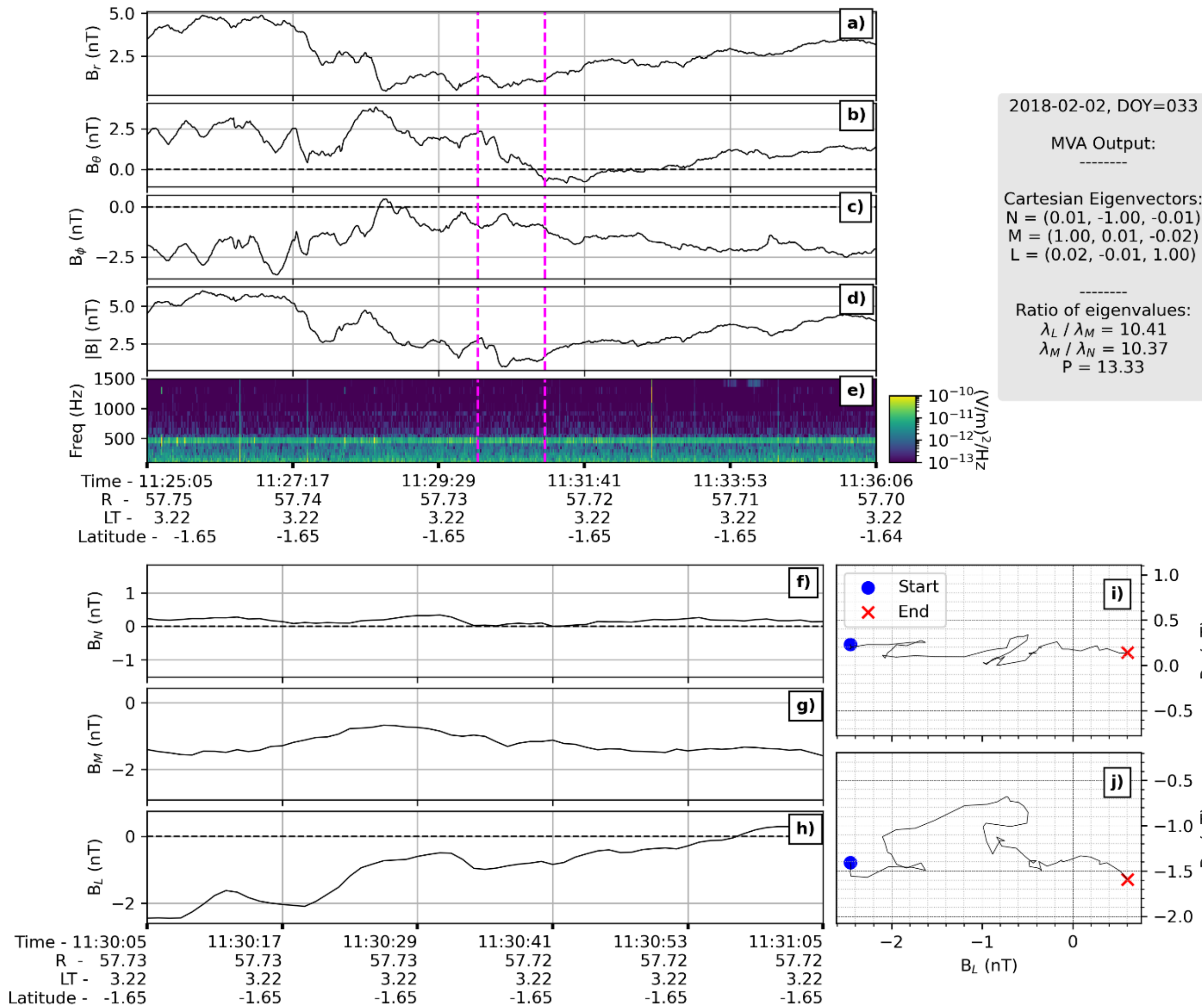
2018-02-02, DOY=033
MVA Output:
Cartesian Eigenvectors:
N = (0.01, -1.00, -0.01)
M = (1.00, 0.01, -0.02)
L = (0.02, -0.01, 1.00)
Ratio of eigenvalues:
λ_L / λ_M = 10.41
λ_M / λ_N = 10.37
P = 13.33
Time - 11:25:05 11:27:17 11:29:29 11:31:41 11:33:53 11:36:06
R - 57.75 57.74 57.73 57.72 57.71 57.70
LT - 3.22 3.22 3.22 3.22 3.22 3.22
Latitude - -1.65 -1.65 -1.65 -1.65 -1.65 -1.64
Time - 11:30:05 11:30:17 11:30:29 11:30:41 11:30:53 11:31:05
R - 57.73 57.73 57.73 57.72 57.72 57.72
LT - 3.22 3.22 3.22 3.22 3.22 3.22
Latitude - -1.65 -1.65 -1.65 -1.65 -1.65 -1.65
Start
End

Figure S57

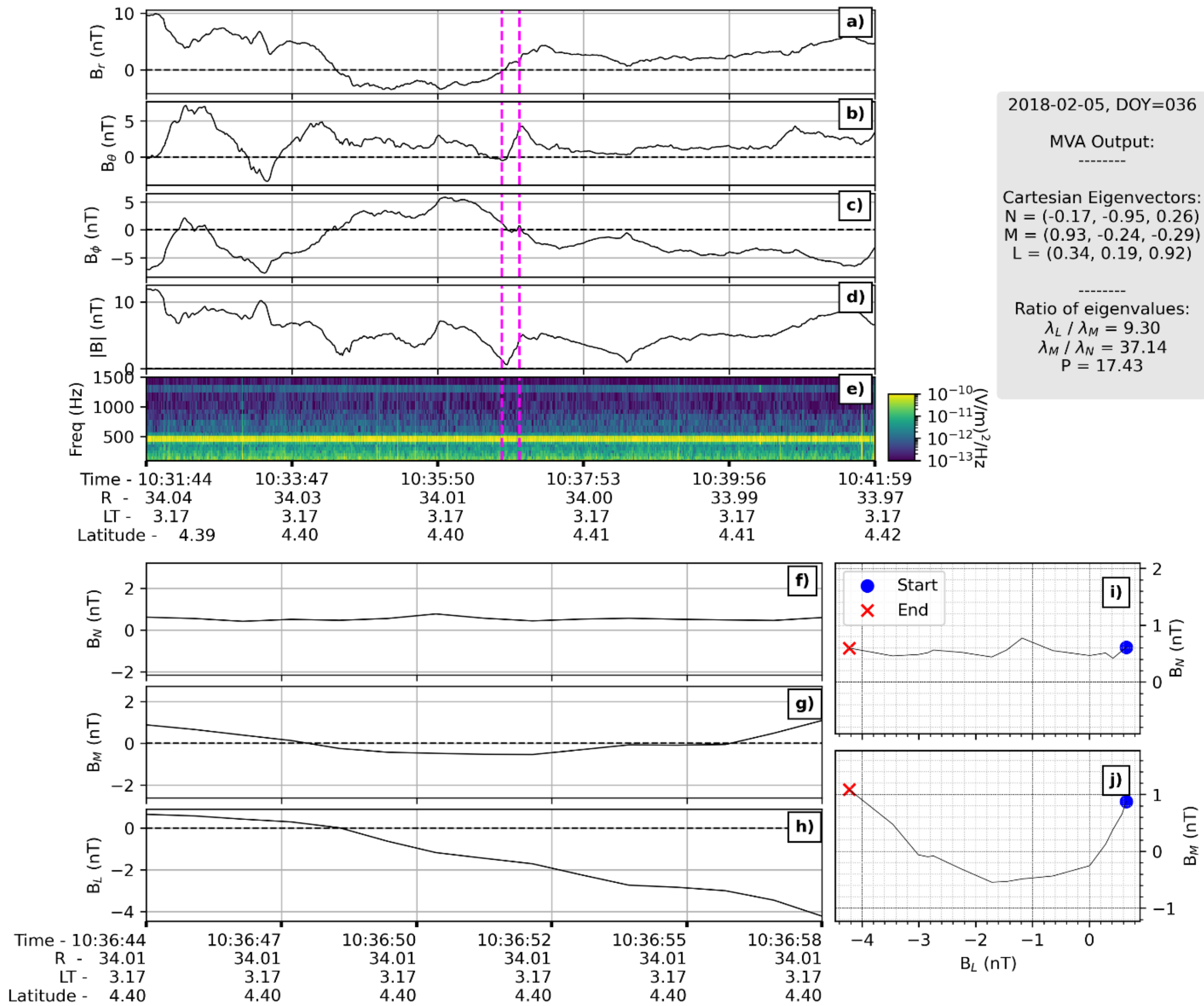
2018-02-05, DOY=036
MVA Output:

Cartesian Eigenvectors:
N = (-0.17, -0.95, 0.26)
M = (0.93, -0.24, -0.29)
L = (0.34, 0.19, 0.92)

Ratio of eigenvalues:
λL / λM = 9.30
λM / λN = 37.14
P = 17.43
Time - 10:31:44 10:33:47 10:35:50 10:37:53 10:39:56 10:41:59
R - 34.04 34.03 34.01 34.00 33.99 33.97
LT - 3.17 3.17 3.17 3.17 3.17 3.17
Latitude - 4.39 4.40 4.40 4.41 4.41 4.42
Time - 10:36:44 10:36:47 10:36:50 10:36:52 10:36:55 10:36:58
R - 34.01 34.01 34.01 34.01 34.01 34.01
LT - 3.17 3.17 3.17 3.17 3.17 3.17
Latitude - 4.40 4.40 4.40 4.40 4.40 4.40
Start
End

Figure S58

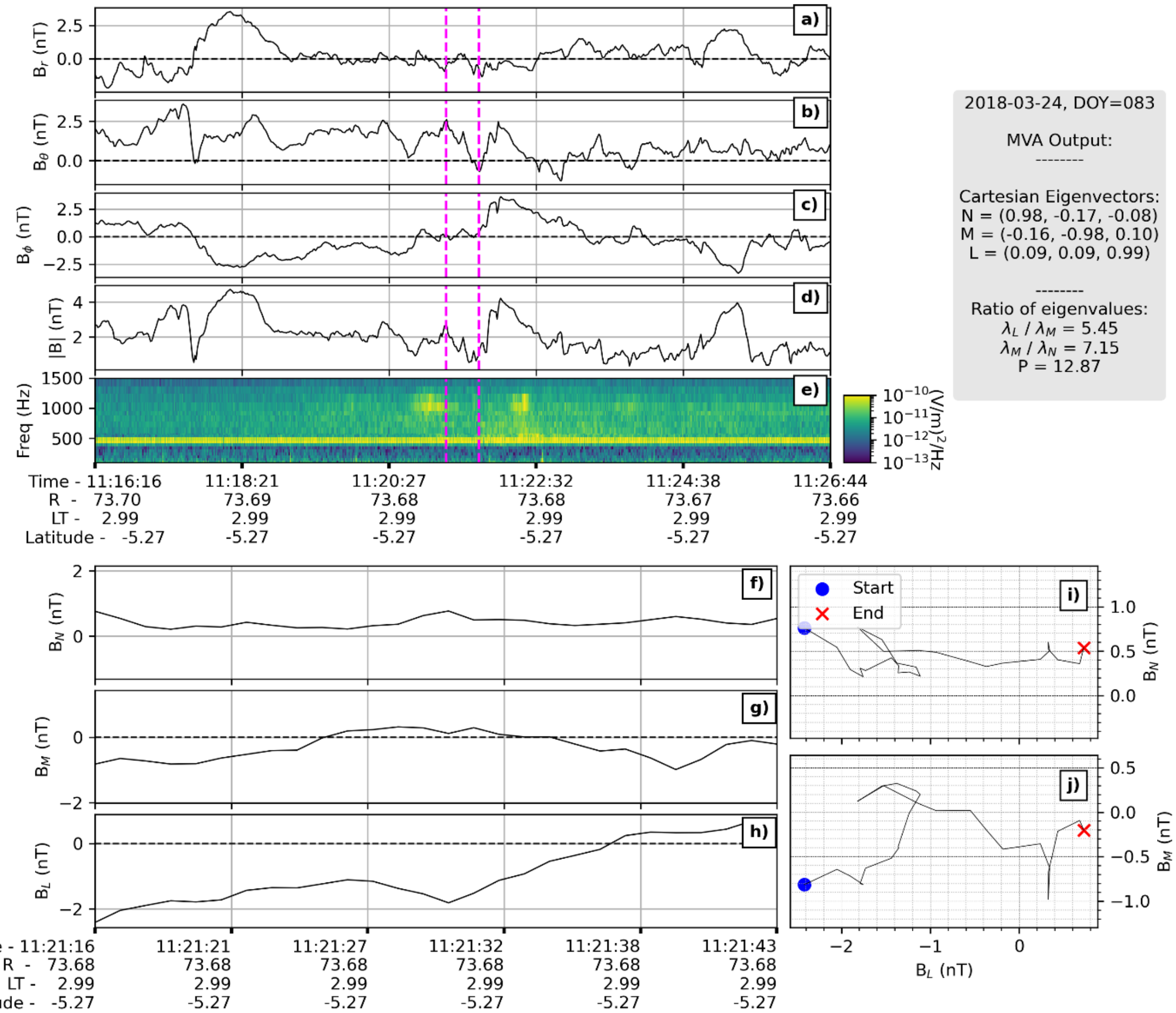

2018-03-24, DOY=083
MVA Output:

Cartesian Eigenvectors:
N = (0.98, -0.17, -0.08)
M = (-0.16, -0.98, 0.10)
L = (0.09, 0.09, 0.99)

Ratio of eigenvalues:
λ_L / λ_M = 5.45
λ_M / λ_N = 7.15
P = 12.87
Time - 11:16:16 11:18:21 11:20:27 11:22:32 11:24:38 11:26:44
R - 73.70 73.69 73.68 73.68 73.67 73.66
LT - 2.99 2.99 2.99 2.99 2.99 2.99
Latitude - -5.27 -5.27 -5.27 -5.27 -5.27 -5.27
Time - 11:21:16 11:21:21 11:21:27 11:21:32 11:21:38 11:21:43
R - 73.68 73.68 73.68 73.68 73.68 73.68
LT - 2.99 2.99 2.99 2.99 2.99 2.99
Latitude - -5.27 -5.27 -5.27 -5.27 -5.27 -5.27
Start
End

Figure S59

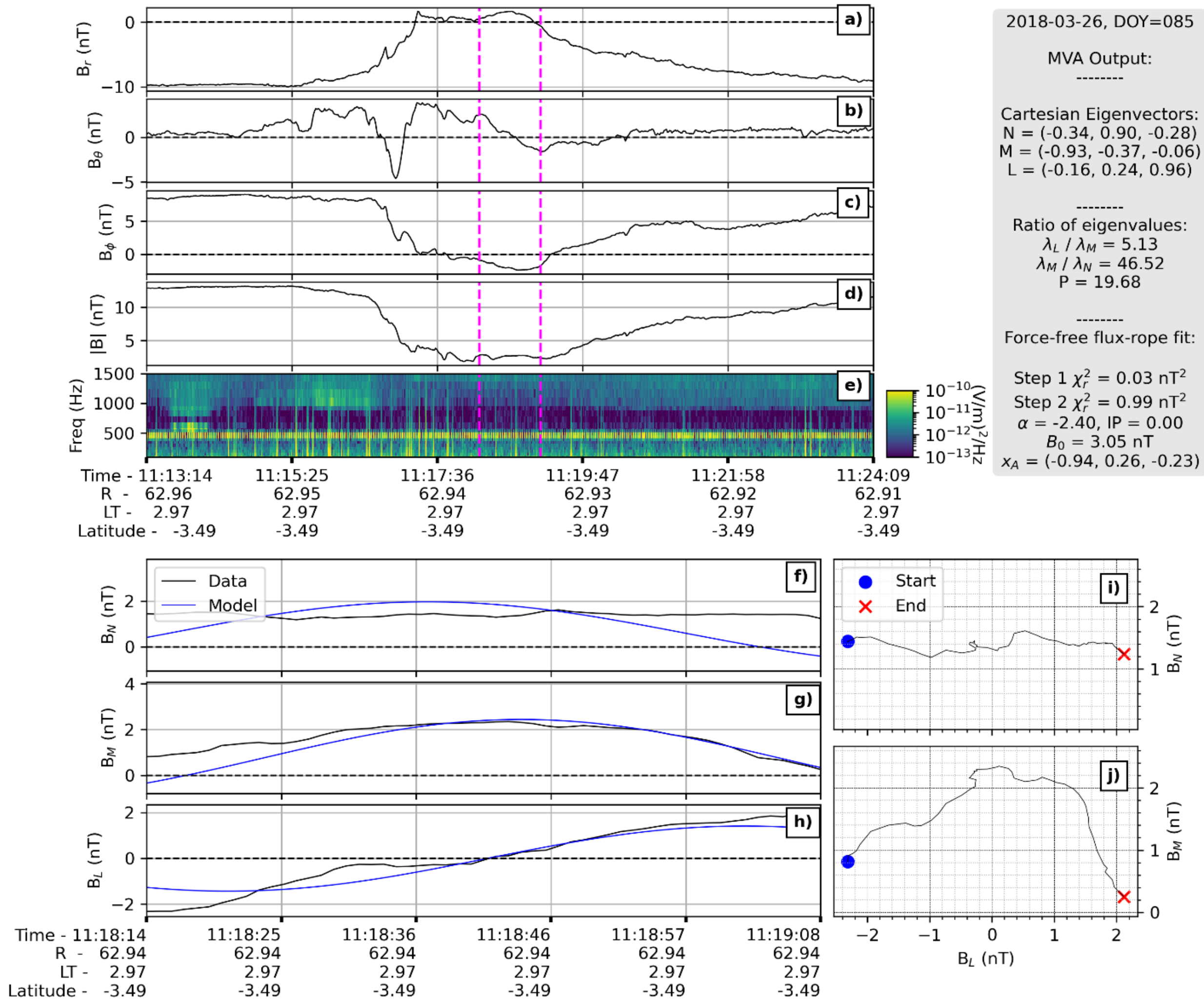

2018-03-26, DOY=085
MVA Output:

Cartesian Eigenvectors:
N = (-0.34, 0.90, -0.28)
M = (-0.93, -0.37, -0.06)
L = (-0.16, 0.24, 0.96)

Ratio of eigenvalues:
λ_L / λ_M = 5.13
λ_M / λ_N = 46.52
P = 19.68

Force-free flux-rope fit:
Step 1 χ_r^2 = 0.03 nT^2
Step 2 χ_r^2 = 0.99 nT^2
α = -2.40, IP = 0.00
B_0 = 3.05 nT
x_A = (-0.94, 0.26, -0.23)
Data
Model
Start
End

Figure S60

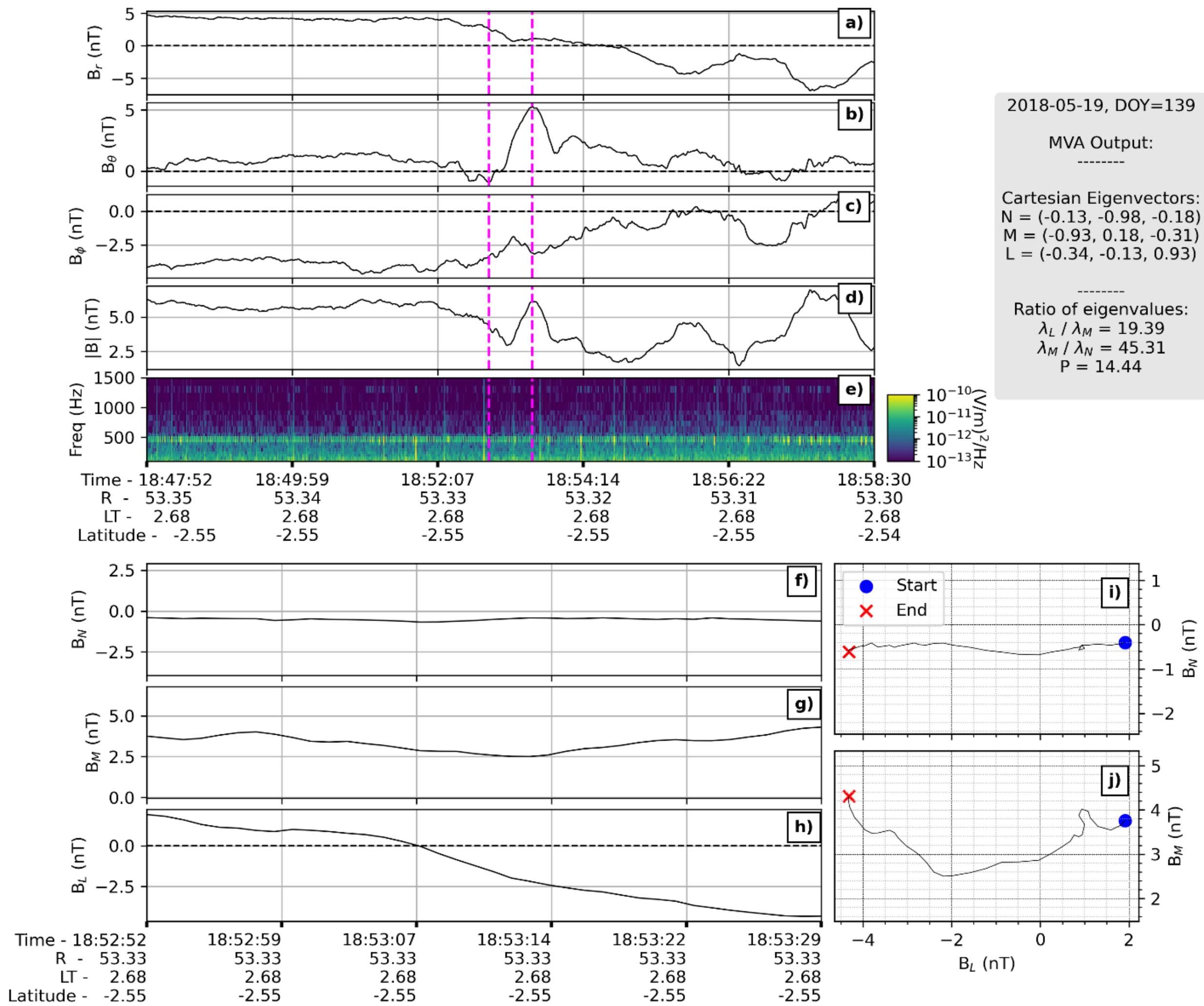
2018-05-19, DOY=139
MVA Output:

Cartesian Eigenvectors:
N = (-0.13, -0.98, -0.18)
M = (-0.93, 0.18, -0.31)
L = (-0.34, -0.13, 0.93)

Ratio of eigenvalues:
λ_L / λ_M = 19.39
λ_M / λ_N = 45.31
P = 14.44
Time - 18:47:52 18:49:59 18:52:07 18:54:14 18:56:22 18:58:30
R - 53.35 53.34 53.33 53.32 53.31 53.30
LT - 2.68 2.68 2.68 2.68 2.68 2.68
Latitude - -2.55 -2.55 -2.55 -2.55 -2.55 -2.54
Time - 18:52:52 18:52:59 18:53:07 18:53:14 18:53:22 18:53:29
R - 53.33 53.33 53.33 53.33 53.33 53.33
LT - 2.68 2.68 2.68 2.68 2.68 2.68
Latitude - -2.55 -2.55 -2.55 -2.55 -2.55 -2.55
Start
End

Figure S61

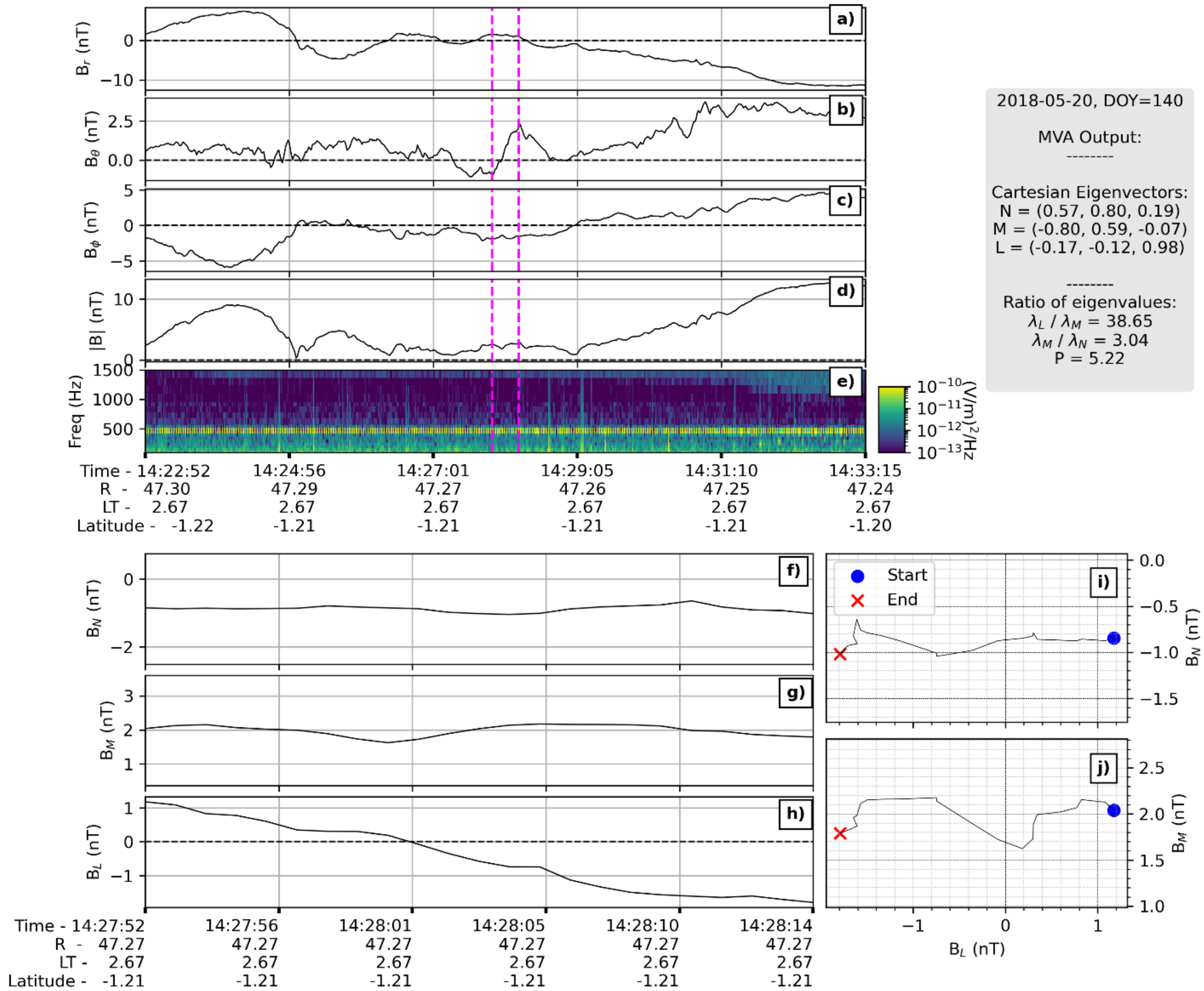
2018-05-20, DOY=140
MVA Output:
Cartesian Eigenvectors:
N = (0.57, 0.80, 0.19)
M = (-0.80, 0.59, -0.07)
L = (-0.17, -0.12, 0.98)
Ratio of eigenvalues:
λ_L / λ_M = 38.65
λ_M / λ_N = 3.04
P = 5.22
Time - 14:22:52 14:24:56 14:27:01 14:29:05 14:31:10 14:33:15
R - 47.30 47.29 47.27 47.26 47.25 47.24
LT - 2.67 2.67 2.67 2.67 2.67 2.67
Latitude - -1.22 -1.21 -1.21 -1.21 -1.21 -1.20
Time - 14:27:52 14:27:56 14:28:01 14:28:05 14:28:10 14:28:14
R - 47.27 47.27 47.27 47.27 47.27 47.27
LT - 2.67 2.67 2.67 2.67 2.67 2.67
Latitude - -1.21 -1.21 -1.21 -1.21 -1.21 -1.21
Start
End
B_L (nT)

Figure S62

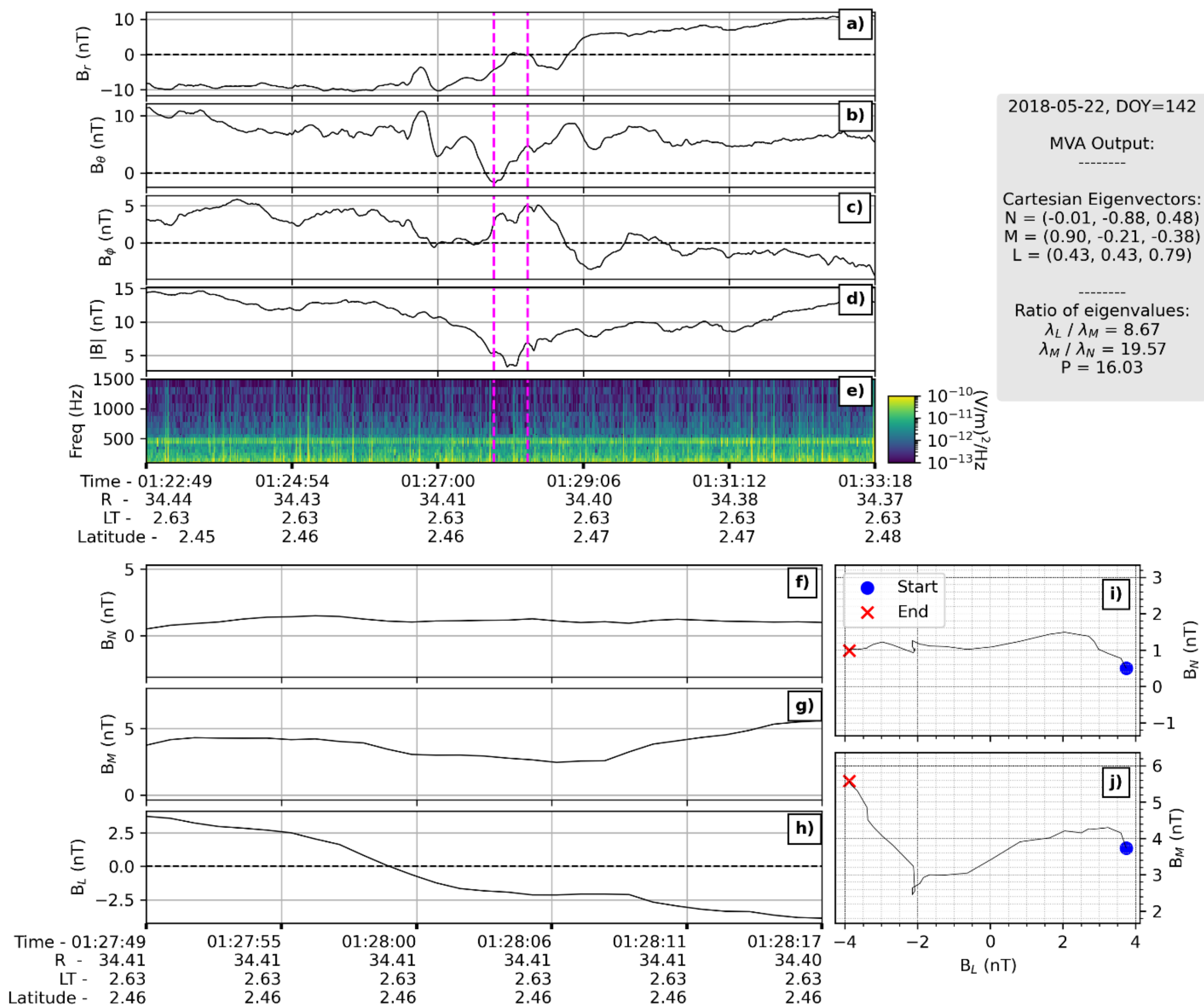
2018-05-22, DOY=142
MVA Output:

Cartesian Eigenvectors:
N = (-0.01, -0.88, 0.48)
M = (0.90, -0.21, -0.38)
L = (0.43, 0.43, 0.79)

Ratio of eigenvalues:
λL / λM = 8.67
λM / λN = 19.57
P = 16.03
Time - 01:22:49 01:24:54 01:27:00 01:29:06 01:31:12 01:33:18
R - 34.44 34.43 34.41 34.40 34.38 34.37
LT - 2.63 2.63 2.63 2.63 2.63 2.63
Latitude - 2.45 2.46 2.46 2.47 2.47 2.48
Time - 01:27:49 01:27:55 01:28:00 01:28:06 01:28:11 01:28:17
R - 34.41 34.41 34.41 34.41 34.41 34.40
LT - 2.63 2.63 2.63 2.63 2.63 2.63
Latitude - 2.46 2.46 2.46 2.46 2.46 2.46
Start
End

Figure S63

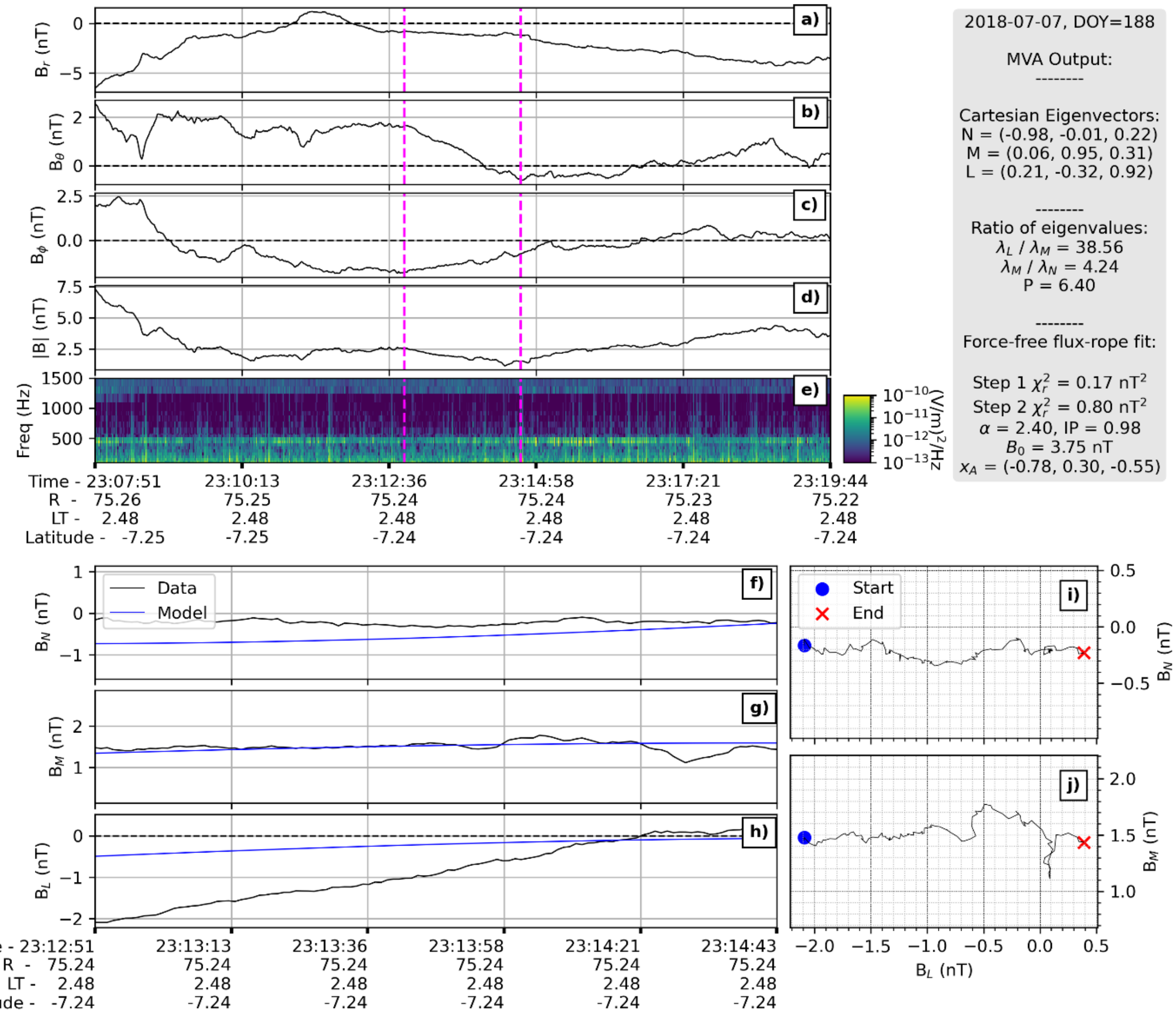
2018-07-07, DOY=188
MVA Output:
Cartesian Eigenvectors:
N = (-0.98, -0.01, 0.22)
M = (0.06, 0.95, 0.31)
L = (0.21, -0.32, 0.92)
Ratio of eigenvalues:
λ_L / λ_M = 38.56
λ_M / λ_N = 4.24
P = 6.40
Force-free flux-rope fit:
Step 1 χ_r^2 = 0.17 nT^2
Step 2 χ_r^2 = 0.80 nT^2
α = 2.40, IP = 0.98
B_0 = 3.75 nT
x_A = (-0.78, 0.30, -0.55)
Time - 23:07:51 23:10:13 23:12:36 23:14:58 23:17:21 23:19:44
R - 75.26 75.25 75.24 75.24 75.23 75.22
LT - 2.48 2.48 2.48 2.48 2.48 2.48
Latitude - -7.25 -7.25 -7.24 -7.24 -7.24 -7.24
Data
Model
Start
End
Time - 23:12:51 23:13:13 23:13:36 23:13:58 23:14:21 23:14:43
R - 75.24 75.24 75.24 75.24 75.24 75.24
LT - 2.48 2.48 2.48 2.48 2.48 2.48
Latitude - -7.24 -7.24 -7.24 -7.24 -7.24 -7.24

Figure S64

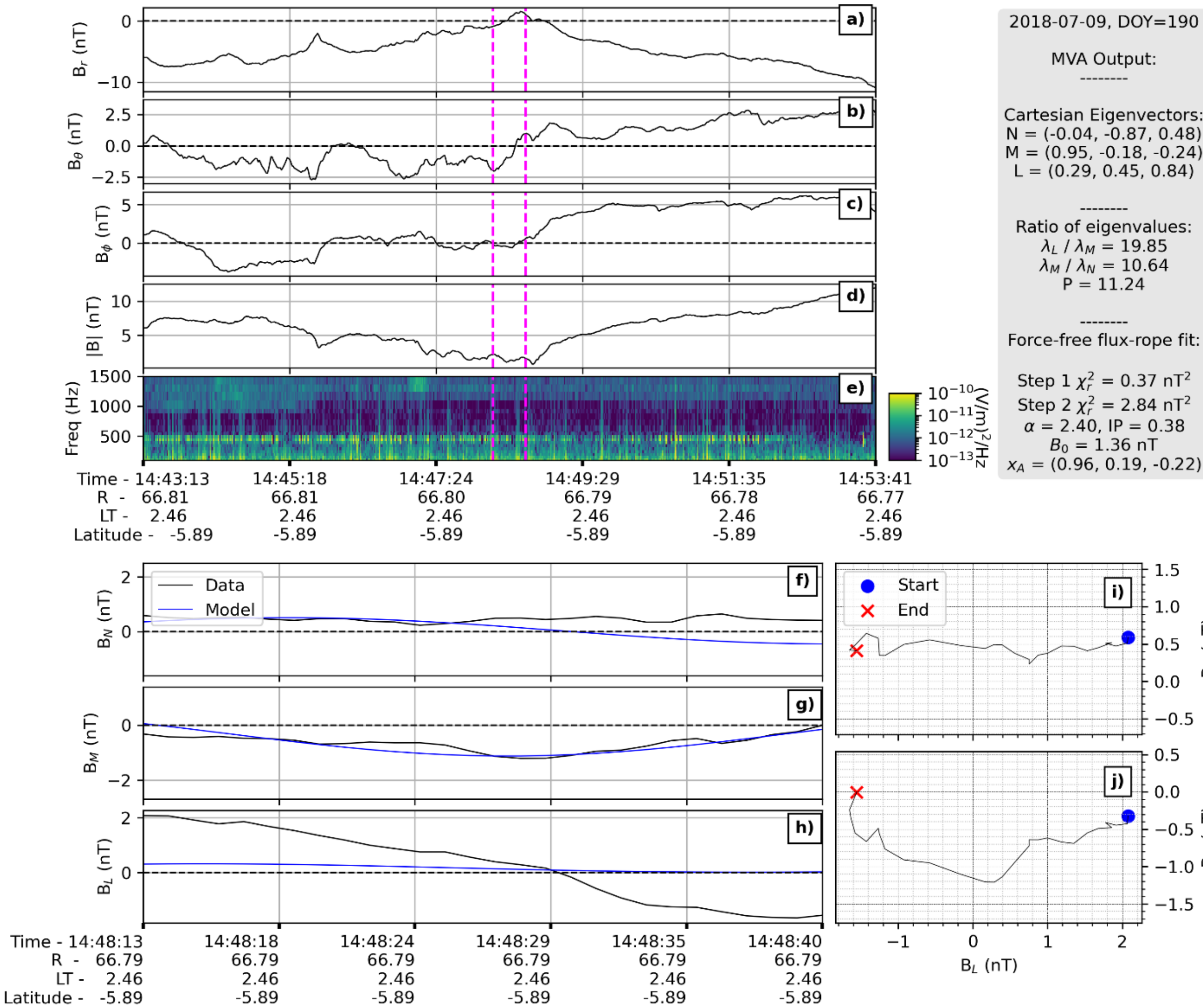

2018-07-09, DOY=190
MVA Output:
Cartesian Eigenvectors:
N = (-0.04, -0.87, 0.48)
M = (0.95, -0.18, -0.24)
L = (0.29, 0.45, 0.84)
Ratio of eigenvalues:
λ_L / λ_M = 19.85
λ_M / λ_N = 10.64
P = 11.24
Force-free flux-rope fit:
Step 1 χ_r^2 = 0.37 nT^2
Step 2 χ_r^2 = 2.84 nT^2
α = 2.40, IP = 0.38
B_0 = 1.36 nT
x_A = (0.96, 0.19, -0.22)
Time - 14:43:13 14:45:18 14:47:24 14:49:29 14:51:35 14:53:41
R - 66.81 66.81 66.80 66.79 66.78 66.77
LT - 2.46 2.46 2.46 2.46 2.46 2.46
Latitude - -5.89 -5.89 -5.89 -5.89 -5.89 -5.89
Data
Model
Start
End
Time - 14:48:13 14:48:18 14:48:24 14:48:29 14:48:35 14:48:40
R - 66.79 66.79 66.79 66.79 66.79 66.79
LT - 2.46 2.46 2.46 2.46 2.46 2.46
Latitude - -5.89 -5.89 -5.89 -5.89 -5.89 -5.89

Figure S65

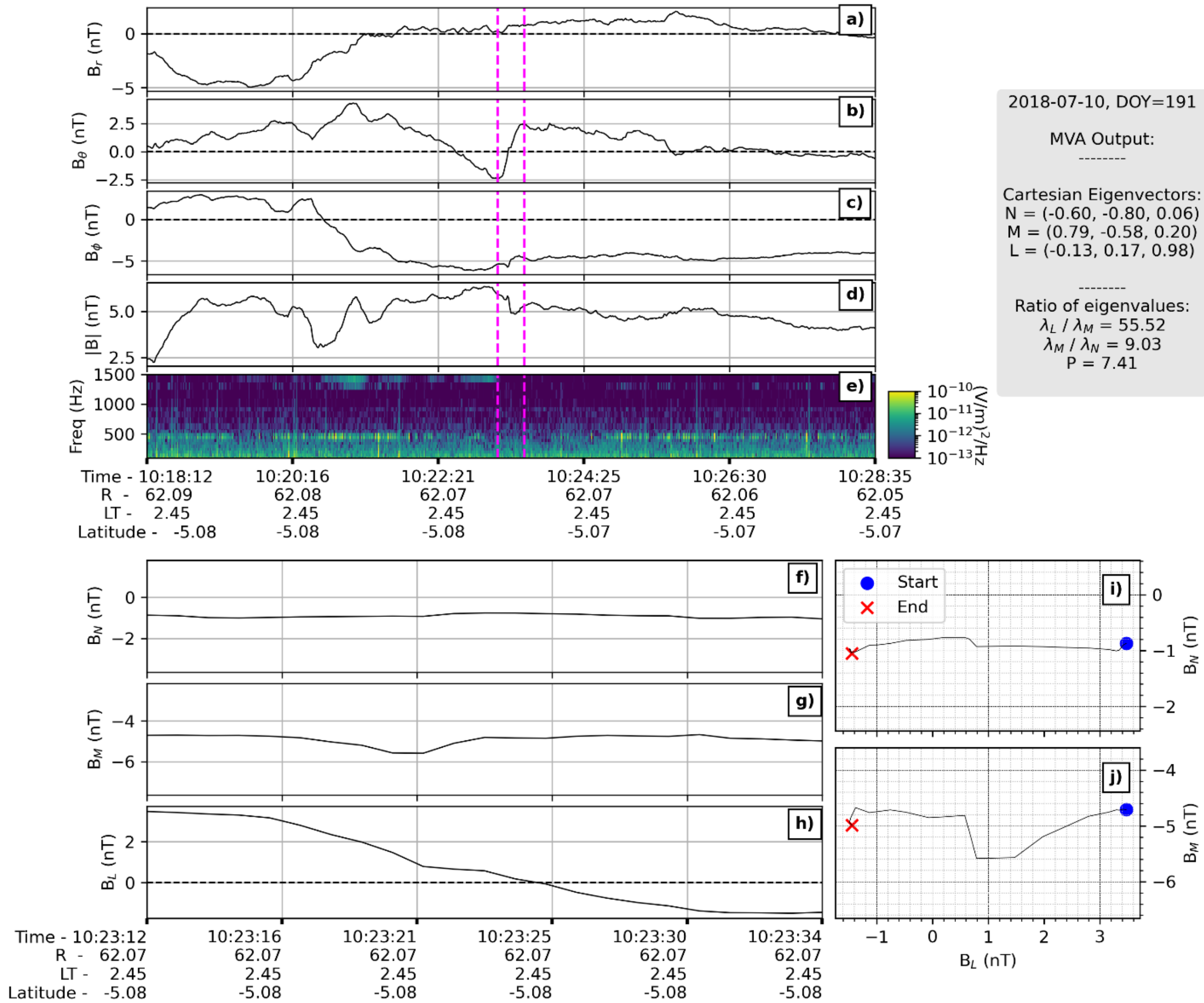

2018-07-10, DOY=191
MVA Output:
Cartesian Eigenvectors:
N = (-0.60, -0.80, 0.06)
M = (0.79, -0.58, 0.20)
L = (-0.13, 0.17, 0.98)
Ratio of eigenvalues:
λ_L / λ_M = 55.52
λ_M / λ_N = 9.03
P = 7.41
Time - 10:18:12 10:20:16 10:22:21 10:24:25 10:26:30 10:28:35
R - 62.09 62.08 62.07 62.07 62.06 62.05
LT - 2.45 2.45 2.45 2.45 2.45 2.45
Latitude - -5.08 -5.08 -5.08 -5.07 -5.07 -5.07
Time - 10:23:12 10:23:16 10:23:21 10:23:25 10:23:30 10:23:34
R - 62.07 62.07 62.07 62.07 62.07 62.07
LT - 2.45 2.45 2.45 2.45 2.45 2.45
Latitude - -5.08 -5.08 -5.08 -5.08 -5.08 -5.08
Start
End

Figure S66

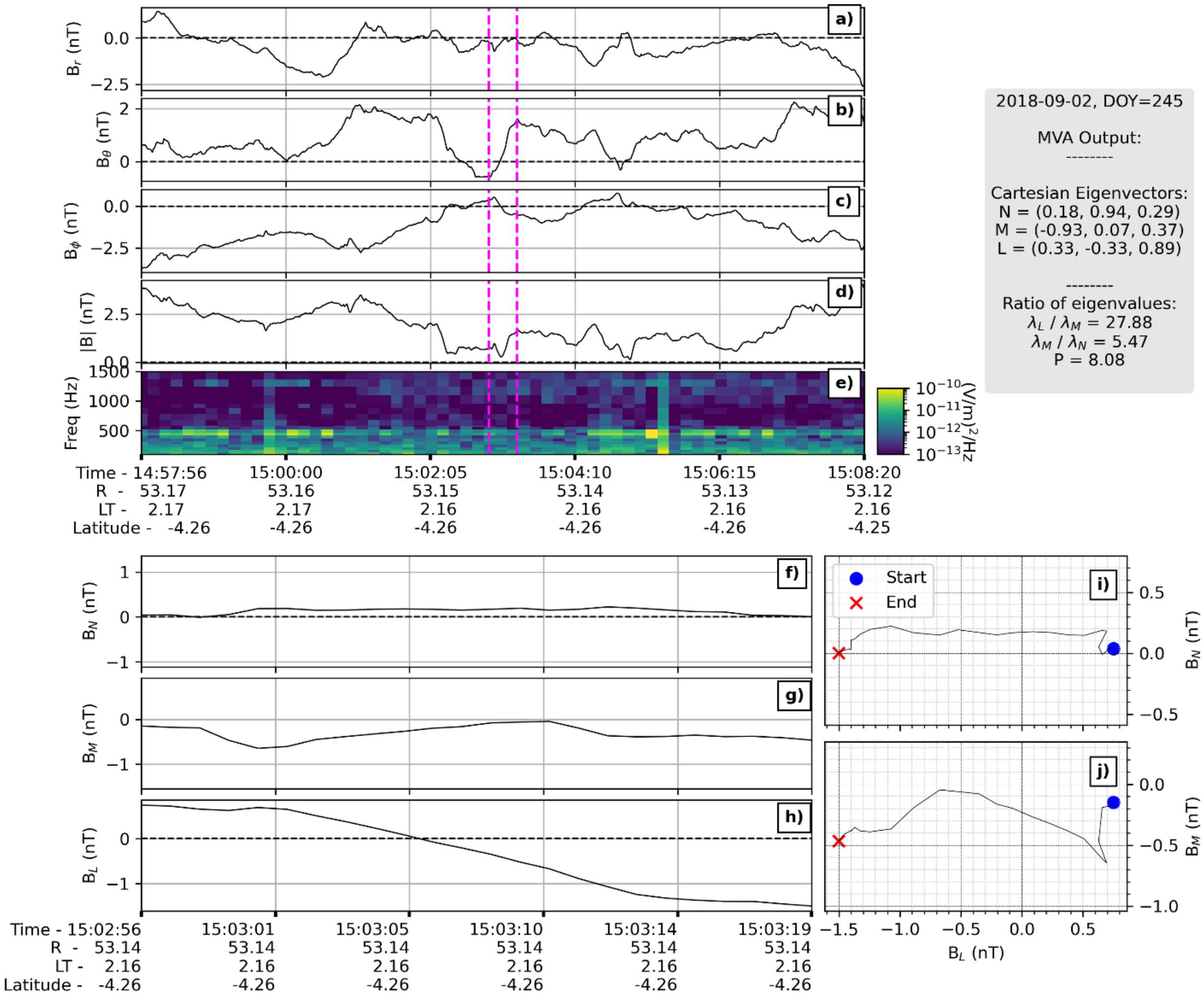
2018-09-02, DOY=245
MVA Output:
Cartesian Eigenvectors:
N = (0.18, 0.94, 0.29)
M = (-0.93, 0.07, 0.37)
L = (0.33, -0.33, 0.89)
Ratio of eigenvalues:
λ_L / λ_M = 27.88
λ_M / λ_N = 5.47
P = 8.08
Time - 14:57:56 15:00:00 15:02:05 15:04:10 15:06:15 15:08:20
R - 53.17 53.16 53.15 53.14 53.13 53.12
LT - 2.17 2.17 2.16 2.16 2.16 2.16
Latitude - -4.26 -4.26 -4.26 -4.26 -4.26 -4.25
Time - 15:02:56 15:03:01 15:03:05 15:03:10 15:03:14 15:03:19
R - 53.14 53.14 53.14 53.14 53.14 53.14
LT - 2.16 2.16 2.16 2.16 2.16 2.16
Latitude - -4.26 -4.26 -4.26 -4.26 -4.26 -4.26
Start
End

Figure S67

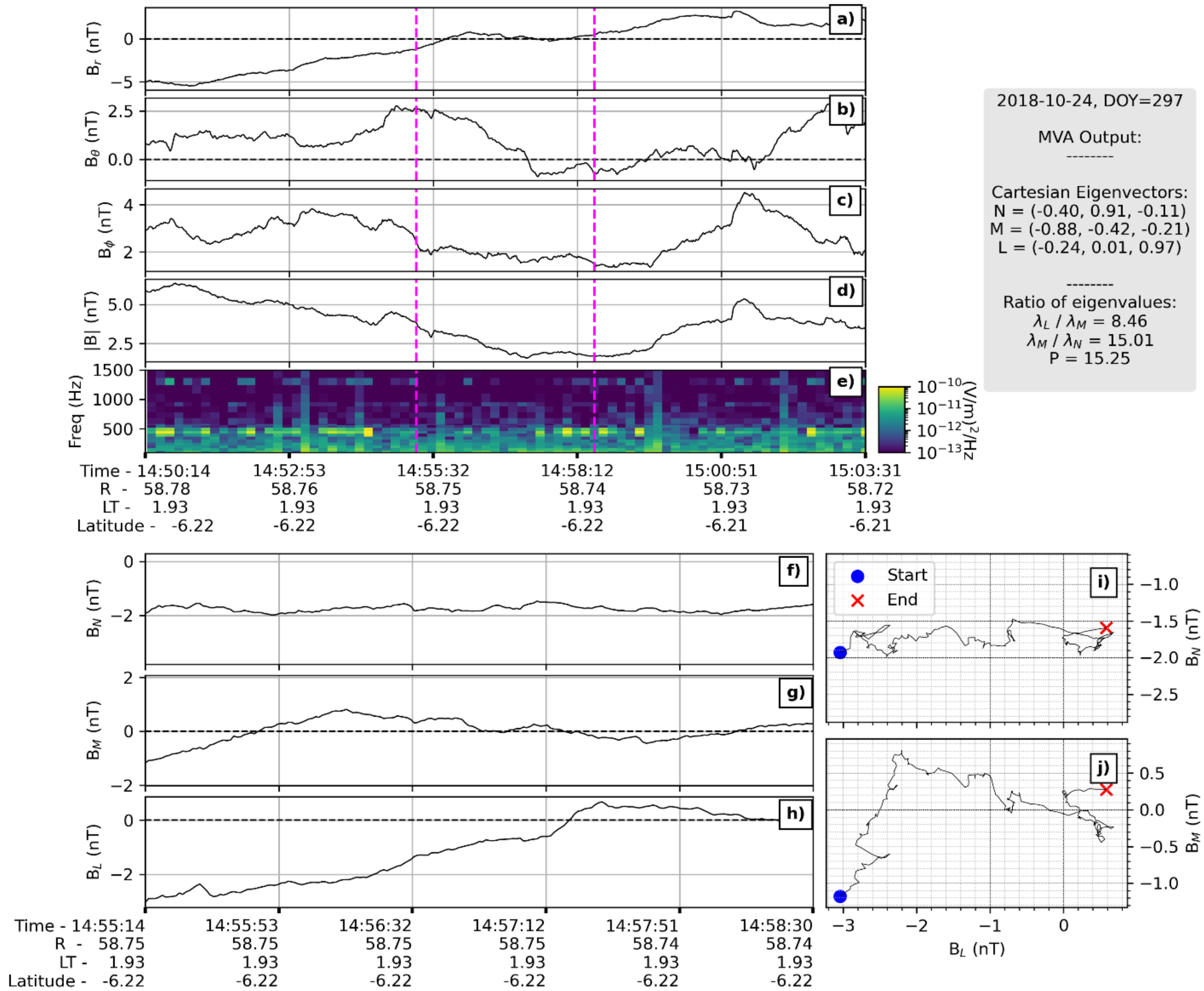
2018-10-24, DOY=297
MVA Output:
Cartesian Eigenvectors:
N = (-0.40, 0.91, -0.11)
M = (-0.88, -0.42, -0.21)
L = (-0.24, 0.01, 0.97)
Ratio of eigenvalues:
λL / λM = 8.46
λM / λN = 15.01
P = 15.25
Time - 14:50:14 14:52:53 14:55:32 14:58:12 15:00:51 15:03:31
Time - 14:55:14 14:55:53 14:56:32 14:57:12 14:57:51 14:58:30
Start
End

Figure S68

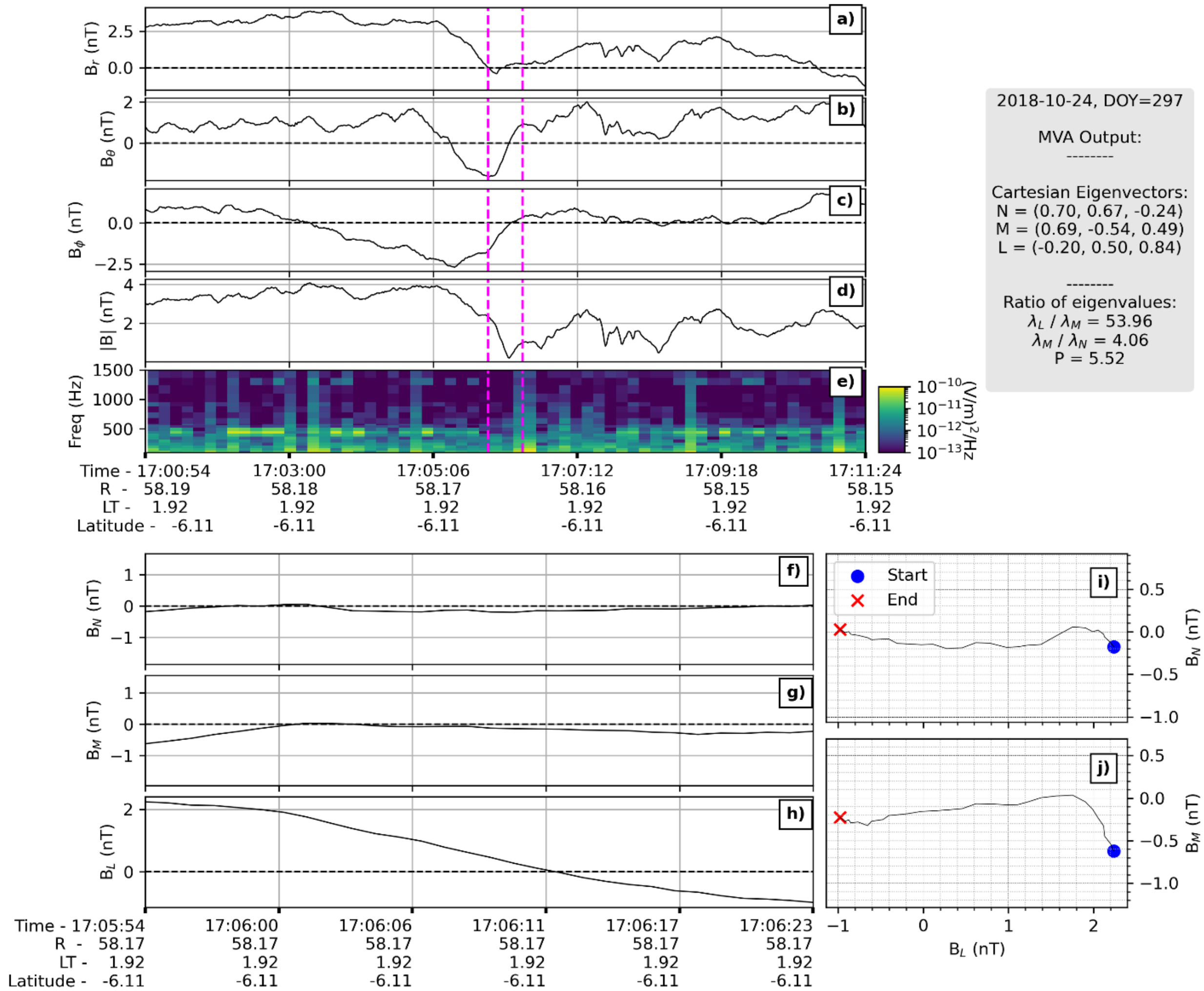

2018-10-24, DOY=297
MVA Output:
Cartesian Eigenvectors:
N = (0.70, 0.67, -0.24)
M = (0.69, -0.54, 0.49)
L = (-0.20, 0.50, 0.84)
Ratio of eigenvalues:
λL / λM = 53.96
λM / λN = 4.06
P = 5.52
Time - 17:00:54 17:03:00 17:05:06 17:07:12 17:09:18 17:11:24
R - 58.19 58.18 58.17 58.16 58.15 58.15
LT - 1.92 1.92 1.92 1.92 1.92 1.92
Latitude - -6.11 -6.11 -6.11 -6.11 -6.11 -6.11
Start
End
Time - 17:05:54 17:06:00 17:06:06 17:06:11 17:06:17 17:06:23
R - 58.17 58.17 58.17 58.17 58.17 58.17
LT - 1.92 1.92 1.92 1.92 1.92 1.92
Latitude - -6.11 -6.11 -6.11 -6.11 -6.11 -6.11

Figure S69

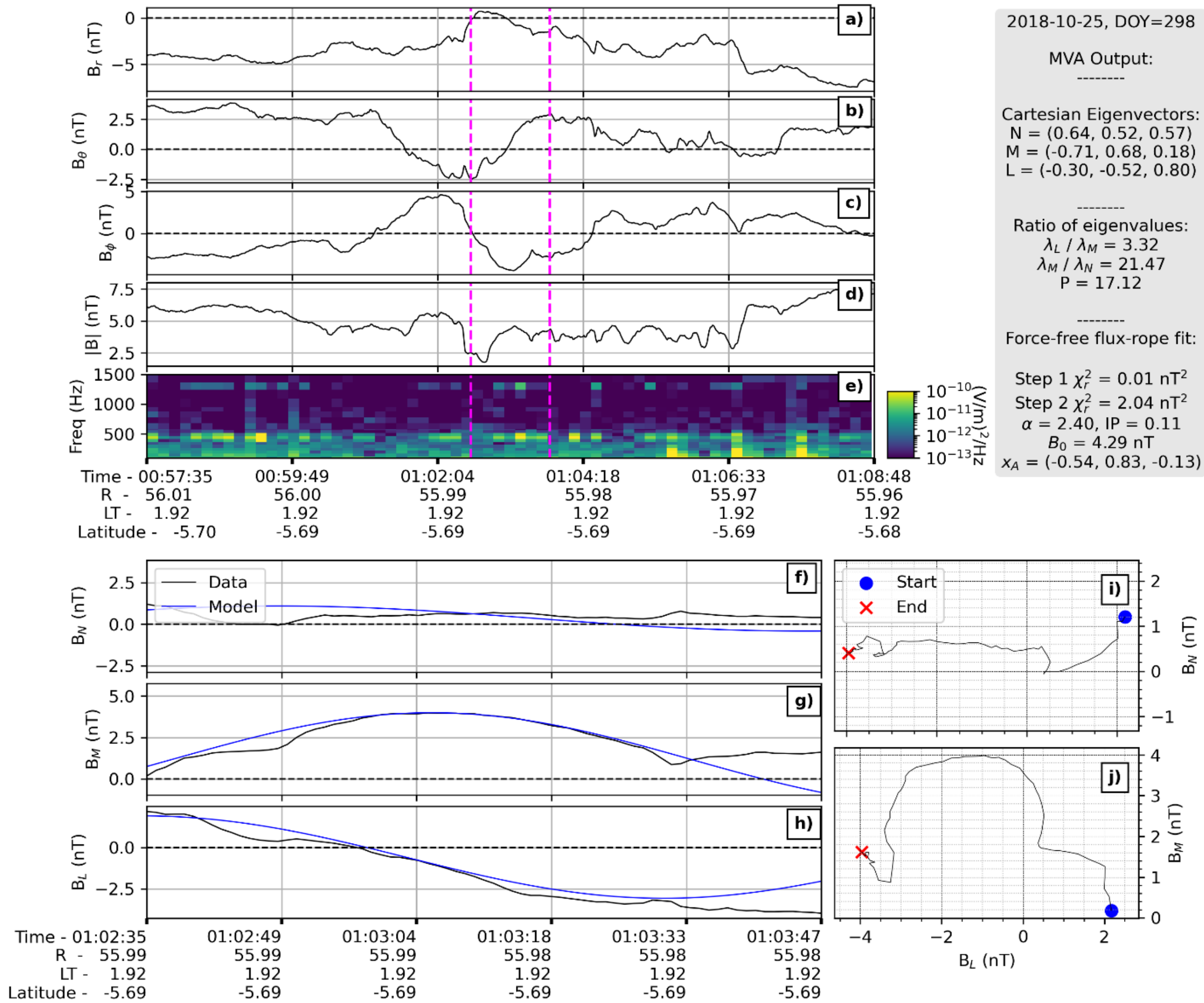
2018-10-25, DOY=298
MVA Output:
Cartesian Eigenvectors:
N = (0.64, 0.52, 0.57)
M = (-0.71, 0.68, 0.18)
L = (-0.30, -0.52, 0.80)
Ratio of eigenvalues:
λ_L / λ_M = 3.32
λ_M / λ_N = 21.47
P = 17.12
Force-free flux-rope fit:
Step 1 χ_r^2 = 0.01 nT^2
Step 2 χ_r^2 = 2.04 nT^2
α = 2.40, IP = 0.11
B_0 = 4.29 nT
x_A = (-0.54, 0.83, -0.13)
Time - 00:57:35 00:59:49 01:02:04 01:04:18 01:06:33 01:08:48
R - 56.01 56.00 55.99 55.98 55.97 55.96
LT - 1.92 1.92 1.92 1.92 1.92 1.92
Latitude - -5.70 -5.69 -5.69 -5.69 -5.69 -5.68
Data
Model
Start
End
Time - 01:02:35 01:02:49 01:03:04 01:03:18 01:03:33 01:03:47
R - 55.99 55.99 55.99 55.98 55.98 55.98
LT - 1.92 1.92 1.92 1.92 1.92 1.92
Latitude - -5.69 -5.69 -5.69 -5.69 -5.69 -5.69

Figure S70

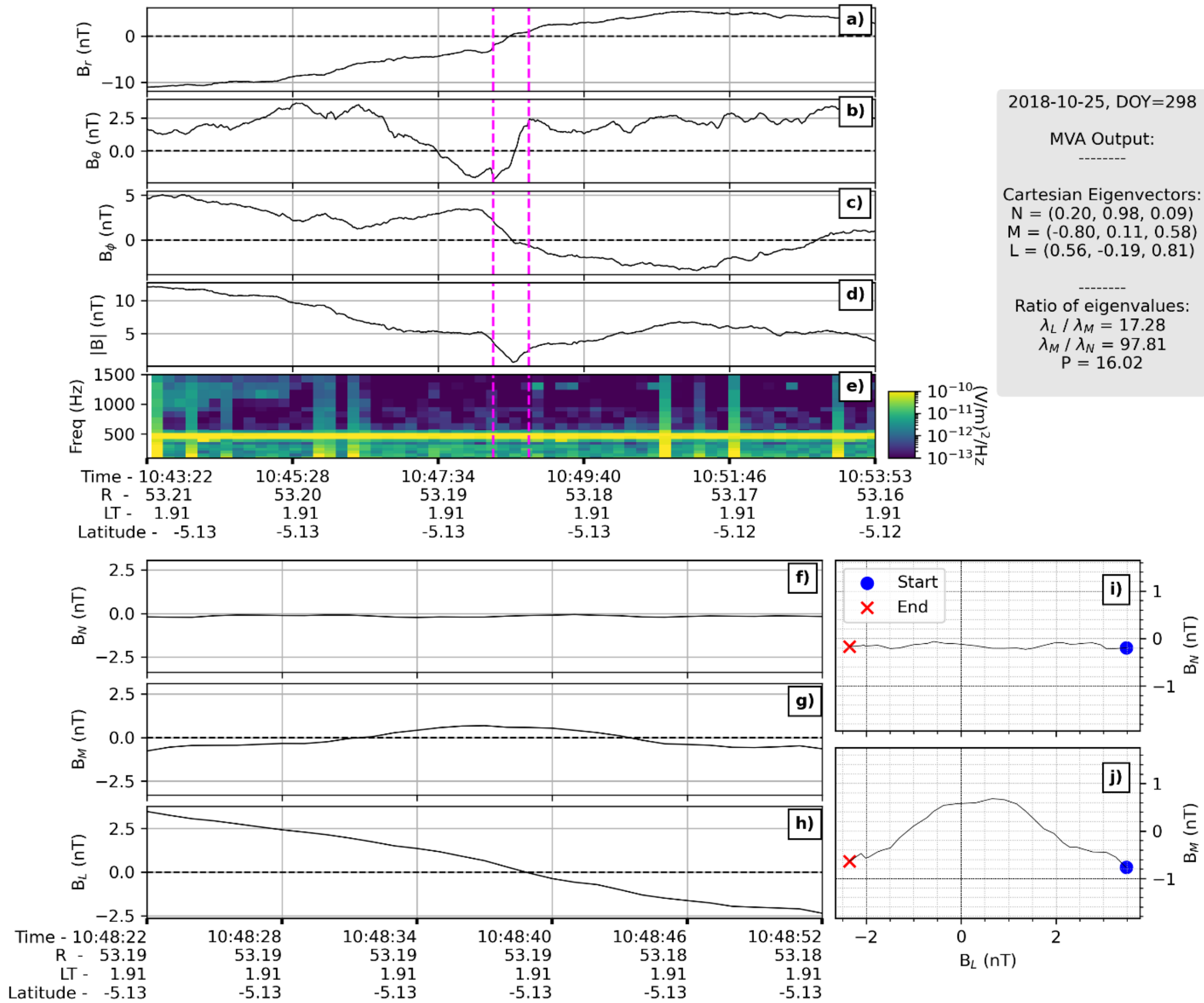

B$_r$ (nT)
a)
B$_\theta$ (nT)
b)
B$_\phi$ (nT)
c)
|B| (nT)
d)
Freq (Hz)
e)
(V/m)^2/Hz
Time - 10:43:22 10:45:28 10:47:34 10:49:40 10:51:46 10:53:53
R - 53.21 53.20 53.19 53.18 53.17 53.16
LT - 1.91 1.91 1.91 1.91 1.91 1.91
Latitude - -5.13 -5.13 -5.13 -5.13 -5.12 -5.12
2018-10-25, DOY=298
MVA Output:
Cartesian Eigenvectors:
N = (0.20, 0.98, 0.09)
M = (-0.80, 0.11, 0.58)
L = (0.56, -0.19, 0.81)
Ratio of eigenvalues:
λ_L / λ_M = 17.28
λ_M / λ_N = 97.81
P = 16.02
B$_N$ (nT)
f)
B$_M$ (nT)
g)
B$_L$ (nT)
h)
Time - 10:48:22 10:48:28 10:48:34 10:48:40 10:48:46 10:48:52
R - 53.19 53.19 53.19 53.19 53.18 53.18
LT - 1.91 1.91 1.91 1.91 1.91 1.91
Latitude - -5.13 -5.13 -5.13 -5.13 -5.13 -5.13
Start
End
i)
j)
B$_L$ (nT)

Figure S71

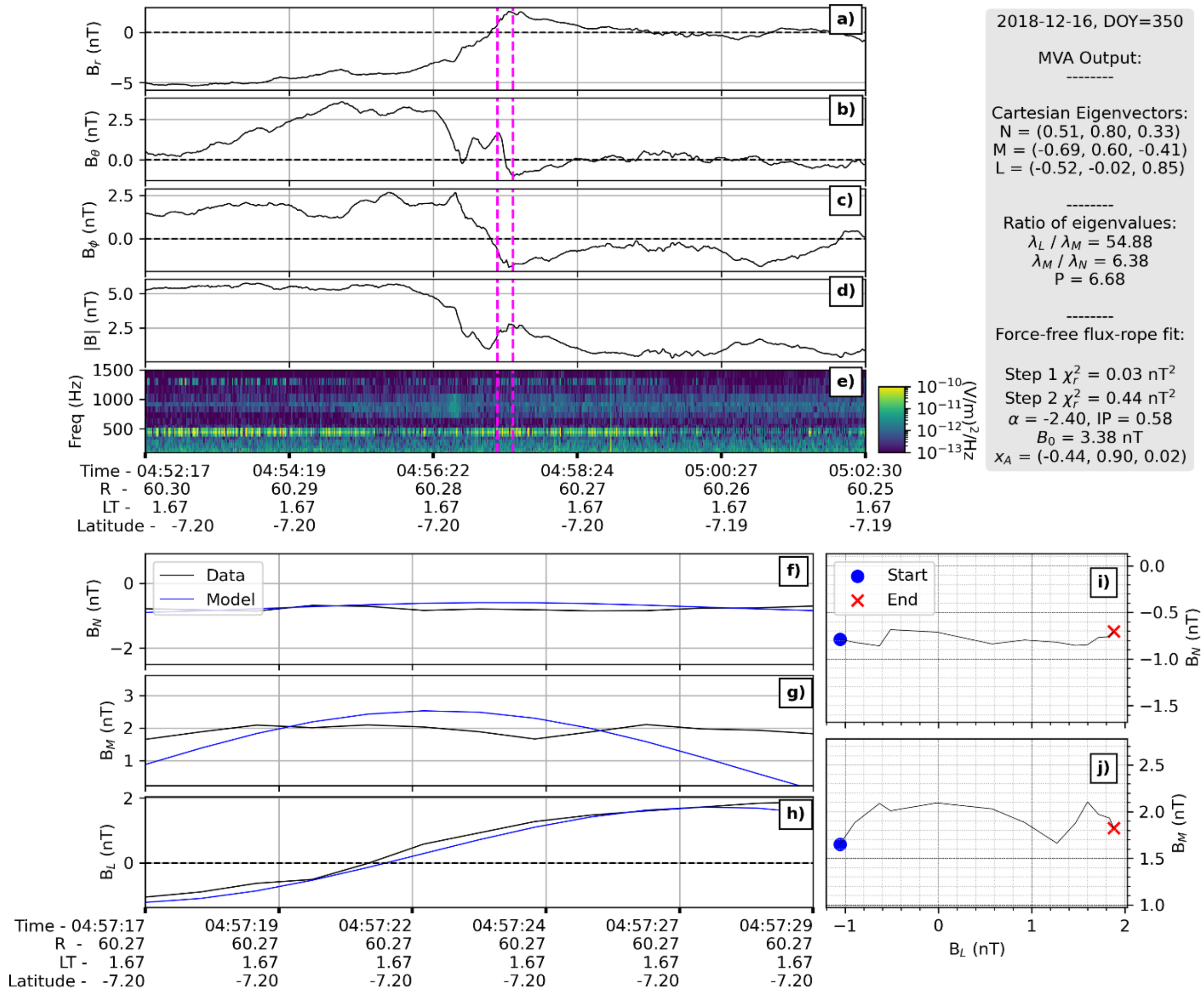
2018-12-16, DOY=350
MVA Output:
Cartesian Eigenvectors:
N = (0.51, 0.80, 0.33)
M = (-0.69, 0.60, -0.41)
L = (-0.52, -0.02, 0.85)
Ratio of eigenvalues:
λ_L / λ_M = 54.88
λ_M / λ_N = 6.38
P = 6.68
Force-free flux-rope fit:
Step 1 χ_r^2 = 0.03 nT^2
Step 2 χ_r^2 = 0.44 nT^2
α = -2.40, IP = 0.58
B_0 = 3.38 nT
x_A = (-0.44, 0.90, 0.02)
Time - 04:52:17 04:54:19 04:56:22 04:58:24 05:00:27 05:02:30
R - 60.30 60.29 60.28 60.27 60.26 60.25
LT - 1.67 1.67 1.67 1.67 1.67 1.67
Latitude - -7.20 -7.20 -7.20 -7.20 -7.19 -7.19
Data
Model
Start
End
Time - 04:57:17 04:57:19 04:57:22 04:57:24 04:57:27 04:57:29
R - 60.27 60.27 60.27 60.27 60.27 60.27
LT - 1.67 1.67 1.67 1.67 1.67 1.67
Latitude - -7.20 -7.20 -7.20 -7.20 -7.20 -7.20
B_L (nT)

Figure S72

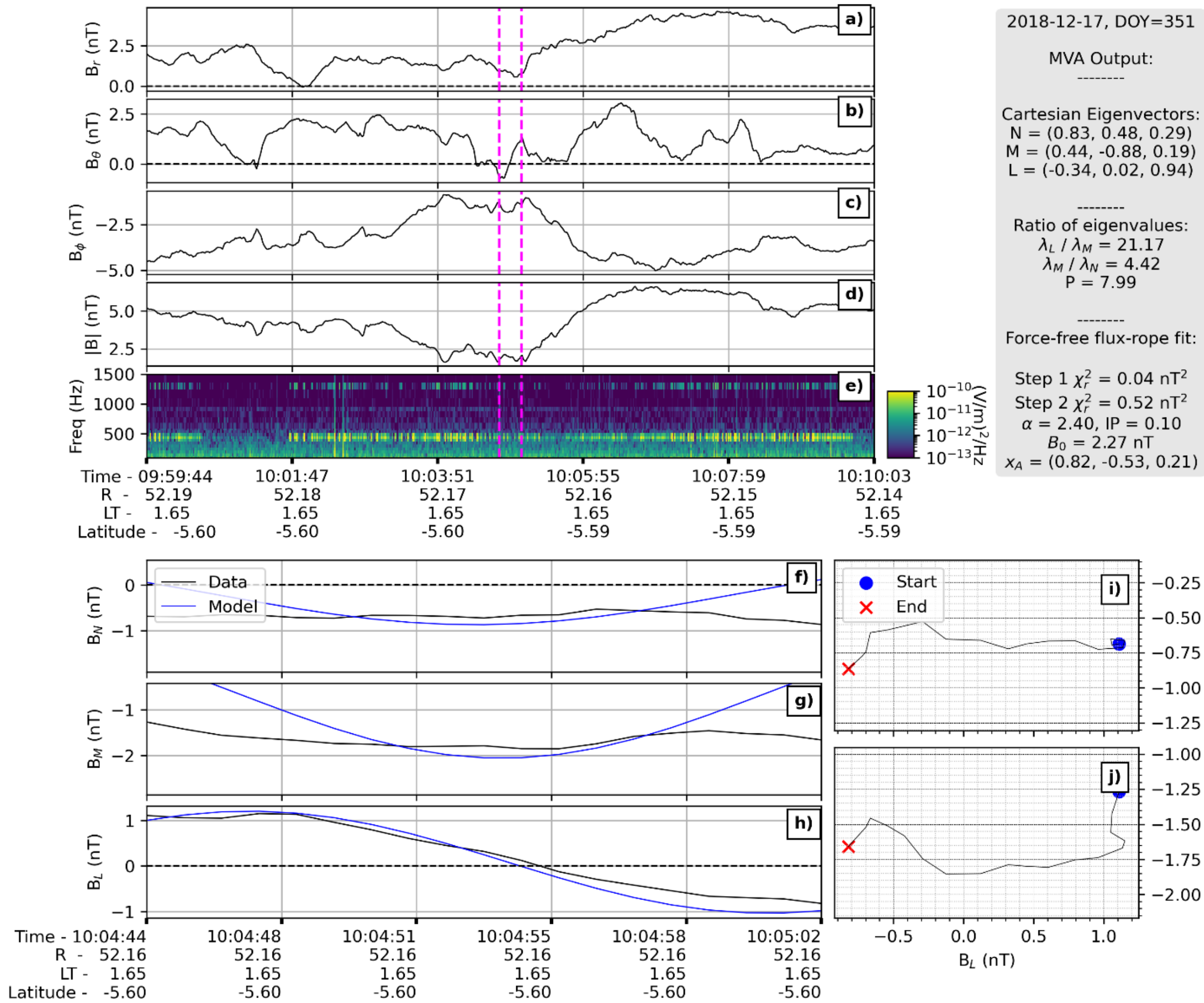
2018-12-17, DOY=351
MVA Output:
Cartesian Eigenvectors:
N = (0.83, 0.48, 0.29)
M = (0.44, -0.88, 0.19)
L = (-0.34, 0.02, 0.94)
Ratio of eigenvalues:
λL / λM = 21.17
λM / λN = 4.42
P = 7.99
Force-free flux-rope fit:
Step 1 χr² = 0.04 nT²
Step 2 χr² = 0.52 nT²
α = 2.40, IP = 0.10
B0 = 2.27 nT
xA = (0.82, -0.53, 0.21)
Time - 09:59:44 10:01:47 10:03:51 10:05:55 10:07:59 10:10:03
R - 52.19 52.18 52.17 52.16 52.15 52.14
LT - 1.65 1.65 1.65 1.65 1.65 1.65
Latitude - -5.60 -5.60 -5.60 -5.59 -5.59 -5.59
Data
Model
Start
End
Time - 10:04:44 10:04:48 10:04:51 10:04:55 10:04:58 10:05:02
R - 52.16 52.16 52.16 52.16 52.16 52.16
LT - 1.65 1.65 1.65 1.65 1.65 1.65
Latitude - -5.60 -5.60 -5.60 -5.60 -5.60 -5.60

Figure S73

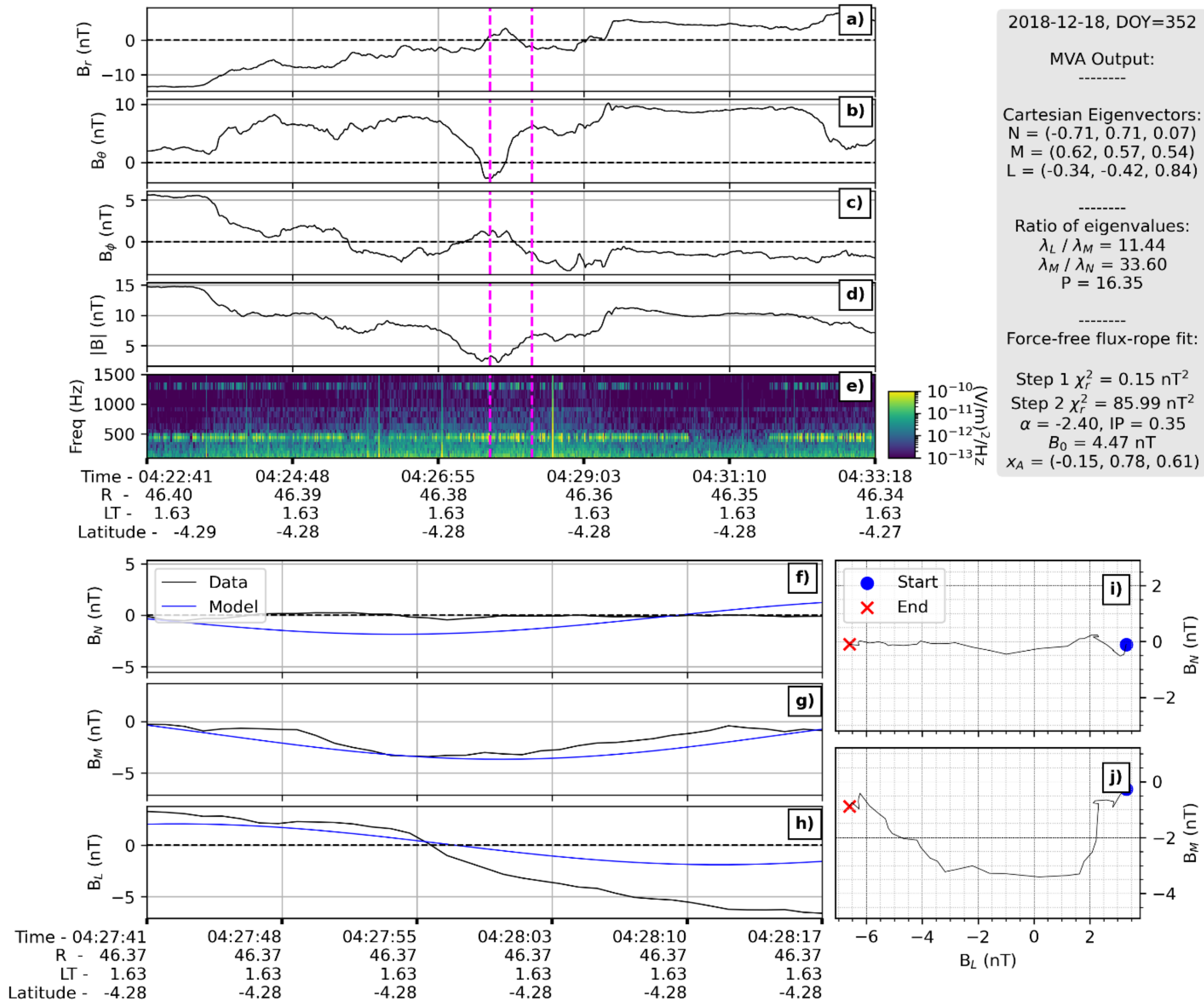

2018-12-18, DOY=352
MVA Output:
Cartesian Eigenvectors:
N = (-0.71, 0.71, 0.07)
M = (0.62, 0.57, 0.54)
L = (-0.34, -0.42, 0.84)
Ratio of eigenvalues:
λ_L / λ_M = 11.44
λ_M / λ_N = 33.60
P = 16.35
Force-free flux-rope fit:
Step 1 χ_r^2 = 0.15 nT^2
Step 2 χ_r^2 = 85.99 nT^2
α = -2.40, IP = 0.35
B_0 = 4.47 nT
x_A = (-0.15, 0.78, 0.61)
Time - 04:22:41 04:24:48 04:26:55 04:29:03 04:31:10 04:33:18
R - 46.40 46.39 46.38 46.36 46.35 46.34
LT - 1.63 1.63 1.63 1.63 1.63 1.63
Latitude - -4.29 -4.28 -4.28 -4.28 -4.28 -4.27
Data
Model
Start
End
Time - 04:27:41 04:27:48 04:27:55 04:28:03 04:28:10 04:28:17
R - 46.37 46.37 46.37 46.37 46.37 46.37
LT - 1.63 1.63 1.63 1.63 1.63 1.63
Latitude - -4.28 -4.28 -4.28 -4.28 -4.28 -4.28

Figure S74

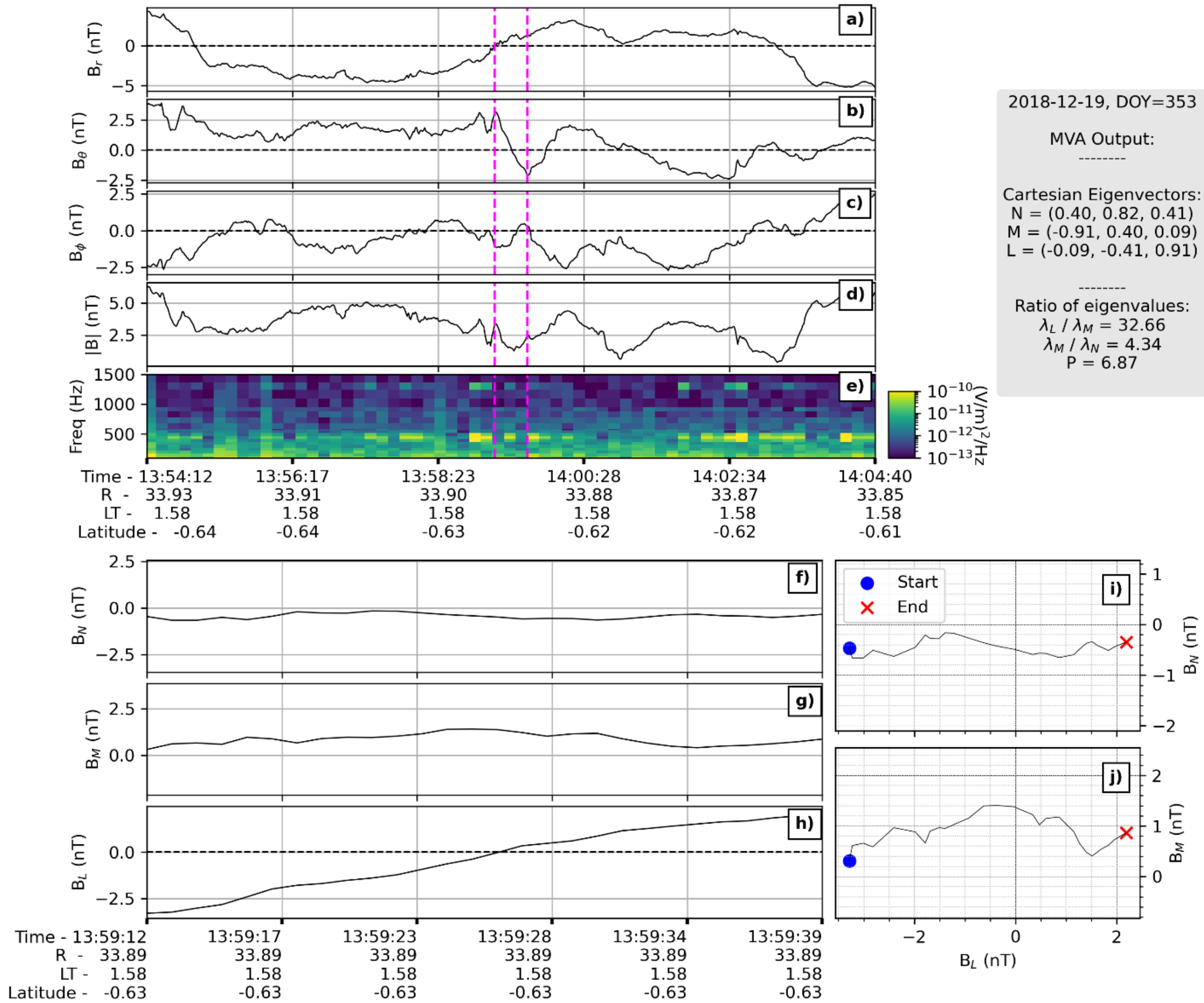
2018-12-19, DOY=353
MVA Output:
Cartesian Eigenvectors:
N = (0.40, 0.82, 0.41)
M = (-0.91, 0.40, 0.09)
L = (-0.09, -0.41, 0.91)
Ratio of eigenvalues:
λL / λM = 32.66
λM / λN = 4.34
P = 6.87
Time - 13:54:12 13:56:17 13:58:23 14:00:28 14:02:34 14:04:40
R - 33.93 33.91 33.90 33.88 33.87 33.85
LT - 1.58 1.58 1.58 1.58 1.58 1.58
Latitude - -0.64 -0.64 -0.63 -0.62 -0.62 -0.61
Start
End
Time - 13:59:12 13:59:17 13:59:23 13:59:28 13:59:34 13:59:39
R - 33.89 33.89 33.89 33.89 33.89 33.89
LT - 1.58 1.58 1.58 1.58 1.58 1.58
Latitude - -0.63 -0.63 -0.63 -0.63 -0.63 -0.63

Figure S75

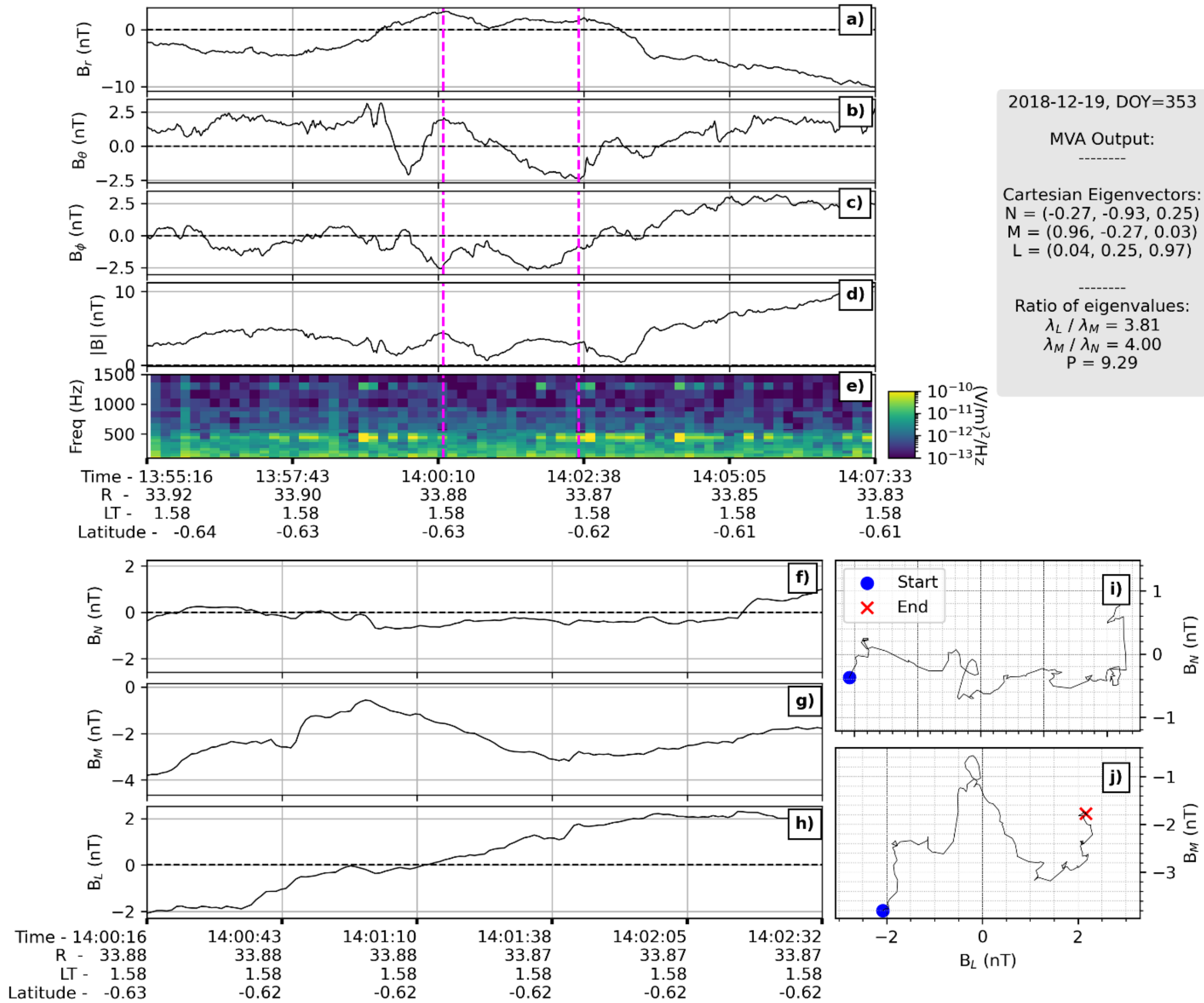

2018-12-19, DOY=353
MVA Output:
Cartesian Eigenvectors:
N = (-0.27, -0.93, 0.25)
M = (0.96, -0.27, 0.03)
L = (0.04, 0.25, 0.97)
Ratio of eigenvalues:
λL / λM = 3.81
λM / λN = 4.00
P = 9.29
a)
b)
c)
d)
e)
f)
g)
h)
i)
j)
Br (nT)
Bθ (nT)
Bϕ (nT)
|B| (nT)
Freq (Hz)
(V/m)²/Hz
BN (nT)
BM (nT)
BL (nT)
Start
End
Time - 13:55:16
R - 33.92
LT - 1.58
Latitude - -0.64
13:57:43
14:00:10
14:02:38
14:05:05
14:07:33
Time - 14:00:16
14:00:43
14:01:10
14:01:38
14:02:05
14:02:32

Figure S76

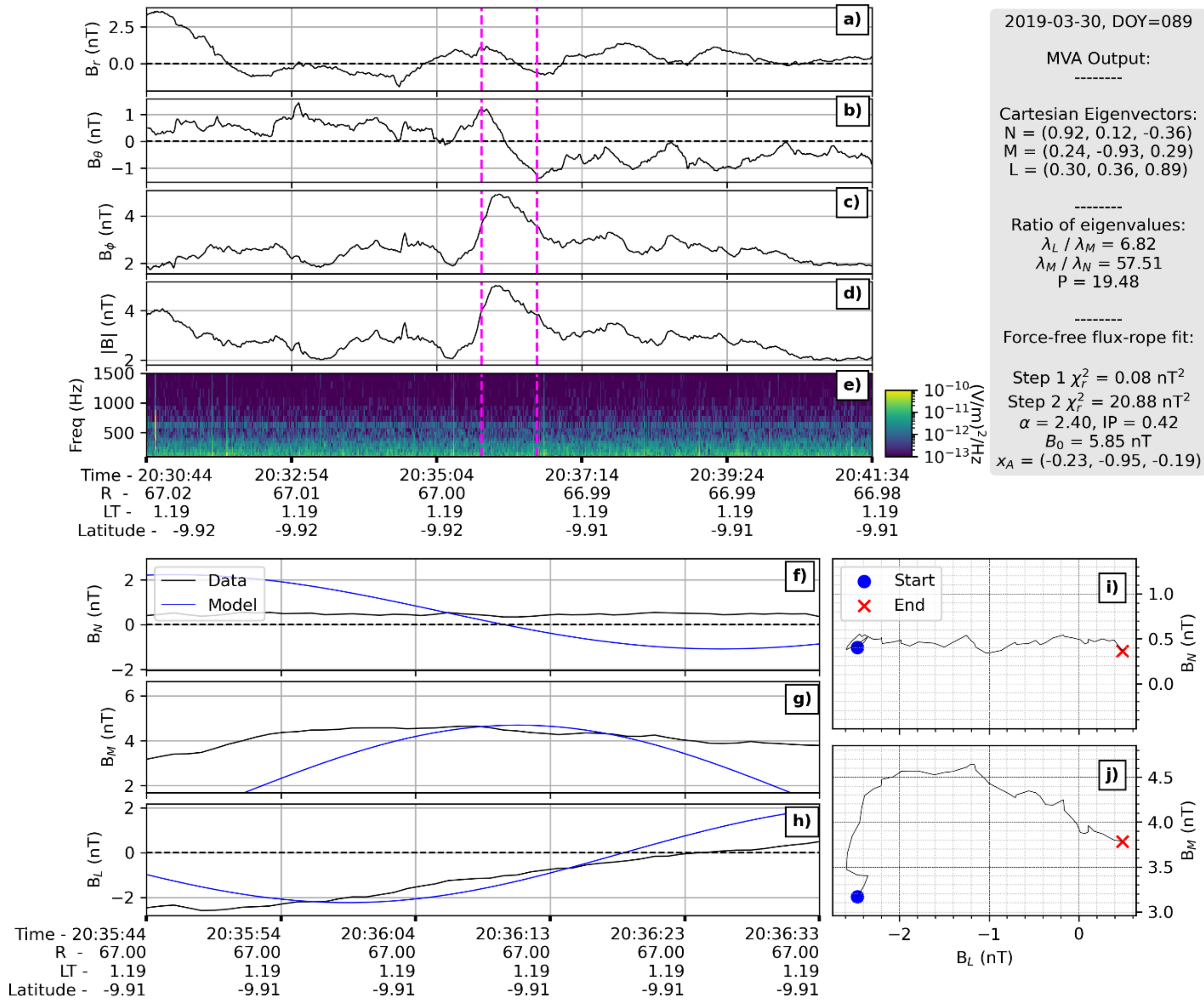
2019-03-30, DOY=089
MVA Output:

Cartesian Eigenvectors:
N = (0.92, 0.12, -0.36)
M = (0.24, -0.93, 0.29)
L = (0.30, 0.36, 0.89)

Ratio of eigenvalues:
λ_L / λ_M = 6.82
λ_M / λ_N = 57.51
P = 19.48

Force-free flux-rope fit:
Step 1 χ_r^2 = 0.08 nT^2
Step 2 χ_r^2 = 20.88 nT^2
α = 2.40, IP = 0.42
B_0 = 5.85 nT
x_A = (-0.23, -0.95, -0.19)
a)
b)
c)
d)
e)
f)
g)
h)
i)
j)
B_r (nT)
B_θ (nT)
B_ϕ (nT)
|B| (nT)
Freq (Hz)
(V/m)^2/Hz
Time - 20:30:44 20:32:54 20:35:04 20:37:14 20:39:24 20:41:34
R - 67.02 67.01 67.00 66.99 66.99 66.98
LT - 1.19 1.19 1.19 1.19 1.19 1.19
Latitude - -9.92 -9.92 -9.92 -9.91 -9.91 -9.91
Data
Model
B_N (nT)
B_M (nT)
B_L (nT)
Time - 20:35:44 20:35:54 20:36:04 20:36:13 20:36:23 20:36:33
R - 67.00 67.00 67.00 67.00 67.00 67.00
LT - 1.19 1.19 1.19 1.19 1.19 1.19
Latitude - -9.91 -9.91 -9.91 -9.91 -9.91 -9.91
Start
End
B_L (nT)

Figure S77

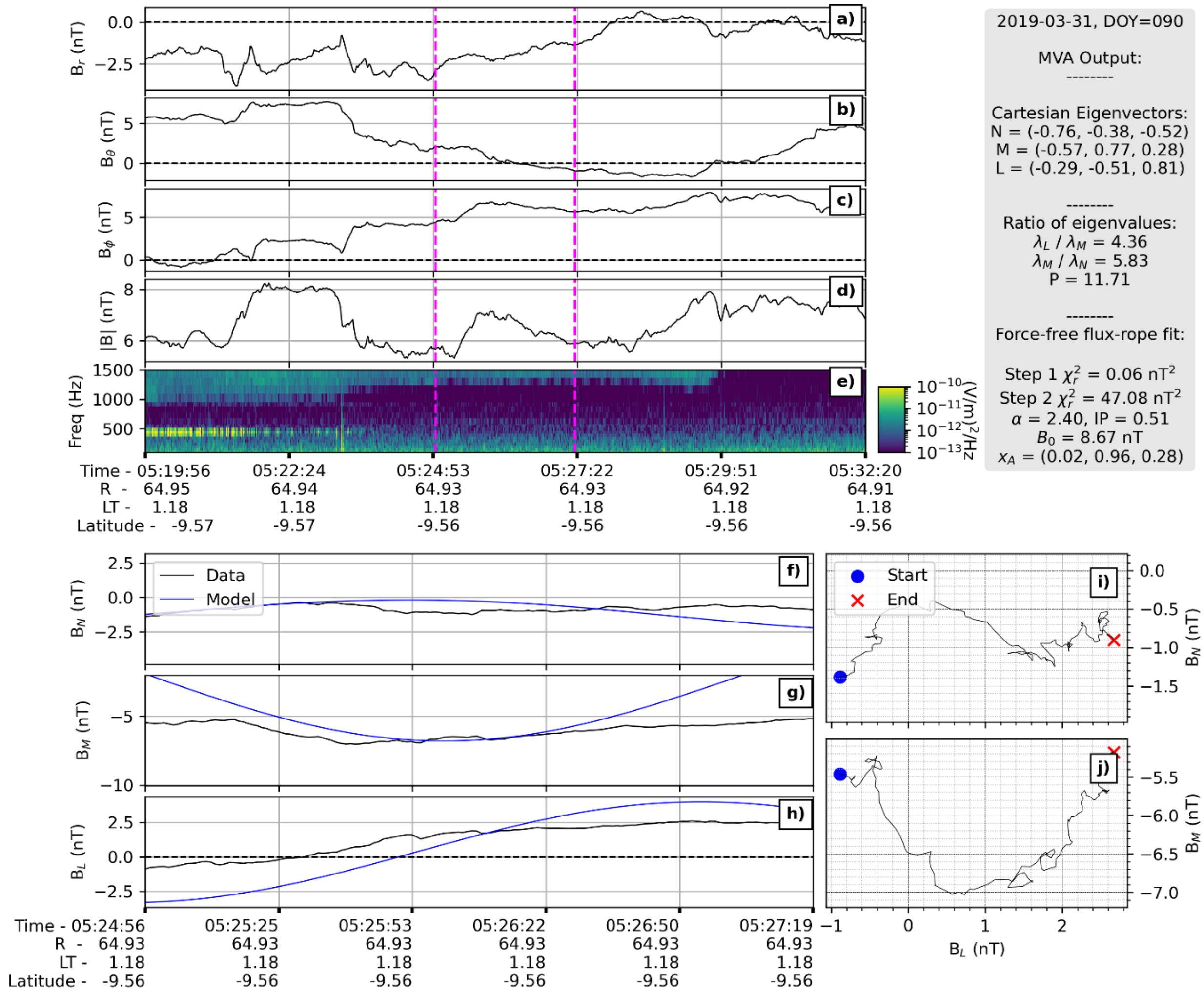

2019-03-31, DOY=090
MVA Output:
Cartesian Eigenvectors:
N = (-0.76, -0.38, -0.52)
M = (-0.57, 0.77, 0.28)
L = (-0.29, -0.51, 0.81)
Ratio of eigenvalues:
λ_L / λ_M = 4.36
λ_M / λ_N = 5.83
P = 11.71
Force-free flux-rope fit:
Step 1 χ_r^2 = 0.06 nT^2
Step 2 χ_r^2 = 47.08 nT^2
α = 2.40, IP = 0.51
B_0 = 8.67 nT
x_A = (0.02, 0.96, 0.28)
Time - 05:19:56 05:22:24 05:24:53 05:27:22 05:29:51 05:32:20
R - 64.95 64.94 64.93 64.93 64.92 64.91
LT - 1.18 1.18 1.18 1.18 1.18 1.18
Latitude - -9.57 -9.57 -9.56 -9.56 -9.56 -9.56
Data
Model
Start
End
Time - 05:24:56 05:25:25 05:25:53 05:26:22 05:26:50 05:27:19
R - 64.93 64.93 64.93 64.93 64.93 64.93
LT - 1.18 1.18 1.18 1.18 1.18 1.18
Latitude - -9.56 -9.56 -9.56 -9.56 -9.56 -9.56

Figure S78

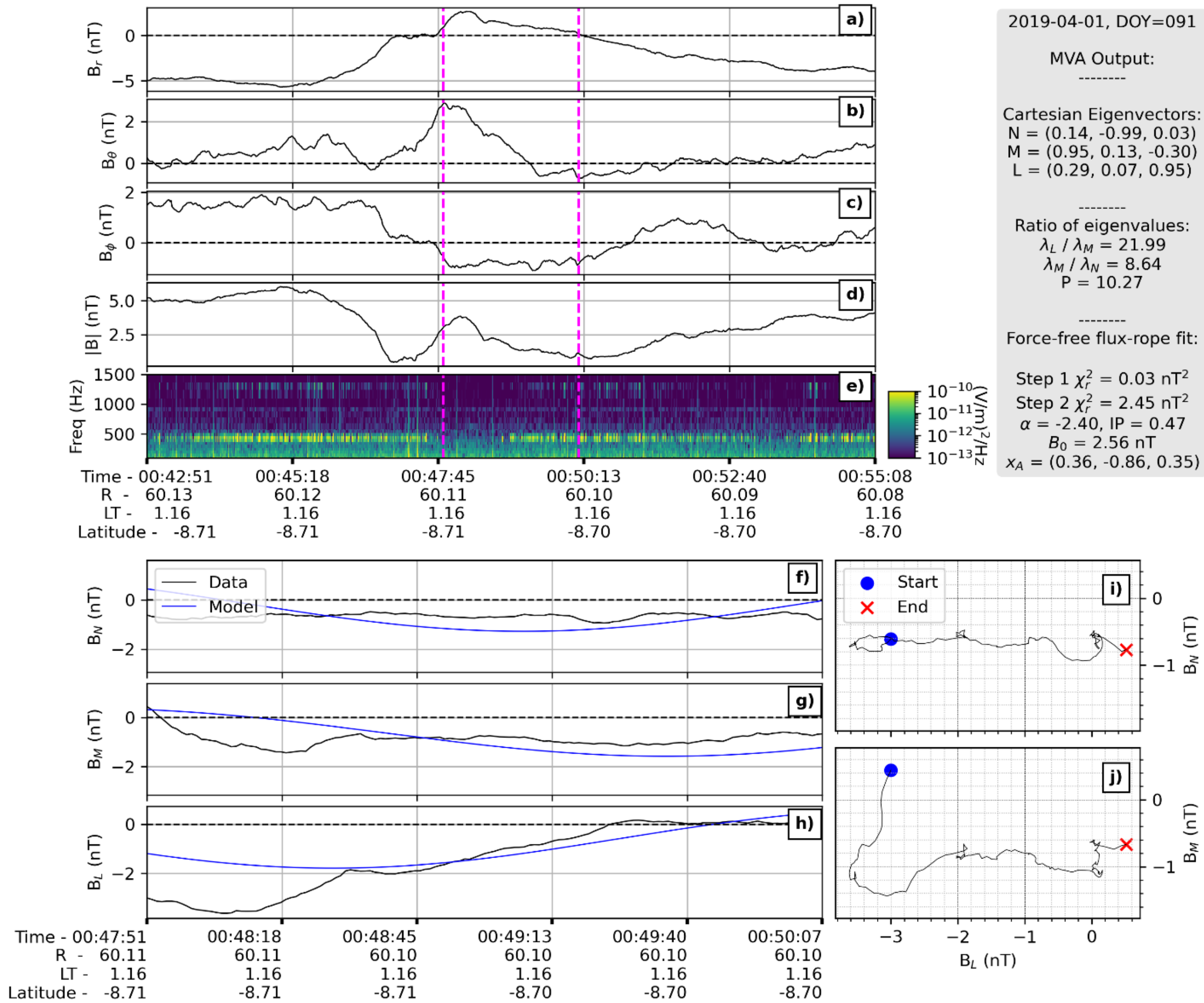
2019-04-01, DOY=091
MVA Output:
Cartesian Eigenvectors:
N = (0.14, -0.99, 0.03)
M = (0.95, 0.13, -0.30)
L = (0.29, 0.07, 0.95)
Ratio of eigenvalues:
λL / λM = 21.99
λM / λN = 8.64
P = 10.27
Force-free flux-rope fit:
Step 1 χr² = 0.03 nT²
Step 2 χr² = 2.45 nT²
α = -2.40, IP = 0.47
B0 = 2.56 nT
xA = (0.36, -0.86, 0.35)
Time - 00:42:51 00:45:18 00:47:45 00:50:13 00:52:40 00:55:08
R - 60.13 60.12 60.11 60.10 60.09 60.08
LT - 1.16 1.16 1.16 1.16 1.16 1.16
Latitude - -8.71 -8.71 -8.71 -8.70 -8.70 -8.70
Data
Model
Start
End
Time - 00:47:51 00:48:18 00:48:45 00:49:13 00:49:40 00:50:07
R - 60.11 60.11 60.10 60.10 60.10 60.10
LT - 1.16 1.16 1.16 1.16 1.16 1.16
Latitude - -8.71 -8.71 -8.71 -8.70 -8.70 -8.70

Figure S79

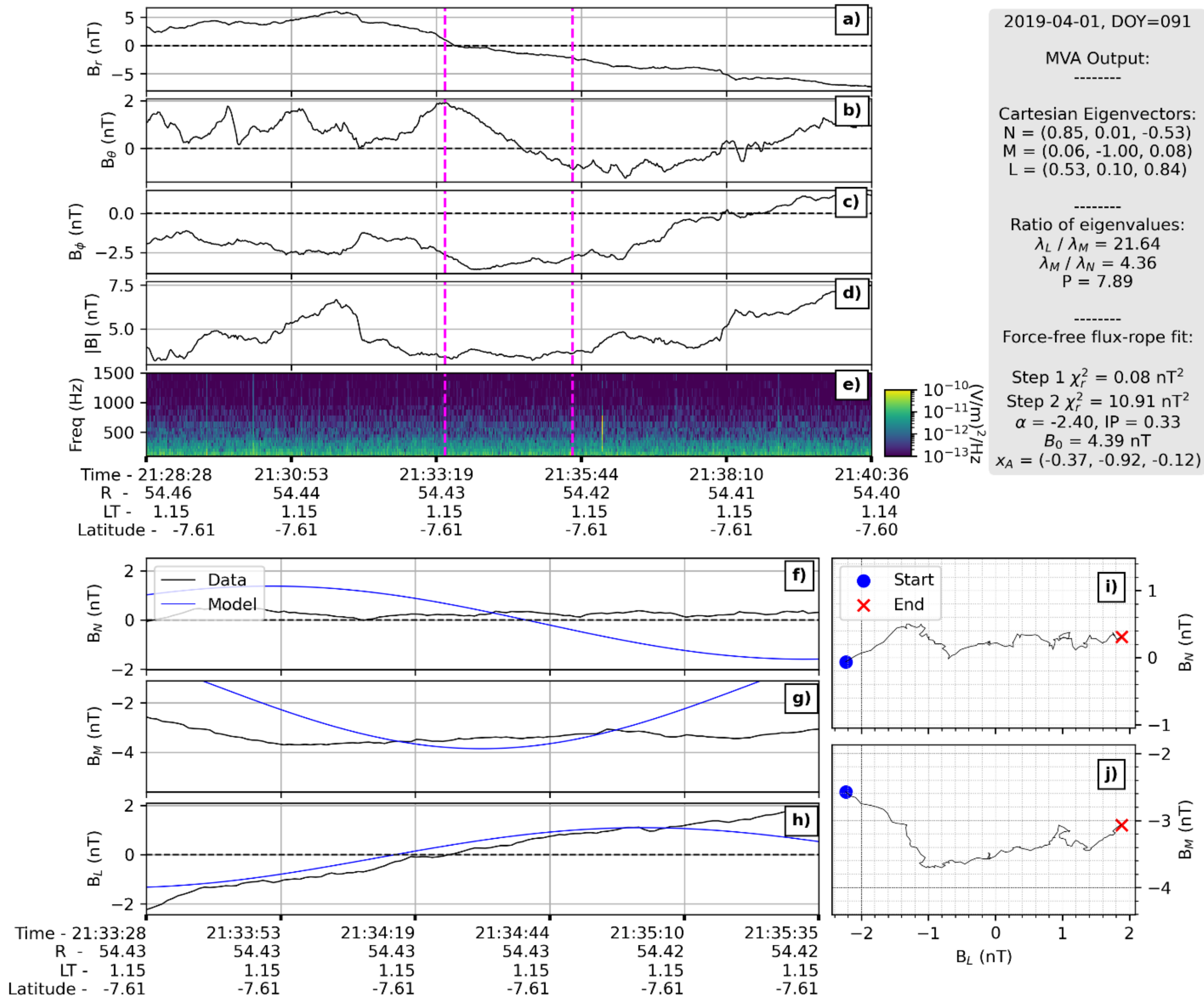

2019-04-01, DOY=091
MVA Output:

Cartesian Eigenvectors:
N = (0.85, 0.01, -0.53)
M = (0.06, -1.00, 0.08)
L = (0.53, 0.10, 0.84)

Ratio of eigenvalues:
λ_L / λ_M = 21.64
λ_M / λ_N = 4.36
P = 7.89

Force-free flux-rope fit:
Step 1 χ_r^2 = 0.08 nT^2
Step 2 χ_r^2 = 10.91 nT^2
α = -2.40, IP = 0.33
B_0 = 4.39 nT
x_A = (-0.37, -0.92, -0.12)
a)
b)
c)
d)
e)
f)
g)
h)
i)
j)
B_r (nT)
B_θ (nT)
B_ϕ (nT)
|B| (nT)
Freq (Hz)
$(V/m)^2/Hz$
Time - 21:28:28 21:30:53 21:33:19 21:35:44 21:38:10 21:40:36
R - 54.46 54.44 54.43 54.42 54.41 54.40
LT - 1.15 1.15 1.15 1.15 1.15 1.14
Latitude - -7.61 -7.61 -7.61 -7.61 -7.61 -7.60
Data
Model
B_N (nT)
B_M (nT)
B_L (nT)
Start
End
Time - 21:33:28 21:33:53 21:34:19 21:34:44 21:35:10 21:35:35
R - 54.43 54.43 54.43 54.43 54.42 54.42
LT - 1.15 1.15 1.15 1.15 1.15 1.15
Latitude - -7.61 -7.61 -7.61 -7.61 -7.61 -7.61

Figure S80

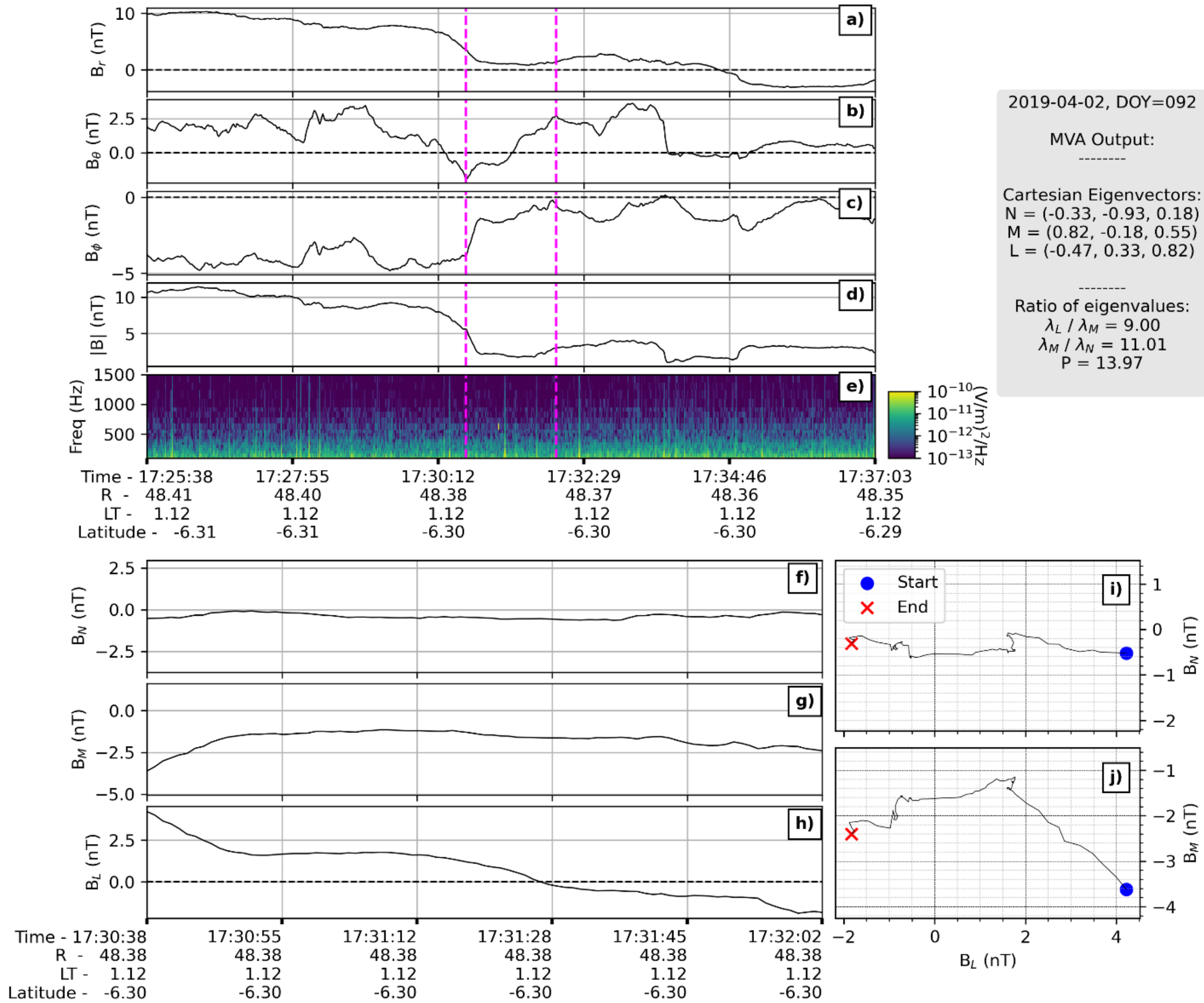

2019-04-02, DOY=092
MVA Output:

Cartesian Eigenvectors:
N = (-0.33, -0.93, 0.18)
M = (0.82, -0.18, 0.55)
L = (-0.47, 0.33, 0.82)

Ratio of eigenvalues:
λL / λM = 9.00
λM / λN = 11.01
P = 13.97
Time - 17:25:38 17:27:55 17:30:12 17:32:29 17:34:46 17:37:03
R - 48.41 48.40 48.38 48.37 48.36 48.35
LT - 1.12 1.12 1.12 1.12 1.12 1.12
Latitude - -6.31 -6.31 -6.30 -6.30 -6.30 -6.29
Time - 17:30:38 17:30:55 17:31:12 17:31:28 17:31:45 17:32:02
R - 48.38 48.38 48.38 48.38 48.38 48.38
LT - 1.12 1.12 1.12 1.12 1.12 1.12
Latitude - -6.30 -6.30 -6.30 -6.30 -6.30 -6.30
Start
End

Figure S81

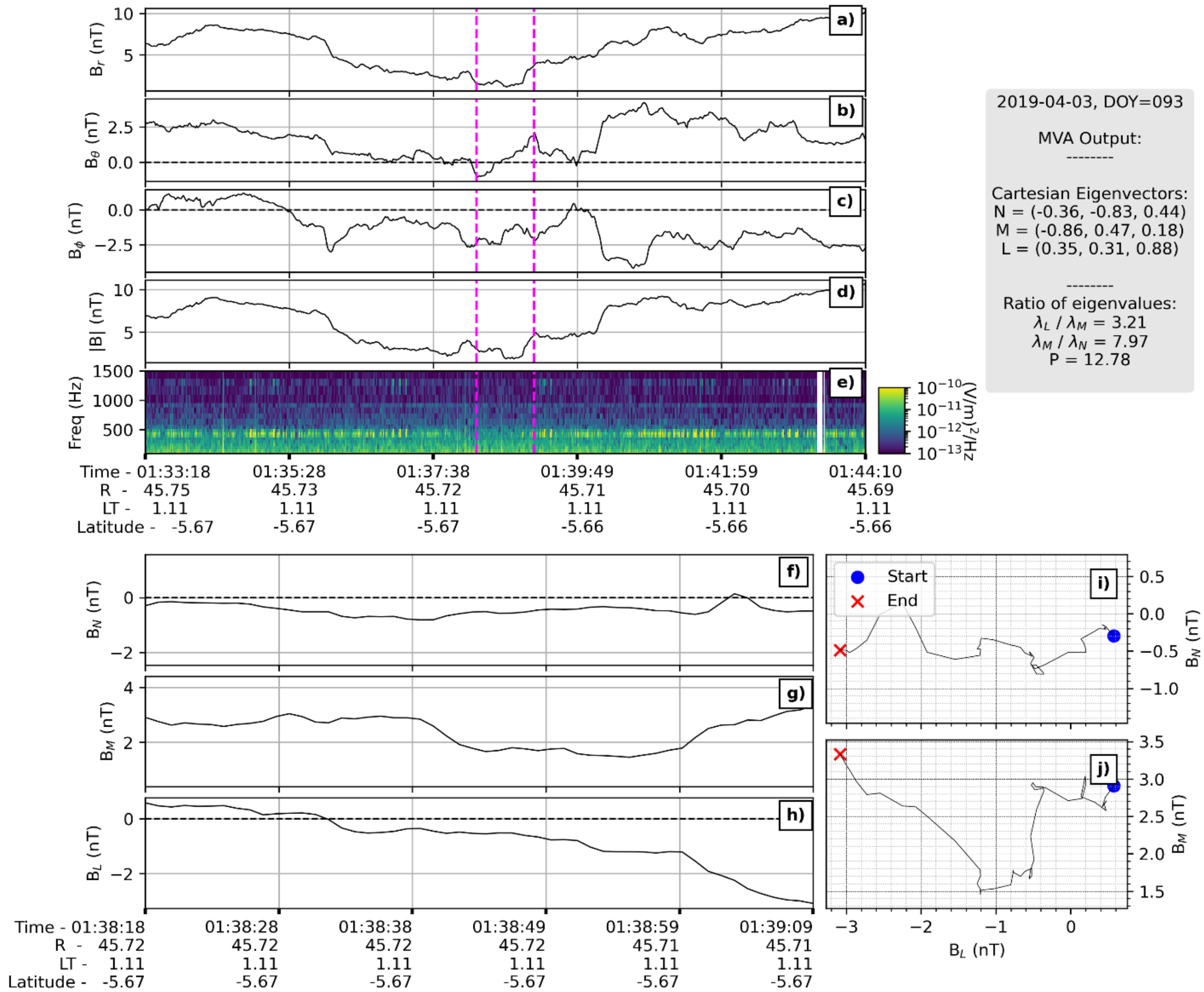
2019-04-03, DOY=093
MVA Output:

Cartesian Eigenvectors:
N = (-0.36, -0.83, 0.44)
M = (-0.86, 0.47, 0.18)
L = (0.35, 0.31, 0.88)

Ratio of eigenvalues:
λ_L / λ_M = 3.21
λ_M / λ_N = 7.97
P = 12.78
Time - 01:33:18 01:35:28 01:37:38 01:39:49 01:41:59 01:44:10
R - 45.75 45.73 45.72 45.71 45.70 45.69
LT - 1.11 1.11 1.11 1.11 1.11 1.11
Latitude - -5.67 -5.67 -5.67 -5.66 -5.66 -5.66
Time - 01:38:18 01:38:28 01:38:38 01:38:49 01:38:59 01:39:09
R - 45.72 45.72 45.72 45.72 45.71 45.71
LT - 1.11 1.11 1.11 1.11 1.11 1.11
Latitude - -5.67 -5.67 -5.67 -5.67 -5.67 -5.67
Start
End

Figure S82

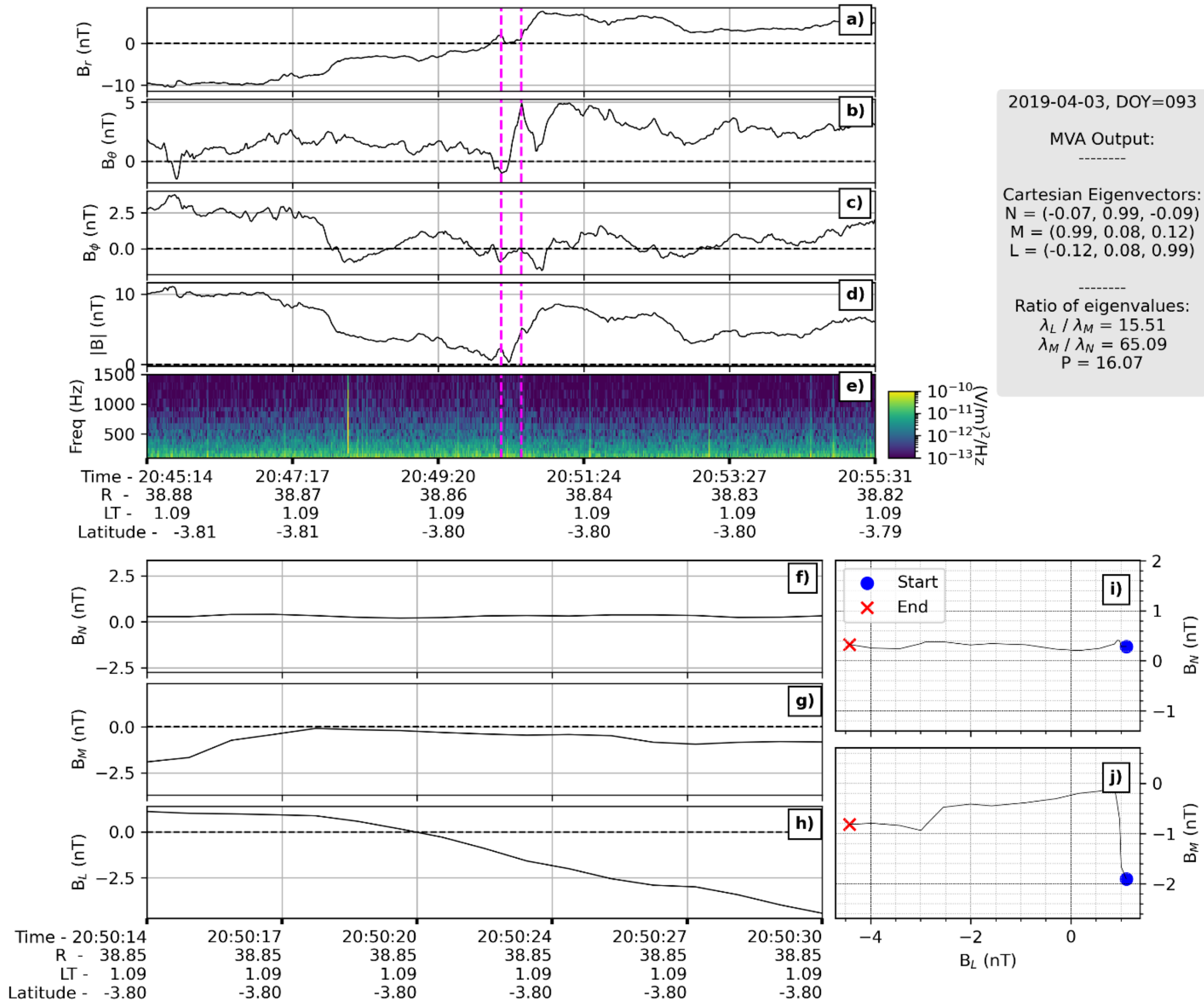
2019-04-03, DOY=093
MVA Output:
Cartesian Eigenvectors:
N = (-0.07, 0.99, -0.09)
M = (0.99, 0.08, 0.12)
L = (-0.12, 0.08, 0.99)
Ratio of eigenvalues:
λL / λM = 15.51
λM / λN = 65.09
P = 16.07
Time - 20:45:14 20:47:17 20:49:20 20:51:24 20:53:27 20:55:31
R - 38.88 38.87 38.86 38.84 38.83 38.82
LT - 1.09 1.09 1.09 1.09 1.09 1.09
Latitude - -3.81 -3.81 -3.80 -3.80 -3.80 -3.79
Time - 20:50:14 20:50:17 20:50:20 20:50:24 20:50:27 20:50:30
R - 38.85 38.85 38.85 38.85 38.85 38.85
LT - 1.09 1.09 1.09 1.09 1.09 1.09
Latitude - -3.80 -3.80 -3.80 -3.80 -3.80 -3.80
Start
End

Figure S83

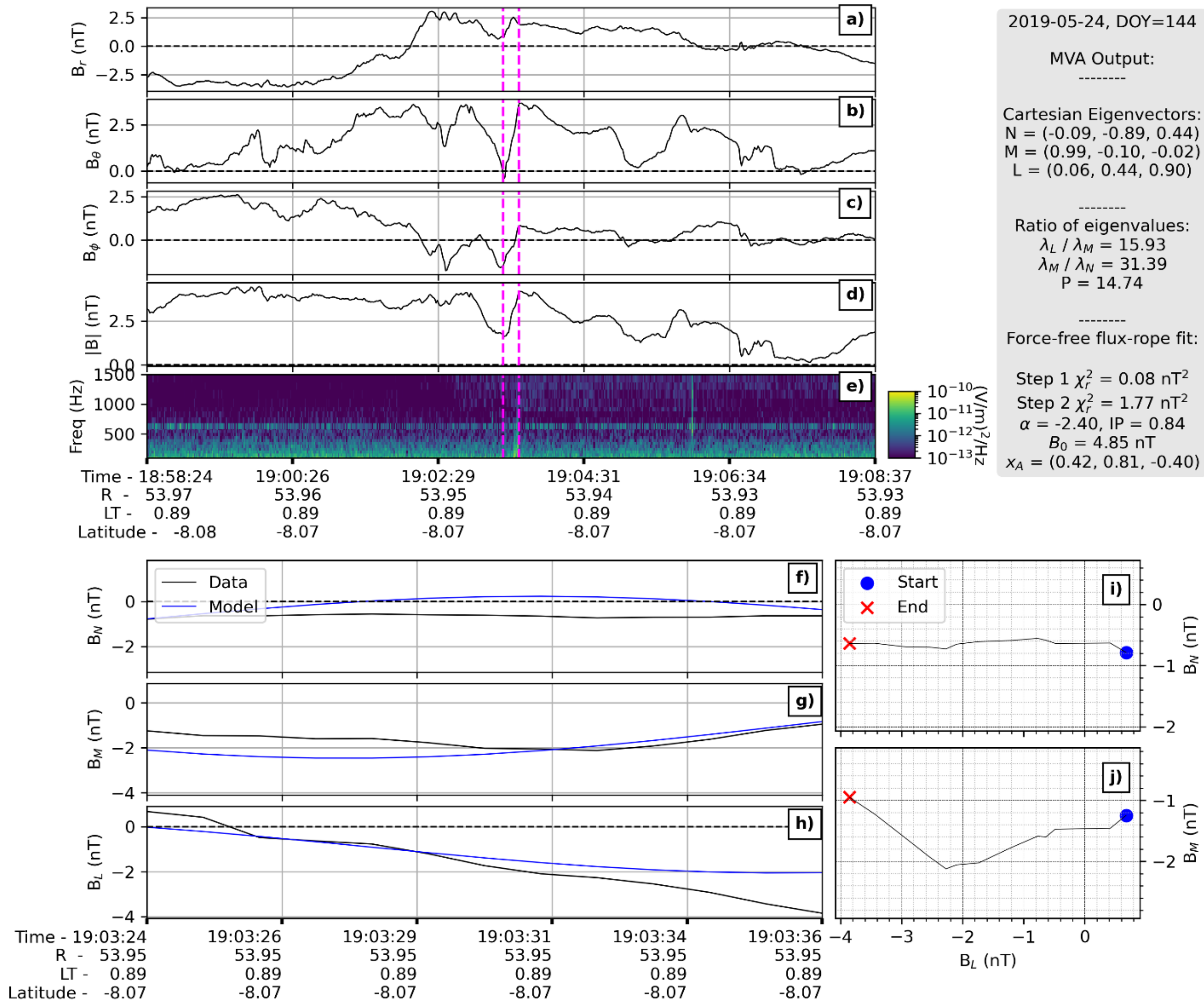

2019-05-24, DOY=144
MVA Output:

Cartesian Eigenvectors:
N = (-0.09, -0.89, 0.44)
M = (0.99, -0.10, -0.02)
L = (0.06, 0.44, 0.90)

Ratio of eigenvalues:
λ_L / λ_M = 15.93
λ_M / λ_N = 31.39
P = 14.74

Force-free flux-rope fit:
Step 1 χ_r^2 = 0.08 nT^2
Step 2 χ_r^2 = 1.77 nT^2
α = -2.40, IP = 0.84
B_0 = 4.85 nT
x_A = (0.42, 0.81, -0.40)
Time - 18:58:24 19:00:26 19:02:29 19:04:31 19:06:34 19:08:37
R - 53.97 53.96 53.95 53.94 53.93 53.93
LT - 0.89 0.89 0.89 0.89 0.89 0.89
Latitude - -8.08 -8.07 -8.07 -8.07 -8.07 -8.07
Data
Model
Start
End
Time - 19:03:24 19:03:26 19:03:29 19:03:31 19:03:34 19:03:36
R - 53.95 53.95 53.95 53.95 53.95 53.95
LT - 0.89 0.89 0.89 0.89 0.89 0.89
Latitude - -8.07 -8.07 -8.07 -8.07 -8.07 -8.07

Figure S84

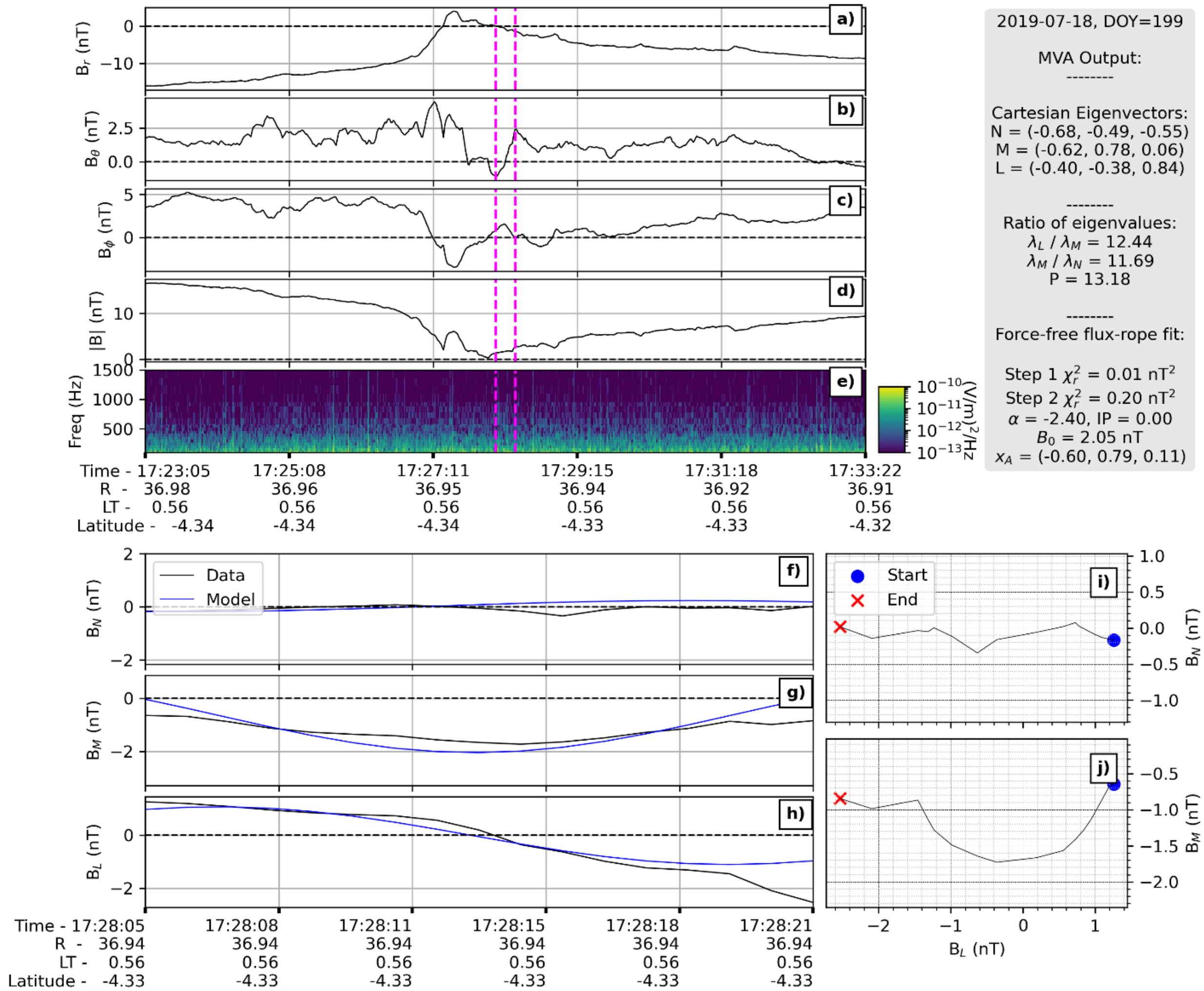

2019-07-18, DOY=199
MVA Output:
Cartesian Eigenvectors:
N = (-0.68, -0.49, -0.55)
M = (-0.62, 0.78, 0.06)
L = (-0.40, -0.38, 0.84)
Ratio of eigenvalues:
λ_L / λ_M = 12.44
λ_M / λ_N = 11.69
P = 13.18
Force-free flux-rope fit:
Step 1 χ_r^2 = 0.01 nT^2
Step 2 χ_r^2 = 0.20 nT^2
α = -2.40, IP = 0.00
B_0 = 2.05 nT
x_A = (-0.60, 0.79, 0.11)
Time - 17:23:05 17:25:08 17:27:11 17:29:15 17:31:18 17:33:22
R - 36.98 36.96 36.95 36.94 36.92 36.91
LT - 0.56 0.56 0.56 0.56 0.56 0.56
Latitude - -4.34 -4.34 -4.34 -4.33 -4.33 -4.32
Data
Model
Start
End
Time - 17:28:05 17:28:08 17:28:11 17:28:15 17:28:18 17:28:21
R - 36.94 36.94 36.94 36.94 36.94 36.94
LT - 0.56 0.56 0.56 0.56 0.56 0.56
Latitude - -4.33 -4.33 -4.33 -4.33 -4.33 -4.33

Figure S85

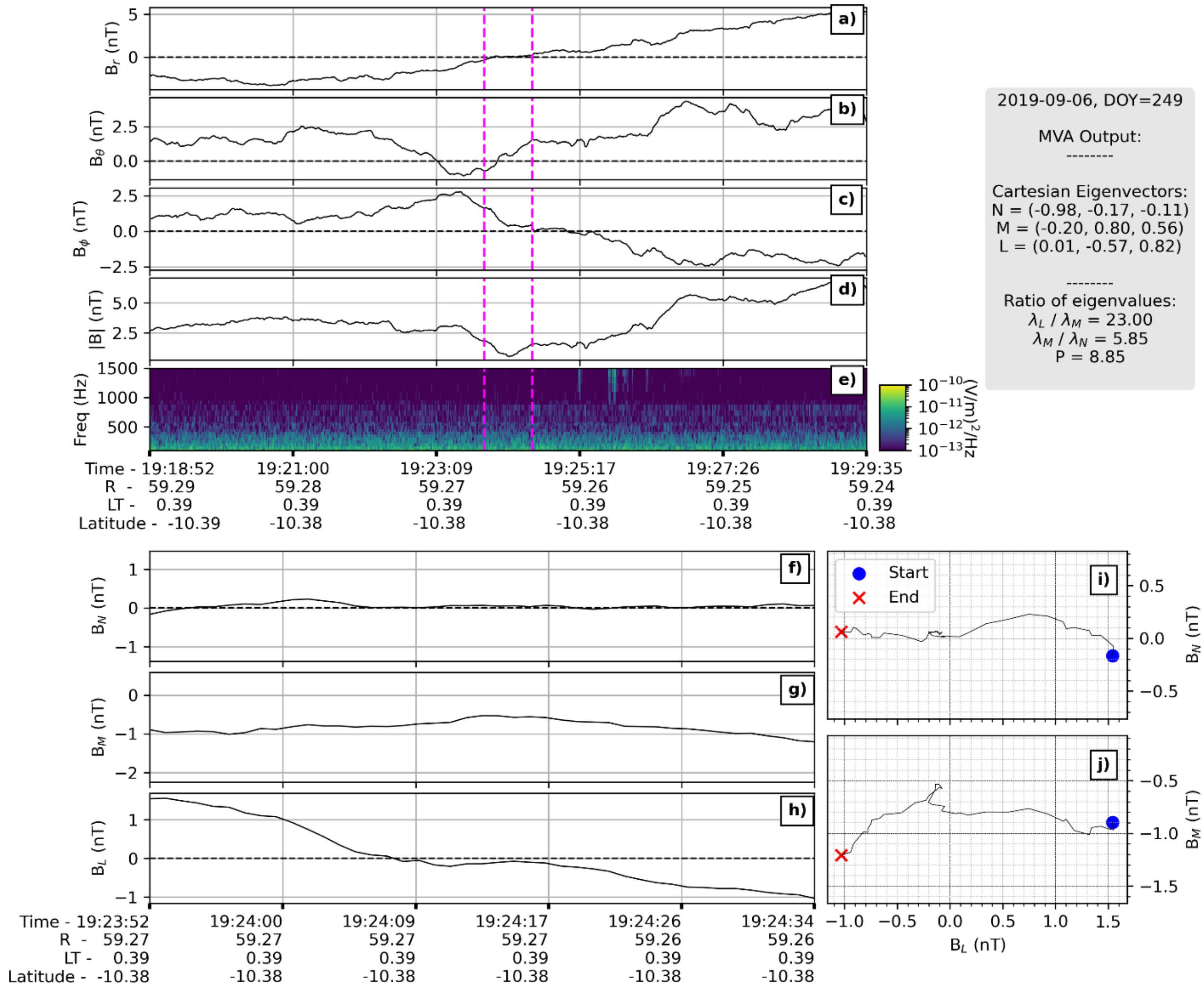
2019-09-06, DOY=249
MVA Output:

Cartesian Eigenvectors:
N = (-0.98, -0.17, -0.11)
M = (-0.20, 0.80, 0.56)
L = (0.01, -0.57, 0.82)

Ratio of eigenvalues:
λ_L / λ_M = 23.00
λ_M / λ_N = 5.85
P = 8.85
Time - 19:18:52 19:21:00 19:23:09 19:25:17 19:27:26 19:29:35
R - 59.29 59.28 59.27 59.26 59.25 59.24
LT - 0.39 0.39 0.39 0.39 0.39 0.39
Latitude - -10.39 -10.38 -10.38 -10.38 -10.38 -10.38
Time - 19:23:52 19:24:00 19:24:09 19:24:17 19:24:26 19:24:34
R - 59.27 59.27 59.27 59.27 59.26 59.26
LT - 0.39 0.39 0.39 0.39 0.39 0.39
Latitude - -10.38 -10.38 -10.38 -10.38 -10.38 -10.38
Start
End
B_L (nT)

Figure S86

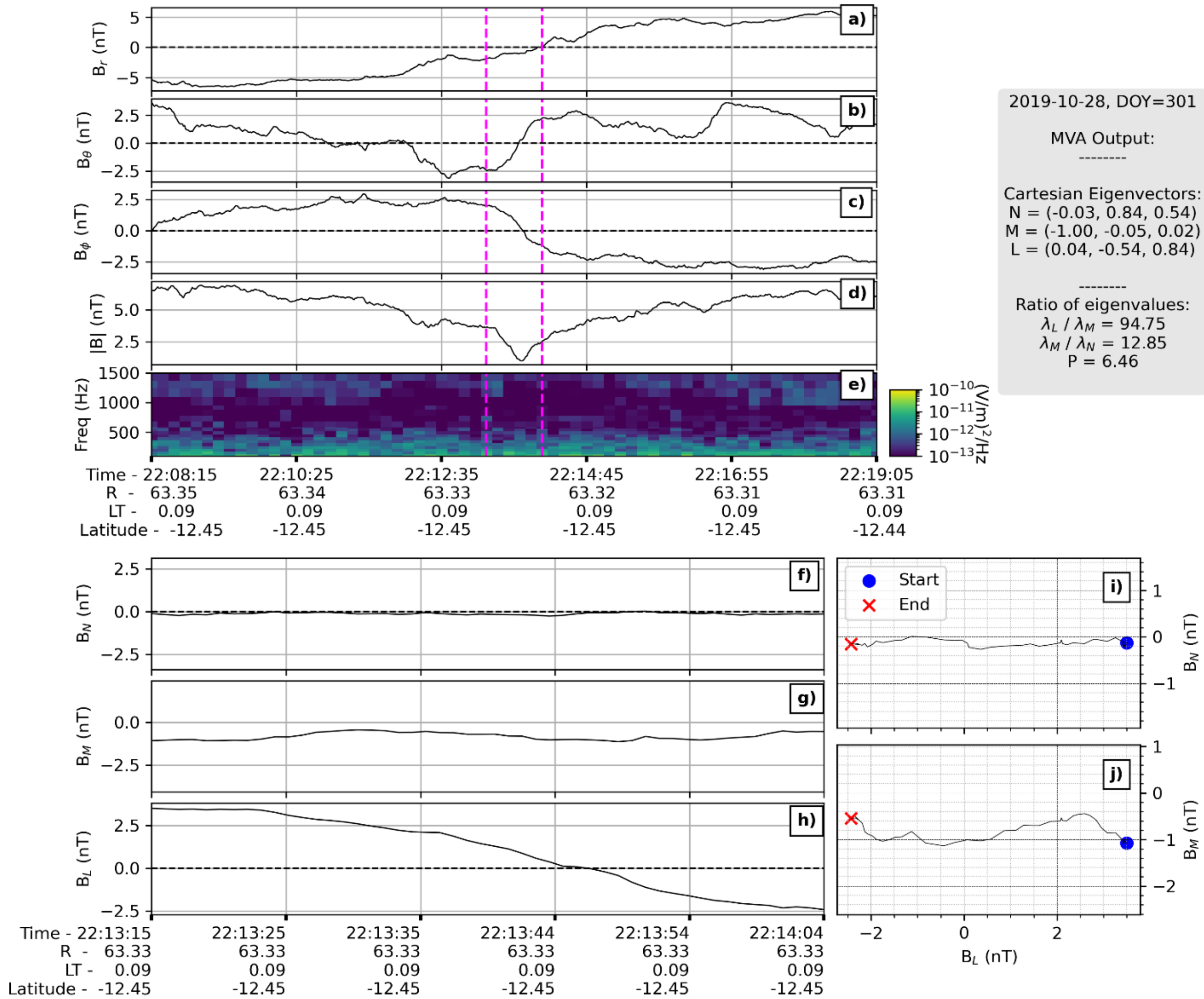
a)
b)
c)
d)
e)
B_r (nT)
B_θ (nT)
B_ϕ (nT)
|B| (nT)
Freq (Hz)
(V/m)^2/Hz
Time - 22:08:15 22:10:25 22:12:35 22:14:45 22:16:55 22:19:05
R - 63.35 63.34 63.33 63.32 63.31 63.31
LT - 0.09 0.09 0.09 0.09 0.09 0.09
Latitude - -12.45 -12.45 -12.45 -12.45 -12.45 -12.44
2019-10-28, DOY=301
MVA Output:

Cartesian Eigenvectors:
N = (-0.03, 0.84, 0.54)
M = (-1.00, -0.05, 0.02)
L = (0.04, -0.54, 0.84)

Ratio of eigenvalues:
λ_L / λ_M = 94.75
λ_M / λ_N = 12.85
P = 6.46
f)
g)
h)
B_N (nT)
B_M (nT)
B_L (nT)
Time - 22:13:15 22:13:25 22:13:35 22:13:44 22:13:54 22:14:04
R - 63.33 63.33 63.33 63.33 63.33 63.33
LT - 0.09 0.09 0.09 0.09 0.09 0.09
Latitude - -12.45 -12.45 -12.45 -12.45 -12.45 -12.45
i)
j)
Start
End
B_L (nT)

Figure S87

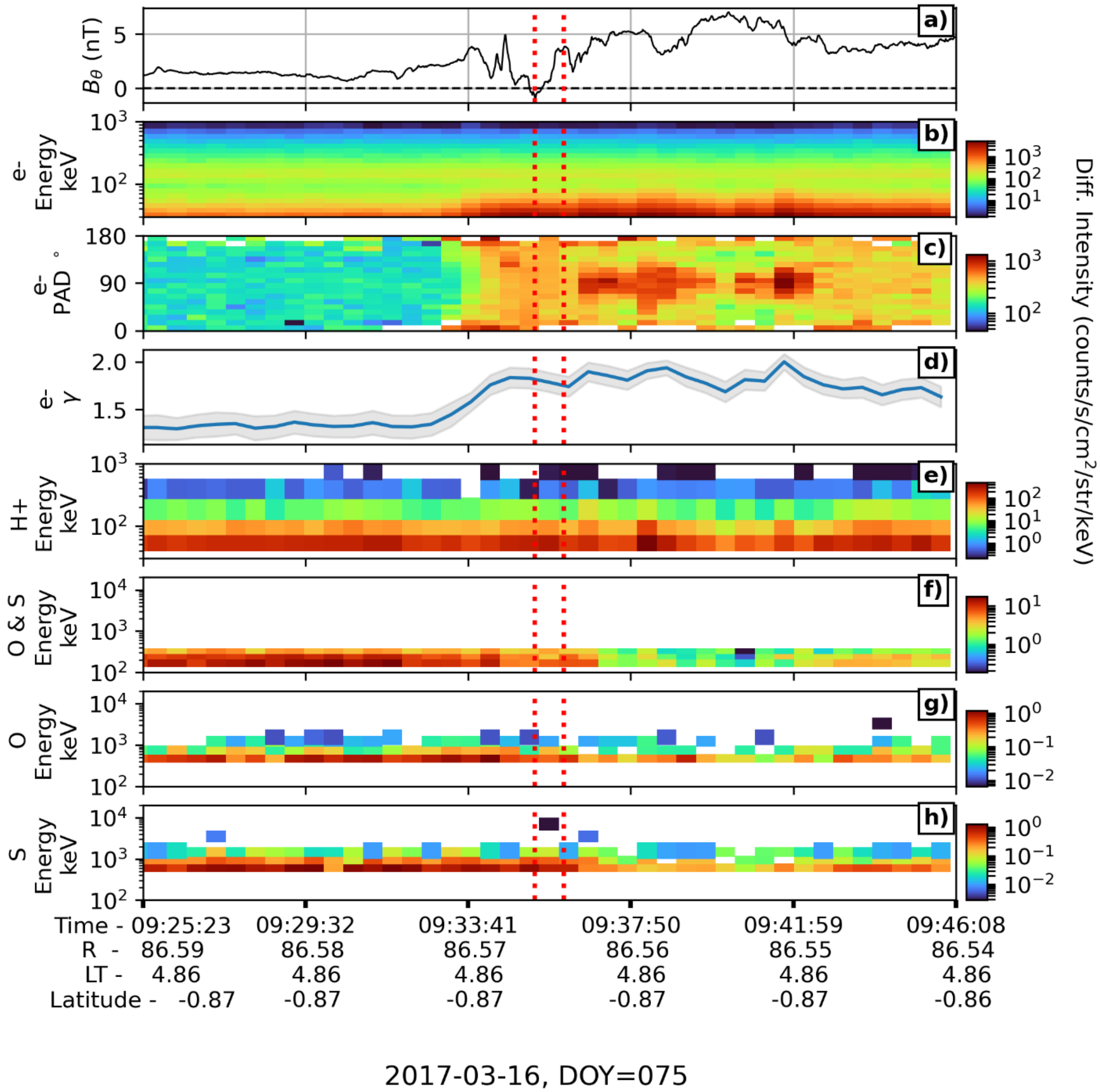

a)
b)
c)
d)
e)
f)
g)
h)
B_θ (nT)
e- Energy keV
e- PAD °
e- γ
H+ Energy keV
O & S Energy keV
O Energy keV
S Energy keV
Diff. Intensity (counts/s/cm²/str/keV)
Time - 09:25:23 09:29:32 09:33:41 09:37:50 09:41:59 09:46:08
R - 86.59 86.58 86.57 86.56 86.55 86.54
LT - 4.86 4.86 4.86 4.86 4.86 4.86
Latitude - -0.87 -0.87 -0.87 -0.87 -0.87 -0.86
2017-03-16, DOY=075

Figure S88

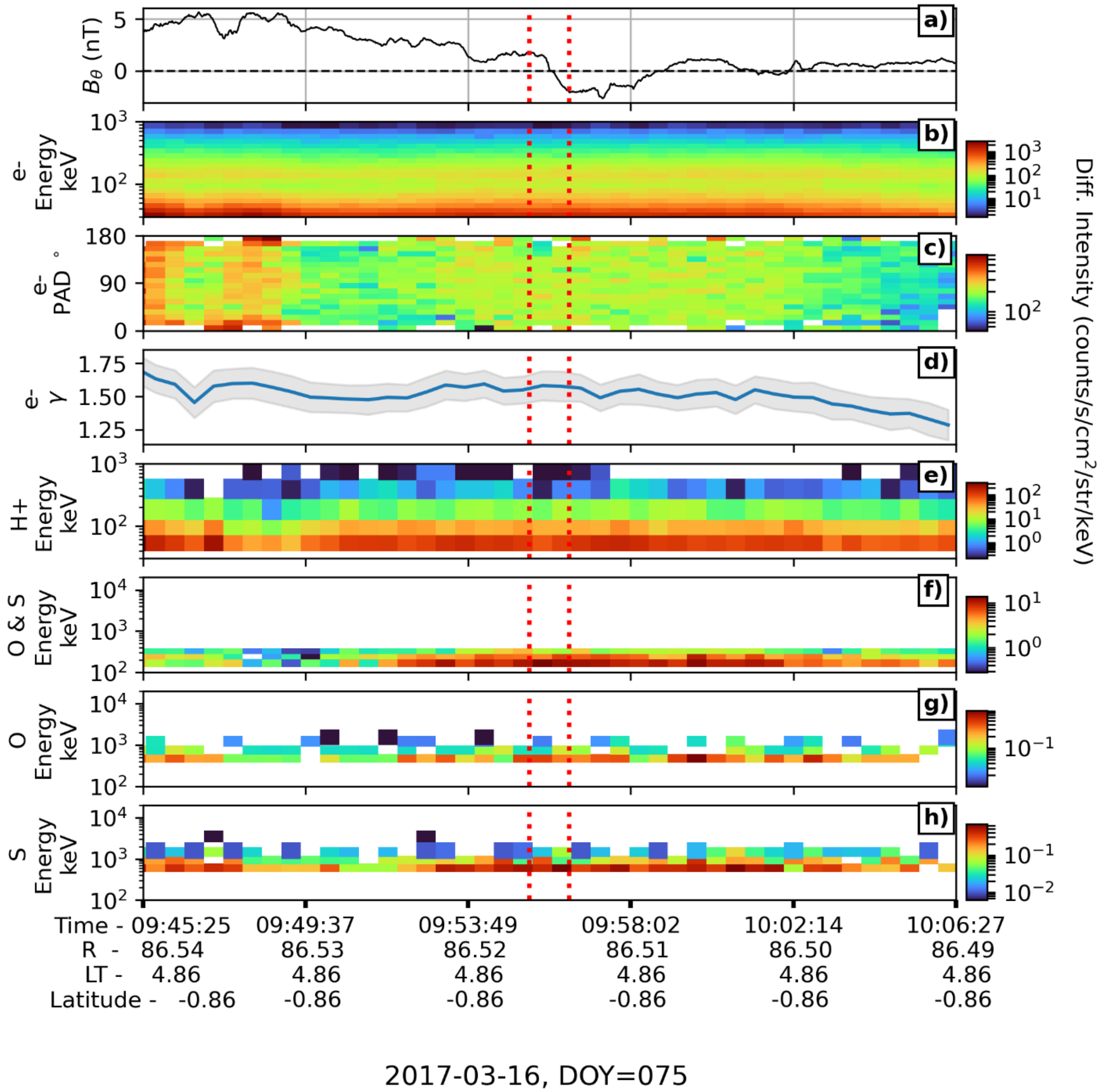

B_θ (nT)
e- Energy keV
e- PAD °
e- γ
H+ Energy keV
O & S Energy keV
O Energy keV
S Energy keV
a)
b)
c)
d)
e)
f)
g)
h)
Diff. Intensity (counts/s/cm^2/str/keV)
Time - 09:45:25 09:49:37 09:53:49 09:58:02 10:02:14 10:06:27
R - 86.54 86.53 86.52 86.51 86.50 86.49
LT - 4.86 4.86 4.86 4.86 4.86 4.86
Latitude - -0.86 -0.86 -0.86 -0.86 -0.86 -0.86
2017-03-16, DOY=075

Figure S89

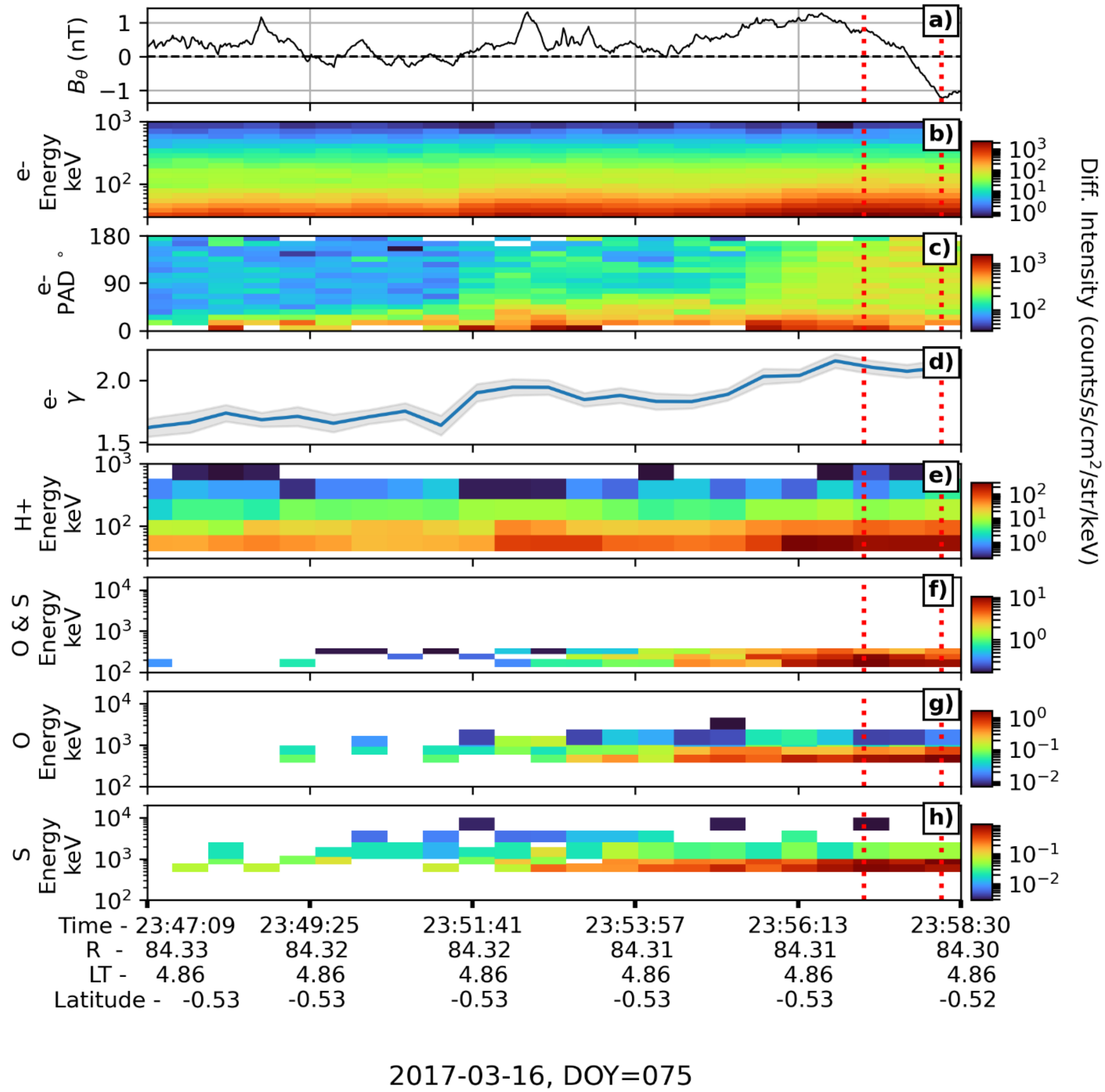
a)
b)
c)
d)
e)
f)
g)
h)
B_θ (nT)
e- Energy keV
e- PAD °
e- γ
H+ Energy keV
O & S Energy keV
O Energy keV
S Energy keV
Diff. Intensity (counts/s/cm^2/str/keV)
Time - 23:47:09 23:49:25 23:51:41 23:53:57 23:56:13 23:58:30
R - 84.33 84.32 84.32 84.31 84.31 84.30
LT - 4.86 4.86 4.86 4.86 4.86 4.86
Latitude - -0.53 -0.53 -0.53 -0.53 -0.53 -0.52
2017-03-16, DOY=075

Figure S90

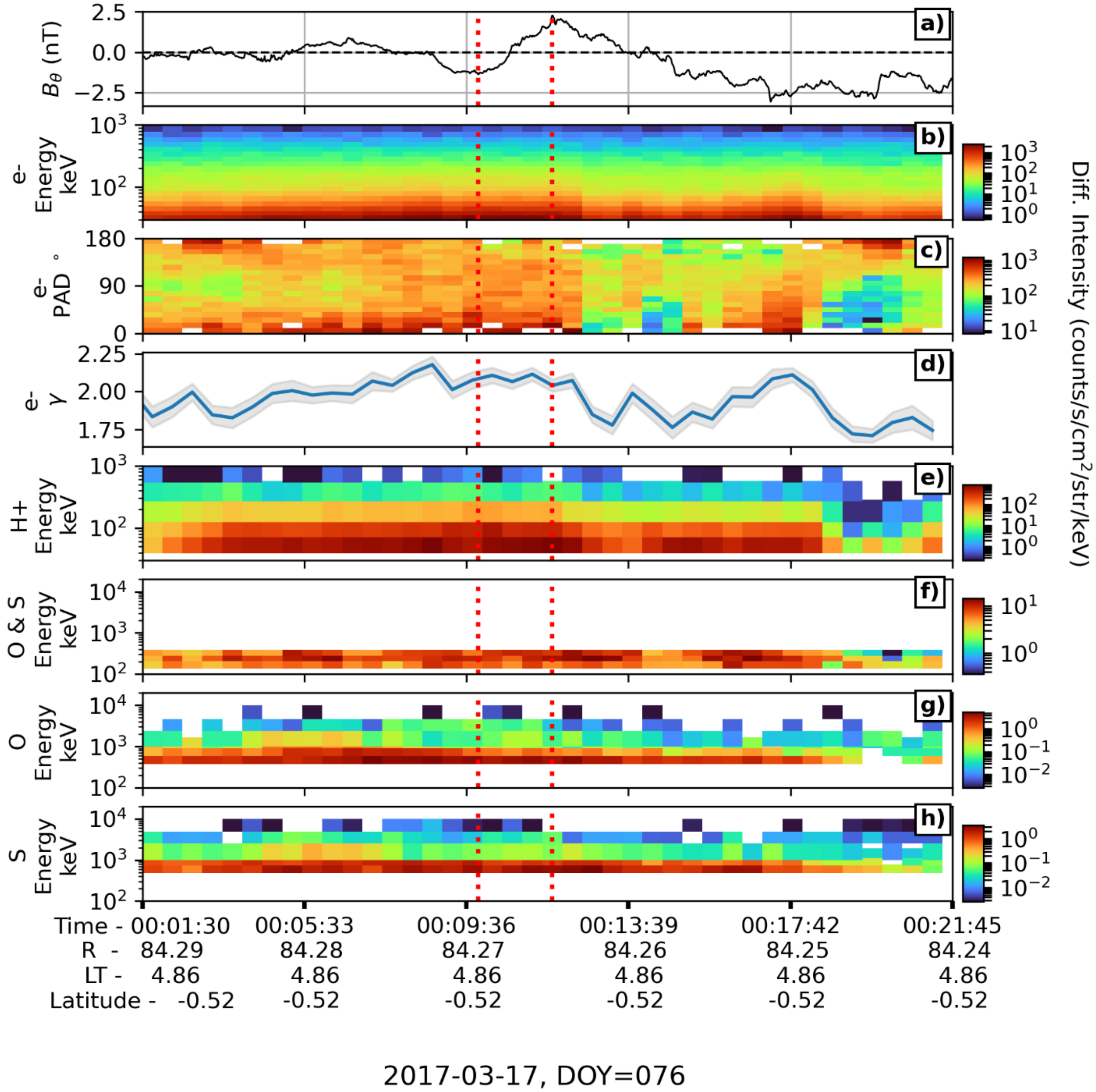

a)
b)
c)
d)
e)
f)
g)
h)
B_θ (nT)
e- Energy keV
e- PAD °
e- γ
H+ Energy keV
O & S Energy keV
O Energy keV
S Energy keV
Diff. Intensity (counts/s/cm^2/str/keV)
Time - 00:01:30 00:05:33 00:09:36 00:13:39 00:17:42 00:21:45
R - 84.29 84.28 84.27 84.26 84.25 84.24
LT - 4.86 4.86 4.86 4.86 4.86 4.86
Latitude - -0.52 -0.52 -0.52 -0.52 -0.52 -0.52
2017-03-17, DOY=076

Figure S91

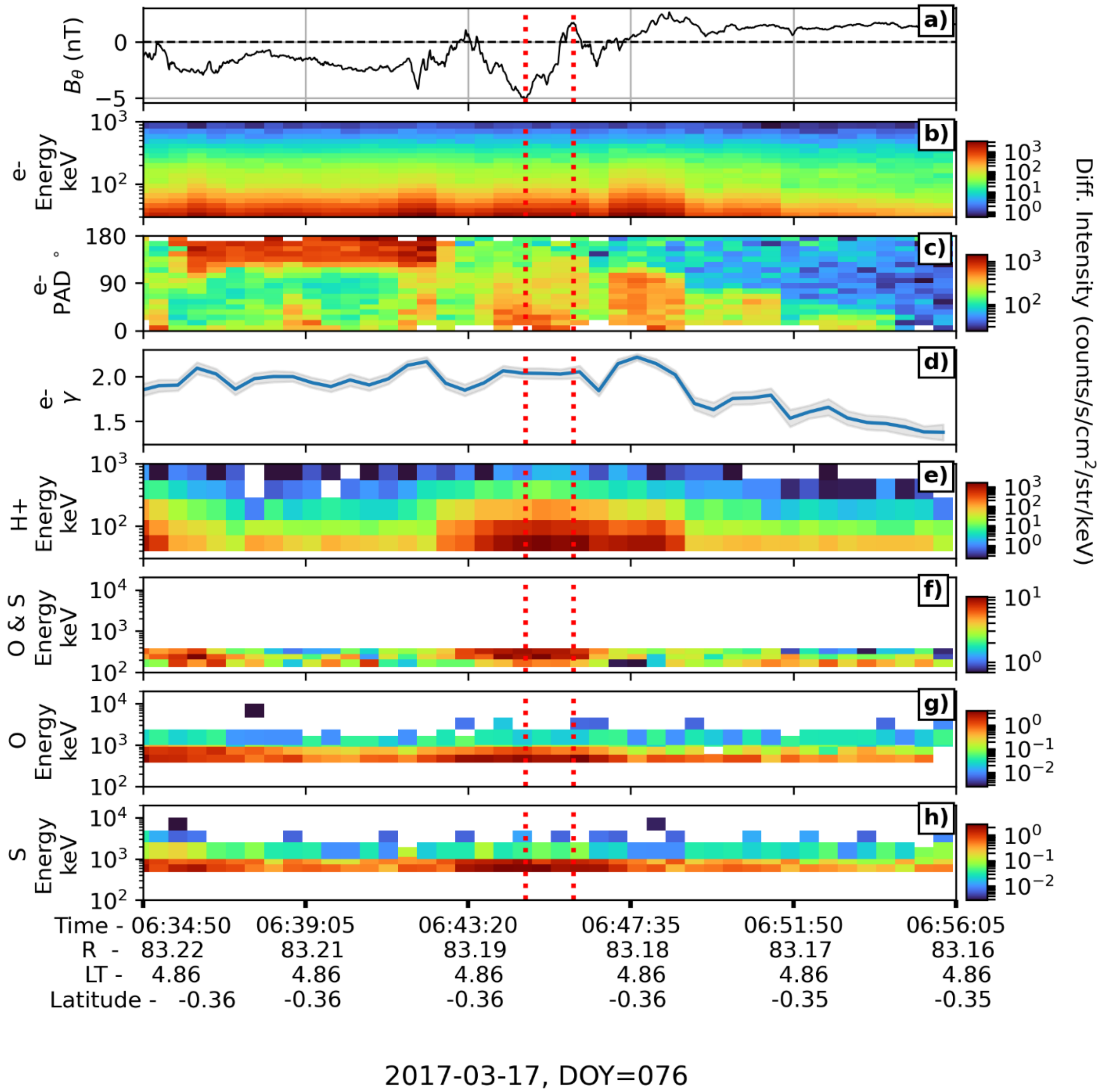

B_θ (nT)
e- Energy keV
e- PAD °
e- γ
H+ Energy keV
O & S Energy keV
O Energy keV
S Energy keV
Diff. Intensity (counts/s/cm^2/str/keV)
Time - 06:34:50 06:39:05 06:43:20 06:47:35 06:51:50 06:56:05
R - 83.22 83.21 83.19 83.18 83.17 83.16
LT - 4.86 4.86 4.86 4.86 4.86 4.86
Latitude - -0.36 -0.36 -0.36 -0.36 -0.35 -0.35
2017-03-17, DOY=076

Figure S92

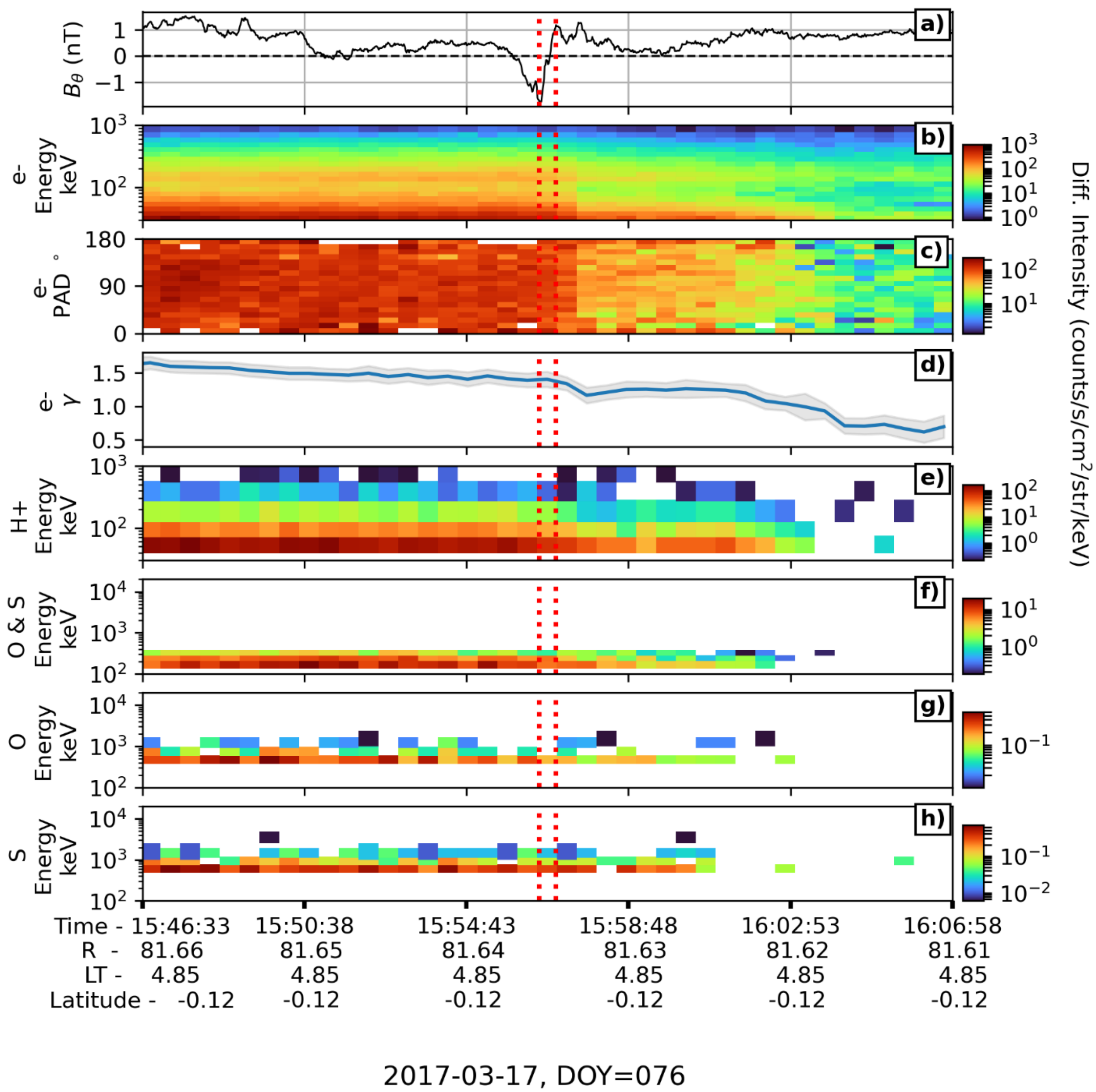
a)
b)
c)
d)
e)
f)
g)
h)
B_θ (nT)
e- Energy keV
e- PAD °
e- γ
H+ Energy keV
O & S Energy keV
O Energy keV
S Energy keV
Diff. Intensity (counts/s/cm^2/str/keV)
Time - 15:46:33 15:50:38 15:54:43 15:58:48 16:02:53 16:06:58
R - 81.66 81.65 81.64 81.63 81.62 81.61
LT - 4.85 4.85 4.85 4.85 4.85 4.85
Latitude - -0.12 -0.12 -0.12 -0.12 -0.12 -0.12
2017-03-17, DOY=076

Figure S93

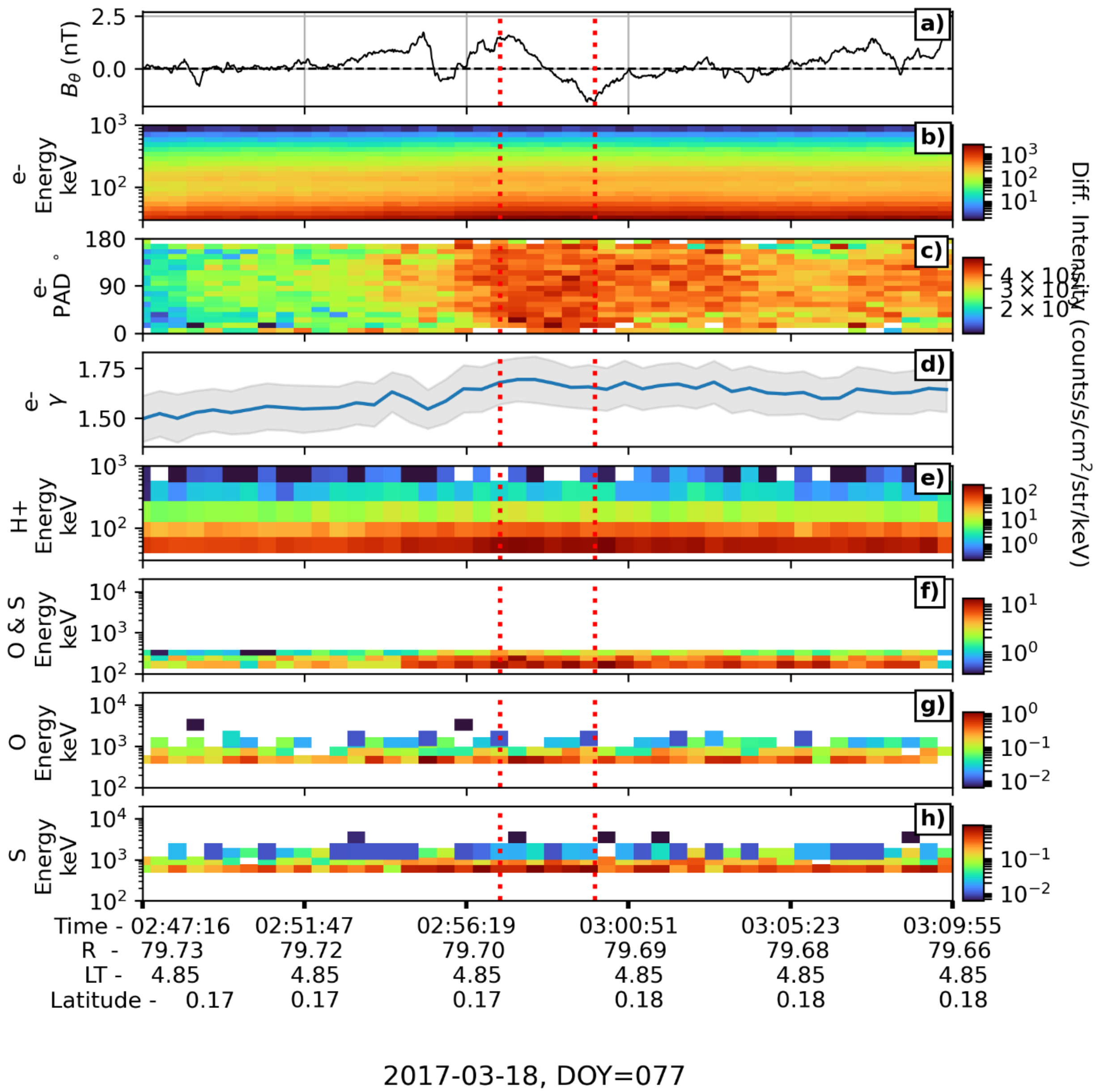
a)
b)
c)
d)
e)
f)
g)
h)
Time - 02:47:16 02:51:47 02:56:19 03:00:51 03:05:23 03:09:55
R - 79.73 79.72 79.70 79.69 79.68 79.66
LT - 4.85 4.85 4.85 4.85 4.85 4.85
Latitude - 0.17 0.17 0.17 0.18 0.18 0.18
Diff. Intensity (counts/s/cm²/str/keV)
2017-03-18, DOY=077

Figure S94

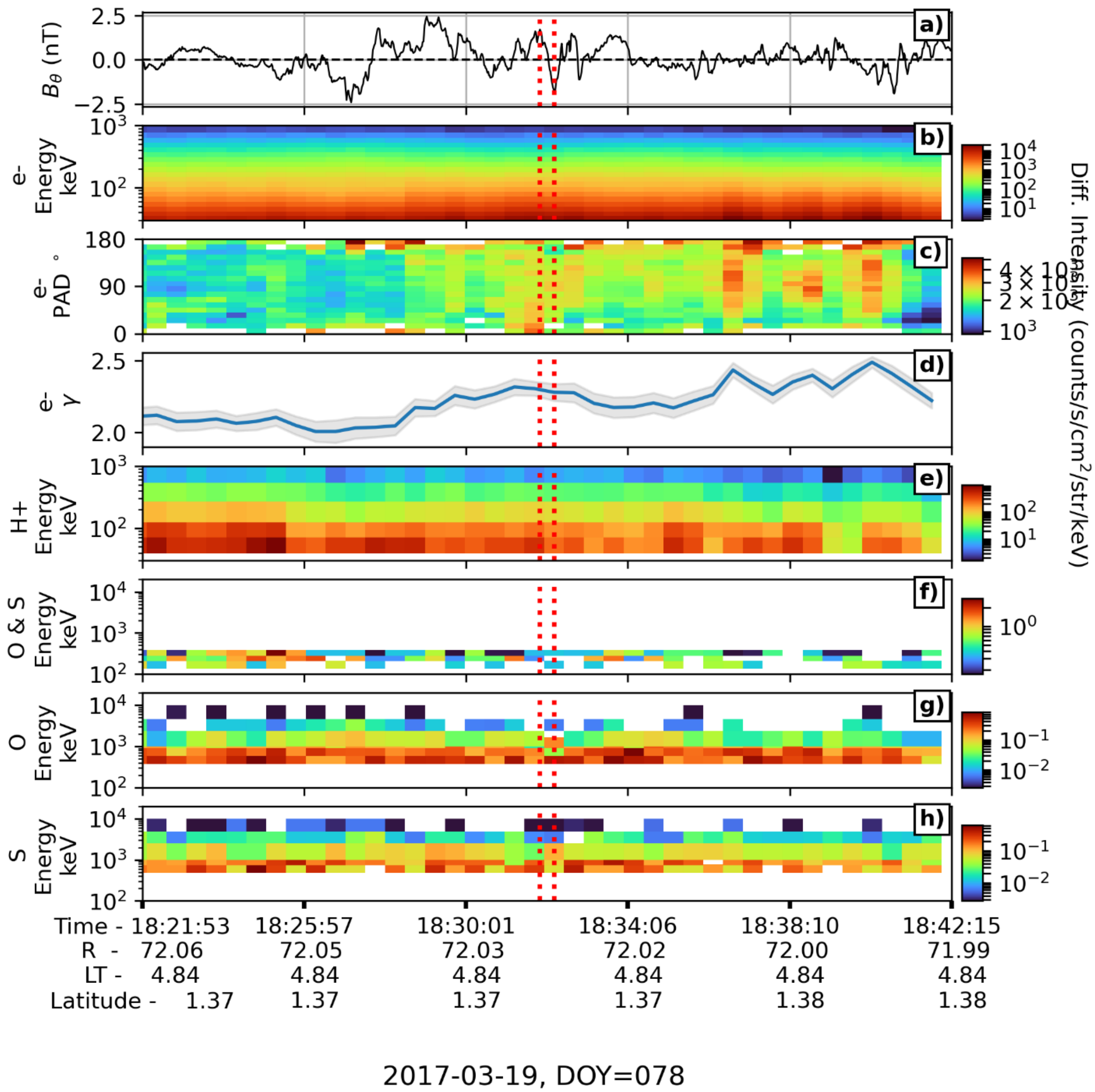

B_θ (nT)
e- Energy keV
e- PAD °
e- γ
H+ Energy keV
O & S Energy keV
O Energy keV
S Energy keV
a)
b)
c)
d)
e)
f)
g)
h)
Diff. Intensity (counts/s/cm^2/str/keV)
Time - 18:21:53 18:25:57 18:30:01 18:34:06 18:38:10 18:42:15
R - 72.06 72.05 72.03 72.02 72.00 71.99
LT - 4.84 4.84 4.84 4.84 4.84 4.84
Latitude - 1.37 1.37 1.37 1.37 1.38 1.38
2017-03-19, DOY=078

Figure S95

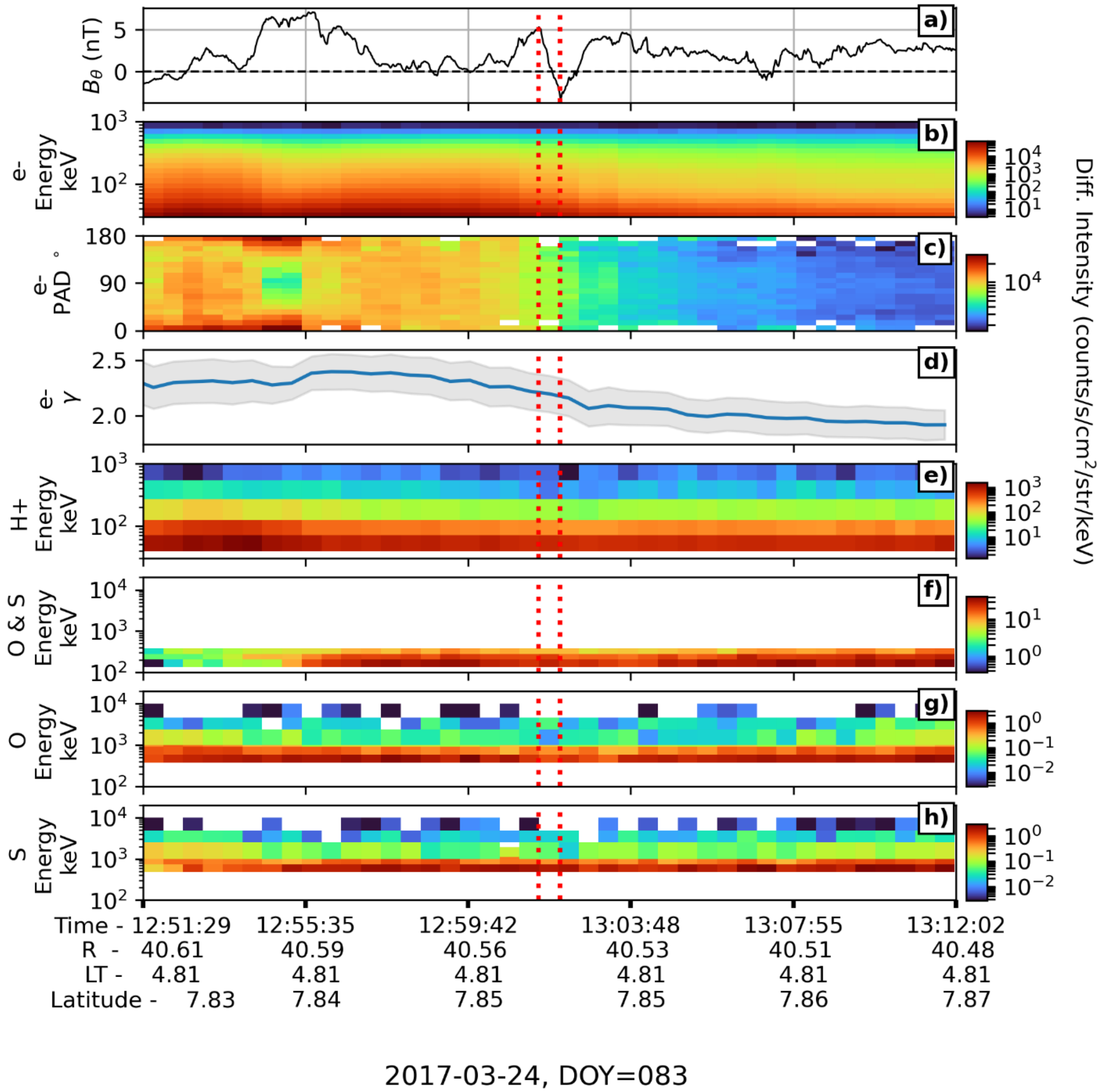
a)
b)
c)
d)
e)
f)
g)
h)
B_θ (nT)
e- Energy keV
e- PAD °
e- γ
H+ Energy keV
O & S Energy keV
O Energy keV
S Energy keV
Diff. Intensity (counts/s/cm^2/str/keV)
Time - 12:51:29 12:55:35 12:59:42 13:03:48 13:07:55 13:12:02
R - 40.61 40.59 40.56 40.53 40.51 40.48
LT - 4.81 4.81 4.81 4.81 4.81 4.81
Latitude - 7.83 7.84 7.85 7.85 7.86 7.87
2017-03-24, DOY=083

Figure S96

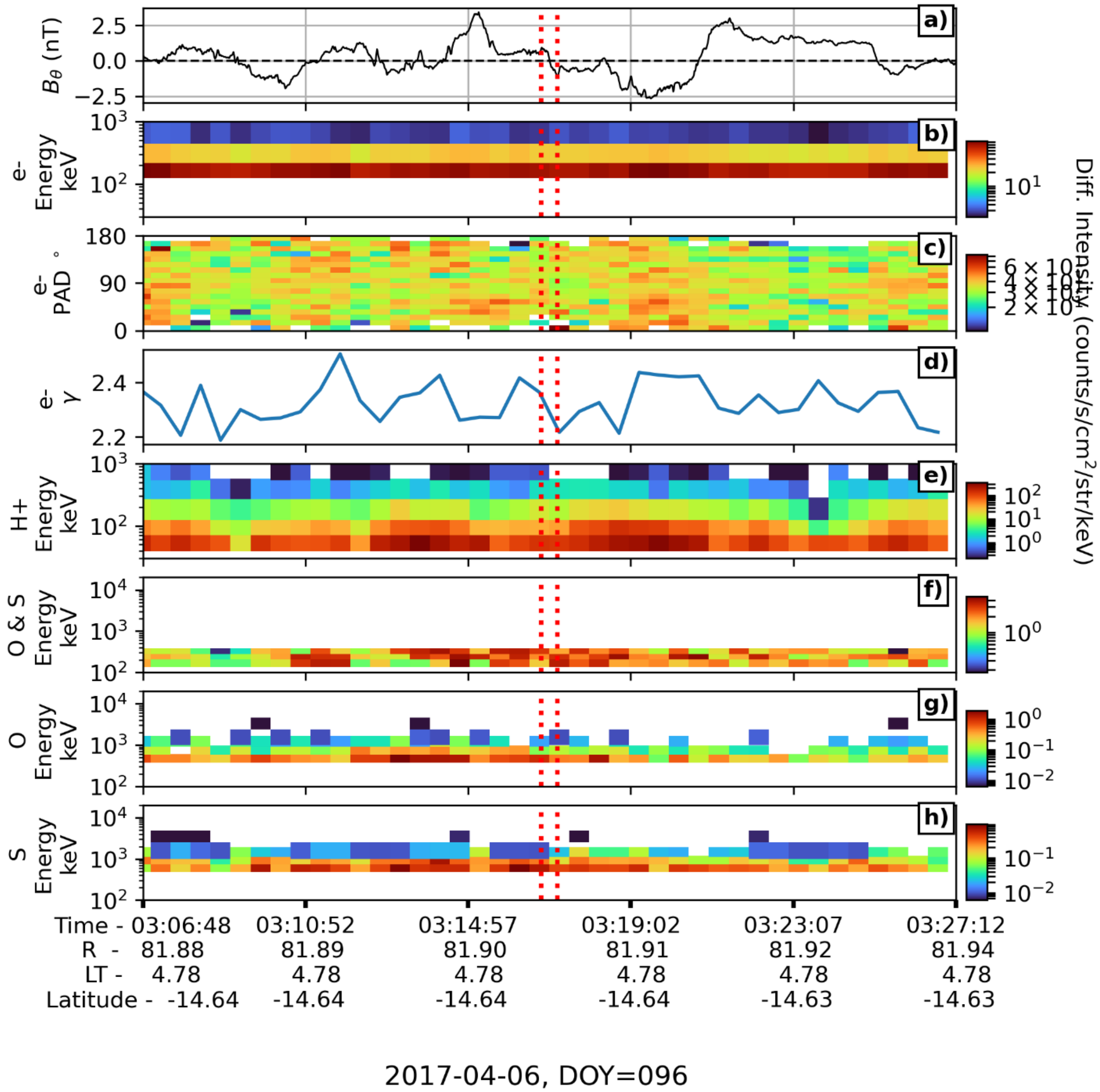

2017-04-06, DOY=096

Figure S97

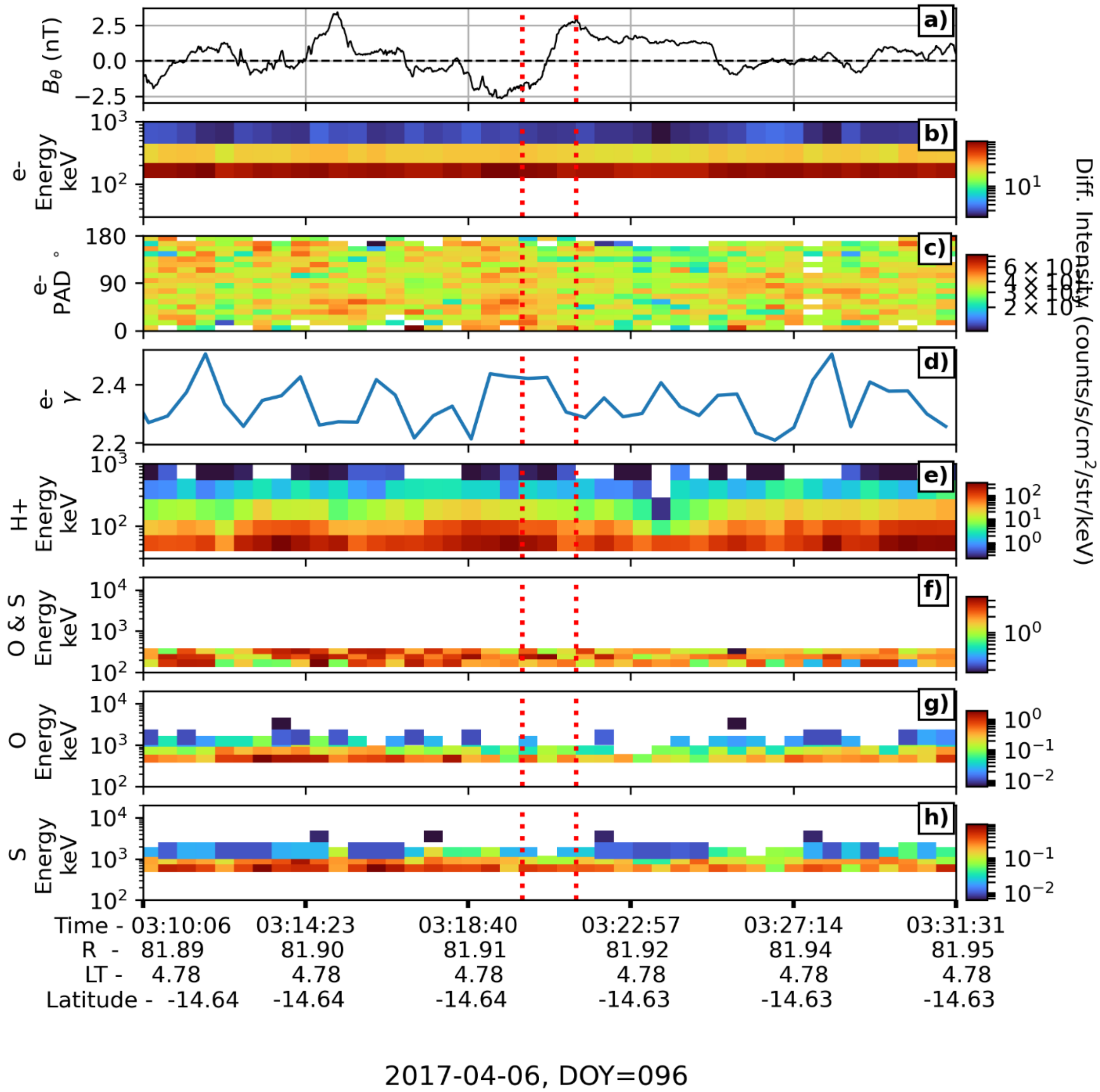
a)
b)
c)
d)
e)
f)
g)
h)
B_θ (nT)
e- Energy keV
e- PAD °
e- γ
H+ Energy keV
O & S Energy keV
O Energy keV
S Energy keV
Diff. Intensity (counts/s/cm^2/str/keV)
Time - 03:10:06 03:14:23 03:18:40 03:22:57 03:27:14 03:31:31
R - 81.89 81.90 81.91 81.92 81.94 81.95
LT - 4.78 4.78 4.78 4.78 4.78 4.78
Latitude - -14.64 -14.64 -14.64 -14.63 -14.63 -14.63
2017-04-06, DOY=096

Figure S98

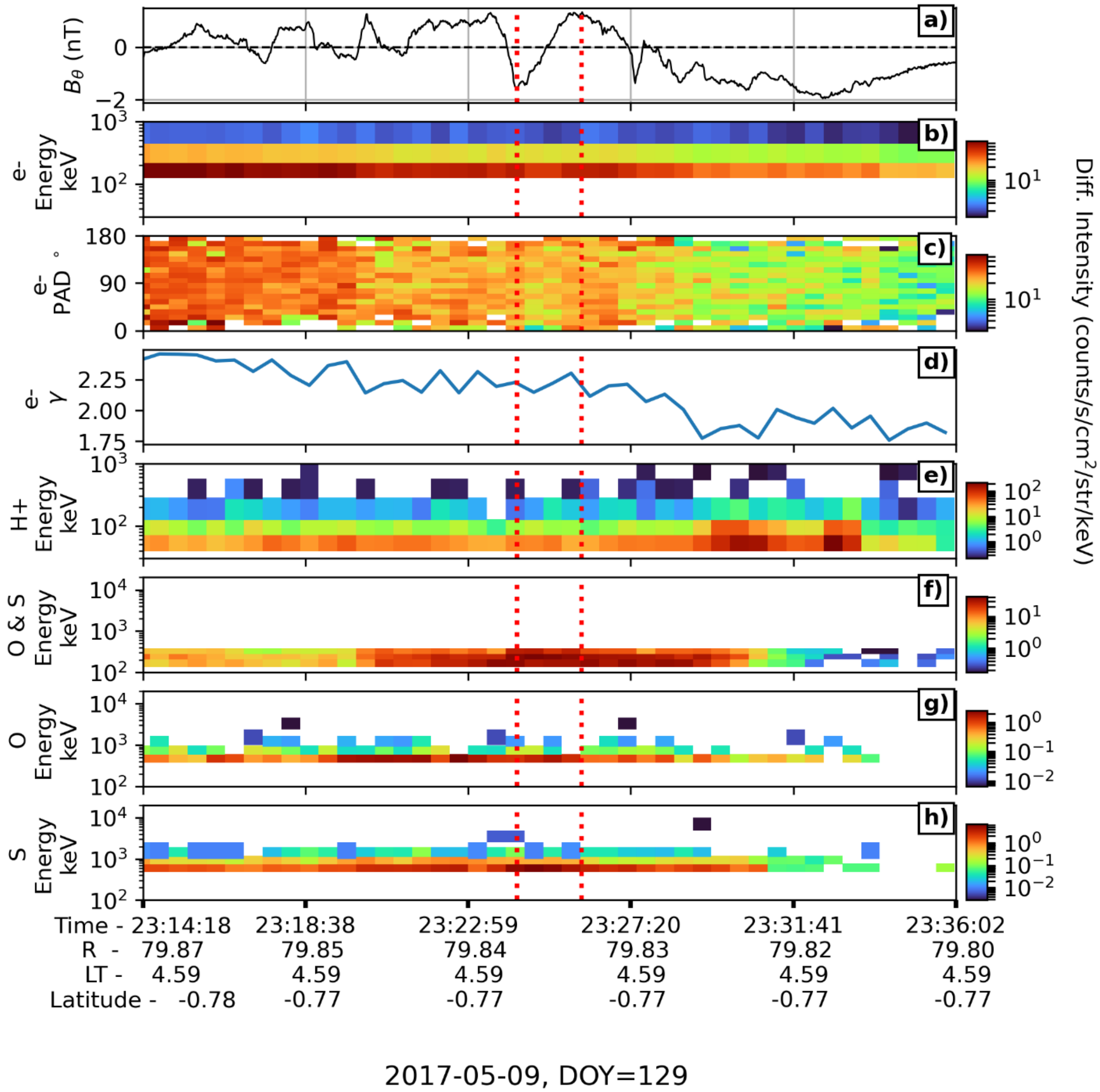

a)
b)
c)
d)
e)
f)
g)
h)
B_θ (nT)
e- Energy keV
e- PAD °
e- γ
H+ Energy keV
O & S Energy keV
O Energy keV
S Energy keV
Diff. Intensity (counts/s/cm²/str/keV)
Time - 23:14:18 23:18:38 23:22:59 23:27:20 23:31:41 23:36:02
R - 79.87 79.85 79.84 79.83 79.82 79.80
LT - 4.59 4.59 4.59 4.59 4.59 4.59
Latitude - -0.78 -0.77 -0.77 -0.77 -0.77 -0.77
2017-05-09, DOY=129

Figure S99

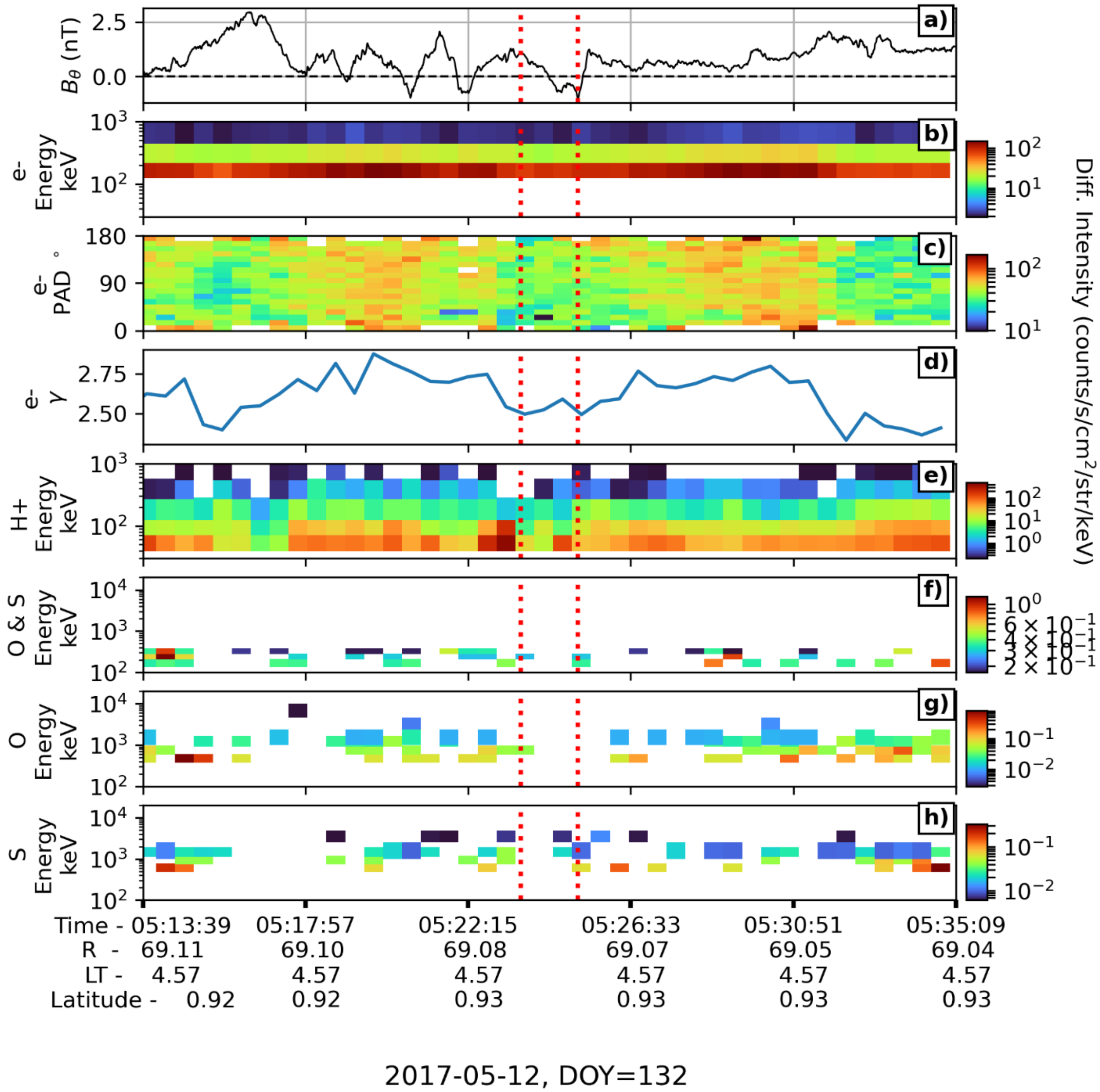
a)
b)
c)
d)
e)
f)
g)
h)
B_θ (nT)
e- Energy keV
e- PAD °
e- γ
H+ Energy keV
O & S Energy keV
O Energy keV
S Energy keV
Diff. Intensity (counts/s/cm^2/str/keV)
Time - 05:13:39 05:17:57 05:22:15 05:26:33 05:30:51 05:35:09
R - 69.11 69.10 69.08 69.07 69.05 69.04
LT - 4.57 4.57 4.57 4.57 4.57 4.57
Latitude - 0.92 0.92 0.93 0.93 0.93 0.93
2017-05-12, DOY=132

Figure S100

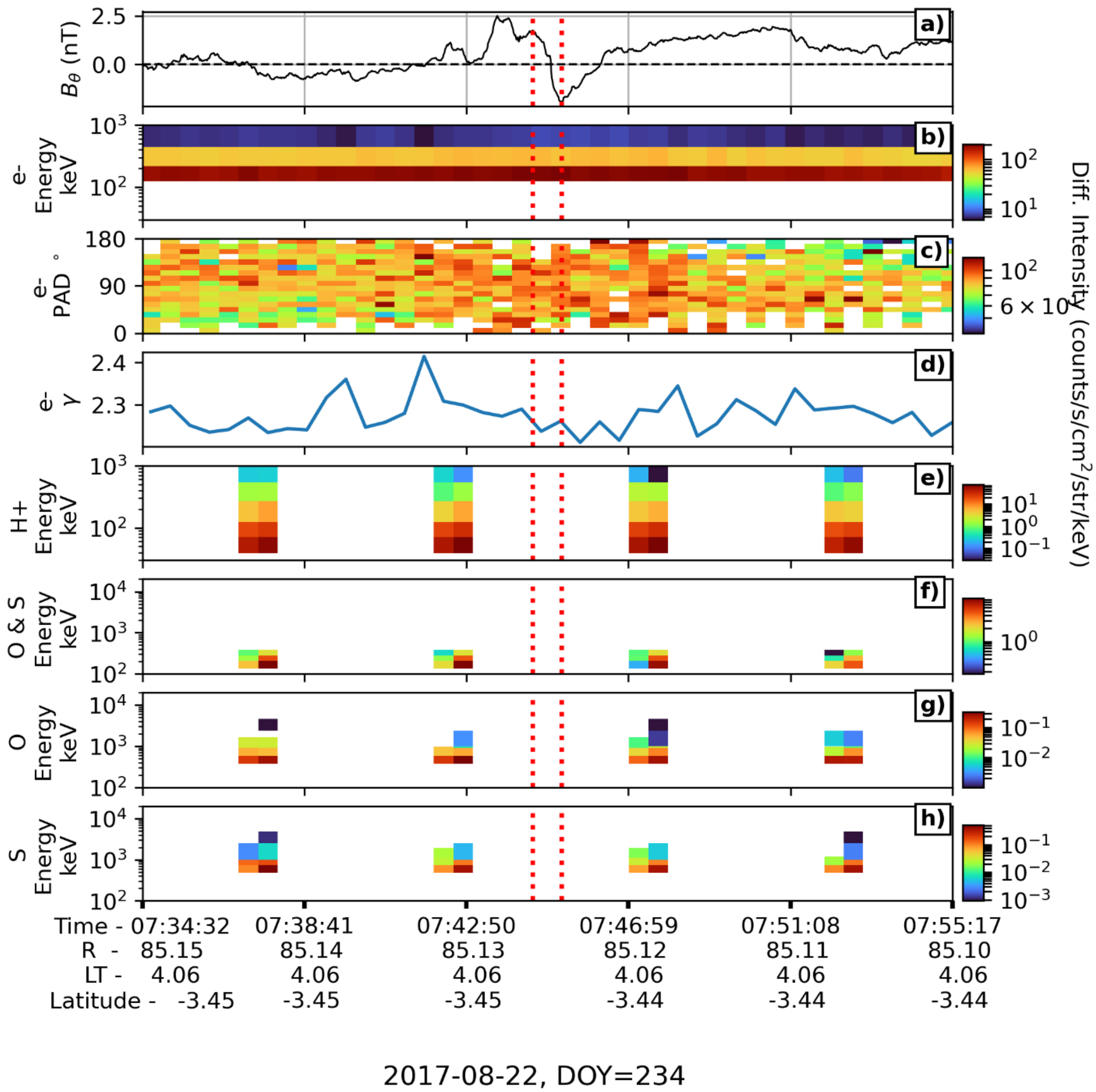

a)
b)
c)
d)
e)
f)
g)
h)
B_θ (nT)
e- Energy keV
e- PAD °
e- γ
H+ Energy keV
O & S Energy keV
O Energy keV
S Energy keV
Diff. Intensity (counts/s/cm^2/str/keV)
Time - 07:34:32 07:38:41 07:42:50 07:46:59 07:51:08 07:55:17
R - 85.15 85.14 85.13 85.12 85.11 85.10
LT - 4.06 4.06 4.06 4.06 4.06 4.06
Latitude - -3.45 -3.45 -3.45 -3.44 -3.44 -3.44
2017-08-22, DOY=234

Figure S101

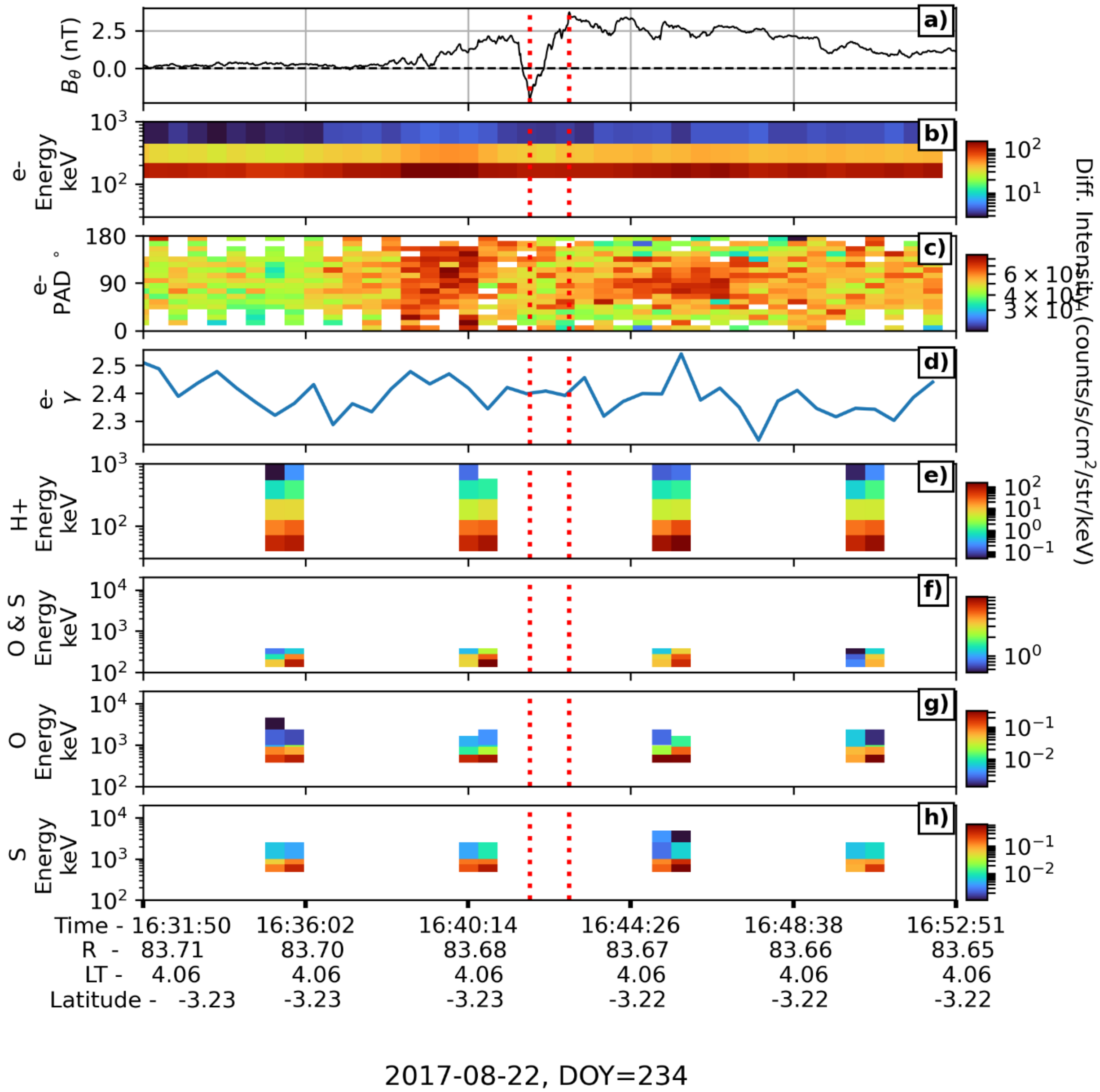
a)
b)
c)
d)
e)
f)
g)
h)
B_θ (nT)
e- Energy keV
e- PAD °
e- γ
H+ Energy keV
O & S Energy keV
O Energy keV
S Energy keV
Diff. Intensity (counts/s/cm^2/str/keV)
Time - 16:31:50 16:36:02 16:40:14 16:44:26 16:48:38 16:52:51
R - 83.71 83.70 83.68 83.67 83.66 83.65
LT - 4.06 4.06 4.06 4.06 4.06 4.06
Latitude - -3.23 -3.23 -3.23 -3.22 -3.22 -3.22
2017-08-22, DOY=234

Figure S102

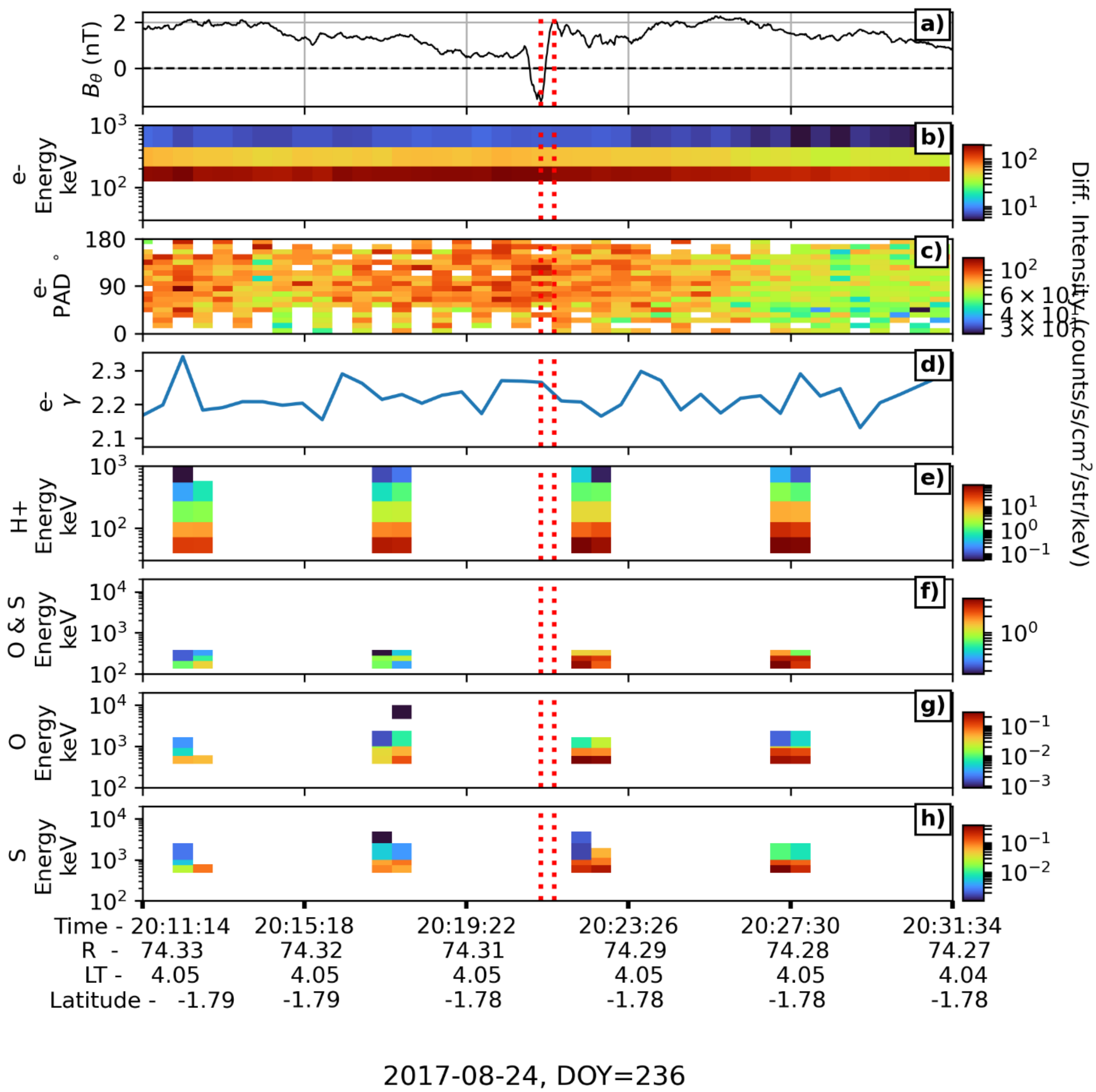
a)
b)
c)
d)
e)
f)
g)
h)
B_θ (nT)
e- Energy keV
e- PAD °
e- γ
H+ Energy keV
O & S Energy keV
O Energy keV
S Energy keV
Diff. Intensity (counts/s/cm²/str/keV)
Time - 20:11:14 20:15:18 20:19:22 20:23:26 20:27:30 20:31:34
R - 74.33 74.32 74.31 74.29 74.28 74.27
LT - 4.05 4.05 4.05 4.05 4.05 4.04
Latitude - -1.79 -1.79 -1.78 -1.78 -1.78 -1.78
2017-08-24, DOY=236

Figure S103

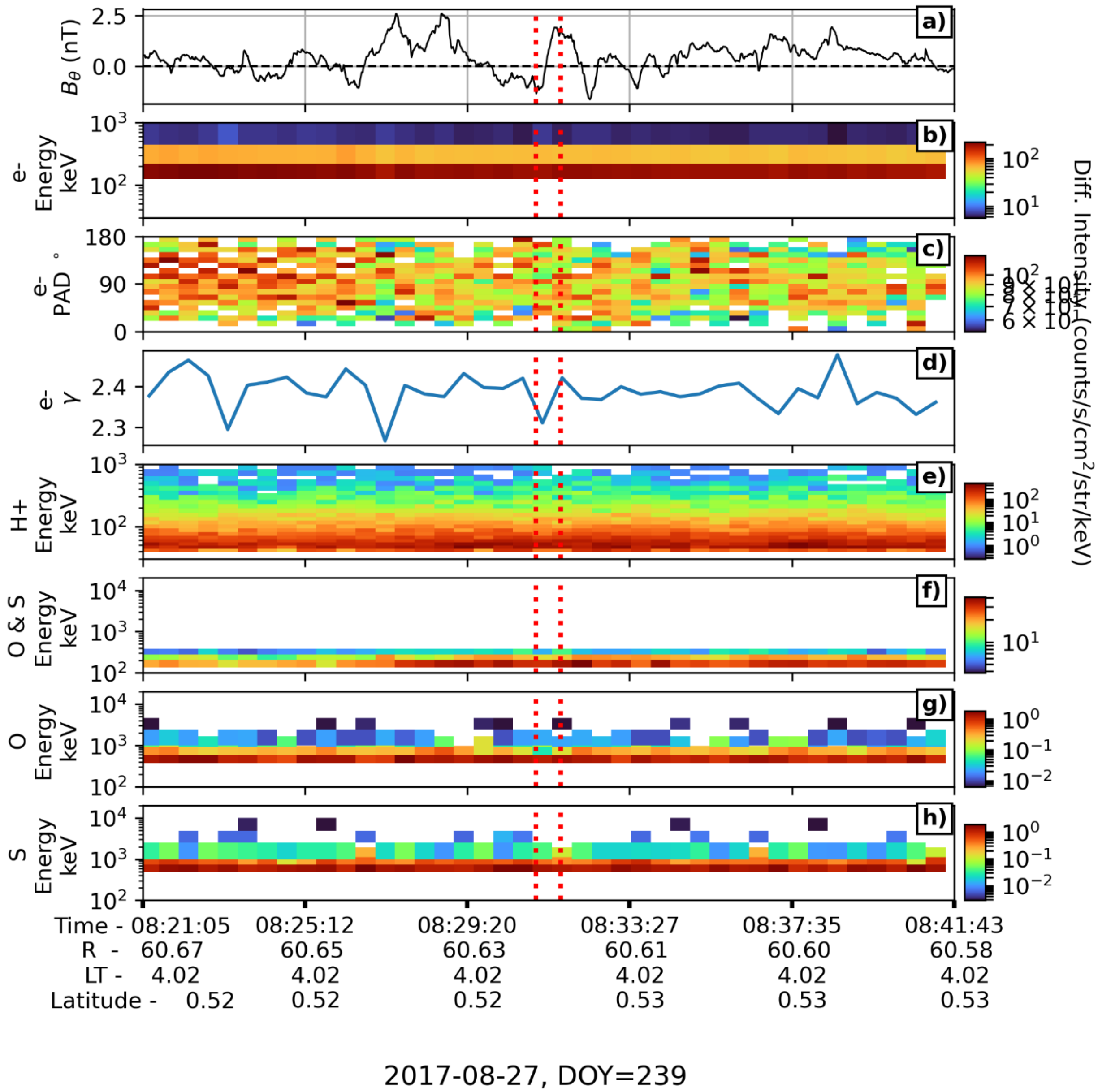

a)
b)
c)
d)
e)
f)
g)
h)
B_θ (nT)
e- Energy keV
e- PAD °
e- γ
H+ Energy keV
O & S Energy keV
O Energy keV
S Energy keV
Diff. Intensity (counts/s/cm^2/str/keV)
Time - 08:21:05 08:25:12 08:29:20 08:33:27 08:37:35 08:41:43
R - 60.67 60.65 60.63 60.61 60.60 60.58
LT - 4.02 4.02 4.02 4.02 4.02 4.02
Latitude - 0.52 0.52 0.52 0.53 0.53 0.53
2017-08-27, DOY=239

Figure S104

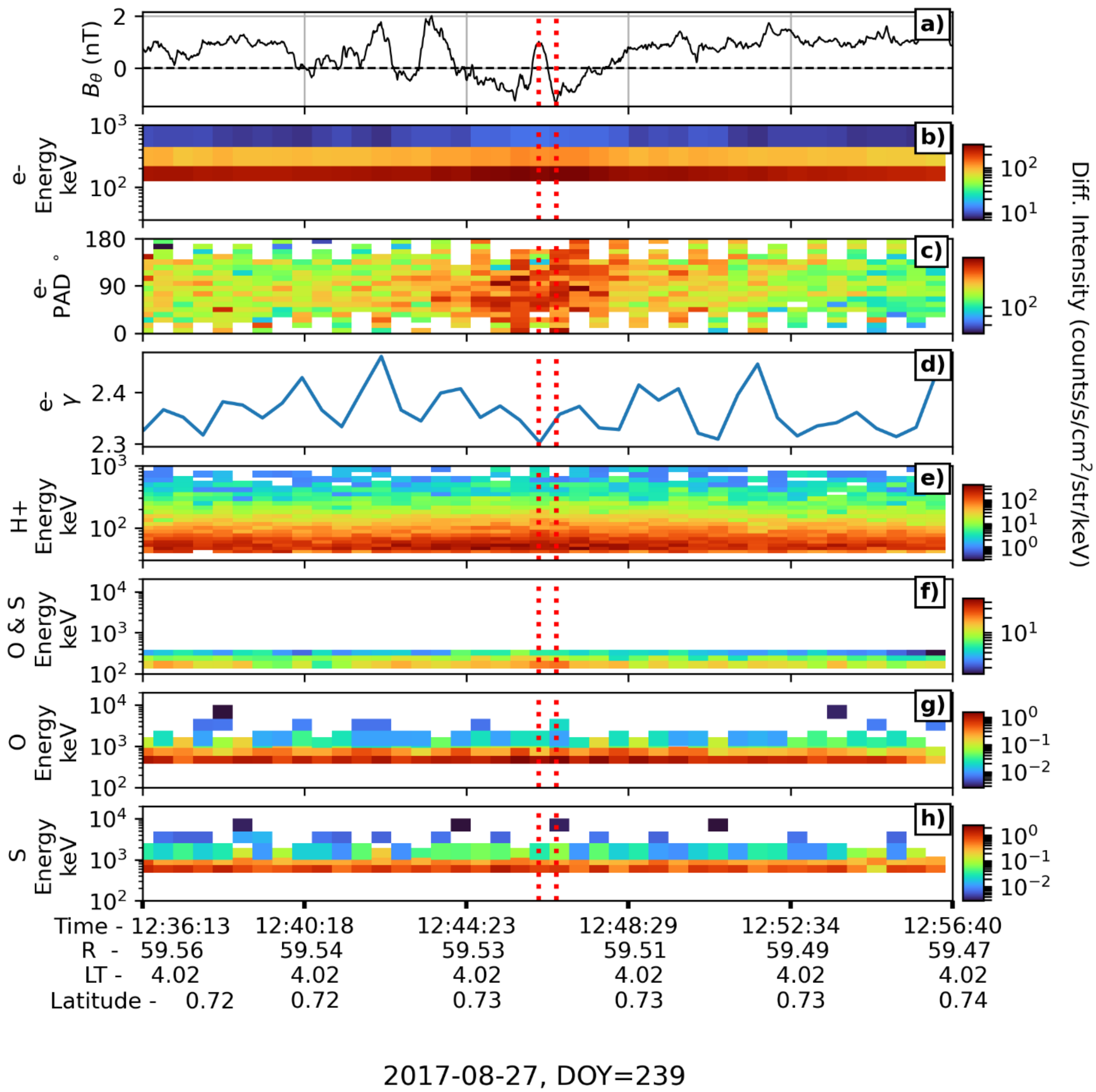

a)
b)
c)
d)
e)
f)
g)
h)
B_θ (nT)
e- Energy keV
e- PAD °
e- γ
H+ Energy keV
O & S Energy keV
O Energy keV
S Energy keV
Diff. Intensity (counts/s/cm²/str/keV)
Time - 12:36:13 12:40:18 12:44:23 12:48:29 12:52:34 12:56:40
R - 59.56 59.54 59.53 59.51 59.49 59.47
LT - 4.02 4.02 4.02 4.02 4.02 4.02
Latitude - 0.72 0.72 0.73 0.73 0.73 0.74
2017-08-27, DOY=239

Figure S105

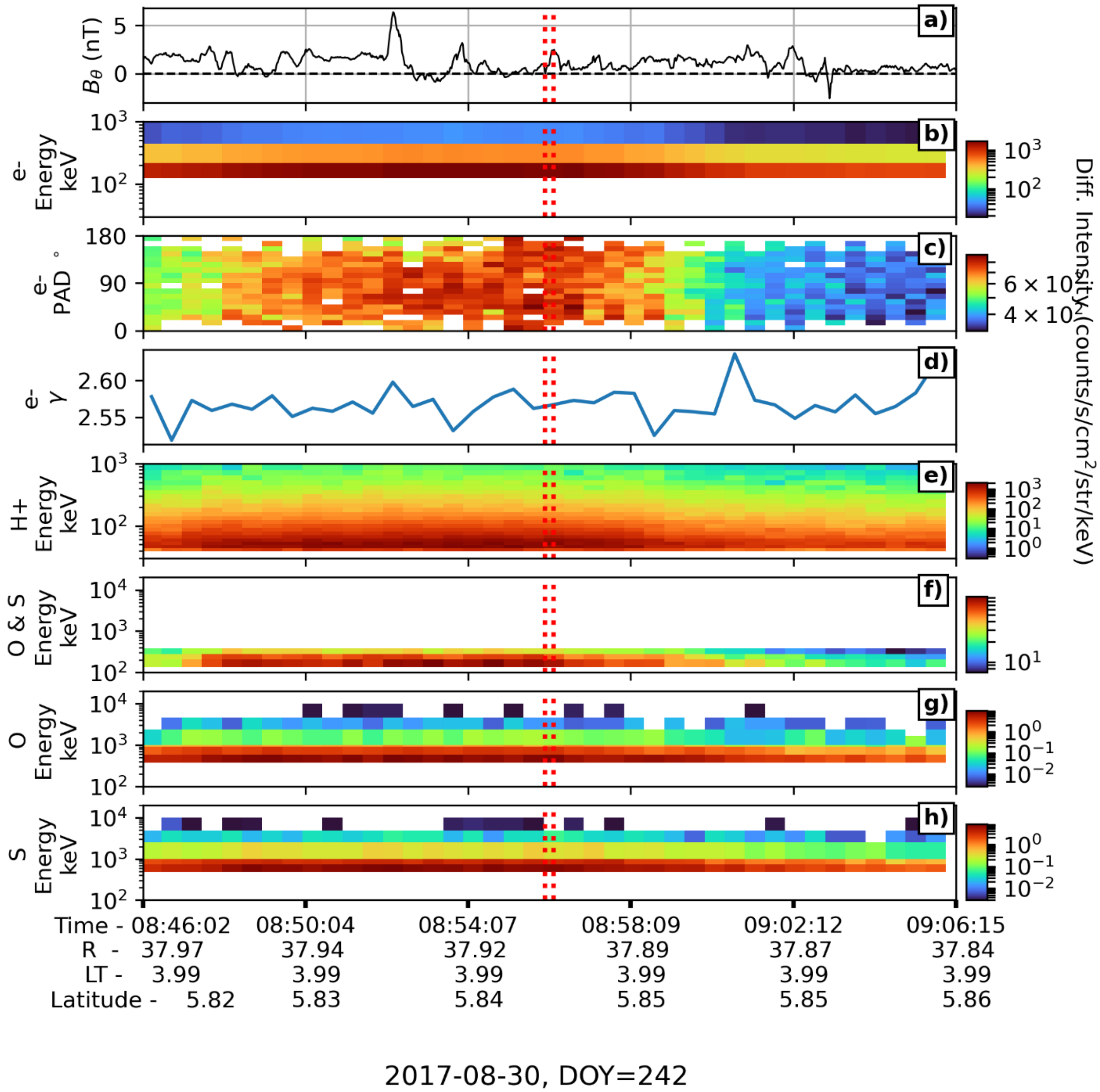

a)
b)
c)
d)
e)
f)
g)
h)
B_θ (nT)
e- Energy keV
e- PAD °
e- γ
H+ Energy keV
O & S Energy keV
O Energy keV
S Energy keV
Diff. Intensity (counts/s/cm²/str/keV)
Time - 08:46:02 08:50:04 08:54:07 08:58:09 09:02:12 09:06:15
R - 37.97 37.94 37.92 37.89 37.87 37.84
LT - 3.99 3.99 3.99 3.99 3.99 3.99
Latitude - 5.82 5.83 5.84 5.85 5.85 5.86
2017-08-30, DOY=242

Figure S106

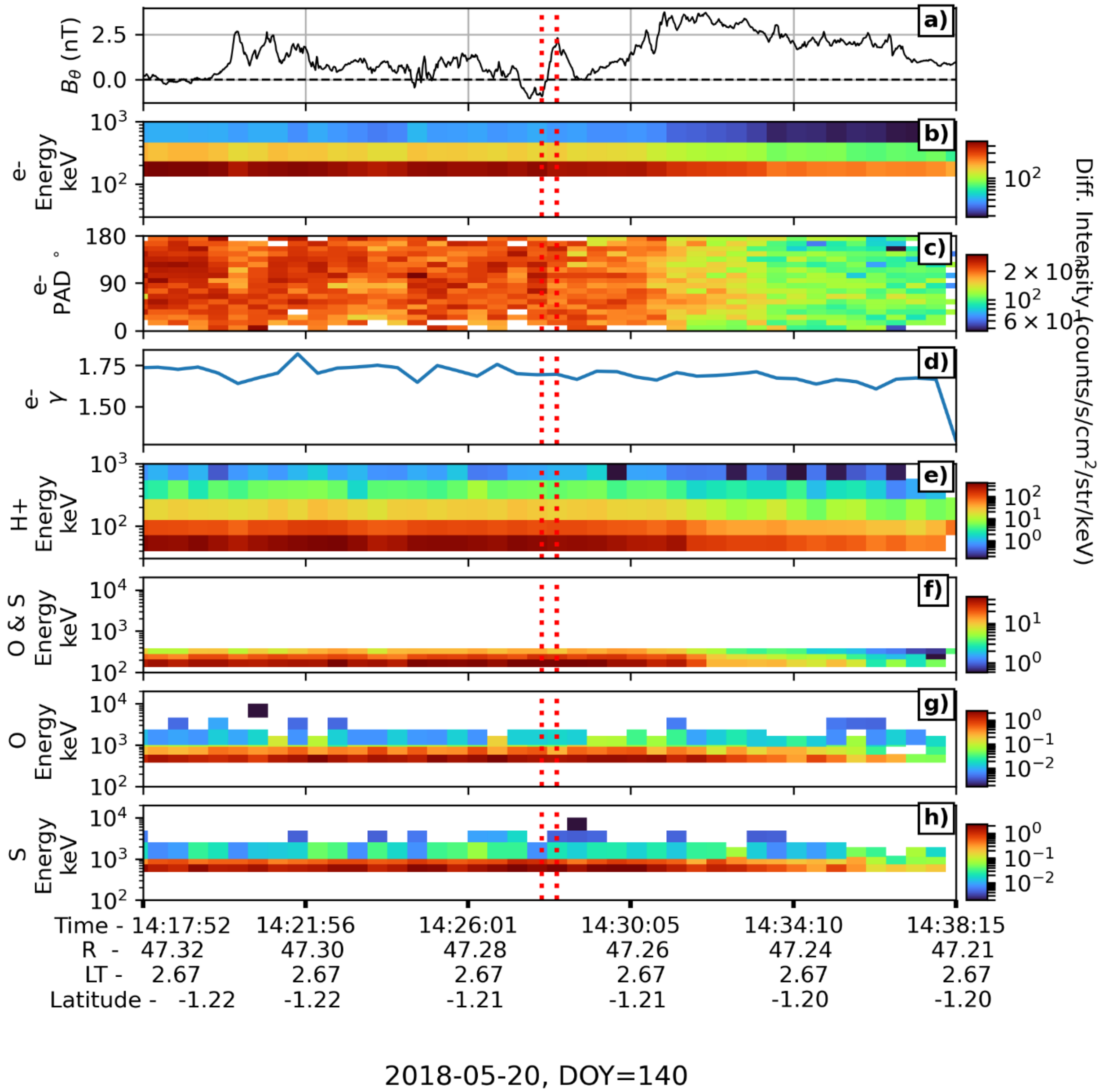

a)
b)
c)
d)
e)
f)
g)
h)
B_θ (nT)
e- Energy keV
e- PAD °
e- γ
H+ Energy keV
O & S Energy keV
O Energy keV
S Energy keV
Diff. Intensity (counts/s/cm^2/str/keV)
Time - 14:17:52 14:21:56 14:26:01 14:30:05 14:34:10 14:38:15
R - 47.32 47.30 47.28 47.26 47.24 47.21
LT - 2.67 2.67 2.67 2.67 2.67 2.67
Latitude - -1.22 -1.22 -1.21 -1.21 -1.20 -1.20
2018-05-20, DOY=140

Figure S107

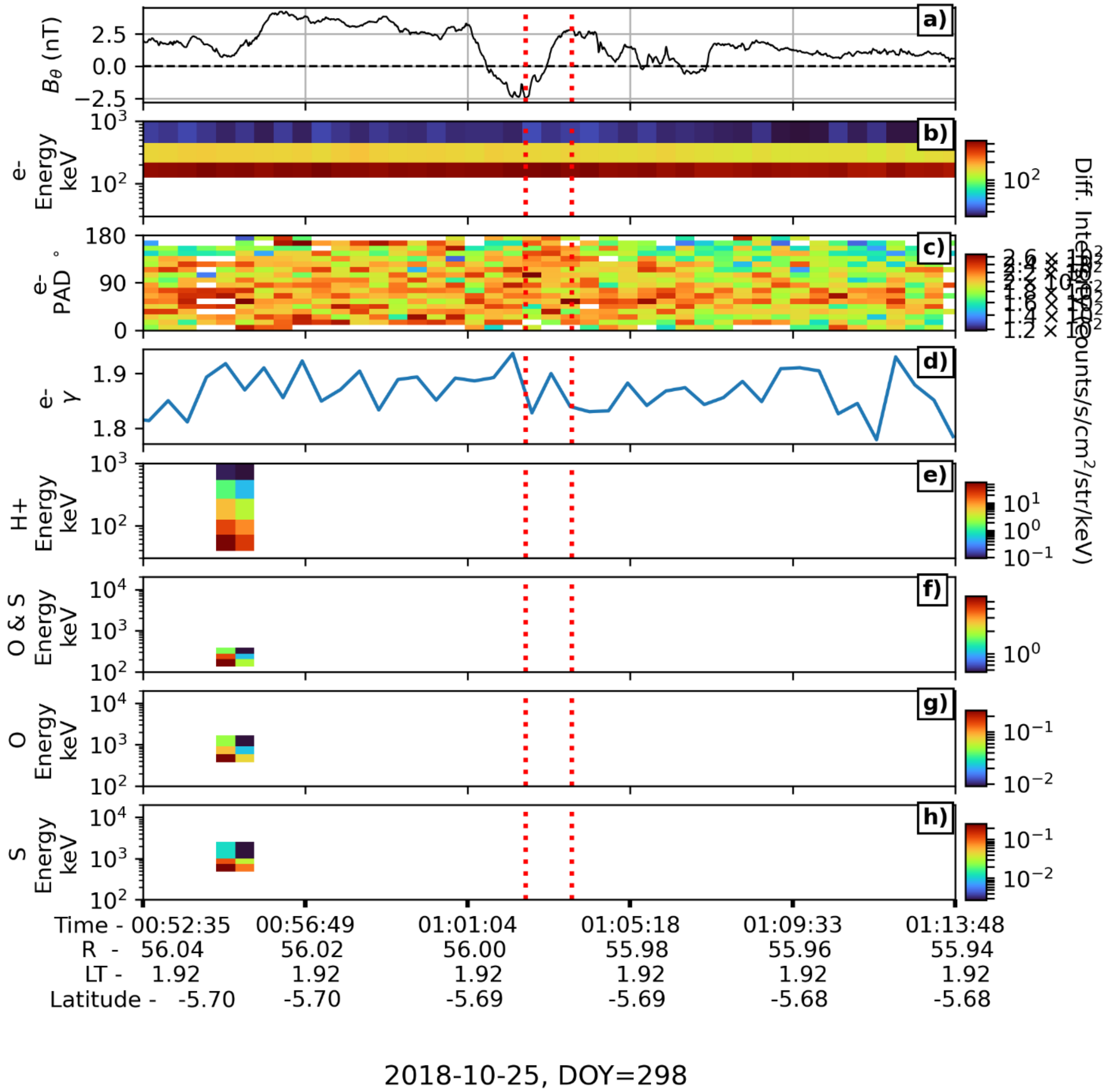
a)
B_θ (nT)
b)
e- Energy keV
c)
e- PAD °
d)
e- γ
e)
H+ Energy keV
f)
O & S Energy keV
g)
O Energy keV
h)
S Energy keV
Diff. Intensity (counts/s/cm^2/str/keV)
Time - 00:52:35 00:56:49 01:01:04 01:05:18 01:09:33 01:13:48
R - 56.04 56.02 56.00 55.98 55.96 55.94
LT - 1.92 1.92 1.92 1.92 1.92 1.92
Latitude - -5.70 -5.70 -5.69 -5.69 -5.68 -5.68
2018-10-25, DOY=298

Figure S108

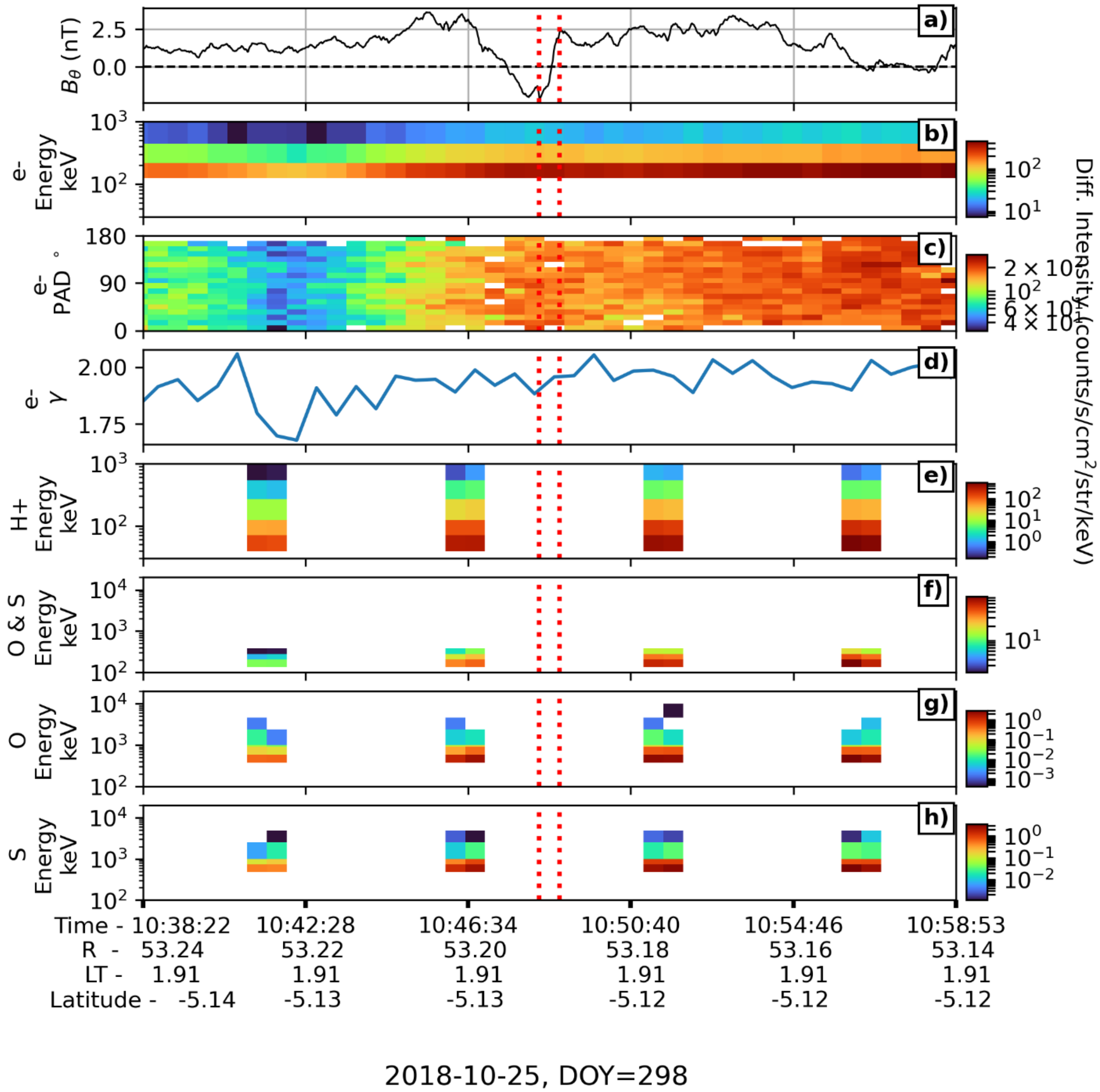

a)
b)
c)
d)
e)
f)
g)
h)
B_θ (nT)
2.5
0.0
e- Energy keV
e- PAD °
e- γ
H+ Energy keV
O & S Energy keV
O Energy keV
S Energy keV
Diff. Intensity (counts/s/cm^2/str/keV)
Time - 10:38:22 10:42:28 10:46:34 10:50:40 10:54:46 10:58:53
R - 53.24 53.22 53.20 53.18 53.16 53.14
LT - 1.91 1.91 1.91 1.91 1.91 1.91
Latitude - -5.14 -5.13 -5.13 -5.12 -5.12 -5.12
2018-10-25, DOY=298

Figure S109

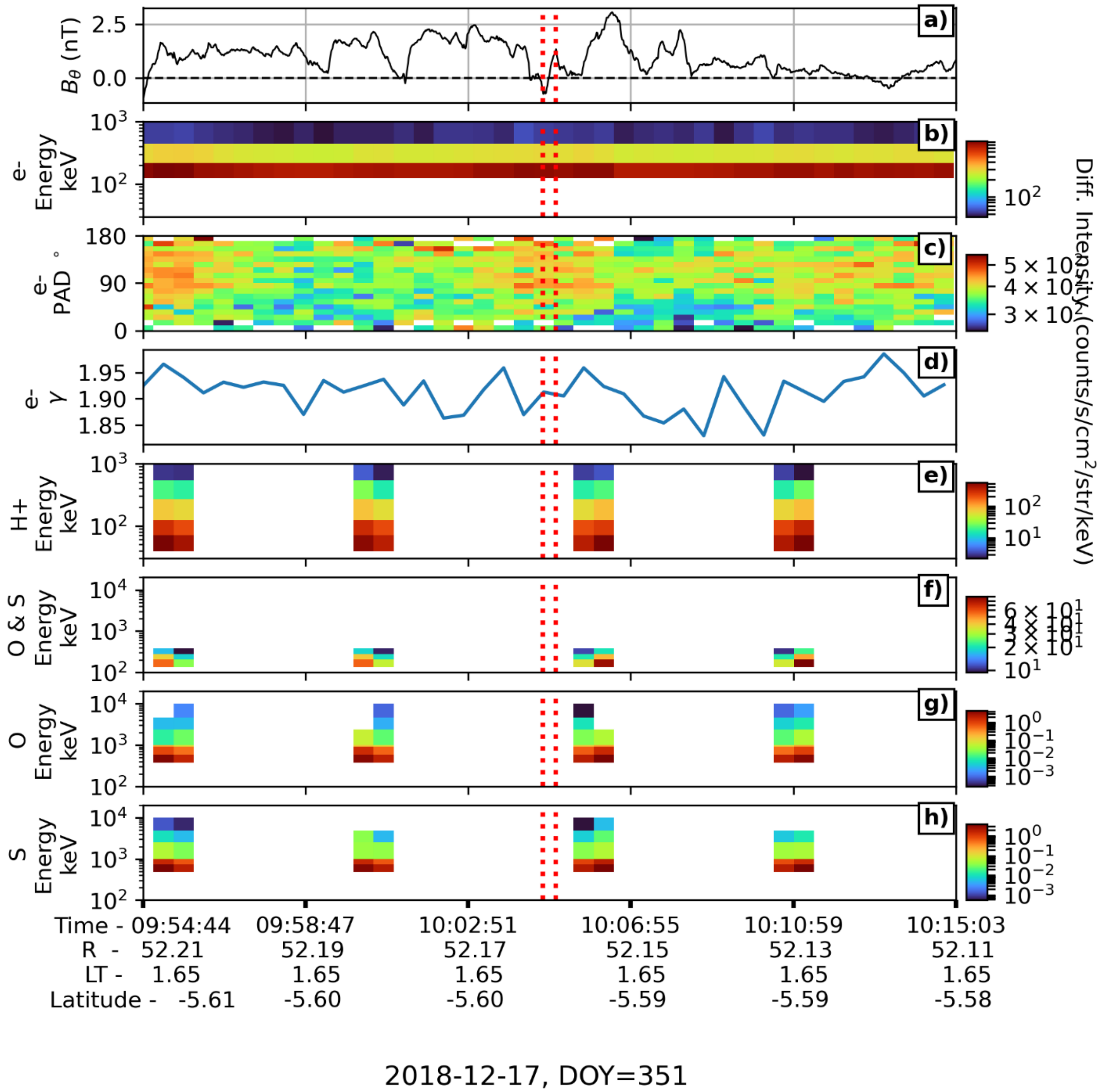

a)
b)
c)
d)
e)
f)
g)
h)
B_θ (nT)
e- Energy keV
e- PAD °
e- γ
H+ Energy keV
O & S Energy keV
O Energy keV
S Energy keV
Diff. Intensity (counts/s/cm^2/str/keV)
Time - 09:54:44 09:58:47 10:02:51 10:06:55 10:10:59 10:15:03
R - 52.21 52.19 52.17 52.15 52.13 52.11
LT - 1.65 1.65 1.65 1.65 1.65 1.65
Latitude - -5.61 -5.60 -5.60 -5.59 -5.59 -5.58
2018-12-17, DOY=351

Figure S110

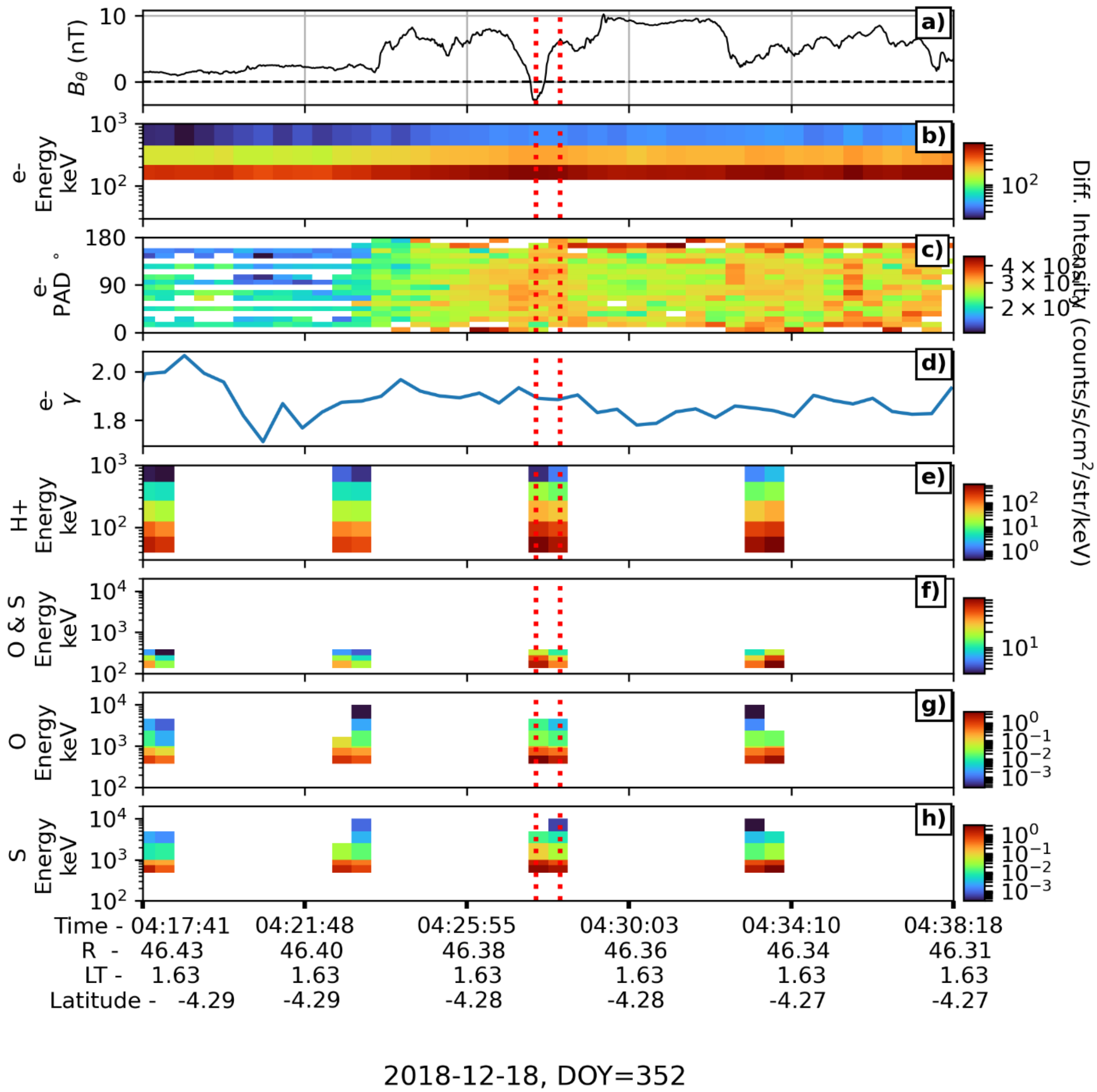

a)
b)
c)
d)
e)
f)
g)
h)
B_θ (nT)
e- Energy keV
e- PAD °
e- γ
H+ Energy keV
O & S Energy keV
O Energy keV
S Energy keV
Diff. Intensity (counts/s/cm²/str/keV)
Time - 04:17:41 04:21:48 04:25:55 04:30:03 04:34:10 04:38:18
R - 46.43 46.40 46.38 46.36 46.34 46.31
LT - 1.63 1.63 1.63 1.63 1.63 1.63
Latitude - -4.29 -4.29 -4.28 -4.28 -4.27 -4.27
2018-12-18, DOY=352

Figure S111

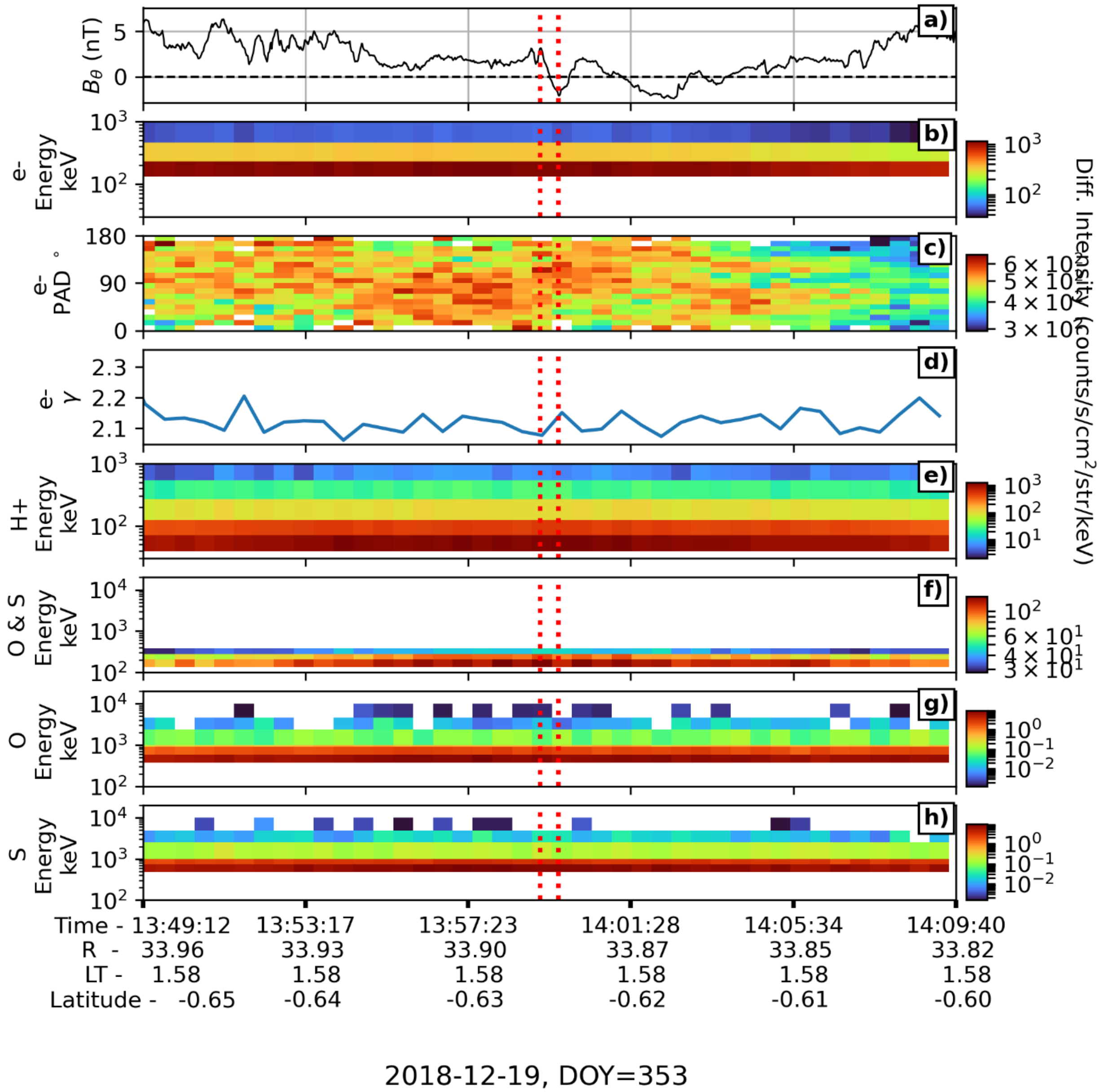

a)
b)
c)
d)
e)
f)
g)
h)
B_θ (nT)
e- Energy keV
e- PAD °
e- γ
H+ Energy keV
O & S Energy keV
O Energy keV
S Energy keV
Diff. Intensity (counts/s/cm²/str/keV)
Time - 13:49:12 13:53:17 13:57:23 14:01:28 14:05:34 14:09:40
R - 33.96 33.93 33.90 33.87 33.85 33.82
LT - 1.58 1.58 1.58 1.58 1.58 1.58
Latitude - -0.65 -0.64 -0.63 -0.62 -0.61 -0.60
2018-12-19, DOY=353

Figure S112

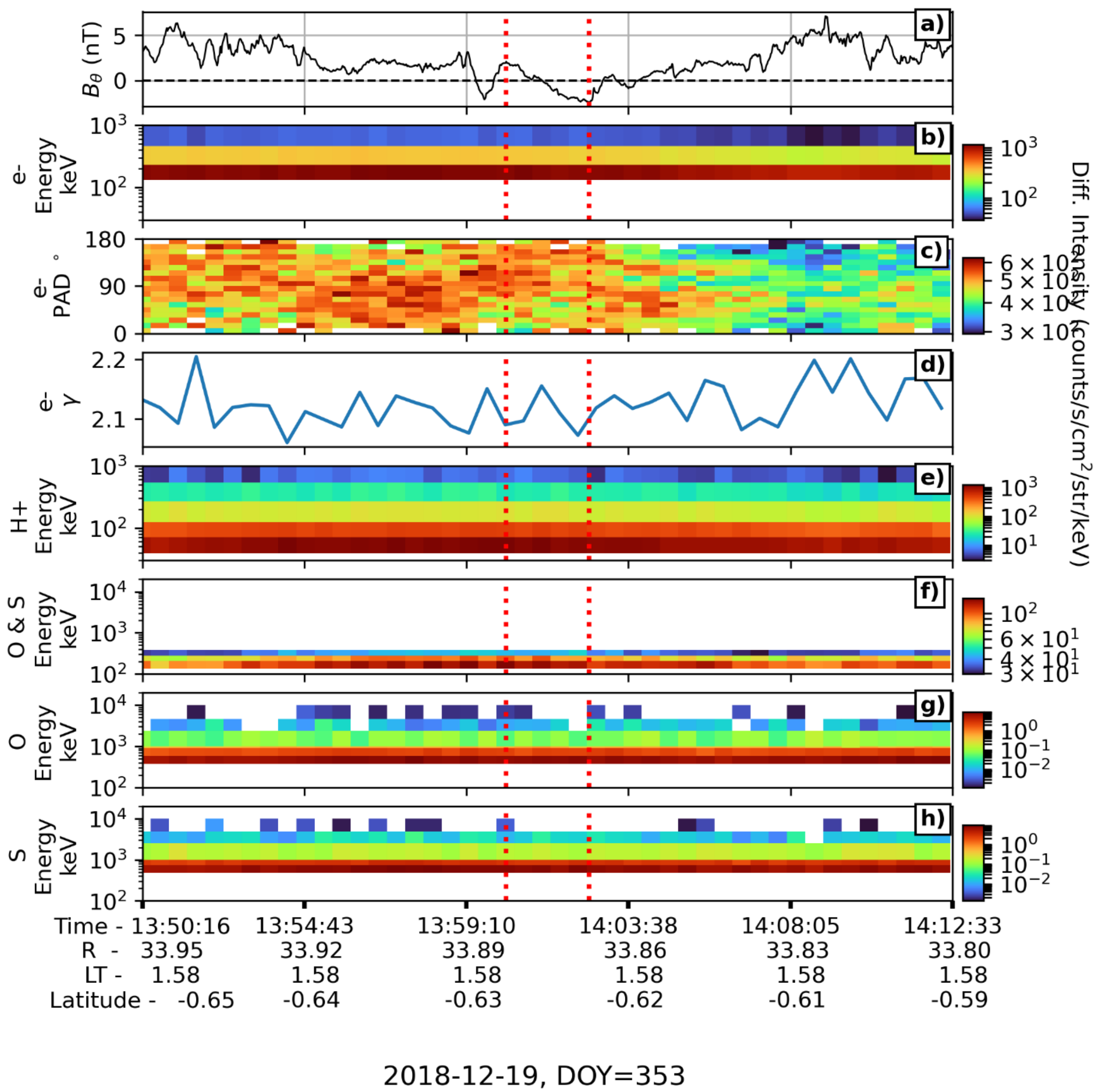
a)
b)
c)
d)
e)
f)
g)
h)
B_θ (nT)
e- Energy keV
e- PAD °
e- γ
H+ Energy keV
O & S Energy keV
O Energy keV
S Energy keV
Diff. Intensity (counts/s/cm^2/str/keV)
Time - 13:50:16 13:54:43 13:59:10 14:03:38 14:08:05 14:12:33
R - 33.95 33.92 33.89 33.86 33.83 33.80
LT - 1.58 1.58 1.58 1.58 1.58 1.58
Latitude - -0.65 -0.64 -0.63 -0.62 -0.61 -0.59
2018-12-19, DOY=353

Figure S113

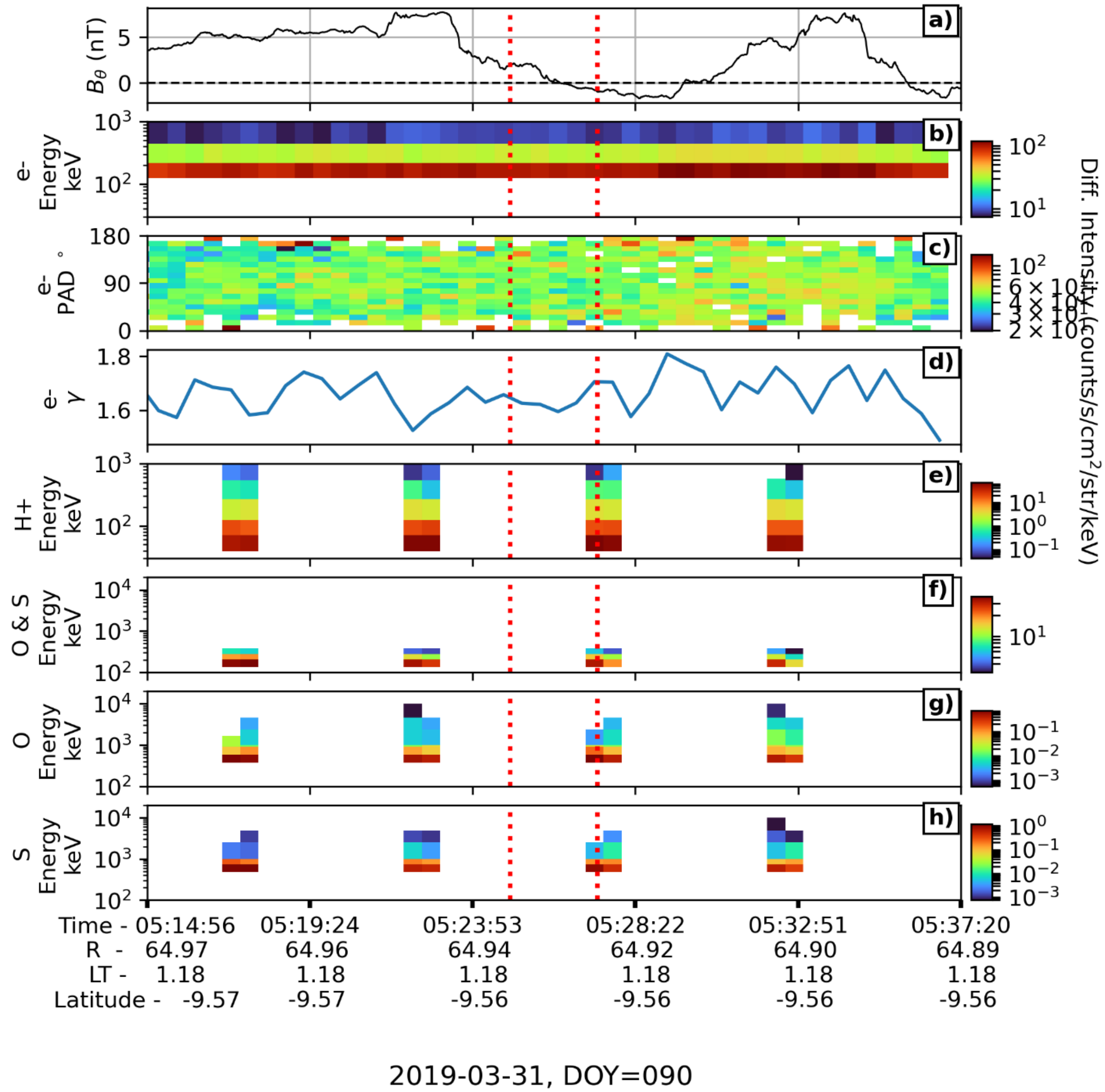

a)
b)
c)
d)
e)
f)
g)
h)
B_θ (nT)
e- Energy keV
e- PAD °
e- γ
H+ Energy keV
O & S Energy keV
O Energy keV
S Energy keV
Diff. Intensity (counts/s/cm²/str/keV)
Time - 05:14:56 05:19:24 05:23:53 05:28:22 05:32:51 05:37:20
R - 64.97 64.96 64.94 64.92 64.90 64.89
LT - 1.18 1.18 1.18 1.18 1.18 1.18
Latitude - -9.57 -9.57 -9.56 -9.56 -9.56 -9.56
2019-03-31, DOY=090

Figure S114

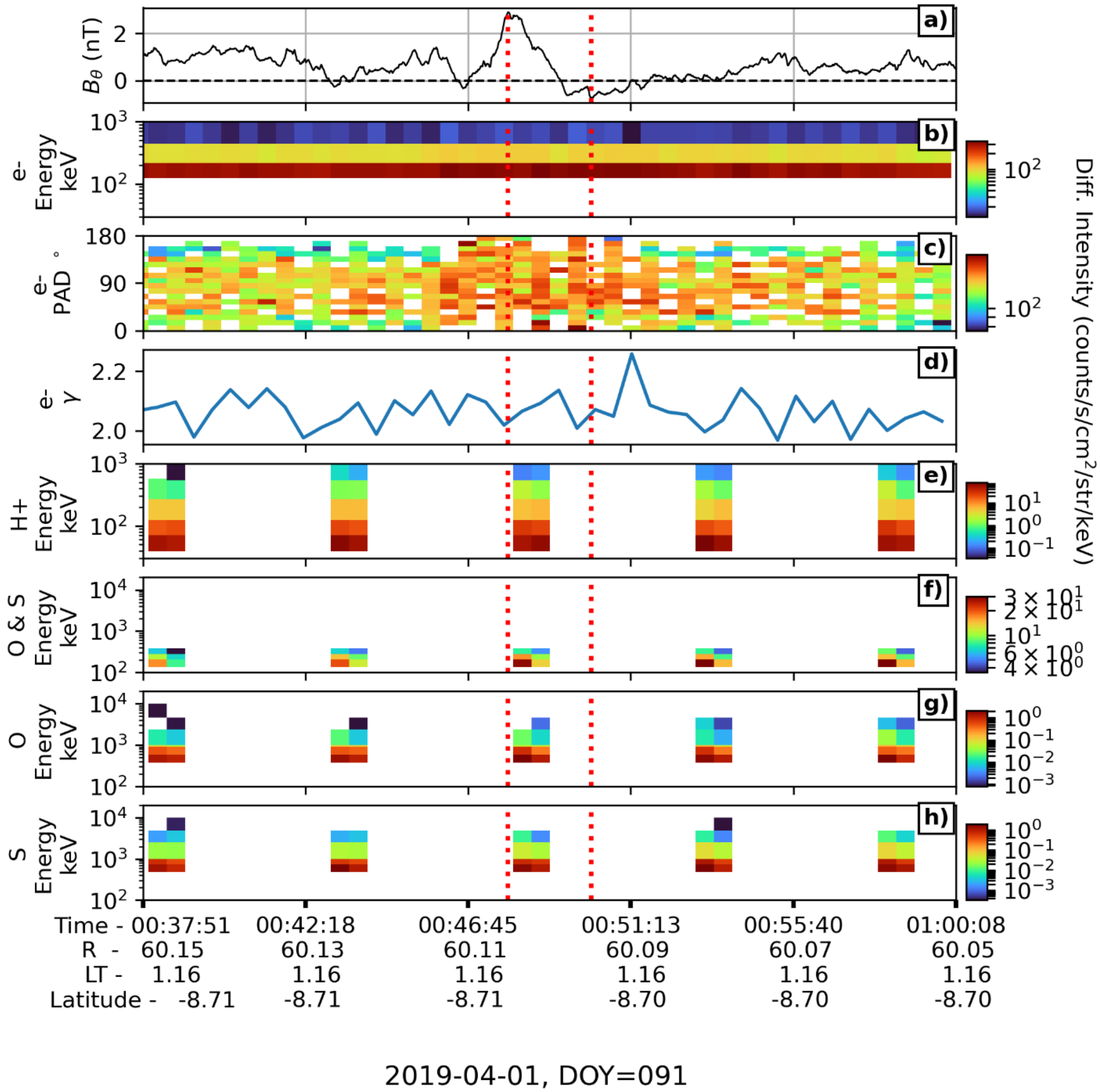

a)
b)
c)
d)
e)
f)
g)
h)
B_θ (nT)
e- Energy keV
e- PAD °
e- γ
H+ Energy keV
O & S Energy keV
O Energy keV
S Energy keV
Diff. Intensity (counts/s/cm^2/str/keV)
Time - 00:37:51 00:42:18 00:46:45 00:51:13 00:55:40 01:00:08
R - 60.15 60.13 60.11 60.09 60.07 60.05
LT - 1.16 1.16 1.16 1.16 1.16 1.16
Latitude - -8.71 -8.71 -8.71 -8.70 -8.70 -8.70
2019-04-01, DOY=091

Figure S115

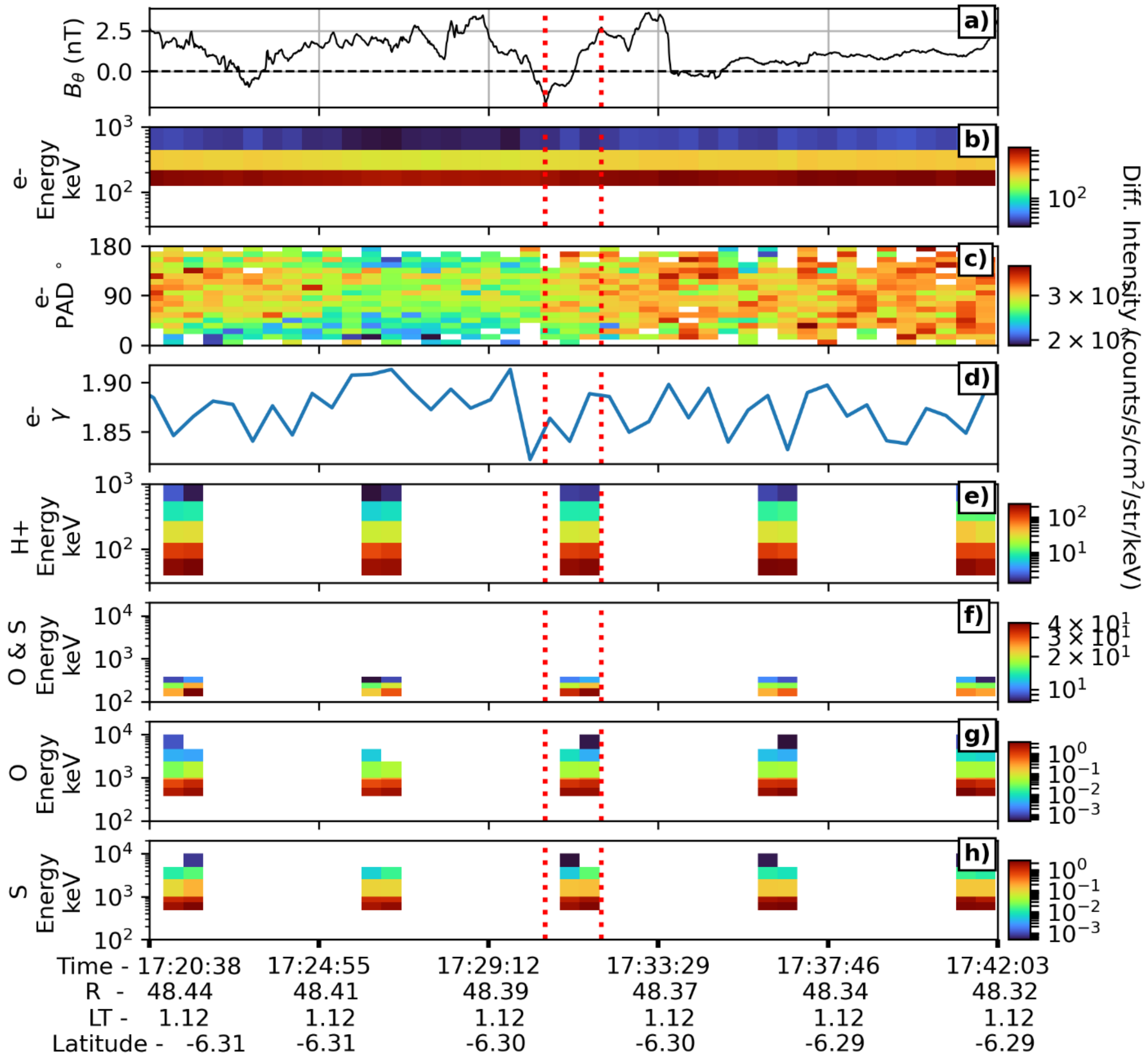

2019-04-02, DOY=092

Figure S116

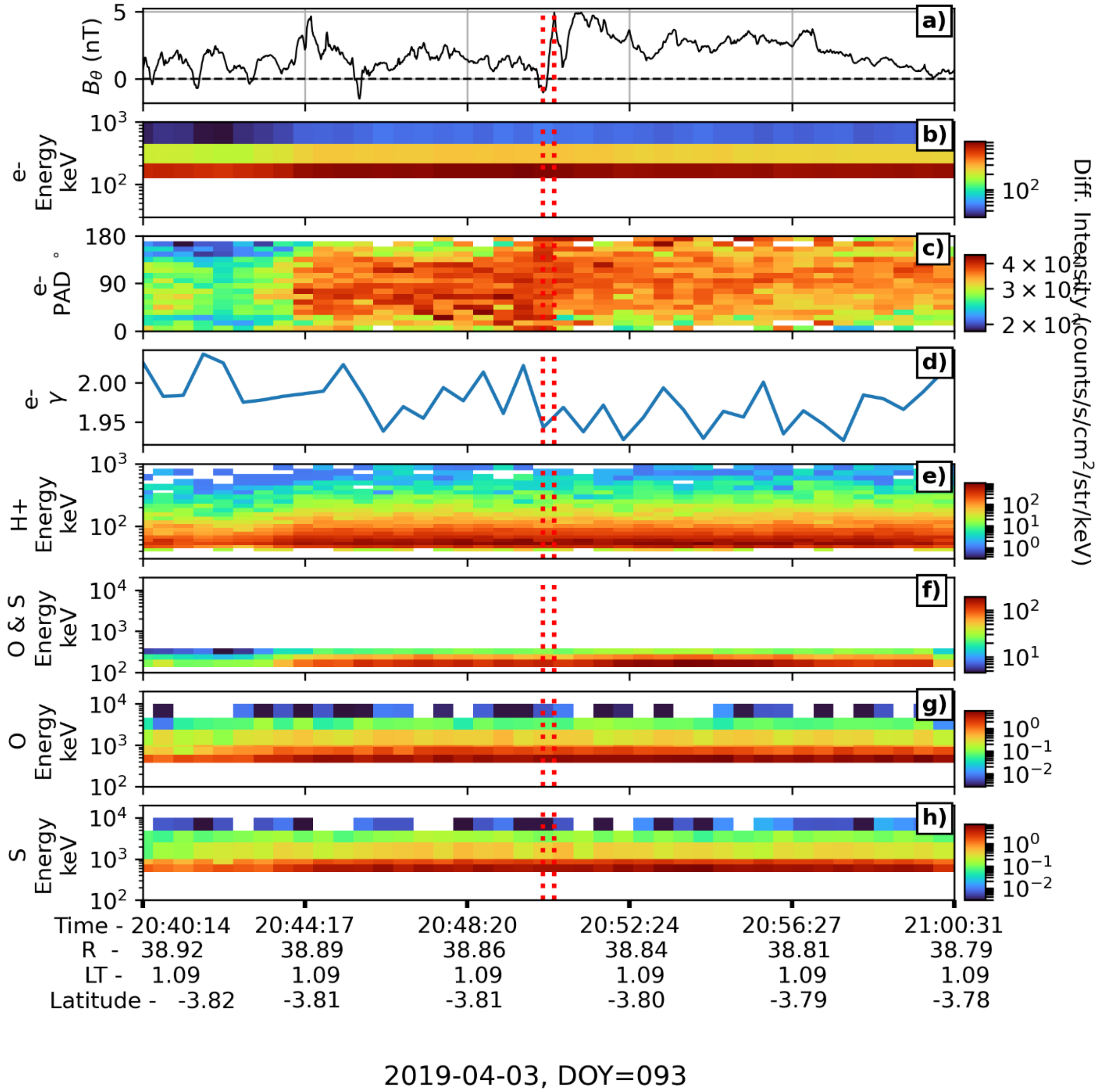

a)
b)
c)
d)
e)
f)
g)
h)
B_θ (nT)
e- Energy keV
e- PAD °
e- γ
H+ Energy keV
O & S Energy keV
O Energy keV
S Energy keV
Diff. Intensity (counts/s/cm^2/str/keV)
Time - 20:40:14 20:44:17 20:48:20 20:52:24 20:56:27 21:00:31
R - 38.92 38.89 38.86 38.84 38.81 38.79
LT - 1.09 1.09 1.09 1.09 1.09 1.09
Latitude - -3.82 -3.81 -3.81 -3.80 -3.79 -3.78
2019-04-03, DOY=093

Figure S117

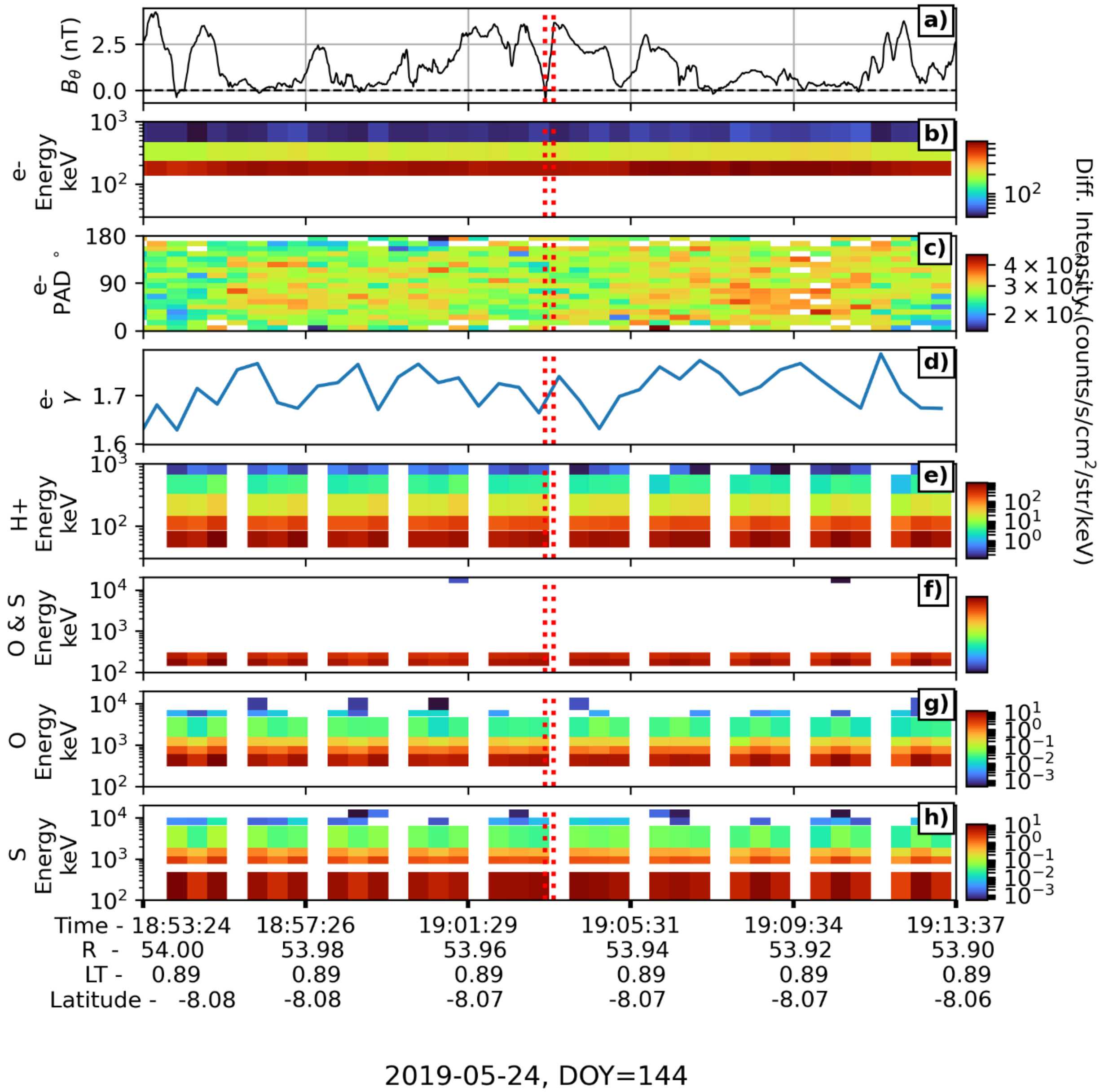
a)
b)
c)
d)
e)
f)
g)
h)
B_θ (nT)
e- Energy keV
e- PAD °
e- γ
H+ Energy keV
O & S Energy keV
O Energy keV
S Energy keV
Diff. Intensity (counts/s/cm^2/str/keV)
Time - 18:53:24 18:57:26 19:01:29 19:05:31 19:09:34 19:13:37
R - 54.00 53.98 53.96 53.94 53.92 53.90
LT - 0.89 0.89 0.89 0.89 0.89 0.89
Latitude - -8.08 -8.08 -8.07 -8.07 -8.07 -8.06
2019-05-24, DOY=144

Figure S118

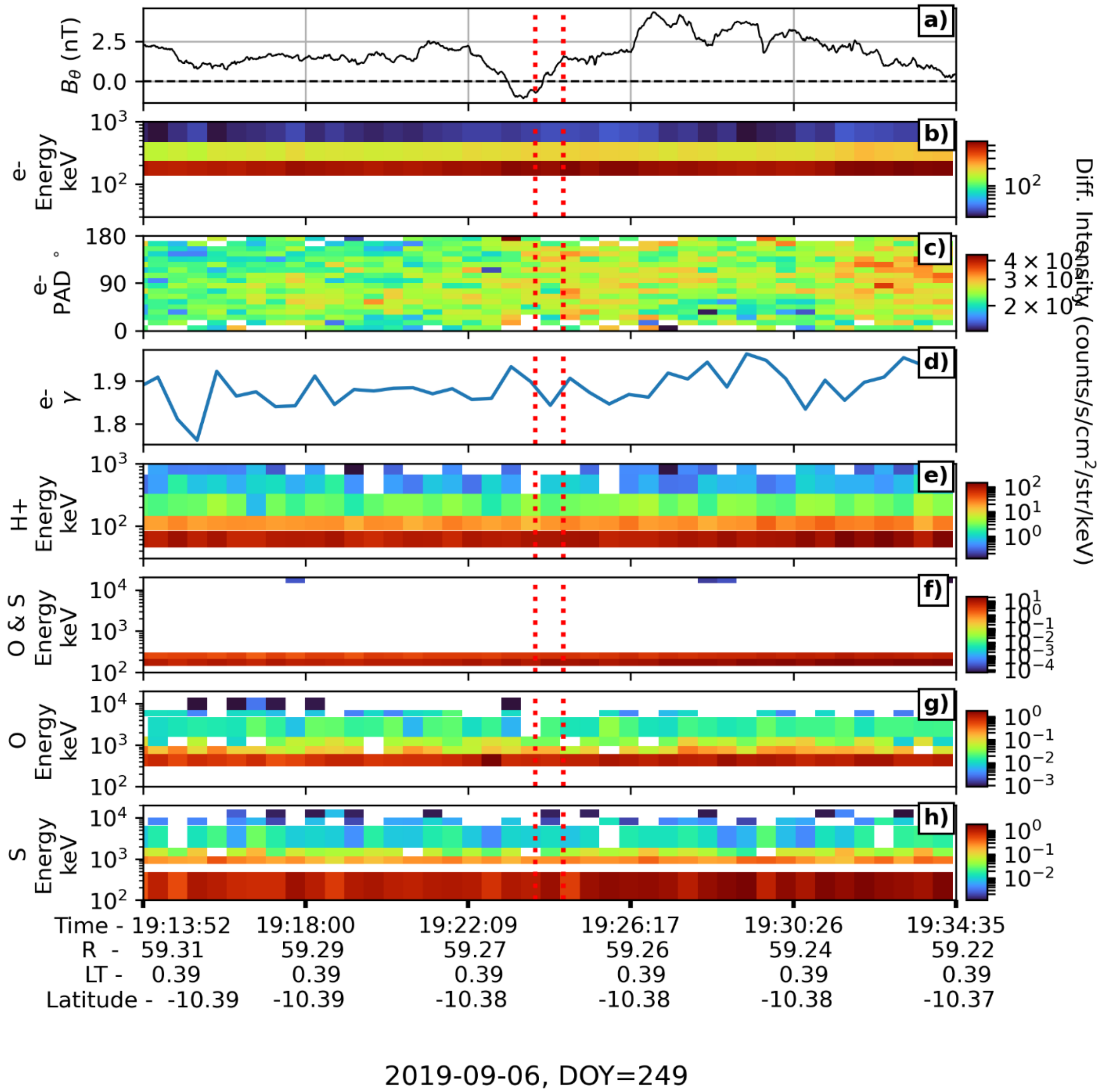
a)
b)
c)
d)
e)
f)
g)
h)
B_θ (nT)
e- Energy keV
e- PAD °
e- γ
H+ Energy keV
O & S Energy keV
O Energy keV
S Energy keV
Diff. Intensity (counts/s/cm^2/str/keV)
Time - 19:13:52 19:18:00 19:22:09 19:26:17 19:30:26 19:34:35
R - 59.31 59.29 59.27 59.26 59.24 59.22
LT - 0.39 0.39 0.39 0.39 0.39 0.39
Latitude - -10.39 -10.39 -10.38 -10.38 -10.38 -10.37
2019-09-06, DOY=249

Figure S119

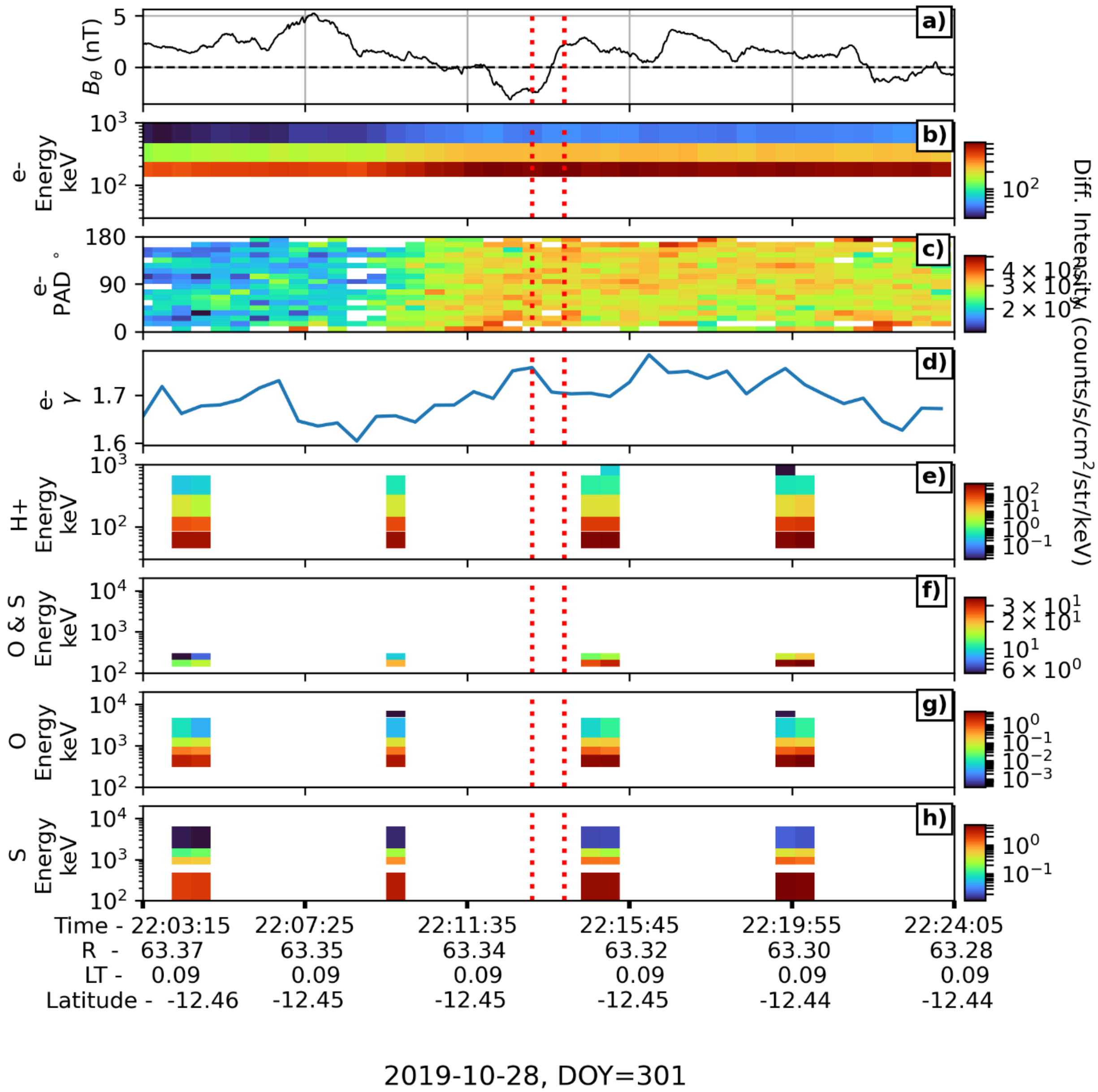
a)
b)
c)
d)
e)
f)
g)
h)
B_θ (nT)
e- Energy keV
e- PAD °
e- γ
H+ Energy keV
O & S Energy keV
O Energy keV
S Energy keV
Diff. Intensity (counts/s/cm^2/str/keV)
Time - 22:03:15 22:07:25 22:11:35 22:15:45 22:19:55 22:24:05
R - 63.37 63.35 63.34 63.32 63.30 63.28
LT - 0.09 0.09 0.09 0.09 0.09 0.09
Latitude - -12.46 -12.45 -12.45 -12.45 -12.44 -12.44
2019-10-28, DOY=301

Figure S120